Universität Hamburg
DER FORSCHUNG | DER LEHRE | DER BILDUNG

GRAVITATIONAL WAVE DETECTION

Tunable Coherence
for straylight suppression in gravitational wave detectors

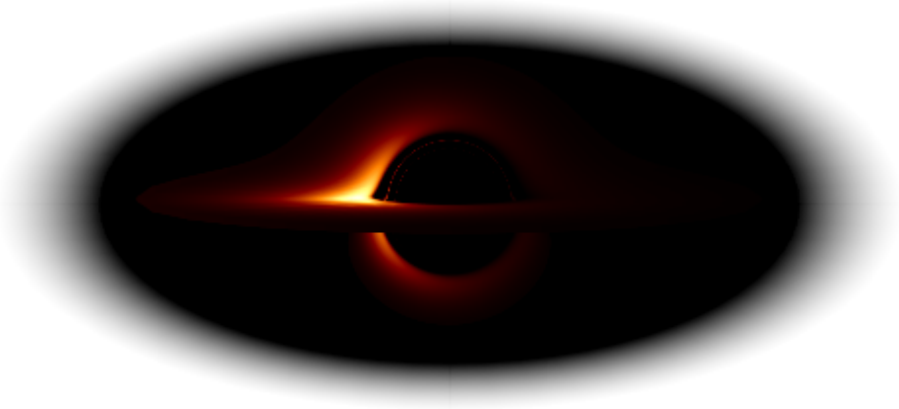

Daniel Jürgen Voigt

Hamburg
2025

The cover art shows a simulated image of a *Schwarzschild* black hole, created using the python-package *luminet* by Bjorge Meulemeester.

The software package simulates and visualizes spherical black holes based on the method described by J.-P. Luminet in
"Image of a spherical black hole with thin accretion disk",
Astronomy & Astrophysics, 75:228-235, May 1979.

Tunable Coherence

for straylight suppression in gravitational wave detectors

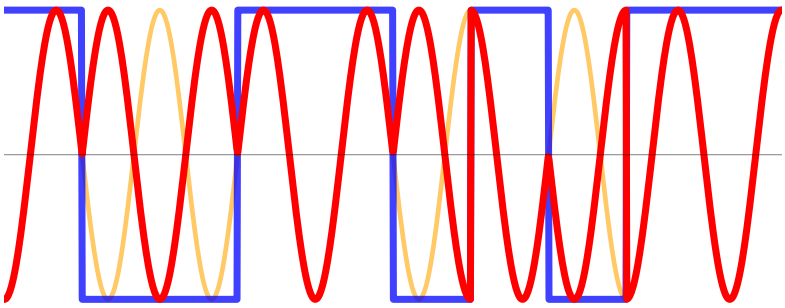

Dissertation
zur Erlangung des Doktorgrades
an der Fakultät für Mathematik, Informatik und Naturwissenschaften
Fachbereich Physik
der Universität Hamburg

vorgelegt von

Daniel Jürgen Voigt

Hamburg
2025

Gutachter der Dissertation:	Prof. Dr. Oliver Gerberding Prof. Dr. Michèle Heurs Prof. Dr. Kirk McKenzie
Zusammensetzung der Prüfungskommission:	Prof. Dr. Oliver Gerberding Prof. Dr. Michèle Heurs Prof. Dr. Katharina-Sophie Isleif Prof. Dr. Ludwig Mathey Prof. Dr. Peter Schleper
Vorsitzender der Prüfungskommission:	Prof. Dr. Ludwig Mathey
Datum der Disputation:	14.08.2025
Vorsitzender des Fach-Promotionsausschusses PHYSIK:	Prof. Dr. Wolfgang Johann Parak
Leiter des Fachbereichs PHYSIK:	Prof. Dr. Markus Drescher
Dekan der Fakultät MIN:	Prof. Dr.-Ing. Norbert Ritter

Abstract

Laser interferometers are highly sensitive to length deviations, making them ideal for detecting gravitational waves. The kilometer-scale detectors used for this are reaching their incredible sensitivity by tackling many different noise sources. One such noise that is gaining more relevance with the increasing detector sensitivities; even beyond quantum mechanical limitations; is induced by straylight. Because it accumulates additional phase by traveling along unintended paths before reentering the readout, it introduces noise limiting the sensitivity, especially at frequencies below 30 Hz. In current detectors, scattered light mitigation is thus already a major effort; achieving even higher sensitivities with future detectors is inconceivable without new straylight mitigation techniques.

In this thesis, *Tunable Coherence* is introduced as a possible new strategy against straylight noise. Further, by conveying *white-light* characteristics to continuous-wave lasers, it advances a nearly unexplored sub-discipline of laser interferometry. The underlying technique, pseudo-random-noise phase modulation, is actively used in ranging and digital interferometry. Employing it at GHz-frequencies on the main laser of a gravitational wave observatory is, however, an audacious proposal. *Tunable coherence* intentionally breaks and controls the coherence of a continuous-wave laser. This leads to coherence loss for unwanted light fields differing in propagation delay, which suppresses their interference. However, it also complicates aspects like resonant power build-up and adds tight constraints on optical layouts. It therefore needs to be demonstrated and verified meticulously that the detectors operation is not negatively impacted by *tunable coherence*.

With this work, initial milestones of this process were achieved, as well as future challenges and opportunities identified. Experimental validation in a Michelson interferometer showed straylight suppression exceeding 40 dB while reducing the coherence length to a few centimeter. Compatibility of *tunable coherence* with optical cavities was then demonstrated with the artificial coherence length reduced down to the wavelength-scale. Optical layouts of gravitational wave detectors combine an interferometer with cavities used to reduce shot noise and increase sensitivity. *Tunable coherence* was demonstrated with such combinations by investigating a power-recycled Michelson interferometer. Here, general compatibility but also first limitations in its current implementation were observed.

The obtained results demonstrate *tunable coherence* as a promising tool for straylight suppression in high precision interferometers. Thus prompting the provided initial study of a possible implementation in current or planned gravitational wave detectors for helping advance low-frequency sensitivity. As these advances enable earlier, longer and more numerous detections, they open new opportunities for e.g. multi-messenger astronomy.

Kurzzusammenfassung

Laser Interferometer sind aufgrund ihrer hohen Sensitivität gegenüber Längenänderungen ideal für die Detektion von Gravitationswellen geeignet. Um die hierfür benötigten besonders hohen Sensitivitäten zu erreichen, müssen die kilometerlangen Detektoren viele verschiedene Rauschquellen überkommen. Eine dieser Rauschquellen wird von Streulicht verursacht und gewinnt durch die immer besser werdenden Sensitivitäten; sogar über quantenmechanische Limitierungen hinaus; immer mehr Relevanz. Da Streulicht auf ungewollten Wegen durch den Detektor zusätzliche parasitäre Phaseninformation aufsammelt, bringt es Rauschen in die Auslesung ein, wenn es in diese gelangt. Dieses Rauschen ist insbesondere im Bereich der Messbandbreite unterhalb von 30 Hz limitierend. In aktuell betriebenen Detektoren ist Streulichtunterdrückung daher bereits eine enorme Herausforderung; das Erreichen der noch höheren Sensitivitäten in geplanten Detektoren ist ohne neue Konzepte hierfür undenkbar.

Mit dieser Arbeit wird das Konzept *Tunable Coherence* als mögliche neue Strategie gegen Streulicht vorgestellt. Durch das Übertragen von Weißlichteigenschaften auf einen Dauerstrichlaser erweitert es außerdem ein nahezu unerforschtes Teilgebiet der Laserinterferometrie. Bisher wird das hierfür genutzte Prinzip, die Phasenmodulation des Lasers mit einer pseudo-zufälligen Sequenz, in Bereichen von Satellitenortung und digitaler Interferometrie eingesetzt. Der Vorschlag, es auch auf den Hauptlaser eines Gravitationswellenobservatoriums anzuwenden, ist hingegen eher gewagt. Mit *Tunable Coherence* wird die Kohärenz des Dauerstrichlasers gezielt gebrochen und die Kohärenzlänge präzise kontrolliert. Dies führt dazu, dass das Streulicht durch seine längeren optischen Wege nicht mehr kohärent mit dem Hauptlaser ist und daher nicht mehr mit der Auslesung interferieren kann. Es hat allerdings den Nachteil, dass der Betrieb eines optischen Aufbaus durch zusätzliche Einschränkungen für beabsichtigte Interferenzerscheinugen komplizierter wird. Deshalb muss der Einfluss, positiv und negativ, von *Tunable Coherence* auf einen Gravitationswellendetektor vor einem potenziellen Einbau gründlich geprüft werden.

Als Teil dieser Arbeit wurden erste Meilensteine dieser Überprüfung erreicht und zukünftige Herausforderungen identifiziert. In experimentellen Demonstrationen konnte eine Streulichtunterdrückung von mehr als 40 dB in einem Michelson Interferometer

gezeigt werden. In diesem Fall wurde die Kohärenzlänge auf wenige Zentimeter reduziert. Zusätzlich wurde gezeigt, dass *Tunable Coherence* auch mit optischen Resonatoren funktioniert. Hier wurde die künstlich eingeführte Kohärenzlänge auf wenige Wellenlängen reduziert. Da Gravitationswellendetektoren in ihrem optischen Aufbau aus einer Kombination eines Interferometers mit weiteren Resonatoren bestehen, wurde die Kompatibilität von *Tunable Coherence* in einem ähnlichen Aufbau demonstriert. Hierfür wurde ein Michelson Interferometer mit einem zusätzlichen Resonator zum Überhöhen der internen Lichtleistung genutzt. In diesem Aufbau konnte *Tunable Coherence* generell demonstriert werden aber es wurden erste Einschränkungen, verursacht durch die momentane Realisierung, beobachtet.

Die gesammelten Ergebnisse zeigen, dass *Tunable Coherence* ein vielversprechendes Mittel für Streulichtreduktion in hochpräzisen Interferometern sein kann. Es wurde daher ein vorläufiges Konzept erarbeitet wie eine mögliche Realisierung in derzeitigen oder zukünftigen Gravitationswellendetektoren aussehen könnte um die Sensitivität dieser im niedrigfrequenten Bereich zu verbessern. Solche Verbesserungen würden viele neue Möglichkeiten für zum Beispiel Multi-Messenger Astronomie bringen, da sie mehr Detektionen und diese früher und für längere Zeitspannen ermöglichen würden.

Contents

1 Introduction

Highly coherent light emitted by a stabilized laser is one of the, if not the most, precise measurement tool currently known. It routinely enables measurement sensitivities limited by quantum noise and can even surpass this standard quantum limit with specifically prepared, squeezed, states. While its application in laser interferometry focuses on the measurement of length changes with extremely high precision, other quantities like rotation and velocity can be measured by using the appropriate interferometer layout. Further, many high precision measurements use laser light, if not as the measure directly, as a tool to access the quantity of interest. For example, using the narrow linewidth of a continuous-wave laser, atomic transitions can be accessed allowing for laser-cooling of atoms. This in turn helps in e.g. the construction of highly precise atomic-clocks. In fact, the working principle of a laser itself is based on the excitation and subsequent stimulated emission of photons by atomic transitions. This allows to take advantage of transitions featuring a narrow linewidth and the accompanying frequency stability and transfer them to the light. The created continues-wave laser inherently achieves a significantly lower linewidth and thus stable wavelength than other light sources; and it can be further stabilized by external references to even surpass its fundamental natural linewidth.

It is therefore no surprise that the first direct measurement of a gravitational wave on the 14th of September 2015 was realized using laser interferometers. This achievement, accomplished by the two Laser Interferometer Graviational-Wave Observatory (LIGO) [1] detectors in Hanford (Washington, USA) and Livingston (Louisiana, USA) is today known as event GW150914 [2, 3].

Since then, many more detections were made, and the current network of second-generation ground-based gravitational wave detectors (GWDs) [4] extended and further improved. It consists of the mentioned two Advanced LIGO detectors, the Advanced[1] Virgo [5] detector near Pisa in Italy, the Kamioka Gravitational Wave Detector (KAGRA) [6] near Toyama in Japan and the GEO600 [7] detector near Hanover in Germany. So far, only the first three were able to reach high enough sensitivities for contributing to any detections. Of the others, KAGRA is designed to reach higher sensitivities but incorporates new technologies starting to bridge the gap to future, so-called third-generation, detectors. GEO600 on the other hand is limited due to its shorter arm length, but did and

[1] The current iteration as second generation detector of the Virgo and the LIGO detectors officially includes the *Advanced* in the name, for convenience this is dropped throughout the rest of this thesis.

does function as a technology test-bed for the current detectors. It was, for example, the first detector to operate with squeezed light [8], successfully demonstrating this prior unproven technology which is nowadays standard in all detectors.

With the so far detected gravitational wave events, interesting new insights into the universe [2, 9, 10] and important contributions to multi-messenger astronomy were gained [11]. To further exploit these capabilities, new and improved detectors are being proposed. With their development and anticipated construction, gravitational wave detection reaches the era of third-generation detectors. Two notable candidates in this regard are Cosmic Explorer (CE) [12, 13] and the Einstein Telescope (ET) [14]. These will not only generally increase sensitivity by around an order of magnitude at a few hundred Hz but, especially for ET, by several orders of magnitude on the low-frequency side below about 30 Hz. Due to many different noise sources, the most relevant ones are further discussed in Chapter 2, this is an immensely challenging task. The resulting scientific benefits and achievements are, however, likewise immense [15, 16], and thus strongly motivating the effort. Specifically improvements at low frequencies could be greatly beneficial for multi-messenger astronomy and also give access to new sources of gravitational waves.

For all these detectors, straylight is a limiting and challenging to reduce noise source, especially towards the low-frequency side of their detection band. Identifying and in the best case subsequently mitigating some of it was possible in the first and the currently operating detectors. However, there is a noticeable gap between the sum of all identified individual noise sources and the total measured noise in the current detectors, the *mystery* noise. This discrepancy is largely accredited to unidentified, thus unknown straylight sources [17, 18]. Further, with achieved improvements in detector sensitivities, the impact of straylight on it becomes increasingly apparent [18], constituting the projection that there could be more, so far undiscovered *mystery* noise. It is thus unclear what other straylight noise contributions might be encountered, especially when pursuing the significant improvements in sensitivity for third-generation detectors. To put this in perspective, as the induced noise scales with straylight power, a recoupling with only 10^{-24} W/W efficiency becomes a limiting factor [19]. Even for the considered circulating power in ET of up to megawatts, this constitutes only about a photon per second. Improving the resilience of the detectors towards straylight is therefore a crucial effort which needs innovative approaches. At the current level, a point has been reached where implemented mitigation techniques like baffles are starting to be problematic themselves [18, 20, 21]. Thus it is very risky to rely on realizing the desired improvements without introducing new ideas and concepts for advanced mitigation techniques.

With this work, a possible alternative concept for straylight mitigation called *Tunable Coherence* is presented and investigated. It relies on pseudo-random-noise (PRN) phase modulation to break and control the coherence of a continuous-wave laser such that a

pseudo-white-light interferometer can be realized. As such, it uses the inherent delay difference of straylight to inhibit it from coherently interfering and thus recoupling with the detector readout. Due to the attributes newly added to the laser light, *tunable coherence* might also be beneficial for other applications even beyond straylight control. The focus of this thesis remains, however, the experimental demonstration and initial investigations and discussion directed towards its implementation for straylight mitigation.

Structure of this thesis

In Chapter 2, the basics of gravitational waves (GWs), their detection and the resulting motivations for this work are laid out. The characteristics and problems arising from straylight in GWDs and laser interferometers in general are presented in Chapter 3. Here, mitigation techniques, current conventional and other investigated concepts are also discussed. Their limitations and the strict requirements for straylight reduction needed in order to realize further sensitivity improvements in current and third-generation detectors motivate the study of new approaches. Chapter 4 presents one of the two techniques investigated as part of this work, with the results of this published in Lohde et al. [22].
The core concept behind the second technique, called *tunable coherence* is presented in detail in Chapter 5. Here, its origins are explained to motivate why transferring techniques used in digital interferometry (DI) to an all-optical approach would be beneficial. As a first impression, Chapter 6 then follows with simulation results of using *tunable coherence* to suppress scattered light in a Michelson interferometer. These also give a first positive impression of its interaction with an optical resonator, encouraging further experimental verification. All simulation results were published in Voigt et al. [23, 2023].
Following that, Chapter 7 to 10 present and discuss experimental results, starting with the implementation of *tunable coherence* in Chapter 7. Chapter 8 then discusses its use in the Michelson and Sagnac interferometer topologies, experimentally demonstrating its ability to suppress straylight. Some of the results in the Michelson and the results from the Sagnac interferometer were published in Voigt et al. [24, 2025] and Eggers et al. [25] respectively. The implications of using *tunable coherence* with optical resonators are the focus of Chapter 9, demonstrating that these can function with the use of *pseudo-white-light*. Some of the there presented results are also part of the publication Voigt et al. [24, 2025]. For a first demonstration in a layout closer resembling a gravitational wave detector, initial investigations of using *tunable coherence* in a power-recycled Michelson interferometer are presented in Chapter 10.
The thesis closes by providing an in-depth discussion of the results and current status of *tunable coherence*, together with an initial study of its possible implementation in Chapter 11. And finally, a conclusion in Chapter 12.
All publications resulting from this work are listed in the List of Publications.

2 | Gravitational Waves

In 1916, Albert Einstein published his *General Theory of Relativity (GR)* [26][2] which lead to a new understanding of gravity and the universe. GR describes gravity as a geometrical property of the four-dimensional spacetime and is a generalization of Einsteins *Special Relativity* [27] published in 1905. This earlier theory, and the Lorentz transformations, introduced the idea that the three space coordinates and the time coordinate are not separate but have to be seen as one continuum – spacetime. The Minkowski space and its metric[3] $\eta_{\mu\nu} = \text{diag}(-1, 1, 1, 1)$ [28] is the most common and one of the simplest descriptions of flat spacetime. As no mass or energy is present, it describes empty space without gravitation; thus one must turn to GR for the effects of gravity to be considered.

2.1 A short derivation

The core of GR are Einstein's field equations given by

$$G_{\mu\nu} \equiv R_{\mu\nu} - \frac{1}{2} R\, g_{\mu\nu} = \frac{8\pi G}{c^4} T_{\mu\nu} \tag{2.1}$$

where $G_{\mu\nu}$ is the Einstein tensor, which is a combination of the Ricci tensor $R_{\mu\nu}$, the curvature scalar R and the metric $g_{\mu\nu}$. On the right side, $T_{\mu\nu}$ is the energy-momentum tensor, G the Newtonian gravitational constant and c the speed of light in vacuum. Thus, the field equations relate the local difference to Euclidean space, the curvature, of a metric; given on the left side; to the present density and flux of energy and momentum; given on the right side. Or, in other words, express that:

> Spacetime tells matter how to move; matter tells spacetime how to curve.
>
> – J. A. Wheeler [29, 30]

Metrics solving these field equations include, for example, the Schwarzschild metric which was the first exact, non-trivial solution [31]. It describes spacetime outside a spherical mass and contains two singularities, of which the one at $r = 0$ is now known to form a black hole. The other at r_s vanishes for a different choice of coordinate system, meaning it is only a coordinate singularity, but describes the event horizon of the massive object.

[2] There were actually several publications by Einstein in 1915 and 1916 discussing parts of GR with this one in 1916 being the consolidation of his previous work on the topic.

[3] Whether the signature of the metric is (-+++) as here or (+---) is only a matter of convention.

If the objects radius becomes smaller than this event horizon, it undergoes gravitational collapse and becomes a black hole [32–34]. These most dense objects possible are a very convenient aid in making the detection of gravitational waves feasible.

The existence of gravitational waves as the gravitational counterpart to electro-magnetic (EM) waves had been theorized before. However, Einstein demonstrated in 1916 that they are a direct result of solving the field equations [35]. The derivation of gravitational waves from Eq. 2.1 can be found in many textbooks and literature with varying degree of detail, e.g. in Misner et al. [29] or Flanagan and Hughes [36]. A short derivation summarizing Misner et al. [29] can be found in Saulson [37]. Following this and other sources [29, 36] for some more detail, a wave equation can be derived from Einsteins field equation (eq 2.1) in linearized gravity. To start with, the metric $g_{\mu\nu}$ is approximated by a small deviation $h_{\mu\nu}$ from the flat Minkowski metric $\eta_{\mu\nu}$:

$$g_{\mu\nu} = \eta_{\mu\nu} + h_{\mu\nu} \qquad \text{with} \qquad \| h_{\mu\nu} \| \ll 1. \tag{2.2}$$

From this, the Ricci tensor and curvature scalar need to be calculated from the Riemann tensor to construct the linearized Einstein tensor $G_{\mu\nu}$. Thus, the Christoffel symbols Γ^i_{jk} describing the affine connection and parallel transport are needed. They are given by

$$\Gamma^i_{jk} = \frac{1}{2} g^{im} \left(\partial_k g_{mj} + \partial_j g_{mk} - \partial_m g_{jk} \right) \tag{2.3}$$

and linearized in $h_{\mu\nu}$ become

$$\Gamma^\mu_{\alpha\beta} = \frac{1}{2} \eta^{\mu\nu} \left(\partial_\beta h_{\nu\alpha} + \partial_\alpha h_{\nu\beta} - \partial_\nu h_{\alpha\beta} \right) \equiv \frac{1}{2} \left(\partial_\beta h^\mu{}_\alpha + \partial_\alpha h^\mu{}_\beta - \partial^\mu h_{\alpha\beta} \right). \tag{2.4}$$

The Riemann tensor R_{ijkl} contains products of form $\Gamma^i_{km}\Gamma^m_{lj}$, which are of second order in h and thus neglected, and additional derivatives of Γ^i_{jk}. Thus, the Ricci tensor and curvature scalar R feature second derivatives:

$$\begin{aligned} R_{\mu\nu} \equiv R^\alpha{}_{\mu\alpha\nu} &= \eta^{\alpha\beta} R_{\alpha\mu\beta\nu} \approx \partial_\alpha \Gamma^\alpha_{\mu\nu} - \partial_\nu \Gamma^\alpha_{\alpha\mu} \\ &= \frac{1}{2} \left(\partial_\alpha \partial_\nu h^\alpha_\mu + \partial_\alpha \partial_\mu h^\alpha_\nu - \Box h_{\mu\nu} - \partial_\nu \partial_\mu h^\alpha_\alpha \right) \end{aligned} \tag{2.5a}$$

$$\begin{aligned} \text{and} \quad R \equiv \eta^{\mu\nu} R_{\mu\nu} &= \frac{1}{2} \left(\partial_\alpha \partial^\mu h^\alpha_\mu + \partial_\alpha \partial^\mu h^\alpha_\mu - \Box h^\mu_\mu - \partial_\mu \partial^\mu h^\alpha_\alpha \right) \\ &= \partial_\alpha \partial^\mu h^\alpha_\mu - \Box h^\mu_\mu. \end{aligned} \tag{2.5b}$$

Here, the Minkowski metric $\eta_{\mu\nu}$ was used for raising and lowering of indices and contracting the Riemann tensor to the Ricci tensor and further to the curvature scalar R. Additionally, the two last terms in the second Christoffel symbol $\Gamma^\alpha_{\alpha\mu}$ canceled and the d'Alembert or wave operator $\Box = \partial_\mu \partial^\mu = \nabla^2 - \frac{1}{c^2}\partial_t^2$ was introduced. Entering this into the field equations directly is still complex, however, choosing a useful coordinate system

– the *transverse* ($\partial_i h_{ij} = 0$) and *traceless* ($h^\mu_\mu = 0$) or TT-gauge – simplifies it. In these coordinates, being described by the world-lines of free falling test masses, the expression becomes

$$-2G_{\mu\nu} = \Box\, h_{\mu\nu} = \left(\nabla^2 - \frac{1}{c^2}\partial_t^2\right) h_{\mu\nu} = -\frac{16\pi G}{c^4} T_{\mu\nu} \tag{2.6}$$

or in vacuum:

$$\Box\, h_{\mu\nu} = \left(\nabla^2 - \frac{1}{c^2}\partial_t^2\right) h_{\mu\nu} = 0. \tag{2.7}$$

These wave equations show that the elements of $h_{\mu\nu}$ can be described as plane waves $h\cos(k_\alpha x^\alpha) = h\cos(\omega t - \vec{k}\cdot\vec{x})$ with amplitude h, the light-like wave-vector $k_\alpha = (\frac{\omega}{c}, \vec{k})$ and thus frequency $f = \frac{|\vec{k}|}{2\pi c}$; propagating at the speed of light – gravitational waves.

The constraints placed on $h_{\mu\nu}$ by the choice of TT-gauge, transverse and traceless, give rise to two possible orthogonal polarizations of these gravitational waves:

$$\hat{h}_+ = \begin{pmatrix} 0 & 0 & 0 & 0 \\ 0 & 1 & 0 & 0 \\ 0 & 0 & -1 & 0 \\ 0 & 0 & 0 & 0 \end{pmatrix} \quad \text{and} \quad \hat{h}_\times = \begin{pmatrix} 0 & 0 & 0 & 0 \\ 0 & 0 & 1 & 0 \\ 0 & 1 & 0 & 0 \\ 0 & 0 & 0 & 0 \end{pmatrix} \tag{2.8}$$

These *plus* and *cross* polarizations represent waves propagating along the $\hat{z}$-direction that can be described by $h_{\mu\nu} = a\hat{h}_+ + b\hat{h}_\times$. The full expression then becomes

$$h_{\mu\nu} = h \begin{pmatrix} 0 & 0 & 0 & 0 \\ 0 & h_+ & h_\times & 0 \\ 0 & h_\times & -h_+ & 0 \\ 0 & 0 & 0 & 0 \end{pmatrix} \cos(\omega t - \vec{k}\cdot\vec{x}) \tag{2.9}$$

where the coefficients a and b were exchanged for h_+ and $h_\times$ respectively.

While these waves do not accelerate or change the coordinates of a single test mass ($\frac{d^2x^\mu}{dt^2} = \partial_0 h_{\mu 0} - \frac{1}{2}\partial_\mu h_{00} = 0$) at linear order, they stretch and compress spacetime orthogonal to their propagation direction. Thereby, they change the *proper* distance $ds^2 = g_{\mu\nu}dx^\mu dx^\nu = 0$ between freely falling test masses. This change of the distance L between two test masses separated by distance L_0 along the x-axis caused by a gravitational wave traveling along the z-axis can be calculated by

$$L = \int \sqrt{ds^2} = \int_0^{L_0} dx \sqrt{1 + h_{xx}} \simeq \int_0^{L_0} dx \left(1 + \frac{1}{2}h_{xx}\right) = L_0 \left(1 + \frac{1}{2}h_{xx}\right). \tag{2.10}$$

The relative change $\delta L/L$ thus becomes

$$\frac{\delta L}{L} \simeq \frac{1}{2}h_{xx} = \frac{1}{2}h_+ \cos(\omega t) \tag{2.11}$$

with the amplitude $h = h_+$ – also known as wave-strain – showing an oscillation of the *proper* distance between the two test masses caused by the gravitational wave.

The strength of this dimensionless amplitude or strain h can be calculated by solving the field equations with a source (eq. 2.6). Examples of this can be found again in various literature (e.g. [29, 36]). However, a simpler approach following e.g. Saulson [37] is looking at the multipole expansion of the gravitational potential which in GR is the metric tensor. From this, the strongest term contributing to radiation can be found analogous to the same approach for EM radiation. While this is simplest for a source with slow internal motion and weak gravity, extending it to the strong gravity case as comprehensively done in e.g. Thorne [38] retains the same description of the strongest contribution.

Contrary to EM radiation, there is only one type of gravitational "charge" which is also equivalent to the body's inertia. The monopole moment therefore corresponds to the total mass or energy of the system, which is conserved and thus has no second derivative. For the dipole component, which corresponds to the center of mass, the first derivative is the total momentum of the system, which is again conserved and thus cannot generate gravitational radiation either. Further, conservation of angular momentum prevents the dipole component defined analogous to the magnetic dipole to generate radiation as it corresponds to the total angular momentum.

Thus, the strongest component allowed to contribute to gravitational radiation is the time variation of the reduced quadrupole moment

$$I_{\mu\nu}(t) \equiv \int \rho(\vec{r}) \left(x_\mu x_\nu - \frac{1}{3}\delta_{\mu\nu} r^2 \right) dV \tag{2.12}$$

leading to the quadrupole formula

$$h_{\mu,\nu}(t, R) = \frac{2G}{Rc^4} \ddot{I}_{\mu\nu}(t - R/c). \tag{2.13}$$

Here R is now the distance from the source, G the gravitational constant, c the speed of light and $\ddot{I}(t - R/c)$ the second time-derivative of the reduced quadrupole moment evaluated at the retarded time. Due to being quadrupole-waves, gravitational waves have a significantly weaker amplitude than EM waves, which can also be seen by the fraction G/c^4, a tiny number (10^{-11}) divided by a very large one (10^{33}).

To get a numerical estimate, one can consider a system of two point masses orbiting each other at a constant frequency $\omega_0 = 2\pi f_0$ and a distance $2r_0$ in the xy-plane, a simple binary system. Calculating the quadrupole moment and its second derivative then yields

$$h_{\mu\nu}(t,R) \approx -\frac{r_{s1}r_{s2}}{r_0 R}\begin{pmatrix} 0 & 0 & 0 & 0 \\ 0 & -\cos(2\omega_0 t) & \sin(2\omega_0 t) & 0 \\ 0 & \sin(2\omega_0 t) & \cos(2\omega_0 t) & 0 \\ 0 & 0 & 0 & 0 \end{pmatrix} \tag{2.14}$$

where the Schwarzschild radius $r_s = 2GM/c^2$ and $f_0^2 = GM/16\pi^2 r_0^3$ were used to simplify the amplitude $h \equiv |h_{\mu\nu}|$ of the perturbation.

With this result, it becomes apparent that to produce a high strain, very massive objects need to orbit each other very closely. Objects best fitting these criteria are black holes as the most massive and compact objects known. Next are neutron stars, which, while less massive, still are compact enough to orbit each other very closely. However, even from two neutron stars of around 1.5 solar masses each, orbiting each other at $r_0 = 20\,\mathrm{km}$ in the nearest galaxy cluster, the strain would only be on the order of $\mathbf{h \approx 10^{-21}}$.

In a revision of his earlier calculations, Einstein published most of these derivations together with discussions which parts of the metric can actually give rise to gravitational waves in 1918 [39]. In this publication, he also showed that gravitational waves carry away energy from the system and calculated the quantity of this energy loss. For many years, these results could not be verified, however, with the discovery of the Hulse-Taylor pulsar (PSR B1913+16) in 1974 [40] and following observations of this binary neutron star system, experimental evidence could be obtained. The decline of its orbital period due to energy being carried away by gravitational waves agrees within less than 0.2 % disparity with Einsteins theory [41].

2.2 Sources of measurable gravitational waves

To directly measure gravitational waves (GWs) on or close to Earth, the only option is constructing a detector capable of measuring relative length deviations on the order of 10^{-21}, the details of which are discussed in the next section. With these detectors, GWs are being detected, however, only few objects are known in the Universe to actually generate waves with such strains. Figure 2.1 shows an overview of sources and detector design sensitivities (see also [42]).

As discussed previously, not every massive object generates GWs, only those having an accelerating multipole moment. This therefore excludes spherical-symmetric objects or dynamics and thus most single body sources. As also seen in Figure 2.1, the most promising sources are binaries of various types. Compact binaries, meaning neutron stars and small ($\lesssim 50$ solar masses) black holes, emit for the current ground-based GW observatories measurable GWs when they inspiral and merge with each other. Additionally, an intermediate mass (100 to 10^5 solar masses) black hole binary has been detected in 2019 [10, 43]

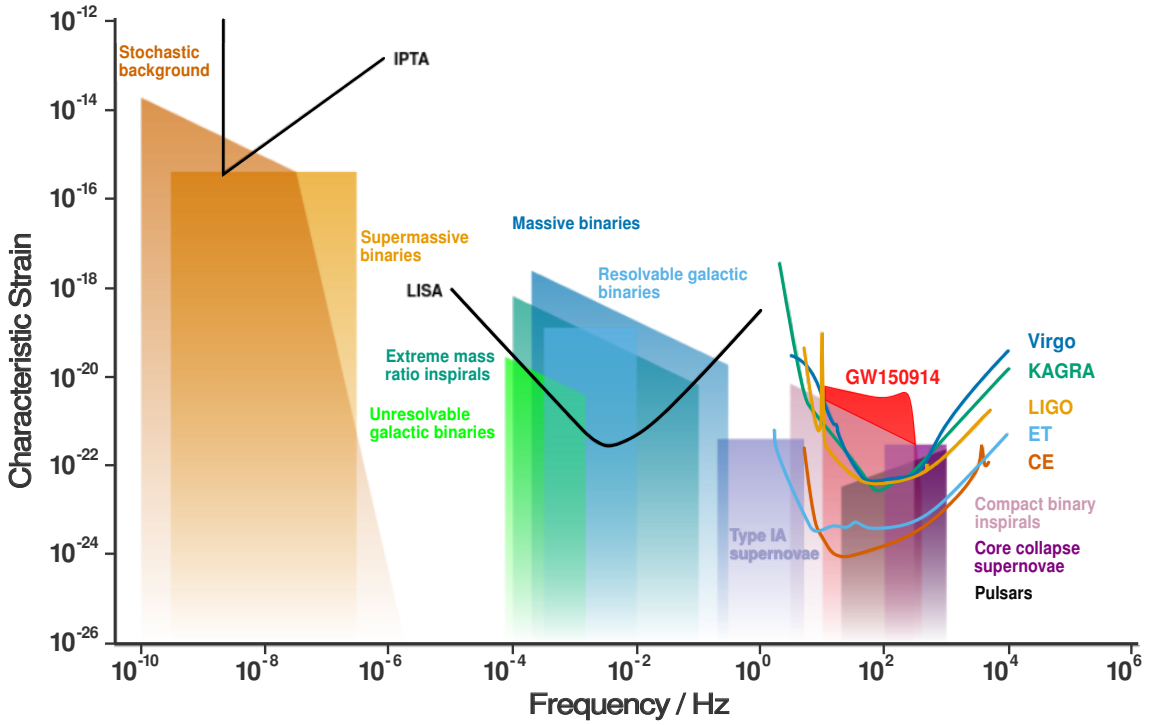

Figure 2.1: Overview of predicted or detected sources for gravitational wave (GW) events shown as a spectrum of their expected frequency with their estimated strain on the y-axis. Also shown are the design sensitivities of several current and planned ground-based detectors in the high-frequencies range, as well as for the LISA mission in the mid-frequency range and the International PTA at the low-frequency end. Not shown is an expected cosmological background at various frequencies. Source: https://gwplotter.com/ [42]

for the first time. An overview of the events detected by the LIGO-Virgo-KAGRA collaboration as of their observation run 3 (O3) can be seen in Figure 2.2.

Binaries of more massive or even supermassive black holes do not get close enough to each other to emit GWs at high enough frequencies for ground-based detection. This is due to the noise limitations these detectors face on Earth below a few Hz. However, with space-based detectors like the planned Laser Interferometer Space Antenna (LISA), more massive sources in the mHz-frequency range become the primary target. These include massive black holes ($10^4 - 10^7$ solar masses) and extreme mass ratio inspirals of stellar-mass sized stars into supermassive black holes. Another important source here are galactic binaries of white dwarfs, which orbit each other at greater distances than neutron stars. Thereby they radiate GWs at frequencies below about a Hz, until their merger results in a type IA supernovae. Due to their abundance and the identification of some detectable system by EM observations, they are the most promising source in this range and also an overlapping of signals into an unresolvable background is expected.

Towards the low frequency end, the collection of sources is complemented by the previously mentioned resolvable supermassive black hole binaries and again a stochastic background created by their high population. These sources in the nHz range are most likely

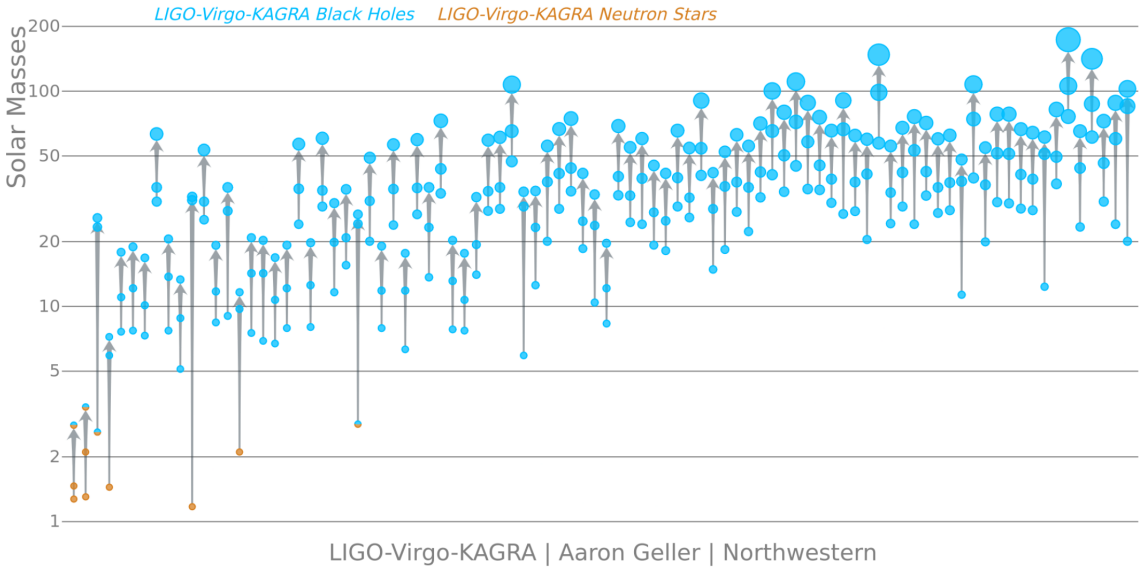

Figure 2.2: Gravitational wave (GW) emitting events detected by the LIGO-Virgo-KAGRA collaboration up to their third observation run (O3). The blue dots represent pre- and post-merger black holes, the orange dots pre- and possibly post-merger neutron stars. The events are sorted by distance along the x-axis and the mass of the initial objects and the resulting object is shown with the y-axis. An interactive version giving the details to each event can be found in the reference. Source: `https://ligo.northwestern.edu/media/mass-plot/index.html` [44]

candidates to be measurable by pulsar timing arrays (PTAs) which measure the change in arrival times of pulses emitted by different pulsars across the sky. These pulses can be timed at the precision level of atomic clocks, especially when done over decade long time-scales. However, the influence of GWs would introduce a specific pattern of spatially correlated variations between different pulsars [45]. And indeed, in 2023 first evidence for a stochastic background of GWs was detected [46]. The estimated sensitivity of the International PTA (IPTA) is depicted as an example for these in Figure 2.1. Additionally, a cosmological stochastic background, the counterpart to the known cosmic microwave background, generated by inflation or phase-transitions in the early Universe is expected at different frequency ranges [47–49] depending on its origin. If detected, this hypothesized background could give insight into the early Universe as GWs are not absorbed by high energy or mass densities. They can therefore have propagated across the Universe from further back in time than EM radiation which was "trapped" due to endless scattering until around 378 000 years after the Big Bang [50].

There are also possibilities of GWs at and above MHz frequencies originating from cosmological phenomena and predictions of beyond standard model physics [51]. As there are no astrophysical sources present in this range, detecting GWs, or a lack of them, there would open a unique possibility for probing such phenomena. For this however, other detector concepts are needed with more details discussed in e.g. Aggarwal et al. [51].

Circling back to the ground-based GW observatories at the here considered higher fre-

quencies; with increased sensitivity, some more interesting sources will become detectable. These include the first single object sources, like core collapse supernovae, which generate GWs if they are not perfectly symmetrical. As this type of supernovae is caused by gravitational collapse of a star once its internal fusion cannot generate enough energy, it has no preceding GW signal. A type IA supernovae on the other hand can be the final event of a white dwarf binary merger and thus generates the typical inspiral GW signal before the event. This might, however, be too weak to detect as a white dwarf can also be feeding on a different companion star instead. As such, especially the proposed Einstein Telescope (ET) might be able to detect at least the final supernovae event but detection of the preceding inspiral remains unlikely. Lastly, another single object source are pulsars or rotating neutron stars themselves if they are not perfectly spherical but have tiny mountains. Due to the enormous density of a neutron star, these can be at most $\sim 10\,\mathrm{cm}$ high but still give rise to a significant quadrupole moment.

All of these sources give interesting new insights into the Universe as detecting the emitted GWs allows to study the sources that generated them. They further also allow searching for otherwise almost unobservable objects like intermediate mass black holes [43]. The waveform of these sources contain a lot of information about e.g. in the case of black holes their masses and spin [2]. If the event also emitted EM waves or particles, this allows for multi-messenger astronomy and studying of extreme events from multiple angles. With the first detected merger of two neutron stars, GW170817 [52], multi-messenger astronomy has been complemented by GWs [11]. The combination of several signals from an event allows for even deeper study of such events. Probing e.g. neutron stars [9] further enables investigation of extreme environments not recreatable in a laboratory and allows to test how our understanding of physics fits to these.

Extending the sensitivity of ground-based gravitational wave detectors (GWDs) especially towards the low-frequencies not only brings new sources into the measurement bandwidth. It also allows for earlier detection of merger events as the frequency of GWs increases towards the collision. Thus, with increased time between first detection and final merger for events creating multiple types of radiation, sky localization and coordinated observation of the different signals can be optimized [53]. Improving the mitigation of straylight noise is a major factor in reaching these higher sensitivities.

2.3 Gravitational wave detection

Besides the indirect detection by e.g. observing the orbital period of binaries or the pulse arrival times over many years with PTAs to measure a background, the direct detection of gravitational waves (GWs) can be done with highly precise interferometers. Currently, all operating and proposed detectors able to detect single events are based

on laser interferometry. While there are other approaches like resonant bars, so-called Weber bars [54], or particle storage rings [55], none of them has so far reached the needed sensitivity or confidently detected GWs. The existing network of interferometric detectors is currently running its fourth observation run O4. Over the accumulated observing time of about 1000 days, it detected more than 200 events and event candidates [18] so far.
To understand how these detectors work, where they are limited and by what noises, the following sections discuss the for this work relevant parts in some detail. Other noise sources, also limiting or problematic are mentioned for comparison, with a focus on the low-frequency side of the detection bandwidth.

2.3.1 Laser interferometry

Splitting a laser beam in two with a beam splitter, sending each of the parts to a mirror at a distance where they are reflected and then recombining them at the original beam splitter creates an interference signal depending on the differential distance traveled by the two beams. This simple description of a Michelson interferometer illustrates directly, why it is a good basis for a GWD if the mirrors are freely falling objects, meaning suspended. As eq. 2.10 and 2.11 show, this length between the beam splitter and mirror at the end of the interferometer arm is changed by a passing GW. Ideally, if the interferometer is perfectly aligned to the polarization of the GW, its two arms are affected in opposite directions by this length change, doubling the differential change between the arms.
The power measured at the output of the interferometer depends, in an ideal simplified case (full derivations follow in later chapters), on the differential length change ΔL as

$$P_{\text{out}} = \frac{P_{\text{in}}}{2}\left[1 + \cos\left(4\pi\frac{\Delta L}{\lambda}\right)\right], \tag{2.15}$$

where P_{in} is the input power and λ the wavelength of the used light. Thus, the changes in distance caused by the GW can directly be measured by the interferometer. However, even in the ideal case the relative differential change in arm length is tiny, on the order of 10^{-21}, so the change in output power is tiny as well. Being able to detect a GW then becomes a question of how small a change in output power can still be measured and how much the influence of the wave on the interferometer can be amplified.

2.3.2 Detector optical layout

To increase the influence of a GW, the layout of a detector – exemplarily shown for the LIGO detectors in Figure 2.3 – is far more complex than the simple Michelson interferometer described before. As the induced strain is relative to the overall length, making the interferometer large is the first step. The current two LIGO detectors for example thus

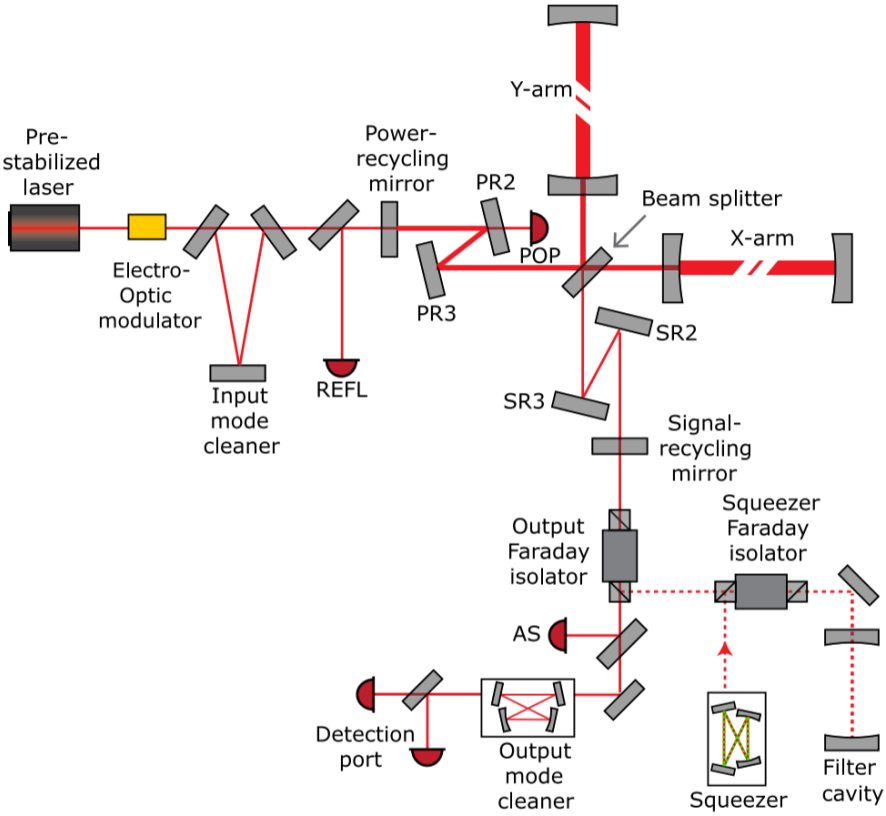

Figure 2.3: Simplified layout sketch of the LIGO detectors. The two arms (X- and Y-arm) of the interferometer are 4 km long cavities, connected via the inner Michelson interferometer between their input mirrors. Additionally two recycling cavities formed by mirrors in both interferometer ports are used for power- and signal-recycling. Both the input and output beams are passed through mode cleaners for spatial mode filtering and frequency dependent squeezed light is injected into the output port for quantum noise suppression. Source: [18, Figure 1]

have an arm length of 4 km and future detectors like ET and CE are planned with 10 km or even 40 km arm length respectively. Another way to maximize the resulting signal is to increase the input power, which also helps in other ways described later. While using a laser with more power is one aspect of this, increasing the power inside the interferometer can additionally be done by using Fabry-Perot cavities (FPCs) in both arms [56, 57]. These cavities, often called arm cavities, increase the circulating power due to their resonance enhancement or in other words let the light experience the length change due to the GW many times while it is circulating in the cavity. A similar approach is the use of a power-recycling cavity (PRC) which is created by keeping the interferometer at an operating point where all the light is effectively back-reflected to the laser. Placing a mirror, the power-recycling mirror (PRM), between the laser and the interferometer then creates another cavity that resonantly enhances the power inside the interferometer [58, 59].
A similar approach as the power-recycling for increasing the circulating power is used for the signal. By placing a partially reflective mirror, the signal-recycling mirror (SRM), in the signal output port, a signal-recycling cavity (SRC) is formed [60, 61]. This enhances

the signal created in the interferometer, effectively a modulation sideband, by including the interferometer in the cavity. There, a parametric effect transfers more light from the carrier field into the sideband [62, Appendix D]. With the combination of all these cavities, the simple Michelson is converted into a dual-recycled Fabry-Perot-Michelson interferometer (DRFPMI), the now standard optical layout of ground-based GWDs.
The optical layout of a detector then features more components used to improve the sensitivity in different ways than direct power or signal enhancement. Mode cleaners in both the input and output beam path are used to remove unwanted spatial modes of the beam. The input mode cleaner (IMC) also stabilizes the polarization and frequency of the beam as well as suppresses beam jitter. The output mode cleaner (OMC) is used to isolate the intentionally through the antisymmetric (signal) port leaving [17] sidebands generated by GWs and carrier light from any other leakage fields. The layout is complemented by the squeezed light injection path which is used to inject frequency dependent squeezed vacuum states into the signal port of the interferometer to suppress quantum noise. In order to achieve frequency dependent squeezing, filter cavities were introduced into the detectors before the current observation run O4 [63, 64].
A real detector is, of course, even more complicated than the layout depicted in Figure 2.3. The here mentioned aspects are, however, the parts relevant for a possible implementation of the straylight mitigation scheme investigated in this thesis. Covering all the other aspects thus goes beyond the scope of this work. Further details on them can be found in e.g. Buikema et al. [17] or Capote et al. [18] and additional literature that was previously referenced for the individual layout parts.

2.3.3 Noise sources

Detecting GWs and extracting information from their waveform relies on a high signal-to-noise-ratio (SNR). There are two ways to increase this, either by reducing the noise or by increasing the signal. Thus, many of the optical layout components are designed to increase the influence of a GW on the detector, but others are used to directly tackle noise sources. All the different noise sources form the noise budget of a detector, which is exemplarily shown for the LIGO Hanford Observatory (LHO) detector measured during the current observation run (O4) in Figure 2.4. The current noise budget for the LIGO Livingston Observatory (LLO) detector can be found in the same publication Capote et al. [18]. Detailed discussion of various noise sources beyond the scope of this thesis can also be found there and in e.g. Martynov et al. [65] or in detail for O3 of the LIGO detectors in Buikema et al. [17]. Discussions in a more general from can be found in e.g. Saulson [37] or Bond et al. [66]. Here, the focus lies on those that are also a factor in the low-frequency range, around and below a few Hz and those that have significance for the investigated straylight suppression. In this regard, straylight can be directly linked

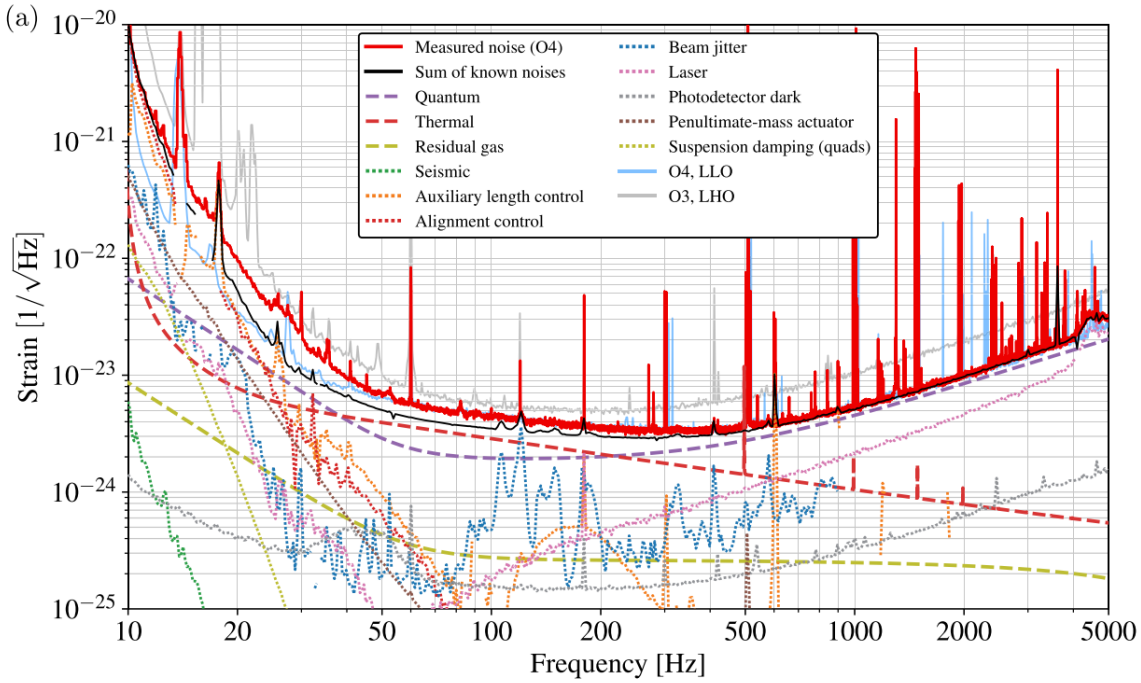

Figure 2.4: Noise budget of the LIGO Hanford Observatory (LHO) measured during observation run 4 (O4), as of December 2023. Source: [18, Figure 5a]

to radiation pressure noise as the power fluctuations caused by it change the impinging force on the mirrors. Additionally, the reduction of radiation pressure noise as part of the quantum noise using squeezed light injection is highly unlikely to be dismissed. Thus any newly introduced scheme needs to be compatible with it.

Quantum noise So far not answered by the optical layout is the aspect of how small a change in power is fundamentally measurable, which is related to the detectors quantum noise. Most important are the random fluctuations in the number of photons detected by the photo-detector (PD), the shot noise. This is one part of the quantum noise, caused by the fluctuation in arrival time of the photons on the detector or in other words the uncertainty in the phase quadrature of the vacuum states entering the interferometer from the signal port [67]. Together with the radiation pressure noise, caused by the uncertainty of the amplitude quadrature of the same vacuum state [68], these two quantum noise sources are a fundamental limit to the detectors sensitivity [17]. The latter, causing a variation in the force exerted on the mirrors by the light in the interferometer, can become limiting below around 50 Hz. It is frequency dependent due to opto-mechanical coupling [64] which increases towards lower frequencies. The frequency independent shot noise then becomes the fundamental limit to measurement precision at frequencies where the opto-mechanical coupling becomes insignificant [64]. As the related SNR scales with the square root of the power in the interferometer, it can be optimized by increasing the input power or amplifying it through the various approaches discussed for the detector

layout. However, operating with high input and internal power also introduces problems related to thermalization and thermal compensation [18], among others, and can thus not be employed unlimited. Another way to reduce the quantum noise is the use of squeezed light injected into the signal port [8] as shown in Figure 2.3. With this, the shot noise could be reduced such that it is now the limiting noise source only above hundreds of Hz, confined by the achievable squeezing factor. So far, the reduction of shot noise was prioritized, however, imposed by the Heisenberg uncertainty, this increases the radiation pressure noise due to anti-squeezing. As both become limiting factors, the use of frequency dependent squeezing, meaning squeezing of different quadratures depending on frequency, was introduced to counteract both noises at frequencies where they are most critical [63, 64].

Suspension, seismic and control noise In order to actually measure GWs, the test masses, which are the mirrors forming the FPCs or arm-cavities, have to be free floating, meaning not experiencing any external forces. To imitate this, these – and many other optics – are suspended by complex pendulum system for passive and active isolation from the surroundings [69, 70]. These pendulum systems strongly suppress noise coupling above there resonance frequency passively. However, the mirrors need to be held precisely in position for the interferometer error signals to behave linearly and controls to work properly. Therefore, also motions at and below this resonance have to be precisely measured and suppressed, even if they are outside the detection band. This is done by actuating on the various stages of the the isolation system and introduces noise caused by the actuators themselves and their control systems [17, 18].
Nevertheless, these suspensions prevent the seismic noise caused by various sources introducing ground motion, like e.g. earthquakes, ocean waves or even wind, to couple to the test masses. Still, some occurrences of e.g. earthquakes and strong winds can lead to the interferometer loosing lock even with these suspensions. As can be seen in Figure 2.4, in the absence of such stronger events, this noise is currently below the detector sensitivity, even though it is stronger at the Livingston site (see [18]). Another noise is the so-called Newtonian noise caused by density fluctuations and thus the gravitational field – or in GR-terminology the metric curvature – of the Earth itself. As it is not possible to shield from this noise in any way, it has to be measured and compensated for in post-processing of the data [71, 72]. For the current detectors, this noise is not yet relevant [17], however, as a low-frequency noise, it will become relevant for future detectors like ET [73, 74].
What becomes apparent when comparing the seismic noise with the actually limiting noise sources is, that the control of the optics, be it for active isolation or alignment and locking the interferometer, is the limiting contribution. Here an important factor is the self-noise of the sensors and actuators which is injected into the control loops. Their limited precision together with used control methods have been directly limiting

the detectors at low frequencies [18]. Thus, improvements of sensors and actuators, as well as optimization of control techniques are needed, especially for next generation detectors.

Laser noise The laser itself also introduces noise into the system caused by frequency and amplitude fluctuations, as well as spatial fluctuations of the beam [75, 76]. By being the measurement device, the laser needs to be as stable as possible in order to achieve such a high precision measurement. Using a Michelson interferometer with almost identical arm lengths already suppresses frequency noise as its change is seen by both arms in almost the same way. However, due to small asymmetries and imperfections, the laser still needs to be actively stabilized in frequency by using three different cavities. One of them is the IMC and another one the 4 km arm-cavities using their common length motion [77], while the third is a comparatively short cavity in the laser preparation setup. With this, the lasers coherence is effectively stabilized to the km-scale of the arm-cavities.
As the measured signal directly depends on the input power, any amplitude fluctuation of the laser contributes to noise. These influences are minimized by the choice of operating point near the dark fringe[4] at the signal port. To further suppress the amplitude noise, the laser is additionally stabilized using several control loops, including one at high power after the IMC [18, 78]. Another purpose of the IMC is to filter unwanted higher order modes; by being resonant to the desired fundamental mode, and stabilize the output beam to this cavity mode, thereby reducing spatial fluctuations [79, 80].

Gap between measured and known noise

There is a noticeable gap between the measured total noise of a detector and the sum of known and individually measured noise sources. This can be clearly seen in every noise budget of the LIGO detectors, see e.g. [17, 18], as shown in Figure 2.4. It is currently not understood where this discrepancy, starting at the low frequency end and extending all the way into the middle of the detection band (around a few hundred Hz), comes from nor is its source identified. One candidate for this *mystery* noise is scattered light, which is known to be problematic in the low-frequency region but not well characterized [18]. A detailed discussion of this noise and ways to mitigate it follows in the next chapter. However, the observable gap makes one thing apparent: if straylight is one or the main cause for it, there is no obvious point to start for its mitigation. Once identified, also straylight noise sources are characterized and if possible mitigated, details of which are discussed in the next chapter. The noise sources constituting the gap are none of this, thus their mitigation would need to work regardless of whether the source can be identified. The approach presented and investigated in this thesis is, to a degree, capable of exactly that in the case of straylight.

[4] meaning the condition for destructive interference

3 | Straylight Noise

Scattered or straylight has been identified as a source of noise in a gravitational wave detector (GWD) already well before the age of the complex current detectors and actual detections of gravitational waves (GWs). This chapter dives deeper into the underlying mechanisms and discusses mitigation techniques currently employed in modern detectors. After the state-of-the-art is presented, other investigated mitigation techniques are briefly summarized to give an overview of work done in the field. Even with all these efforts, scattered light noise is still a major unsolved challenge which needs to be tackled for the improvements in sensitivity envisioned for upgraded and next-generation detectors. In this work, new approaches for straylight mitigation are presented, which build upon some of the previously proposed and investigated techniques.

3.1 Straylight in gravitational wave detectors

The phenomenon of unintended coherent light fields disturbing a detector is often called *straylight*, *scattered light* or *ghostbeams*. While sometimes intended to describe different kinds of disturbances – like e.g. using the phrase ghostbeam to describe beams resulting from reflections on secondary surfaces – no distinction is made between them in the context of this work. Further, all light taken to be straylight or scattered light (the term ghostbeam is rarely used) is considered to have its origin in the main (science) laser of the experiment or detector. Thus the term straylight or scattered light refers to light being lost from the main beam by any means before coherently coupling back into the readout in any way. The effects described in this chapter are only possible because this straylight is coherent. Non-coherent light can in principle also disturb measurements, however, not with the dynamics described here as it does not introduce any phase changes but just an additional offset.

Historical overview

Negative influences on the detectors sensitivity caused by the influence of coherent scattered light was already identified as an issue in one of the first prototype gravitational wave detectors (GWDs) build in Garching near Munich, Germany [81]. The group of

Heinz Billing encountered significantly higher noise than expected in their first experiments using an interferometer with optical delay lines as described in e.g. Billing et al. [58]. In their work covered in Schilling et al. [82], they attribute frequency noise to scattered light interfering with the main beam after traveling a longer path. In this case, the scattered light was even considered static, not contributing a time-variable phase error but only coupling the frequency noise of the laser into the measurement. To stay below the shot noise limit, they estimated a frequency stability of better than $10^{-2}\,\mathrm{Hz}/\sqrt{\mathrm{Hz}}$ would be needed for scattered light on the order of 10^{-4} in amplitude. A stability seeming impossible to achieve at the time [82]. As measure against such scattered light, they proposed and demonstrated a technique using phase modulation in Schilling et al. [82] and Schnupp et al. [83] – as it can be seen as an earlier iteration of *Tunable Coherence*, this is discussed deeper in Chapter 5.

This first encounter of scattered light was especially problematic due to it occurring in delay lines designed to keep the light spatially separated between round-trips – a problem that is partially solved by using Fabry-Perot cavities (FPCs) instead. It is, however, by no means the only one as the existence of straylight is nearly impossible to avoid in any interferometer anywhere simply due to its nature.

The problematic influence of scattered light and how to mitigate or minimize it was an important topic in the development of modern detectors [84–86] and is still an important factor. In first generation detectors, the presence of coherent scattered light was a major problem [87], making its mitigation an important aspect when moving to the current second generation [88]. The increasing sensitivity of these detectors is now making scattered light noise more evident again [17, 18]. Nowadays, especially non-static scattered light which can introduce highly non-linear phase noise, as described in the following sections, is a major concern. Looking further ahead, the sensitivities aimed for in third generation detectors are making better mitigation techniques even more necessary. It is in this regard inconceivable that currently employed techniques are sufficient [89, 90], thus new approaches need to be considered and investigated.

3.1.1 Scattered light in modern detectors

The noise induced by scattered light into the detectors was clearly identified early on. Therefore, detailed calculations of the coupling into the readout and the resulting erroneous strain signal were done by e.g. Vinet et al. [85]. In works done by e.g. Martynov et al. [65], Ottaway et al. [89], Accadia et al. [91] and Canuel et al. [88] towards the commissioning of second generation detectors, this was continuously expanded on. Most recent examples like e.g. Soni et al. [92] now investigated these detectors during and between their observation runs.

Especially the earlier works like Vinet et al. [85, 86], Ottaway et al. [89] and Canuel et al.

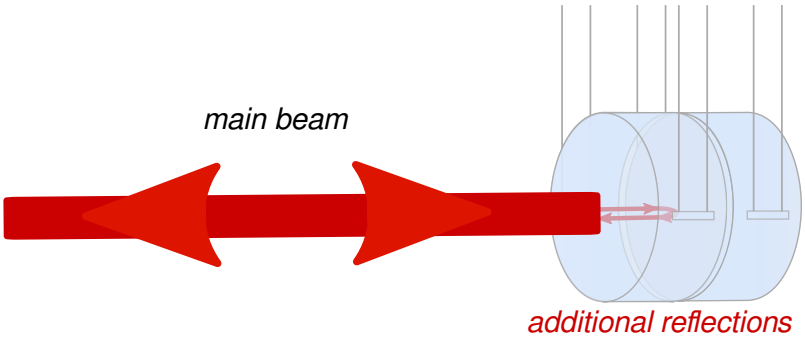

Figure 3.1: Simplified sketch showing light transmitted through the ETM to the reaction mass (specifically the golden ESD trace, not shown) coupling back into the main beam, discovered by Soni et al. [92].

[88] focused on estimating and predicting the influence of scattered light. For this, they used models for scattering sources and propagated these through the layout. Sophisticated estimates of how much noise might be introduced from various sources like e.g. ground motion were made. This was done using e.g. the bidirectional reflectance distribution function (BRDF) for the relevant surfaces and coupling coefficients for the recoupling of the straylight into the interferometer. For these estimates, it is important to know or have a good assumption of possible scatter sources and while the estimate itself is by no means trivial, identifying all contributing sources beforehand is an immense challenge.
In Soni et al. [92] an example is given with a straylight beam created at the end test masses (ETMs) of the LIGO detectors. This beam contained light transmitted by the mirror and being reflected from the electrostatic drive (ESD) traces on the reaction mass positioned behind the ETM, this is also sketched in Figure 3.1. The resulting phase noise in terms of strain sensitivity, considering the coupling inside the arm cavity, is then given by [91, 92]

$$h_{ph}(f) = E_{\mathrm{sc}} \frac{\lambda}{8\pi L} \mathscr{F}\left[\sin \delta\phi(t)\right], \tag{3.1}$$

where L is the length of the arm cavity, λ the wavelength and $\mathscr{F}$ the Fourier transformation of the time-dependent scattered light phase $\delta\phi(t)$. Additionally, due to the buildup of this additional field in the arm cavity, it also contributes a radiation pressure noise component given by [89, 92]

$$h_{\mathrm{rad}}(f) = E_{\mathrm{sc}} \frac{2\Gamma P}{Mc} \frac{2}{\Omega^2 - \omega^2} \mathscr{F}\left[\cos \delta\phi(t)\right], \tag{3.2}$$

with the cavity gain Γ, P the arm power, M the mirror mass, c the speed of light and Ω the suspension eigenfrequency. In addition to this example, Figure 3.2a shows a similar effect originating at the optics of the auxiliary laser system. These optics are placed partially on-axis behind the ETMs to inject light at a different wavelength for locking the arm cavities in e.g. LIGO [1, 93]. For this system, which also includes intentional transmission of some light from the main laser through the ETMs, to work, meticulous shielding of the test masses and suspension of additional optics is needed. In this context, Figure 3.2b shows a close-up of how straylight is created by reflections on secondary surfaces, here the

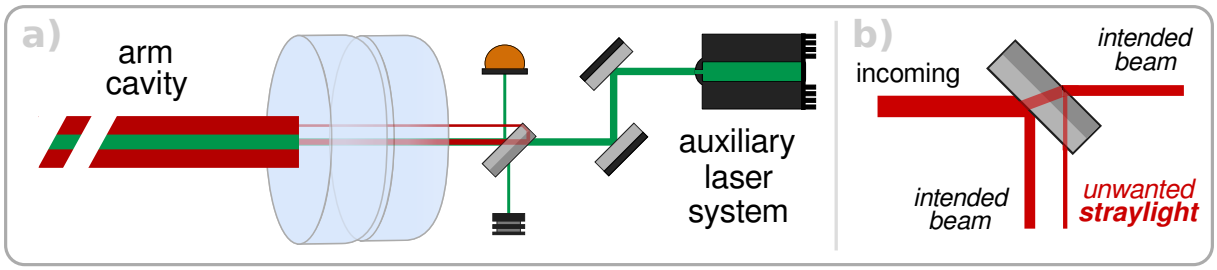

Figure 3.2: Simplified sketch showing how scattered light can be created by reflections on secondary surfaces, in this case sometimes also called *ghost beams*. a) shows a drastically simplified version of how parts of the main beam can be back-reflected by on-axis positioned optics behind the ETMs used for the auxiliary laser system. Even though this operates at a different wave length, spurious beams can be created. b) shows a close-up of a beam splitter optic where a secondary beam is created by reflection on the AR-coated backside of the optic.

anti-reflective (AR) coating of a beam splitter. Even optics manufactured for different wavelengths, as is the case for many behind the ETMs, can cause spurious beams to be created due to residual reflectivities.

Besides the already mentioned reflections on secondary surfaces, other possible ways for the creation of scattered light include, but are not limited to, mirror imperfections or defects like point absorbers, remaining particles in the vacuum system or dust particles outside the vacuum system and diffraction on edges [94]. Examples for the reflecting surfaces then include, but are again not limited to, the beam tubes, vacuum access windows and other optics, basically everything that moves relative to the test masses. Further, the high sensitivity current detectors reach, now leads to situations were even baffles used to mitigate scattered light are becoming a relevant sources for additional scattered light noise [18, 20, 21].

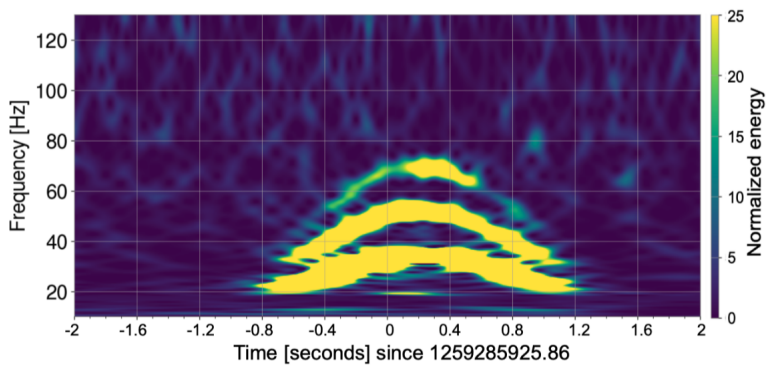

(a) Spectogram showing how scattered light shows up as arches in these types of measurements with the presence of multiple arches indicating a scatter path with multiple reflections. Source: [92]

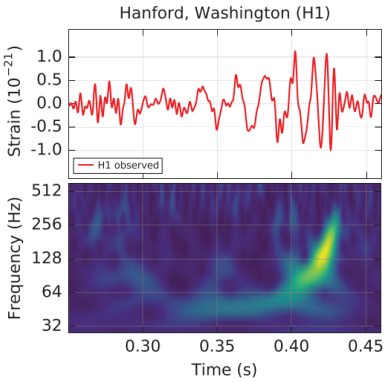

(b) Waveform and spectogram of GW150914 measured by the LIGO LHO detector. Source: [2]

Figure 3.3: Impact of scattered light on the measurement of GWs visualized with a spectogram. On the left side showing scattered light with it characteristic arches for strong scatter events, on the right the signal measured for GW150914 at the LHO detector for comparison. It is easy to see how the scattered light can mask or cover the signal of interest.

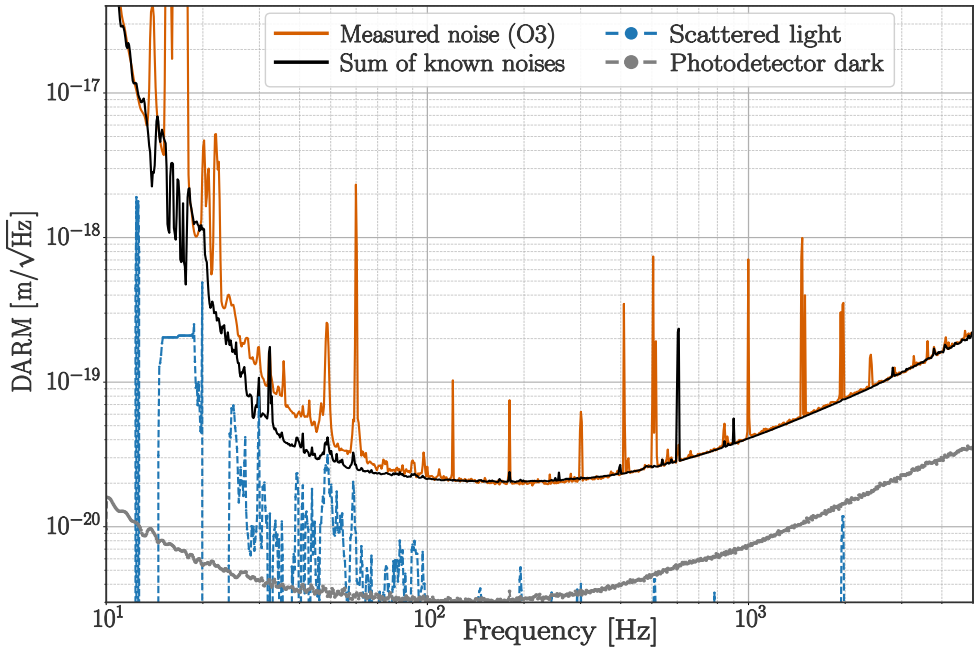

Figure 3.4: Selected noise budget of the LIGO Hanford Observatory (LHO) measured during O3 showing the identified and measured scattered light impact on the detector. Note that here instead of strain, differential arm length change (DARM) is used on the y-axis. As the detector has an arm length of 4 km, the values correspond to a strain about three orders of magnitude smaller than the given DARM-values. Source: Interactive plot of Buikema et al. [17, Figure 2a] generated with `https://ccahilla.github.io/lho_noisebudget.svg` [97]

Some illustrative examples of reasons for the movement of the scattering surfaces include the previously mentioned ESD trace [92] and seismic activity be it of natural (e.g. earth quakes, microseism and wind) or anthropogenic origin [17, 18, 21, 95]. One prominent anthropogenic source at the LLO site are trains passing a little over 3 km south of the Y-arm [95]. However, this is just one among many other human activities in the areas around the detectors. A rather peculiar "natural" cause for scattered light events at the LHO site was identified to be the pecking of thirsty ravens on ice buildup on the cryogenic system coupling back into the detector readout [96].

A useful way of looking at scattered light signals is the use of time-frequency spectograms which show the evolution of spectral densities over time. In these, scatter events are visible as arches, often spanning one to several seconds for so-called slow scattering and only fractions of a second for fast scattering [21, 92]. The process of slow scattering is visualized in the spectogram shown in Figure 3.3 in comparison to the measurement of GW150914 [2]. While slow scattering is characterized by lower frequencies and higher amplitude, fast scattering gets its name from the higher frequencies of the event.

Scattered light is, at least nowadays, a non-stationary noise as evident by e.g. the term scatter event and how they appear in spectograms. Reasons for this are for example non-static or non-permanent sources or time-dependent movement amplitudes of scattering surfaces. This also complicates identification and mitigation of scatter sources. In general,

scattered light is a way for various environmental noises to couple into the detector. Figure 3.4 shows a selection of the LHO noise budget measured during O3 indicating the identified scattered light contributions. The way these are identified and measured by intentional shaking and light injection is discussed further in Sec. 3.2.1. However, in general the coupling is highly dependent on the various parameter of the interferometer configuration so that many unknown sources are anticipated [17, 18]. It is therefore fully feasible that a non-stationary background of unidentified straylight noise is present in the detectors. This might be partly reduced by other improvements being made, like the reduction of suspended part's root-mean-square (RMS) motions due to reduction in control noise. Still, scattered light is often considered a prime contributor to the noticeable gap between the known and measured noise [18] clearly observable in e.g. Figure 3.4.

3.1.2 Effects of scattered light

The coupling of scattered light can be easily visualized using a phasor diagram as shown in Figure 3.5. As the measurement of coherent light fields depends on the (relative) phase of all individual fields and not only the accumulated phase of the main light field, the complex phasor sum is the quantity of interest. The measured field thus is the sum of the nominal field traveling the intended path with its phasor described as $\vec{E}_0 = E_0 \exp(i\varphi_0)$ and the scattered light field described by the phasor $\vec{E}_{\mathrm{sc}} = E_{\mathrm{sc}} \exp(i\varphi_{\mathrm{sc}})$ or even a sum of scattered light fields[5]. Here, E_0 and E_{sc} are the amplitudes and φ_0 and φ_{sc} the phases of the respective fields. As shown in Figure 3.5a this can be in an arbitrary constellation. It thus leads to an influence of both φ_0 and φ_{sc} on the amplitude $E_{\mathrm{meas}} = E_0 + \delta E_{\mathrm{meas}}$ and phase φ_{meas} of the measured field:

$$\vec{E}_{\mathrm{meas}} = \vec{E}_0 + \vec{E}_{\mathrm{sc}} = (E_0 + \delta E_{\mathrm{meas}})\, e^{i\delta\varphi_{\mathrm{meas}}}. \tag{3.3}$$

The (time-dependent) measured amplitude including the erroneous deviation δE_{meas} as indicated in Figure 3.5c is then given by

$$E_{\mathrm{meas}} = E_0 + \delta E_{\mathrm{meas}} = \sqrt{E_0^2 + E_{\mathrm{sc}}^2 + 2E_0 E_{\mathrm{sc}} \cos(\varphi_0 - \varphi_{\mathrm{sc}}(t))}, \tag{3.4}$$

where the difference between the two phases $\varphi_0 - \varphi_{\mathrm{sc}}(t)$ indicates a time-dependent fluctuation. Further, the (time-dependent) change in measured phase $\delta\varphi_{\mathrm{meas}}$ indicated in Figure 3.5d, meaning the induced phase error $\varphi_{\mathrm{err}}(t)$, is given by

$$\varphi_{\mathrm{err}}(t) \equiv \delta\varphi_{\mathrm{meas}} = \tan^{-1} \frac{E_0 \sin\varphi_0 + E_{\mathrm{sc}} \sin\varphi_{\mathrm{sc}}(t)}{E_0 \cos\varphi_0 + E_{\mathrm{sc}} \cos\varphi_{\mathrm{sc}}(t)}. \tag{3.5}$$

[5] In reality, the electrical field is not complex but only the real part of this expression, it is, however, a very convenient way for calculations when handled properly.

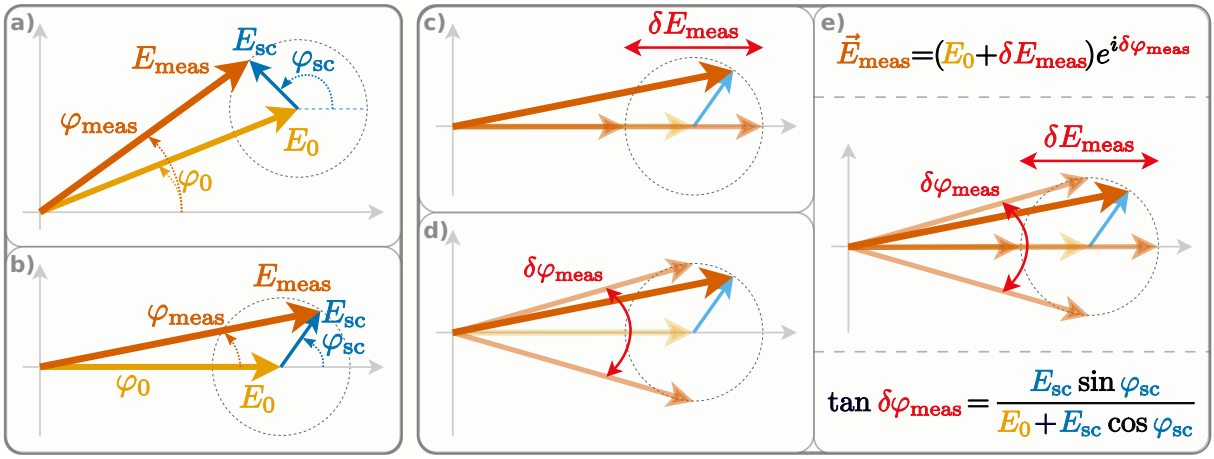

Figure 3.5: Vector depiction of scattered light coupling into the measurement. Instead of the undisturbed amplitude E_0 and phase φ_0 the scattered light is added to the measurement. For high dynamics, this can change both the phase and the amplitude. a) shows the case for an arbitrary constellation of the nominal field with addition of scattered light and the resulting light field. b) shows the simplified case were φ_0 is set to be zero with c) and d) indicating the range of change in amplitude and phase caused by the scattered light. The full combination is shown in e) together with the equations for the resulting field and phase error.

For simplicity, it is convenient to choose $\varphi_0 = 0$ as shown from Figure 3.5b onward, giving

$$\varphi_{\mathrm{err}}(t) = \tan^{-1} \frac{E_{\mathrm{sc}} \sin \varphi_{\mathrm{sc}}(t)}{E_0 + E_{\mathrm{sc}} \cos \varphi_{\mathrm{sc}}(t)}. \tag{3.6}$$

As normally $E_{\mathrm{sc}} \ll E_0$, which is always a reasonable assumption in a GWD, this expression simplifies to

$$\varphi_{\mathrm{err}}(t) \approx \frac{E_{\mathrm{sc}}}{E_0} \sin \varphi_{\mathrm{sc}}(t) = \sqrt{\frac{P_{\mathrm{sc}}}{P_0}} \sin \varphi_{\mathrm{sc}}(t) \tag{3.7}$$

giving the approximation $P_{\mathrm{sc}} \leq 3.6 \cdot 10^{-21} P_0$ for a strain sensitivity of 10^{-21} over 10 km, if the phase of the scattered light is not constraint to be very small.

Using this simple approach and values for the Einstein Telescope (ET) [19], one can estimate that even single photons per second constitute too much scattered light power for the planned sensitivity improvements. Following what was done by Hild [87, Ch. 3] for the GEO detector, the ET design parameter imply that the tolerable scattered light power is on the order of only 10^{-22} W for the Einstein Telescope Low-Frequency detector (ET-LF). In reality the coupling into a detector readout is more complex than this simple phasor estimate, it depends on the position, transfer function and many other parameters, like e.g. interferometric contrast. Comprehensive calculations of this coupling were done by e.g. Vinet et al. [85] for the first generation of detectors and then continuously updated and adapted for the current generation in e.g. Ottaway et al. [89] or Canuel et al. [88].

Sticking with a more simplified approach for now, one can calculate a simplified expression for the measured output power of a simple Michelson interferometer (depicted in e.g. Figure 6.1) including some scattered light. Starting with the electric field given for the

asymmetric or south port[6] by

$$E_{\text{asym}} = \frac{i}{2}\, E_0 \left[e^{i\omega\tau_{\text{N}}} - (1-r_{\text{sc}}^2)\, e^{i\omega\tau_{\text{E}}} + r_{\text{sc}}^2\, e^{i\omega(\tau_{\text{E}}+\tau_{\text{sc}})} \right]. \tag{3.8}$$

Here i is the imaginary number representing the additional phase due to transmission through the beam splitter, ω the lasers angular frequency, r_{sc} is the amplitude reflectivity of an optic coupling scattered light out and back into the main beam and the respective τ's represent the optical delay of the north and east arm, as well as the additional scattered light path. From this, the power can be calculated with $P = |E|^2 = E\overline{E}$, where $\overline{E}$ is the complex conjugate, which results in[7]

$$\begin{aligned} P_{\text{asym}} = \frac{P_0}{2}\Big[& (1-r_{\text{sc}}^2)[1+\cos(\omega\tau+\pi)] \\ & + r_{\text{sc}}^2\, [\cos(\omega(\tau+\tau_{\text{sc}})) - \cos(\omega\tau_{\text{sc}})] + r_{\text{sc}}^4\, [1+\cos(\omega\tau_{\text{sc}})] \Big]. \end{aligned} \tag{3.9}$$

The first line represents the (reduced) normal output[8] and the second line the additional terms caused by the scattered light coupling. The microscopic delay difference $\tau_{\text{E}} - \tau_{\text{N}}$ between both arms, determining the relative phase, is now defined as simply τ and the scattered light's additional delay to it as τ_{sc}. This additional delay will become important later as it allows for suppression of scattered light by *tunable coherence*. Assuming a simple, sinusoidal dynamic of the scattered light source, this additional delay can be modeled by

$$\tau_{\text{sc}} = \frac{d_{\text{sc},0} + d_{\text{sc}} \sin(2\pi f_{\text{sc}} t)}{c}, \tag{3.10}$$

where d_{sc} is the amplitude and f_{sc} the frequency of the scattering surface's movement. Simulating this for different choices of parameter shows how scattered light creates a characteristic spectrum as depicted in Figure 3.6. This often called *scatter shoulder* visualizes an important property of scattered light noise, the non-linear up-conversion to higher frequencies caused by fringe wrapping already for movements on the scale of a wavelength [85]. Noise for movements above $\simeq \lambda/4\pi$ is thus not only injected at the scatter frequency f_{sc} as phase modulation but as broadband noise at higher harmonics up to a cutoff frequency $f_{\text{max}} \simeq f_{\text{sc}} \frac{4\pi}{\lambda} \delta x_{\text{sc}}$ [85, 91] with δx_{sc} being the RMS value of the scatter displacement. It is therefore not only problematic if scatter sources are moving at

[6] As any field components common to both arms are reflected back to the laser, this side of the interferometer is commonly known as the *symmetric* port. Differential components leave through the other port, which is thus referred to as the *asymmetric* port.

[7] Again, the complex notation of electric fields was used for mathematical convenience, the result here remains the same also when disregarding that only the real part of the equation actually constitutes the physical field.

[8] There is an additional phase shift of π in one of the arms due to double transmission through an optic where the scattered light couples in and out in this calculation

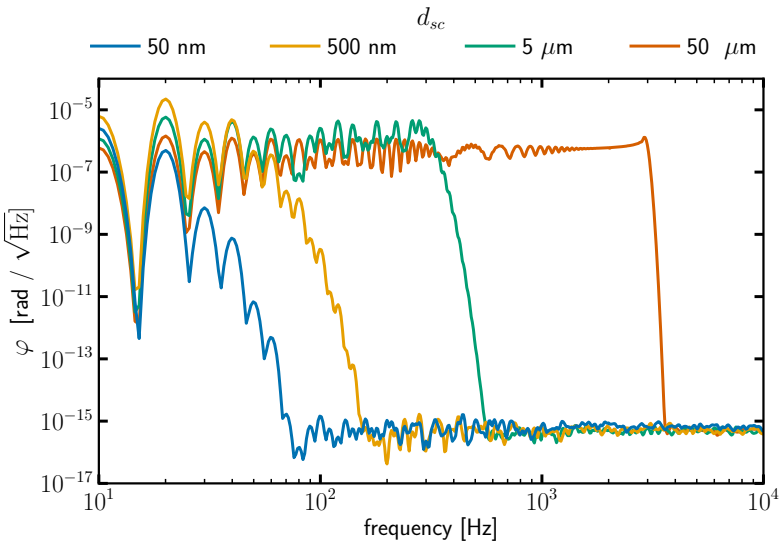

Figure 3.6: Simulated scattered light couplings into a simple Michelson as described by eq. 3.9. All cases with $f_{sc} = 10\,\text{Hz}$ and various movement distances according to the model described by eq. 3.10 show the characteristic scatter shoulder to different extends.

frequencies inside the measurement bandwidth of a detector but also (far) below it. An example using such a model for identifying and fitting a scattered light path and the in it contained power is shown e.g. in Figure 3 of Chua et al. [90].
Another aspect of scattered light is the coupling not only with phase but also amplitude components for larger displacements [89] as can also be seen in the depictions in Figure 3.5. One can therefore also calculate the coupling into the amplitude and phase quadrature of the interferometer outputs as e.g. done for a simple Michelson further discussed in Section 4.1 and the accompanying publication Lohde et al. [22].

3.2 Mitigation techniques

As it is apparent that scattered light is already a significant noise source in current detectors and the increase in sensitivity only makes this more evident [18], the effort to mitigate its influence becomes increasingly important. Several conventional methods are already deployed at the different detector sites, and alternative ones have been and are investigated.

3.2.1 Conventional mitigation techniques

If scatter sources can be identified, the best mitigation is their removal. One example for this is a window separating the vacuums containing the SRM and OMC of the LIGO detectors which was identified to couple acoustic noise into the main interferometer beam passing through it. It was removed before the current observation run 4 (O4), leading to an improvement of a few megaparsecs[9] compared to the ∼150 Mpc in operating range [18].

[9] The sensitivity of the detectors is often given in the range they achieve to detect a binary neutron star merger with a SNR of 8 or more using matched filtering of the data.

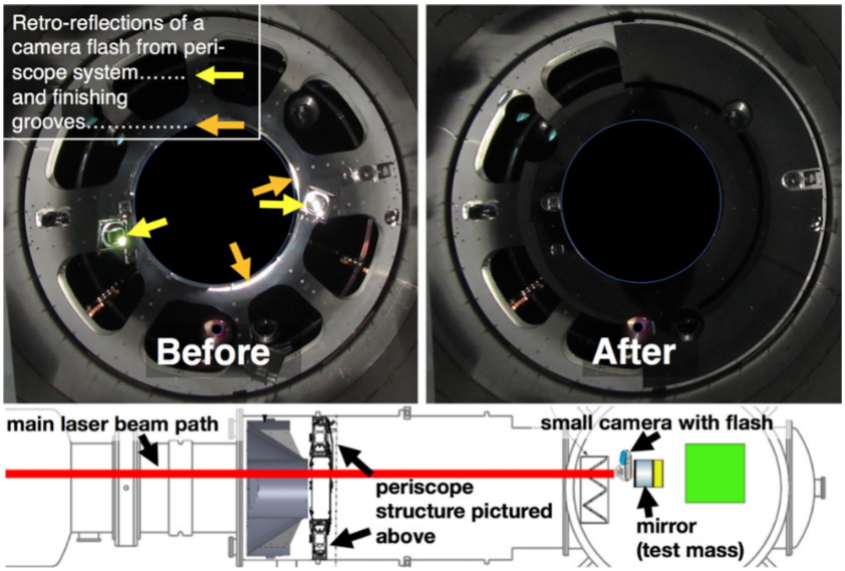

Figure 3.7: Picture taken from the point of view of the main laser beam in the LIGO detectors identifying scatter sources on telescope optics and edges. On the left before mitigation and on the right after additional baffling was installed. Below a sketch of the investigated detector part.
Source: [20, Figure 12]

However, often the sources can not easily be removed, as for example with the ESD traces on the reaction mass or baffles designed to block scattered light. In such cases, the best way to mitigate their influence is dampening the relative motion of the scattering objects in order to minimize the scatter shoulder and thus the up-conversion into the measurement bandwidth. Examples for this can be found in e.g. Soni et al. [21, 92] and Nguyen et al. [20] for the ESD trace example and others.
In order to identify scatter sources in the first place, there are several techniques applied. Most of them include intentional injection of scattered light or intentional shaking or modulation of probable scattering objects or surfaces. An example of this is e.g. the path length modulation between the output Faraday isolator (FI) and squeezed light injection optics as done in Chua et al. [90] to identify scattering between these optics. Another tool is using video or camera footage, the former often together with targeted vibration injection [18, 20]. Figure 3.7 shows such an example using a camera with a flash to identify scattered light sources from the point of view of the main laser beam.

3.2.1.a Baffles

All of these so far mentioned mitigation approaches are an ongoing effort in the detectors, in addition to the already installed baffles which are part of the detector design. First estimates and calculations on the necessity of baffles were done by e.g. Vinet et al. [86], showing that the desired noise levels of second generation detectors are unachievable without the use of baffles for scattered light mitigation. One of the main application of baffles is to shield from straylight bouncing back from the beam tubes as depicted in Figure 3.8. Already current detectors have many, around 160 per arm [94], baffles installed for this reason. One example is the previously mentioned auxiliary laser system requiring additional shielding of the ETMs by baffles. An overview of baffle placement

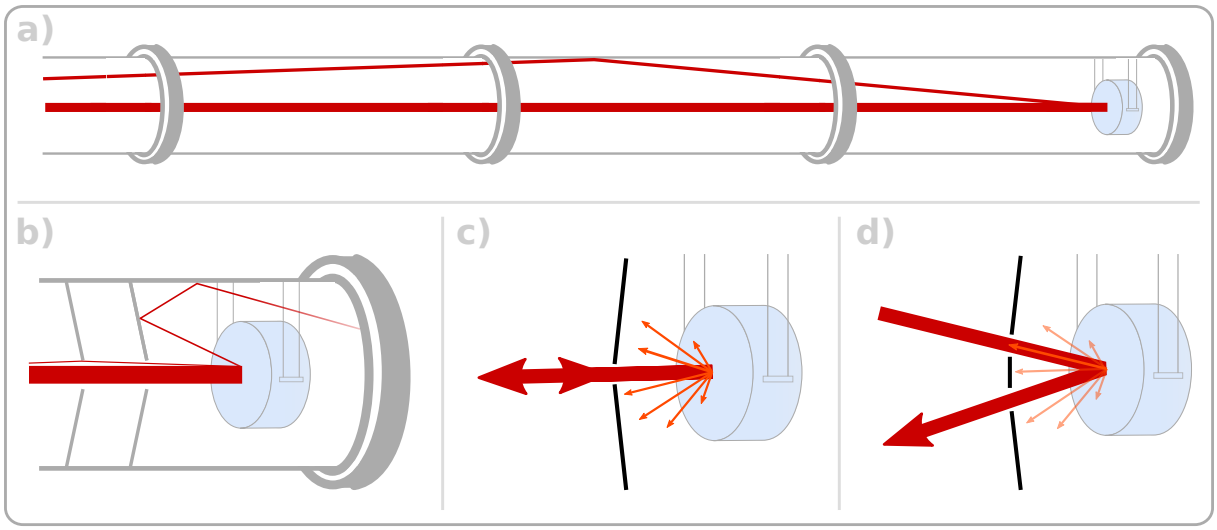

Figure 3.8: Simplified sketch of how scattered light could be created inside a detector with a focus on the beam tubes. a) shows how a scattered beam path created at a mirror is reflected from the (vibrating) vacuum tube and thus directed back to the main beam. b) shows how baffles installed inside the vacuum tube can shield this by reflecting (or absorbing) the scattered light. c) demonstrates how this can be effective against scattered light for a beam being reflected into itself at a mirror as all other paths can be shielded. d) shows how this does not work for a beam being reflected into a different direction at the mirror as now so-called backscatter can occur into the incoming beam.

for the LIGO detectors is shown in the Appendix in Figure A.4. Additionally, pictures of such baffles can be seen in Figure 3.7 and in Figure 3.9 for scale comparison.
Baffles are designed to block all light outside the main beam as shown in Figure 3.8c. However, in applications like a Sagnac interferometer, were incoming and outgoing beams at a mirror are not spatially identical, scattering between these cannot be avoided as shown in Figure 3.8d.
Further, even though baffles are necessary to suppress scattered light to a tolerable degree, it was also known from the beginning that they themselves can be the source of more scattered light [84, 86]. An example of this can be seen in Figure 3.7 and at the current sensitivity levels of e.g. the LIGO detectors such scattered light influences become increasingly problematic [17, 18, 20, 95]. Many baffles are therefore suspended and their motion damped to avoid scattered light noise entering the measurement bandwidth [17, 18, 20, 21, 95].

Figure 3.9: Picture of the installation of a baffle in the LIGO beam tube. Image credit: LIGO/Caltech/MIT/Matt Heintze

Another iteration on the currently used baffles is the addition of sensors in order to better characterize and measure the scattered light

hitting them. These were installed for demonstrations in the IMC of the Virgo detector for the current observation run [98, 99]. For the next observation run, it is planned to install them at the end mirrors [100]. So far, they have been demonstrated to be a useful tool for better understanding straylight around their positions and help with pre-alignment due to additional light hitting their sensors in misaligned configurations.
In a recent study done by Andrés-Carcasona et al. [101] for the Einstein Telescope (ET), it was estimated that for only shielding the arm cavities from scattered light a number of baffles on the order of $200 - 250$ per arm would be needed. With two arms per detector and six detectors in total (HF and LF), this means around 2500 baffles, not including the areas close to the mirrors where scattering might be even more problematic [20]. Additionally, even baffles designed to meet scattered light requirements in these positions can suffer from unexpected motions or other effects, making additional damping or reworks necessary [18, 21]. Thus, while almost certainly a necessity to be used, reaching the design sensitivities of ET or CE or even improving the sensitivities of current detectors with only the use of baffles remains challenging at best.
Additionally, the geometrical design of the baffles, normally adapted to the beam parameters, can complicate upgrades or changes if, for example a mirror is enlarged and by this the beam widened. Upgrades planned for the fifth observation run of the Virgo detector are such a case. Even though, estimates currently suggest that the installed baffles will not be a problem, at least under ideal conditions [102].
In general, even though they are very useful and necessary, baffles are a costly and major effort to be installed, be it during construction or upgrades. Most of them are inside the vacuum system, meaning increased surface areas that are unfavorable when pumping out the air.

3.2.2 Alternative mitigation techniques

The so far mentioned mitigation techniques, which are all already implemented in current detectors, are insufficient in the long run [89]. Besides the already mentioned and in Chapter 5 further discussed approaches using phase modulation on the main laser [83], other ideas have thus been suggested and investigated.
Another method using phase modulation but on the scattered light instead of the main laser was investigated by Lück et al. [103]. In this approach, a component able to phase modulate passing light is inserted into the scatter path. This leads to the resulting spectrum being a sum of the original scattered noise spectrum shifted by multiples of the modulation frequency and scaled by the Bessel functions [103]. Choosing the modulation index such that the first Bessel function or zero component vanishes, the scattered light can be shifted out of the measurement bandwidth. In their work, they achieve this by inserting another optic of which the optical path length can be modulated using piezo-electric

elements. The obvious downside of this is that the scattered light must be identified first and it needs to be possible to insert a phase modulating component into its path. Additionally, the authors point out that the spectrum of the scattered noise must be restricted to below the modulation frequency. Nevertheless, with this technique, they achieved an order of magnitude, or 10 dB suppression in the detection path of the GEO detector without any negative impact on its sensitivity [103].

A different approach was suggested and demonstrated by Steinlechner et al. [104] called *quantum-dense-metrology*. In this technique, the entanglement between two-mode squeezed states is used to readout two orthogonal observables, the phase and the amplitude quadrature of the field at the interferometer output. As scattered light, for large enough dynamics, couples into both quadratures but the GW or science signal only couples into the amplitude quadrature, additional information is gained by reading out both. Normally, only the amplitude quadrature is measured and scattered light can mask the science signal. By observing the other quadrature where only the scattered light shows up, the measurement period with the disturbance can be identified and vetoed [104]. For the experimental realization, one part of the entangled state is injected into the interferometer similar to the injection of squeezed light into today's GWDs, the other is overlapped with the light exiting the interferometer at the beam splitter used to split it. Two beams then result from this beam splitter, both a superposition of the interferometer output and the second part of the entangled state. These are measured with two balanced-homodyne-detectors (BHDs), each measuring a different of the two orthogonal quadratures.

In later works of Meinders and Schnabel [105], they demonstrate in a simpler version without the entangled states that instead of vetoing the period with scattered light, the additional information from the second quadrature can be used to model and subtract it instead. Lastly, in Ast et al. [106] the entangled squeezed states are reintroduced to reach sub-shot-noise performance [106, 107]. While the results were promising, there are some drawbacks coming with this approach. So far, the readout of the interferometer signal is not using a BHD, however, this will be implemented for the next observation run [18, 108] and is planned for ET [19]. Still, a second one would have to be implemented. Additionally, two-mode squeezing to generate the entangled states would have to be implemented as otherwise the splitting of the output signal between two readouts increases the shot noise and even then, a slight increase is unavoidable. Lastly, the mitigation techniques relies on modeling of the scattered light, requiring additional post processing. Nevertheless, around 15 dB of straylight suppression and a broadband nonclassical noise suppression of 5 dB below the shot noise level were demonstrated with this technique [106, 107].

A similar approach investigated by Steier [109] and Fleddermann et al. [110] for the fiber linking the optical benches inside the satellites of the LISA mission benefits from the heterodyne interference in this case. By using balanced detection of both output

ports of the heterodyne interferometer, they showed that scattered light can be strongly suppressed. This is the case as it couples in-phase into both outputs while the beat note carrying the signal is 180° out of phase. Thus subtracting the complex signals recorded in both outputs removes the scattered light noise [110]. As in their case the scattered light occurred mainly as back-reflections inside the fiber, they demonstrated around 36 dB suppression of phase noise not common in both propagation directions.

Auxiliary measurement channels

In general, auxiliary measurement channels, meaning any PD not part of the main interferometer readout, are used to identify scatter glitches and scatter sources [21, 92]. However, recently more schemes are being investigated to remove only the scattered light instead of the whole data. Similar to LIGO, the Virgo detector also features suspended optical benches behind the ETMs where significant straylight contributions originate. By using data from auxiliary PDs located there, Wąs et al. [111] were able to reconstruct both quadratures of the scattered light measured there. Together with a model describing its coupling into the main interferometer, this data was used to fit the straylight noise contributions and reduce their influence on the strain measurement by around 16 dB.

3.3 Conclusion

In this chapter, the noise caused by scattered light was introduced and discussed in detail. The mechanisms behind it and its influence on modern detectors were analyzed and its characteristics presented. By doing so, it was motivated and reasoned why the presented current mitigations schemes are insufficient for future upgrades and new detectors. Using the derived estimations of the induced phase error depending on the straylight power, limitations for a tolerable amount of it could be made. With the example of the Einstein Telescope (ET), its design parameter lead to the realization that even the power carried by single stray photons per second would compromise the desired sensitivity at a few Hz. Thus, new and innovative mitigation techniques will be needed. One investigated as part of this work, taking the approach of using auxiliary channels one step further, is discussed in the next chapter. In the chapters after that, the focus then shifts towards the concept of *tunable coherence* as a possible straylight mitigation scheme.

4 | Dual Balanced Readout

As a supervised Master's Thesis, another new scheme for straylight mitigation, called *dual balanced readout* (DBR), was investigated together with André Lohde [112] as part this work. The results were published in Lohde et al. [22], titled *Dual balanced readout for scattered light noise mitigation in Michelson interferometers* (doi: 10.1103/PhysRevD.111.022004), and are summarized here. This chapter thus closely follows Lohde et al. [22][10] in a shortened and adapted form.

In a simplified way, this DBR can be seen as a combination of the before mentioned approaches using the readout and combination of different quadratures at both interferometer outputs to subtract scattered light. For this, a scheme using two BHDs to read out orthogonal quadratures at the antisymmetric and the symmetric interferometer port (i.e. the commonly used output port and the back-reflection towards the laser) of a Michelson interferometer was studied. By combining the resulting signals in an appropriate way, scattered light can be suppressed.

4.1 Theory

For an electric field with frequency ω and complex amplitude $\alpha(t)$ defined as

$$E(t) = \frac{1}{2}\alpha(t)\exp(i\omega t) + c.c., \tag{4.1}$$

one quadrature $Q(t)$ is defined to be the real part of the field amplitude $\alpha(t)$ and the other quadrature $P(t)$ is defined to be the imaginary part. Here, a laser field described by the field amplitude $\alpha_0(t) = E_0$ is assumed to be entering the interferometer from the symmetric port (s-port in Fig. 4.1). In the interferometer, the field picks up additional phases $\Phi_{X/Y} = 2kL_{X/Y}$ due to the propagation from the central beam splitter to the X/Y end mirror and back, where k is the wavenumber and $L_{X/Y}$ the macroscopic arm length of the X/Y interferometer arm respectively. As described in Sec. 3.1.2, straylight is expressed as parasitic fields with phase φ_{sc} and amplitude $\alpha_{sc}(t) = E_{sc}$. These fields can enter both interferometer arms with amplitudes $|\alpha_{sc}| \ll |\alpha_0|$, again, this is always a good assumption in a GWD. They are then treated as additional terms appearing in the

[10] The manuscript for this work was mainly written by A. Lohde under my supervision, the published version was corrected and finalized by all authors. I am corresponding author for this publication.

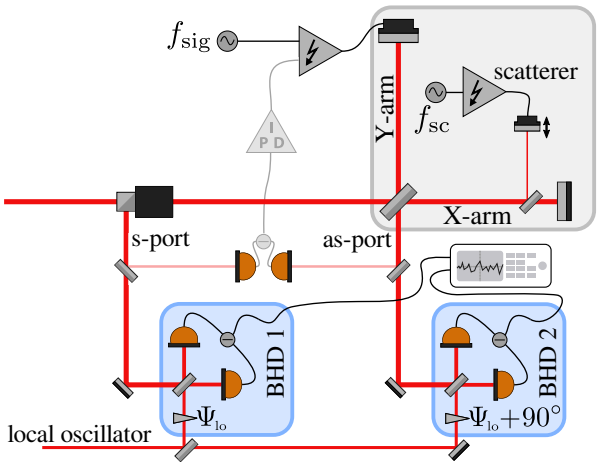

Figure 4.1: Sketch of the experimental setup for testing DBR. The Michelson interferometer featured a PZT end mirror in one of the arms referred to as the Y-arm while in the other arm (X-arm), some light was scattered out of the beam using a low-reflectivity window and back-scattered from another PZT. The interferometer was operated at mid fringe with a simple locking scheme using a BD. The symmetric port BHD1 read out the P quadrature, while the antisymmetric port BHD2 read out the Q quadrature. Adapted from Lohde et al. [22].

resulting electric fields at symmetric and antisymmetric port (as-port in Fig. 4.1). This gives the following expressions for the quadratures at the antisymmetric port:

$$\begin{aligned} Q_{as}(t) = &-\frac{E_0}{2}\left[\sin(\Phi_Y)+\sin(\Phi_X)\right] \\ &+\frac{1}{\sqrt{2}}\left[-E_{\mathrm{sc,Y}}\sin(\varphi_{\mathrm{sc,Y}}(t))+E_{\mathrm{sc,X}}\cos(\varphi_{\mathrm{sc,X}}(t))\right] \end{aligned} \tag{4.2a}$$

$$\begin{aligned} P_{as}(t) = &\frac{E_0}{2}\left[\cos(\Phi_Y)+\cos(\Phi_X)\right] \\ &+\frac{1}{\sqrt{2}}\left[E_{\mathrm{sc,Y}}\cos(\varphi_{\mathrm{sc,Y}}(t))+E_{\mathrm{sc,X}}\sin(\varphi_{\mathrm{sc,X}}(t))\right] \end{aligned} \tag{4.2b}$$

with $\varphi_{\mathrm{sc,X/Y}}$ being the phase of the parasitic field originating in the east/north interferometer arm. At the symmetric interferometer port, the quadratures are then:

$$\begin{aligned} Q_s(t) = &\frac{E_0}{2}\left[\cos(\Phi_Y)-\cos(\Phi_X)\right] \\ &+\frac{1}{\sqrt{2}}\left[E_{\mathrm{sc,Y}}\cos(\varphi_{\mathrm{sc,Y}}(t))-E_{\mathrm{sc,X}}\sin(\varphi_{\mathrm{sc,X}}(t))\right] \end{aligned} \tag{4.3a}$$

$$\begin{aligned} P_s(t) = &\frac{E_0}{2}\left[\sin(\Phi_Y)-\sin(\Phi_X)\right] \\ &+\frac{1}{\sqrt{2}}\left[E_{\mathrm{sc,Y}}\sin(\varphi_{\mathrm{sc,Y}}(t))+E_{\mathrm{sc,X}}\cos(\varphi_{\mathrm{sc,X}}(t))\right]. \end{aligned} \tag{4.3b}$$

It can be observed that different combinations of the two quadratures allow for the elimination of contributions from the X or the Y interferometer arm. Assuming a readout of the Q quadrature at the antisymmetric port and the P quadrature at the symmetric port, following combinations arise:

$$\begin{aligned} S_1(t) = &\frac{1}{2}\left(Q_{as}(t)+P_s(t)\right) \\ = &-\frac{1}{2}E_0\sin(\Phi_X)+\frac{1}{\sqrt{2}}E_{\mathrm{sc,X}}\cos(\varphi_{\mathrm{sc,X}}(t)) \end{aligned} \tag{4.4a}$$

$$\begin{aligned} S_2(t) =& \frac{1}{2}\left(P_s(t) - Q_{as}(t)\right) \\ =& \frac{1}{2}E_0 \sin(\Phi_Y) + \frac{1}{\sqrt{2}}E_{\mathrm{sc,Y}} \sin(\varphi_{\mathrm{sc,Y}}(t)). \end{aligned} \tag{4.4b}$$

These simple arithmetic combinations show that the field contributions from each arm can be read out individually. When also considering the readout of the respective orthogonal quadrature at both ports, it is possible to obtain two more signals:

$$\begin{aligned} S_3(t) =& \frac{1}{2}\left(Q_s(t) + P_{as}(t)\right) \\ =& \frac{1}{2}E_0 \cos(\Phi_Y) + \frac{1}{\sqrt{2}}E_{\mathrm{sc,Y}} \cos(\varphi_{\mathrm{sc,Y}}(t)) \end{aligned} \tag{4.5a}$$

$$\begin{aligned} S_4(t) =& \frac{1}{2}\left(P_{as}(t) - Q_s(t)\right) \\ =& \frac{1}{2}E_0 \cos(\Phi_X) + \frac{1}{\sqrt{2}}E_{\mathrm{sc,X}} \sin(\varphi_{\mathrm{sc,X}}(t)). \end{aligned} \tag{4.5b}$$

In each of the four signals defined here, only contributions from either the X or the Y interferometer arm are present, allowing for an individual arm readout. They further allow for scattered light noise mitigation, e.g. when scattering occurs only in one interferometer arm or the contribution of scattering is unequal in the interferometer arms. Thus, a readout of orthogonal quadratures at the symmetric and the antisymmetric port offers the possibility of mitigating scattered light noise.

Notably, the choice of an operating point for the interferometer does not have a direct impact on the signal combinations when not considering shot noise and other readout effects and does not seem to impact the DBR.

4.2 Experimental realization

The readout of two orthogonal quadratures can be experimentally realized by implementing two BHDs, as these are sensitive to a quadrature selected by tuning the phase of the local oscillator. The measured signal is the result of interference between a local oscillator beam serving as a phase reference with the signal to be probed and is proportional to [113, p. 141]:

$$\mathrm{BHD}(t) \propto E_{\mathrm{lo}}\left(\sin(\Psi_{\mathrm{lo}})Q_{\mathrm{sig}} - \cos(\Psi_{\mathrm{lo}})P_{\mathrm{sig}}\right). \tag{4.6}$$

To demonstrate a proof-of-principle of the scattered light noise mitigation scheme, a Michelson interferometer was set up. Into this, a deterministic scattered light signal to mimic noise was intentionally introduced. Using the additional information from the readout of the symmetric port, it was possible to partially subtract this noise from the readout of the antisymmetric port.

Setup

The used Michelson interferometer had a total of three readouts as depicted in Figure 4.1. A balanced-detector (BD) was used to keep the interferometer at midfringe by using the differential power between the two interferometer ports as error signal for the actuation of the Y arm. Additionally, two BHDs were used to read out the quadrature P_s at the symmetric port (BHD1) and the quadrature Q_{as} at the antisymmetric (BHD2). The light used for the local oscillator (LO) was picked off in front of the Faraday rotator (FR) used to direct the back-reflected light towards the symmetric port readout.
Scattered light was introduced into the interferometer using a partially reflective "scatter window" (reflectance of a few percent) in the X-arm of the interferometer. The diverted straylight beam was directed towards a piezo-electric actuated (PZT)-mirror – actuated for a modulation at scatter frequency f_{sc} – and then back-reflected into the interferometer. This lead to a straylight amplitude of a few percent of the carrier beam. In addition to this scattered light signal, a modulation of the Y-arm PZT-mirror at signal frequency f_{sig} was introduced. These modulations were kept at frequencies far above the control loop bandwidth, such that the signals could be observed directly in the readout of the detector rather than the control signal. This was further intended to find a virtually flat noise floor, which was given at the chosen frequency around 1.2 MHz. Consequently, the motional amplitude of the scatter-mirror was limited at this frequency by the capacity of its PZT and the slew rate of the power supply. The amplitude was further strictly smaller than one wavelength (1064 nm), as no harmonics were observed. The PZTs were driven using custom-made voltage amplifier and PID-controller (see Appendix A.4), and a standard signal generator. To achieve sufficient modulation depth at these high frequencies the PZTs were modulated at resonance frequencies.

Results

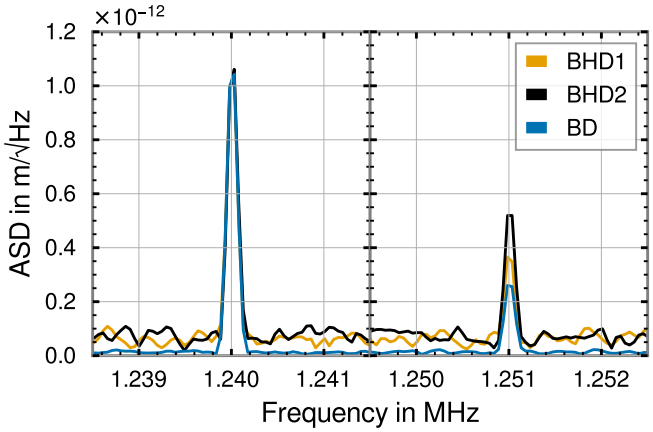

Figure 4.2: ASD plot showing the BHD signals (BHD1 and BHD2) in comparison with the BD. The balanced homodyne signals are normalized to the signal peak at $f_{sig} = 1.24$ MHz, on the left side. The scatter peak is shown on the right side, at $f_{sc} = 1.251$ MHz. Adapted from Lohde et al. [22].

Short time-series of 20 ms were recorded, acquiring the signals from all three detectors.

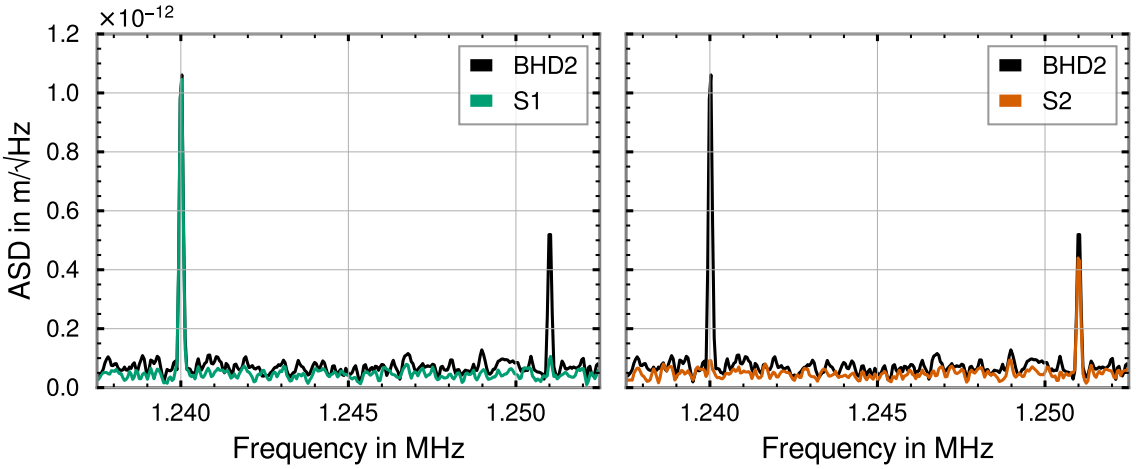

Figure 4.3: ASD plots showing the scattered light noise suppression/the arm signal discrimination in the signal combinations S_1 and S_2. Left: S_1 shows a scattered light noise peak at 1.251 MHz that is suppressed almost completely in comparison with the quadrature readout of BHD2 at the antisymmetric port, while the signal at 1.24 MHz remains. Right: S_2 depicts a vanishing signal at 1.24 MHz, while the scattered light noise peak largely remains.
Adapted from Lohde et al. [22].

The calibration factor of the BD was determined to be $31.2 \pm 0.2\,\mathrm{nm\,V^{-1}}$ with a calibration measurement by ramping through several fringes using the PZT mirror in the interferometers Y arm. Using this calibration factor, the BD signal was calibrated and both BHD signals were normalized to contain the same signal power at 1.24 MHz, which was the signal injected in the Y arm. Figure 4.2 shows the amplitude spectral density (ASD) for the displacement signal in all three channels around f_{sig} and f_{sc}. To compute the ASD's, Welch's method [114] was used with a bandwidth of 50 Hz, an overlap of 50 % and Blackman windowing. It shows that all three detector signals detected some scattered light signal, although at different levels. Assuming that BHD1 truly measured P_{s} and BHD2 measured Q_{as}, it would be expected that both signals inhibit the same scattered light power, since the signal should show in the same way, according to eq. 4.3 and 4.2b. Furthermore both BHD readouts inhibited a higher overall readout noise level at around $60\,\mathrm{fm}/\sqrt{\mathrm{Hz}}$ in contrast to a noise level of about $12\,\mathrm{fm}/\sqrt{\mathrm{Hz}}$ in the BD signal. Nevertheless, it is possible to demonstrate scattered light signal suppression and the individual readout of both interferometer arms. The combined signals S_1 and S_2 were computed according to eq. 4.4 and their respective ASD's are depicted in comparison with the one of the BHD2 readout in Figure 4.3. In the case of S_1 shown in Fig. 4.3a it can be observed that the scattered light noise peak at 1.251 MHz is nearly fully suppressed. The simulated GW peak at 1.24 MHz is unaffected, leading to a SNR improvement of about 13.2 dB in comparison to BHD2. For signal S_2 shown in Fig. 4.3b, the opposite result can be seen. Here, the signal peak is strongly suppressed, by about 18.3 dB in relation to BHD2. The scattered light noise peak is largely unaffected.

Discussion

In the described experiment, scattered light suppression via implementation of one BHD at each interferometer port was demonstrated. This technique allows for the partial subtraction of noise (or signal in this experiment) stemming from either one of the interferometer arms by allowing for the discrimination between phase changes in either of the two arms. This stands in stark contrast to conventional readout techniques, in which a differential arm length change is measured.

The measurement showed a suppression of scattered light induced signal by 13.2 dB in one of the combined signals. Additionally, the suppression of the signal generated with a length modulation of one of the arms by 18.3 dB in the other obtained signal was shown. Limiting was most likely the implementation (discussed below), as the theory laid out before in Sec. 4.1 indicates no theoretical suppression limit except the shot noise limit. Demonstration of more suppression should be possible, however, for this the experimental setup would need to be improved. This could be done by reducing electrical crosstalk at the used modulation frequencies in the experiment. As was later seen in the experiments discussed in Chapter 8, the use of different PZTs can help with this. The then used ones had better displacement capabilities, improving the modulation range of the scattered light peak and thus increased the signal strength at lower driving voltages. Additionally, a reduction of the readout noise, which was measured to be above the expected shot noise limit, could lead to a more prominent scattered light noise peak.

Further, the locking scheme for the BHDs was limiting the precision of the quadrature readout. It was possible to lock one of the BHD's quadratures by using its readout as an error signal to control the LO phase. However, since the other BHD had to be adjusted to an orthogonal quadrature, this meant its signal was not usable directly as an error signal (the DC component was non-zero at the right quadrature). Thus, it was adjusted manually and the quadrature was consequently slightly detuned from being orthogonal. This could explain why the scattered light signal peaks inhibit different amplitudes, despite the coupling supposedly being equal in both quadratures. Additionally, the readout at both ports was placed at differing distances from the central beam splitter. It was ensured this difference would be small enough such that the signal phase does not inherently change, i.e. below 30 cm. However, it could be possible that the overlap between the modes of the scattered light signal and the carrier signal differed from the symmetric and the antisymmetric port. As beam clipping can not be excluded due to a small aperture at the FR used to separate the symmetric output port, this could have influenced the readout.

Evidently, here only a simple Michelson interferometer was considered, thus in the next section enhanced topologies are discussed for the application of scattered light noise subtraction in gravitational wave detectors (GWDs).

4.3 Advanced interferometer topologies

A comprehensive study of applying this technique to the complex layout of a GWD as described in Sec. 2.3.2 and shown in Figure 2.3 has not been done yet. However, the role of the different used cavities is shortly discussed here. Considering the effects of arm cavities, it can be observed that for each obtained signal combination (eq. 4.4 and 4.5) one respective interferometer arm does not contribute. This is independent of the actual phase, and a brief derivation can easily show that the suppression of the contribution of one arm is also irrespective of the actual field amplitude. Assuming a beam splitter in the same orientation as in Figure 4.1 with electric fields entering from the X- and Y-direction, described by field amplitudes $\alpha_{\mathrm{X/Y}} = Q_{\mathrm{X/Y}} + iP_{\mathrm{X/Y}}$, the outgoing amplitudes are

$$\alpha_{\mathrm{as}} = \frac{1}{\sqrt{2}}(\alpha_X + i\alpha_Y),\ \alpha_{\mathrm{s}} = \frac{1}{\sqrt{2}}(\alpha_Y + i\alpha_X). \tag{4.7}$$

Consequently, the quadratures yield:

$$Q_{\mathrm{as/s}} = \frac{1}{\sqrt{2}}(Q_{\mathrm{X/Y}} - P_{\mathrm{Y/X}}),\ P_{\mathrm{as/s}} = \frac{1}{\sqrt{2}}(Q_{\mathrm{Y/X}} + P_{\mathrm{X/Y}}). \tag{4.8}$$

As before, combinations of orthogonal quadratures lead to a read out of separate quadratures of the fields in the interferometer arms. This shows, that the separation of signals is a general result. A quadrature readout at both exit ports of a beam splitter allows the reconstruction of two interfering fields entering the beam splitter. In the case of a GWD, this enables the individual arm readout also for a Fabry-Perot Michelson interferometer. As such, this technique could be tested in interferometers that do not employ optical recycling techniques, such as GWD prototype facilities [115].

However, it must be assumed that power- and signal-recycling, as well as the necessary and desired dark-port operation, pose a challenge for the scheme. Remaining in the picture of a separation of the fields in the interferometer arms, the effect of, e.g., power-recycling would be to mix those amplitudes further before enabling the readout. This non-trivial process seems to make a separation of fields challenging.

Another effect of a power-recycling scheme is that the removed amplitude noise is present in the field reflected from the PRM towards the laser and might thus hinder a readout of that field. Consequently a different amplitude stabilization may be needed to implement the DBR scheme if using the field in reflection of the PRC. Alternatively, one could look for a way to combine both schemes.

There are several aspects for DBR that need to be further studied. Regarding the topology, it should be considered how to modify the readout to measure the scattered light noise, by moving the readouts or adding additional ones. Further, the effect of recycling techniques and resonant sideband extraction needs to be addressed. The potentially

necessary detection of quadratures from bright fields could, theoretically, be realized by applying additional squeezed light when attenuating the bright fields [116] or by using opto-mechanical detection of bright fields [117]. Generally, implementing balanced homodyne detection at the symmetric port, even without including the just mentioned techniques, brings additional complexities. Balanced detection for the asymmetric port requires a number of additional optics and beam paths to use e.g. a pick-off from the central beam splitter as LO [108]. This effort would need to be effectively doubled to also enable balanced homodyne detection at the symmetric port. Future effort also needs to be directed towards addressing the limitation of the scheme through different types of laser noise. Or whether the readout is also able to subtract the effect of opto-mechanical coupling of scattered light noise, the in Sec. 3.1.2 discussed radiation pressure noise component. Further, it is important to note that the sensitivity for each signal depends on the operating point. Thus for an optimal sensitivity it may be necessary to read out two orthogonal quadratures at each port or to find a compromise between the sensitivities of arm length changes in the two individual interferometer arms. Finally, the compatibility with quantum noise reduction by e.g. squeezed light would need to be investigated.

4.4 Conclusion

Despite all the caveats presented, the here presented experiment and additional study, as well as the in the previous chapter (especially Sec 3.2.2) mentioned studies [105–107] illustrate that additional readouts may improve the knowledge about an observed signal. This is further stressed by the there also discussed use of auxiliary readouts for removing scattered light in the Virgo detector [111, 118]. Subsequent research could thus focus on examining each quadrature of each potential pick-off port – i.e. transmission through test masses, other pick-offs at e.g. the PRM or inside the interferometer – for potential use as a scattered light noise readout.

As part of this work, a reduction of straylight noise of about 13.2 dB was demonstrated by using DBR. When treating the stronger peak caused by the simulated GW signal as the parasitic influence, the observed reduction was even higher at 18.3 dB. This puts DBR on a level with the referenced scheme tested in Virgo [111].

With this first, promising demonstration done, the focus of the project and this work shifted towards the implementation of *Tunable Coherence*. The following chapters now discuss its concept, first impressions made by simulations and finally the experimental implementation and demonstrations.

5 | Tunable Coherence

As was generally discussed in the previous chapters and more specifically in Chapter 3, the fundamental problem of straylight is its coherence with the main laser. Without it, straylight could not coherently interfere with the readout and thus only contribute errors that are easily filtered out. The idea of *Tunable Coherence* is to accomplishing exactly such a breaking of coherence, but in a controlled manner so that only the straylight is affected. To achieve this, binary pseudo-random-noise sequences (PRN) can be modulated onto the laser light to almost fully reduce its temporal coherence to timescales below the modulation frequency period. In principle, this idea is not new and has even been suggested at the beginning of gravitational wave detector (GWD) development. However, only with more recent technological advances has its implementation become feasible.
Nowadays these modulation schemes are combined with digital signal processing and demodulation of the recorded signal. Contrary to this, with *tunable coherence* everything stays in the optical domain and no digital demodulation is used. Only when measuring a signal on a PD, the bandwidth for this is chosen so that the modulation is filtered out. The readout is thus not limited by a minimal but a maximal bandwidth, something generally simpler to realize and thus more easily allowing high modulation frequencies.
In this chapter, the preceding ideas and the now used concept and implementation of *tunable coherence* transferred from digital interferometry (DI) are introduced in detail. Thereby, the core ideas behind its capability to suppress scattered light while not inhibiting high coherence when it is actually needed are presented. Concrete demonstrations follow in subsequent chapters, simulated ones in Chapter 6 and experimental ones in Chapter 7 - 10.

Origins

First ideas for removing scattered light by using phase modulations on the main laser were already investigated at the GWD prototype in Garching. Here, it was identified as an issue in the used Herriott delay line [82]. This scattered light was taken to have a relatively fixed delay compared to the main beam running through the delay line. The reasoning behind this was its origin inside the delay line, traveling a different path between reflections through it before overlapping with the main beam again. A first approach described and demonstrated in Schilling et al. [82] thus was to use a sinusoidal phase

modulation with a frequency matched to this delay. This led to the scattered light being on average half the time in one phase relation to the main beam and the other half in the opposite. A time average then led to its removal from the measurement for this delay and any odd multiple of it. While the modulation frequency needed to be chosen to lie above the measurement bandwidth and comply with constraints given by the minimal delay, it could be adjusted such that other certain multiples would be suppressed as well. With this, they reached a suppression between 30 and 35 dB and the realization that proper adjustment of modulation frequency and depth were crucial. Taking this one step further, several sinusoidal modulations at different frequencies were added, enabling the suppression of more multiples of the delay. However, this had the downside that the scattered light could not be completely canceled out anymore [82, 83].

In private communication with the group, Rainer Weiss proposed 1982 to use *white noise* as modulation input to optimize the approach [83]. Even though not reaching quite that far yet, Schnupp et al. [83] proposed and discussed the use of orthogonal square-waves for the modulation as a solution for the declining suppression when using several sinusoidal inputs. All multiples up to the number of individual slices could be suppressed by dividing the modulation into elementary time-slices corresponding to the minimal delay. From this, the modulation sequence was constructed by choosing appropriate orthogonal square wave functions. As an example, for a division into five orthogonal square waves all but every fifth multiple could be suppressed. However, at the time they saw a strong limitation in the achievable switching times and thus frequencies of the square waves due to technical limitations [83].

Another demonstration using square wave functions resembling white noise was done by Dewey [119, Appendix I]. Here the result was, that successful suppression of scattered light was possible. However, the achievable frequencies and introduction of additional noise were strongly limited by the available electronic and optic components at the time. Thus the remaining coherence of the laser, limited by this modulation frequency as deeper discussed in Sec. 5.3, could not yet be reduced to meaningful scales for this application.

5.1 Pseudo-Random-Noise sequences

Before discussing modern applications relying on pseudo-random-noise (PRN) sequences as input for laser phase modulations, some groundwork needs to be laid. Thus this section introduces the relevant characteristics of these sequences and ways to generate them.

PRN sequences are binary sequences constructed in a way so that they show white noise characteristics but remain deterministic and repeating. While a truly random binary sequence is uncorrelated with itself for any given delay $\tau \neq 0$, a PRN sequence has one crucial difference in this regard – it is fully correlated to itself at every integer multiple

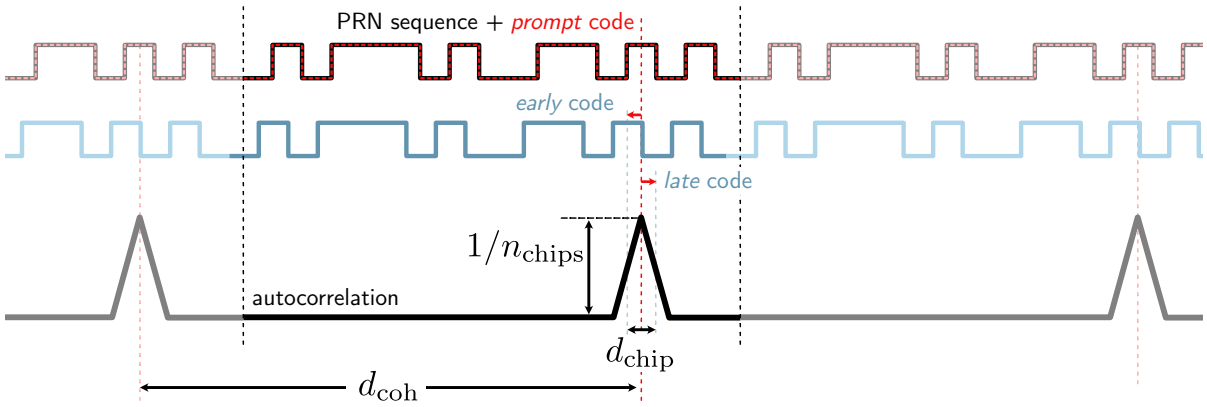

Figure 5.1: Auto-correlation properties of a PRN sequence visualized with prompt, early and late code segments showing the resulting characteristic auto-correlation function (ACF). Taken from Voigt et al. [24].

of its repetition time. For the applications discussed in Sec 5.2, this is not necessarily important, it is, however, very relevant for *tunable coherence* as discussed in Sec. 5.3.
Due to its white noise properties, modulating a PRN sequence onto a slower signal spreads the information contained in the slow signal over the higher modulation bandwidth. Instead of the signal, only random, uncorrelated noise is perceived unless the signal is properly demodulated. For this, the deterministic property becomes relevant, as knowing or being able to reconstruct the sequence makes demodulation easily possible. These properties made PRN sequences an ideal simple application in communications as they not only encrypted messages to a degree but also avoided single frequency transmission [120, 121]. These characteristics are also what makes them useful for multiplexing in later described applications like DI as the unwanted signals are spread into broadband white noise while only the properly demodulated one is recovered.
The two important properties can be summarized in the requirement for the auto-correlation function (ACF) to be two-level; equal to one for any delay equaling an integer repetition (including zero) of the sequence and zero or very close to zero otherwise. This characteristic is visualized in Figure 5.1 which shows a PRN sequence and its auto-correlation with a prompt and delayed version, showing an ACF with the described properties. Further, two length scales are introduced, both later relevant for *tunable coherence*. The first is the width of the correlation peak with its full-width-half-maximum (FWHM) relating to the length, here denoted d_{chip}, of the individual sequence components. These are called *chips* and represent the shortest constant period or smallest unit of the sequence. The second is the distance (in time) between repetitions that lead to regaining of full correlation, here denoted d_{coh}. Both length scales are related to the respective times by the speed of the used carrier for the modulation, i.e. in the later discussed cases a laser and thus the speed of light. For the here used sequences, the lower level of the ACF is further given by the inverse of the sequence's total length in contained chips n_{chips}.

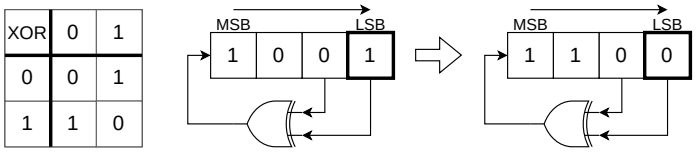

Figure 5.2: Truth table of an XOR logic-gate and example of an LFSR using a seed of four bits and the 1st and 2nd bit from the LSB as feedback taps into the MSB.

There are several representatives of such PRN sequences, including Barker codes [122] and Gold [123] and Kasami [124] codes. Another example are complementary sequence pairs, often called Golay pairs [125]. In this work, one of the most common representatives of PRN sequences, the so-called maximum-length sequence (*m*-sequence), is used. A possible way to generate *m*-sequences is therefore described next.

5.1.1 Linear Feedback Shift Registers and *m*-sequences

One often employed and simple approach to generate a PRN sequence, specifically an *m*-sequence, is the use of an linear feedback shift register (LFSR). This is a sequence, called register, of bits on which a shifting operation is executed, normally at each clock cycle. While one bit is dropped by this operation, a new one is generated using a linear feedback operation tapping specified bits of the register. These bits are therefore called taps and the choice of taps is important for the resulting pattern. A simple example of this is shown in Figure 5.2 for an LFSR using a seed of 4 bits and feedback taps at the 1st and 2nd position counted from the least significant bit (LSB). The current state of the register is then shifted from most significant bit (MSB) towards LSB, meaning the newly generated bit is inserted at the MSB. This represents the implementation of a Fibonacci LFSR, an alternative form would be the Galois implementation which has an internal feedback instead of the here described external. The generation of the new bit is normally done with an exclusive OR (XOR) logic-gate but alternative implementations using its logical complement, the XNOR gate, are possible.
Bit-shifting operations as described are a representation of finite field arithmetic expressed as a modulo 2 polynomial, meaning the polynomials coefficients can be either zero or one. As a binary state represents a number in powers of 2 the exponents of the polynomial give the bit positions of the taps and the $+1 = +x^0$ term resembles the generation of a new LSB to be added. So technically, the polynomial describes the exactly mirrored shifting and generating operations to the ones shown in Figure 5.2. However, it can easily be seen that this is equivalent, only reversing the order of states iterated through if the seed is not symmetrical. The shown 4-bit LFSR can thus be described by the polynomial $x^4 + x^3 + 1$ or as shown in Figure 5.3. As also shown in Figure 5.3, some lengths need more than two taps to work in the desired way. Generally, the register cycles through a number of states before returning to the initial state, unless it reaches the state where all bits are '0'. As then all newly created bits would still be '0', it never leaves this state.

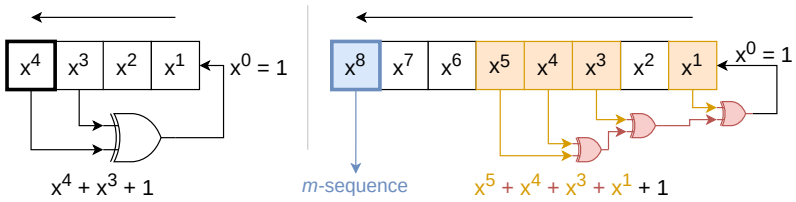

Figure 5.3: LFSRs representing primitive polynomials to generate *m*-sequences by collecting the MSB of every iteration to form the sequence.

The number of states it cycles through depends on the choice of taps. For the correct choice, an LFSR will cycle through all possible states, except the all-'0' case, and thereby generate a *m*-sequence. This was proposed by Golomb [126, 127] and can be achieved by using primitive polynomials for the feedback. The two examples in Figure 5.3 represent such polynomials. The sequence is then generate by collecting the MSB as a so-called *chip* for each iteration. Of course, technically any bit can be sampled as long as it is always the same, this would shift but not change the sequence. There can, however, be several possible implementations for a given length using different taps, resulting in different *m*-sequences.

An *m*-sequence, from now on denoted as $s_0(t)$, has the for a PRN sequence required two important properties. First, the sequence is repeating and second, it has a perfect two-level auto-correlation function (ACF) which is approximated by the Kronecker δ-function with a small offset from zero [127, 128]. This ACF is also repeating due to the repeating nature of the *m*-sequence $s_0(t)$, meaning

$$R(t,\tau) = \frac{1}{T}\int_{t-T}^{t} s_0(t)\, s_0(t-\tau)dt \tag{5.1a}$$

$$= \delta(\tau - m t_{\text{seq}}) \left(1+\frac{1}{n_{\text{chips}}}\right) - \frac{1}{n_{\text{chips}}} = \begin{cases} 1 & \text{if } \tau = 0 \pmod{t_{\text{seq}}} \\ -\frac{1}{n_{\text{chips}}} & \text{if } \tau \neq 0 \pmod{t_{\text{seq}}} \end{cases} \tag{5.1b}$$

where δ is the Kronecker δ-function, $m \in \mathbb{N}_0$, n_{chips} is the length of the sequence in chips and t_{seq} the time of one sequence repetition. This is related with $d_{\text{coh}} = c\, t_{\text{seq}}$, c being the used carrier speed, to the earlier used distance between correlation peaks. In any real implementation however, these peaks at every instance of $\tau = m t_{\text{seq}}$ are not a sharp δ-function. They instead have a rising and falling edge, each covering the length of one chip $d_{\text{chip}} = c\, t_{\text{chip}}$. Thus for $|\tau| \leq t_{\text{chip}}$ the ACF is given by

$$R(\tau) = 1 - \frac{|\tau|}{t_{\text{chip}}}\left(1 + \frac{1}{n_{\text{chips}}}\right) \tag{5.2}$$

which is plotted in Figure 5.4 for the first six sequence lengths used in this project. It also shows that the longer the used sequence is, the better the approximation of the ACF with the δ function becomes.

Due to the way they are generated, *m*-sequences have a length of $2^n - 1$ chips with an

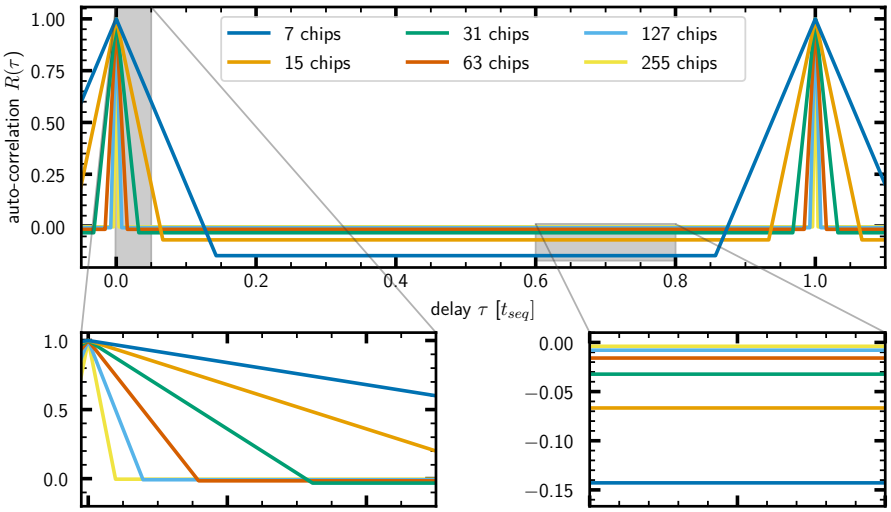

Figure 5.4: ACFs of the six shortest *m*-sequences used in this work. The left insert shows the falling edges caused by partial overlap of identical chips for delays shorter than one chip-length, the right insert shows the different minimal values depending on the sequence length.

almost evenly distributed number of '0's and '1's. As the only state the underlying LFSR never reaches is all '0's, the *m*-sequence has one '0' less than it has '1's which leads to the offset in the ACF.

Bit-shifting and logic gate operations can easily be implemented in digital hardware, making the generation of *m*-sequences a fast process in for example a field programmable gate array (FPGA). Without any additional complexity, an LFSR can easily generate new chips at the frequency of integrated system clocks, normally in the order of hundreds of MHz. However, especially for longer LFSRs, several bits can often be computed in the same cycle as the taps for the next cycle are just the bits that are going to be shifted there in the current cycle. By employing this parallelization, the rate can easily be increased if the used LFSR has a beneficial taps distribution. An example for an LFSR with a length of 6 bits is shown in Figure 5.5.

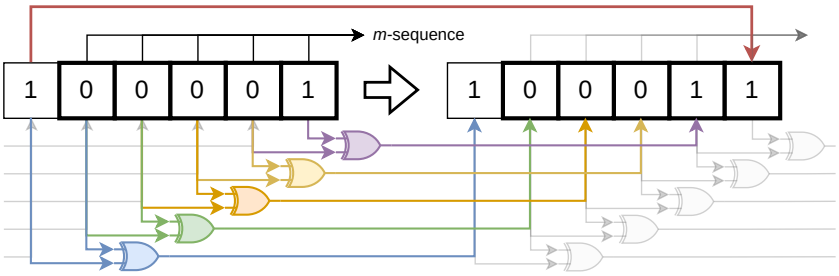

Figure 5.5: Exemplary implementation of a 6-bit long LFSR generating 5 new chips per cycle.

5.2 Digital Interferometry

The implementation of precise high speed phase modulation, following described PRN sequences was made possible by improvements in components which are now commonly used in e.g. telecommunications. Digital interferometry (DI) is now an established field using this concept and thereby motivates to revisit the old proposals for straylight miti-

gation using the same core techniques. Starting with a simple, illustrative example of the used concept, this can be found in satellite ranging as done for e.g. the global positioning system (GPS). Here, a PRN code is modulated onto the carrier onboard the satellites. By aligning a copy of the same code in the receiver, the time of arrival of a specific code segment can be determined. Together with the (in the orthogonal quadrature) also encoded time of transmission, the distance to the satellite can then be calculated. A similar approach is also used for the synchronization signals between the satellites of the planned LISA mission [129].

5.2.1 Digitally enhanced heterodyne interferometry

The idea of determining the time of flight of a signal by using PRN modulation on the carrier in order to imprint a time signature was taken over to interferometric measurements, introducing DI. Shaddock [130] proposed to combine heterodyne interferometry, often used for its high dynamic range, with binary phase modulation of the probing laser following a PRN sequence.

Instead of only generating a modulation sideband containing a fraction of the carrier field that caries the PRN modulation, here the phase of the probing laser is fully flipped by 180° or π following the sequence $s_{\pm1}(t)$. The resulting electrical field $E_{\mathrm{PRN}}(t)$ given by

$$E_{\mathrm{PRN}}(t) = s_{\pm1}(t) E_0 e^{i(\omega t + \varphi)}$$

is depicted in a simplified manner in Figure 5.6. By imprinting these phase reversals, the amplitude of the heterodyne signal is "randomly" inverted following the PRN sequence and thus spread out. In heterodyne interferometry, the probed beam then beats with a LO beam as a reference. The measured signal of this beat is then proportional to the amplitude product $Re(\overline{E}_{\mathrm{LO}} E_{\mathrm{PRN}})$ of both electric fields [130]. And as the amplitude of the probe beam is randomly inverted, averaging the signal over time results in (almost) zero. At a first glance, this destroys the measurement by effectively inhibiting interference and suppressing the otherwise measured beat between the probe laser and the laser used as LO [130]. However, if the signal is recorded with enough bandwidth such that the modulation is resolved in the time-series, it can be demodulated with an identical copy of the sequence. As $s_{\pm1}(t)^2 = 1$, this then reverses the inverted amplitudes back to normal and thereby restores the measurement.

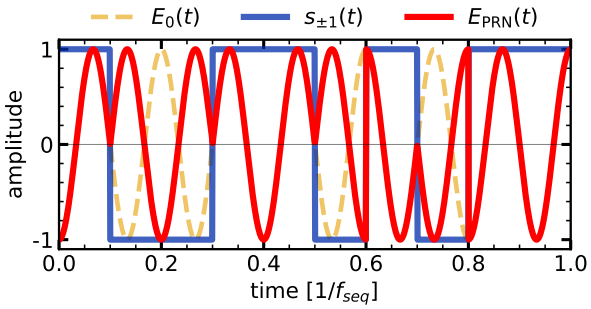

Figure 5.6: Example of an electrical field phase modulated following a PRN sequence. The parameters are optimized for better visualization and do not represent a real modulation sequence or frequency.

The benefit of this is the distinction of probed signals by their respective time of flight of the probing beam. Only the signal to which the demodulation copy of the sequence matches in delay is recovered. The others stay suppressed due to the earlier introduced characteristics of the PRN sequence and its ACF being almost zero for unmatched delays. In an example given in Shaddock [130], three mirrors at different distances are probed, in the measured signal, all of them are suppressed without demodulation due to the beat note itself being suppressed. However, demodulation with a sequence delayed to match the time of flight to one of the mirrors recovers only the signal induced by its movement while signals from the other mirrors stay suppressed.
Using this technique, it is therefore possible to simplify experimental setups as multiple targets can easily be probed with the same beam while the cross-contamination between the individual measurements can be minimized by using an appropriate sequence [130]. Experimental realizations of this technique have demonstrated this multiplexing [131] to picometer sensitivities [132] and allowed for simplification and shrinking of optical sensor designs [133]. Due to the isolation of the signal of interest depending on time delays, this technique is inherently almost insensitive to scattered and straylight, a characteristic that becomes relevant later.
The idea and demonstrations are not calling for or using especially high modulation frequencies. On the contrary, the need to resolve the modulation in the measured signal incentivizes the use of lower modulation frequencies to avoid having to use high speed electronics for modulation and measurement. de Vine et al. [132] and Wuchenich et al. [131] for example, used only 80 MHz, while Lay et al. [133] used 250 MHz with sampling at the same frequency. The caveat of having slower modulation frequencies is, however, a larger minimal delay between probed objects or the signal of interest and unwanted signals. This is limited by the length of the chips, the elementary symbols of the modulation, and thus longer for slow modulations.
An increase in modulation frequency and thus reduction in minimal resolvable distance was done by Isleif et al. [134], demonstrating 1.25 GHz modulation frequency and thus only 36 cm separation between targets. While this required not only modulation but also sampling at GHz rates, improvements in commercially available components made and continue to make such implementations easier and cheaper.

Further applications of digital interferometry

Today, DI is a commonly employed technique to simplify and enhance optical setups. Besides the previously described use in heterodyne interferometers, homodyne applications reducing the need for a frequency shifted laser have been demonstrated by Sutton et al. [135], Dey et al. [136] and more detailed in Sutton [137, Part III]. In other works, the number of simultaneously possible measurement and how it affects the cross-talk between them

was estimated to be in the thousands [138], demonstrating that discrimination between large numbers of signals is possible. Additionally, reductions in cross-talk between measurement channels have been achieved by using additional demodulation techniques [139] or complementary sequence pairs [140].
DI is now used in fiber interferometers [141] to suppress Rayleigh backscattering and for common-mode phase noise suppression in phasemeters [142]. Further, it is employed to enhance molecular dispersion spectroscopy measurement [143–145].
These various and numerous application of DI demonstrate that it is an established and highly useful technique with broadening impact for cross-talk and phase noise reduction in different experimental setups. Adapting it for straylight suppression in GWDs by removing the necessity for digital demodulation in post-processing is therefore an encouraged next step to transfer the tested benefits to this all-optical application.

5.3 Introducing all-optical self-demodulation

While DI has many advantages, one disadvantage is the necessity to record data with sampling frequencies exceeding the PRN frequency f_{PRN} and the following demodulation, which can get quite complex. In an attempt to counteract this limitation, the use of a second laser to demodulate the signal has been investigated [146, 147]. In this alteration of the scheme described in Sec. 5.2.1, the LO laser is also modulated with a delayed copy of the used PRN sequence. This moves the demodulation to the optical domain while the delay matching is done by shifting the modulation sequence on the second laser. In this work, the functionality of optical demodulation was demonstrated and thus the need for high-speed sampling removed. Further, the inherent near insensitivity to straylight of these concepts inspires an interesting approach for straylight mitigation.
For *Tunable Coherence*, one laser is again phase modulated with a modulation depth $\theta = \pi$ following a PRN sequence s_0, but no demodulation is implemented. Instead, data is recorded in such a way that every sample is an average over at least one full sequence. Thereby, the auto-correlation (ACF) is formed directly during the sampling process, removing the modulation from the data. Thus, the PRN sequence is now self-demodulated during the sampling. This means, only fields matching in sequence can coherently interfere. For fields having an unmatched delay to each other, the random properties of the PRN sequence cause the relative phase between them to oscillate such that their average is almost zero. In other words, the beams have no proper phase relation anymore and only add incoherently, except for a small remaining fraction. As the discussion in Chapter 3 showed, for scattered light it is the norm to travel a different path and thus be delay mismatched to the main laser beam. Thus, unless this additional delay matches a sequence repetition, it is prevented from coherently interfering by the PRN modulation. However,

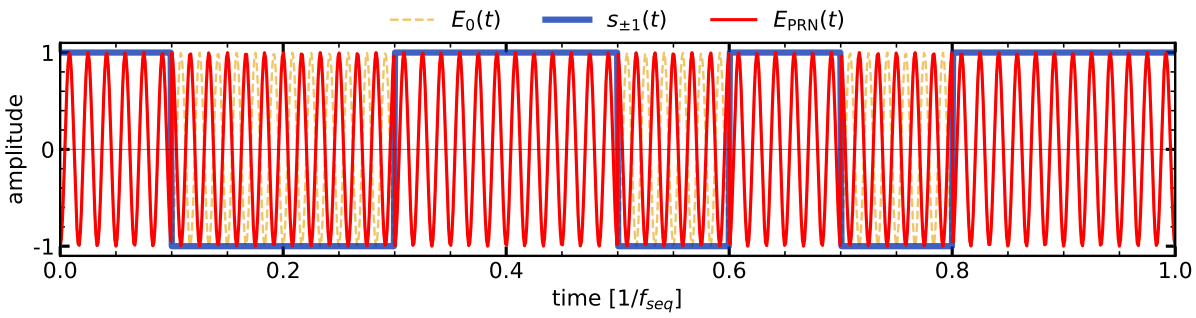

Figure 5.7: Adapted version of Figure 5.6 with a higher carrier frequency to showcase the remaining coherence inside each chip.

as the modulation cannot easily be removed from the laser, intended interference is also restricted to matched delays, complicating certain aspects as discussed later.
The PRN modulated field with amplitude E_0, frequency ω and phase φ as shown in Figure 5.7 can again be described by

$$E_{\mathrm{PRN}}(t) = E_0 e^{i(\omega t+\varphi+s_0(t)\theta)} = s_{\pm1}(t) E_0 e^{i(\omega t+\varphi)}, \tag{5.3}$$

where the second equality is true for $\theta = \pi$. Then the *m*-sequence $s_0(t) \in \{0, 1\}$ translates into an amplitude inversion with $s_{\pm1}(t) \in \{-1, 1\}$. The now resulting field remains only coherent within the timescale of an individual chip, on larger scales it becomes a kind of hybrid. This can be seen in Figure 5.7: for the duration of each chip the field remains unchanged, even between chips it only experiences a constant phase shift, thus individual chips still interfere constructively or destructively. However, looking at timescales covering more than one chip, these randomly appearing reversing interference pattern result in the before mentioned loss of properly defined phase relation and thus coherence. This newly introduced coherence length is now determined by the length of the individual chips. Assuming a PRN frequency f_{PRN} and the speed of light c, the optical path length corresponding to one chip is the in Sec. 5.1.1 introduced chip length d_{chip}, given by

$$d_{\mathrm{chip}} = c \cdot t_{\mathrm{chip}} = \frac{c}{f_{\mathrm{PRN}}}. \tag{5.4}$$

With the frequency bandwidth given by the inverse of the coherence time, now associated to the time of one chip, this creates a new effective bandwidth (follow e.g. [148, Sec. 7.4.3]) $\Delta\nu_{\mathrm{TC}} = 1/t_{\mathrm{chip}} = f_{\mathrm{PRN}}$ given by the PRN frequency. The associated artificially induced linewidth of the laser then is $\Delta\lambda_{\mathrm{TC}} = \lambda_0^2/d_{\mathrm{chip}}$, with λ_0 being its mean wavelength.
Comparing the so far introduced aspects with coherence theory [148, Sec. 12.4], the full similarity becomes apparent. Analogous to the mutual coherence function $\widetilde{\gamma}_{1,2}(\tau)$ defined via the cross-correlation between fields, now the ACF $R(\tau)$ of the PRN sequence additionally restricts the coherence. The *degree of coherence* now varies with $R(\tau)$ following

eq. 5.1 and eq. 5.2 between fully coherent at $\tau = mt_{\text{seq}}$ and almost fully incoherent outside the slope of partial coherence described by eq. 5.2. Coherent interference of the modulated light is thus reduced to lengths significantly shorter than this new coherence length d_{chip}. And as d_{chip} directly depends on the modulation frequency, this can be used to tune it, thus *Tunable Coherence*. Employing the technique at PRN frequencies in the GHz-range then reduces the remaining coherence down to centimeters and below. For example at $f_{\text{PRN}} = 1\,\text{GHz}$, it lies around 30 cm, thus a PRN frequency of even 10 GHz would make e.g. straylight originating at the secondary surface of thicker mirrors incoherent.

5.3.1 Pseudo-white-light interferometer

Due to the discussed reduction in coherence, an interferometer only works normally if its optical paths are equal or close to equal in length. This is very similar to a *white-light* interferometer. However, a true white-light interferometer only works for exactly matched arm lengths, here the macroscopic chip length introduced by *tunable coherence* gives some more tolerance. Sticking with the 1 GHz example and a laser wavelength of $\lambda = 1064\,\text{nm}$, around 281760 wavelengths still fit into one chip.

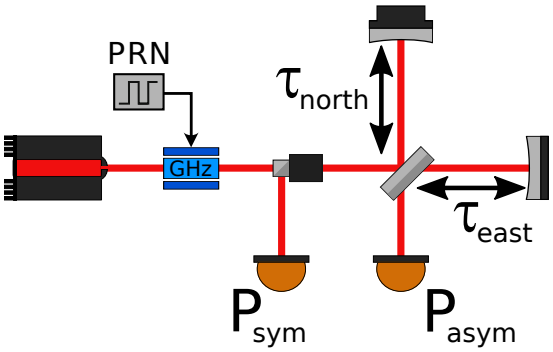

Figure 5.8: Sketch depicting a Michelson interferometer with a PRN modulated laser.

Generally, the power at either port of a Michelson interferometer as shown in Figure 5.8 with a modulated field according to eq. 5.3 is given by

$$P_{\text{asym}} = \frac{P_0}{2}\left[1 + R(\Delta\tau)\cos(\Delta\varphi)\right] \tag{5.5a}$$

$$\text{and} \quad P_{\text{sym}} = \frac{P_0}{2}\left[1 - R(\Delta\tau)\cos(\Delta\varphi)\right] \tag{5.5b}$$

with $\Delta\varphi = \omega\Delta\tau$ the phase difference between the two arms and $\Delta\tau$ the relative delay. This example clearly shows the previously described effect that the coherent part leading

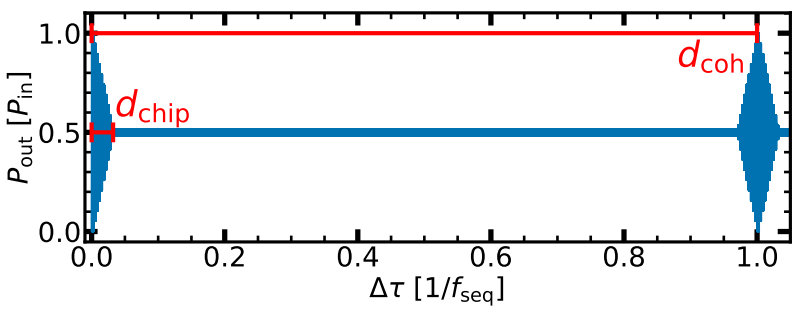

Figure 5.9: Two new lengths are introduced by *tunable coherence*, the microscopic chip length d_{chip} giving a measure for how long coherence remains and the macroscopic recoherence length d_{coh} after which coherence is regained.

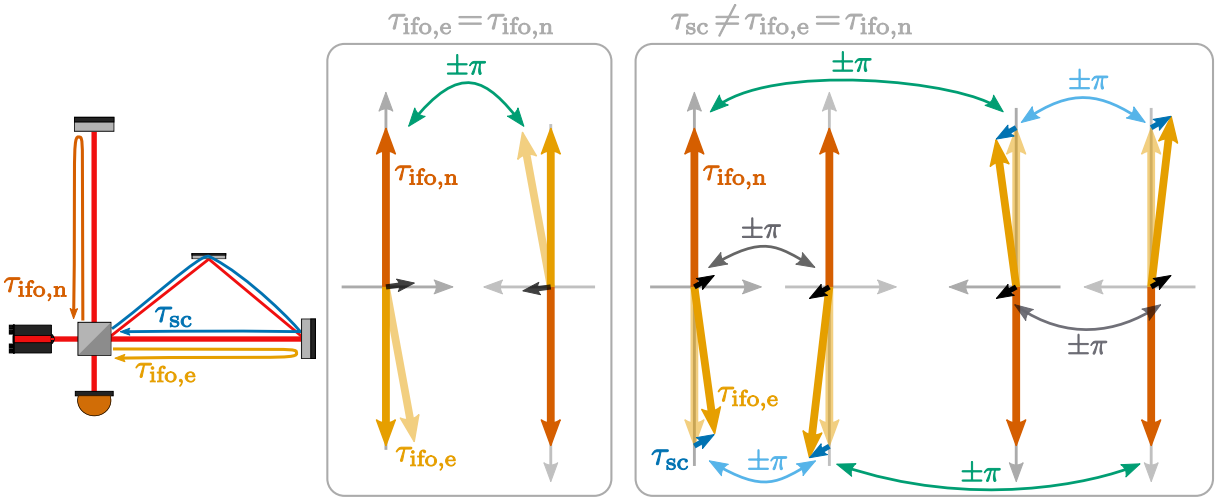

Figure 5.10: Sketch depicting the phase relations in a simple Michelson interferometer when using *tunable coherence*. The interferometer sketch on the left shows the three important delays $\tau_{ifo,n}$, $\tau_{ifo,e}$ and τ_{sc} of which $\tau_{ifo,n}$ is chosen as the reference, $\tau_{ifo,e} = \tau_{ifo,n}$ and τ_{sc} is longer by the length of more than one chip compared to the two others. The first box then depicts the case without scattered light but a signal in one of the arms. Looking at this from the fixed reference phase of the north arm, the PRN modulation flips the phases in both arms in synchrony (depicted by the green arrow), thus not changing the relative phase between the two arms but merely flipping the reference with it. Contrary to this, when also introducing an additional scattered light beam with a delay exceeding the length of a chip, there are four possible combinations. These are shown in the second box, the first two show the case in which only the scattered light sees a flip relative to the two arms (depicted by the blue arrow). The next two represent the same, now with the two matched beams also seeing a flip, however, as they both see the same, again the whole reference experiences the flip. This results in effectively two different combination which have the scattered light out of phase by the flip, in this case π. The way the chips in an *m*-sequence are distributed, both combinations are almost equally common with the case of a relative flip existing one more time than the other. Thus, an average over a full sequence has all but this one occurrence cancel each other.

to phase dependent interference is strongly suppressed for unmatched delays as it depends on the ACF, $R(\Delta\tau)$. Thus, for a relative delay outside the chip length, both ports receive around half the input power with only a small remnant of the original interference. The output power calculated following eq. 5.5 is plotted in Figure 5.9 showcasing this effect and the length scale d_{chip}. The other characteristic length of sequence repetition d_{coh}, which becomes important for optical resonators (discussed in Sec. 5.3.2), is also shown. Consequently, if the two arms of the interferometer are delay matched but scattered light is not, the interferometer works as intended but can be made very resilient towards scattered light influences. The degree of resulting straylight suppression is given by the minimum of the ACF $R(\tau)$ which depends on the PRN sequence's length in chips (eq. 5.1). The reachable suppression in decibel depending on sequence length l_{seq} is thus estimated by

$$\text{suppression} = -20\log_{10}\left(\frac{1}{l_{seq}}\right) = -20\log_{10}\left(\frac{1}{n_{chips}}\right). \tag{5.6}$$

To visually showcase the functionality of straylight suppression with *tunable coherence*, Figure 5.10 depicts in phasor form how scattered light interacts with the main interferometer. Similar to the argument for the main beams recombining after a relative delay exceeding the chip length, the scattered light now experiences random phase inversion relative to the two main beams. As again these flips are almost evenly distributed between the two states (see Sec. 5.1.1), all but one of them cancel in the time average. If however, one would record the power with higher sampling rate than the PRN frequency, thus resolving individual chips, this effect would vanish. Instead, for a constant straylight phase, the recorded power would randomly jump around a small offset to the power without scattered light. This offset is caused by the small imbalance resulting from the lost light in one arm now recoupling as straylight. The observable pattern then follows the convolution of the PRN sequence with its delayed version as shown in Figure 5.11. The before mentioned time average is also shown as the solid line, experiencing a slight offset from the nominal power again due to the light lost as straylight. As the modulation is orders of magnitude faster than the scattered light fluctuation, the depiction is a valid approximation also if the phase is not fixed. How in turn a varying scattered light phase causes a change in power is depicted in Figure 5.12, together with its suppression by *tunable coherence* using a simple example of a 7 chips long PRN sequence. The observable small offset is here again due to the light lost as the recoupling straylight. A more comprehensive calculation of the interferometer output with scattered light and PRN modulation is further done in Chapter 6 for the simulations discussed there.

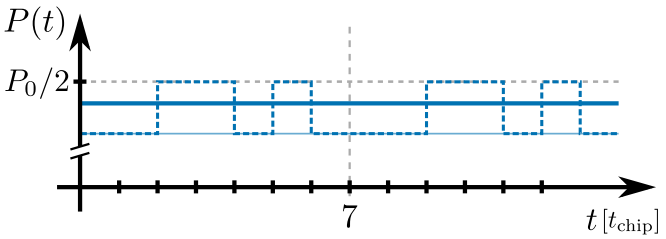

Figure 5.11: Time-series showing the recorded power with each chip of the PRN sequence resolved (dashed) and averaged (solid). Without straylight, the interferometer would be at mid-fringe ($P_{\mathrm{out}} = P_0/2$ at both ports).

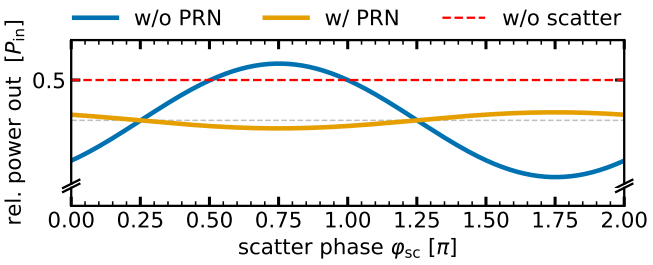

Figure 5.12: Output power depending on the scattered light phase φ_{sc} without and with PRN modulation using a 7 chips *m*-sequence. Without straylight, the interferometer would be at mid-fringe ($P_{\mathrm{out}} = P_0/2$ at both ports).

5.3.2 Recoherence and optical resonators

In order to implement *tunable coherence* in high precision interferometers, it needs to be functional in other setups than only basic interferometers as well. As presented in Sec. 2.3.2, especially gravitational wave detectors (GWDs) employ various optical resonators for e.g. shot noise reduction. Thus for *tunable coherence* to be viable as a straylight suppression technique in these detectors, it has to be functional with optical cavities. Simply put, a cavity relies on the constructive interference between light fields taking multiple round-trips in it. This implies that the length of a cavity needs to be a multiple of the used wavelength and that the light needs to remain coherent over many round-trips. Further, using a highly stable cavity length as a reference, the lasers linewidth can even be narrowed and stabilized, somewhat the opposite to what *tunable coherence* is effectively doing (see Sec. 5.3). Specifically, white light or a truly random modulation sequence would completely inhibit this functionality, the use of PRN sequences, however, adds a crucial difference. Because a PRN sequence is periodic, its ACF reaches unity again after each repetition and coherence is regained. Thus modulated light having a relative delay matching a full integer of this repetition can interfere without any constraints. The optical path length corresponding to a full sequence repetition is thus called the recoherence length d_{coh} as coherence is regained for any integer multiple of it. For a PRN sequence containing n_{chips} chips, repeating at a frequency of f_{rep} it is given by:

$$d_{\mathrm{coh}} = n_{\mathrm{chips}} \cdot d_{\mathrm{chip}} = n_{\mathrm{chips}} \cdot \frac{c}{f_{\mathrm{PRN}}} \tag{5.7a}$$

$$= c \cdot \frac{1}{f_{\mathrm{rep}}} = c \cdot t_{\mathrm{seq}} \tag{5.7b}$$

with the speed of light c and the chip length d_{chip} (eq. 5.4). Figure 5.9 shows both new length scales introduced by *tunable coherence* visualized with the output power of a Michelson interferometer. In that setup, the length of one arm is changed relative to the other over a length of a full sequence repetition.

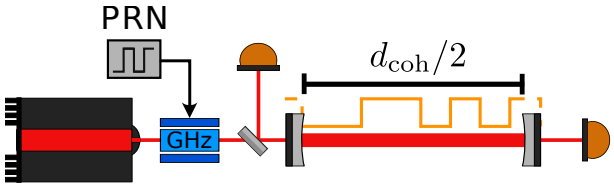

Figure 5.13: Sketch depicting a cavity with a PRN modulated input field.

This regaining of coherence then allows cavities to work with *tunable coherence* if the optical round-trip length of a cavity and the recoherence length of the PRN sequence are matched. For a simple two-mirror cavity as shown in Figure 5.13 this means the physical length between the mirrors l_{cav} must be equal to half the recoherence length, meaning $l_{\mathrm{cav}} = d_{\mathrm{coh}}/2$. Alternatively, as any integer multiple m also works, as long as the PRN modulation is consistent in quality over time, $l_{\mathrm{cav}} = m\, d_{\mathrm{coh}}/2$.

For more complex resonator setups, the general condition that the optical round-trip length d_{rt} has to match an integer multiple of the recoherence length ($d_{\mathrm{rt}} = m\, d_{\mathrm{coh}}$) stays true. However, as further discussed in Sec. 8.2.2, it can be beneficial to introduce additional constraints on the distance between individual mirrors for additional scattered light suppression. An overview of possible cavity lengths l_{cav} that would fit to the here used *m*-sequences at different PRN frequencies between 1 GHz and 20 GHz is shown in Figure 5.14. Some typical length scales of cavities used in GWDs are also marked. How these length fit together with a realistic implementation of *tunable coherence* is further discussed in Ch. 11, for now they are only given for a simplified comparison. As can be seen, shorter sequences can fit table-top sized cavities even at lower GHz modulation frequencies. However, longer sequences can quickly reach hundreds of meters in needed length. Compared to the scales of interferometers used for GW detection, reaching 3-4 km in the case of currently existing ones or even between 10 and 40 km for future ones, such lengths are not unrealistic. On these scales, PRN sequences of hundreds of chips in length could still be feasible which would allow for straylight suppression of somewhere around 40 dB (see eq. 5.6).

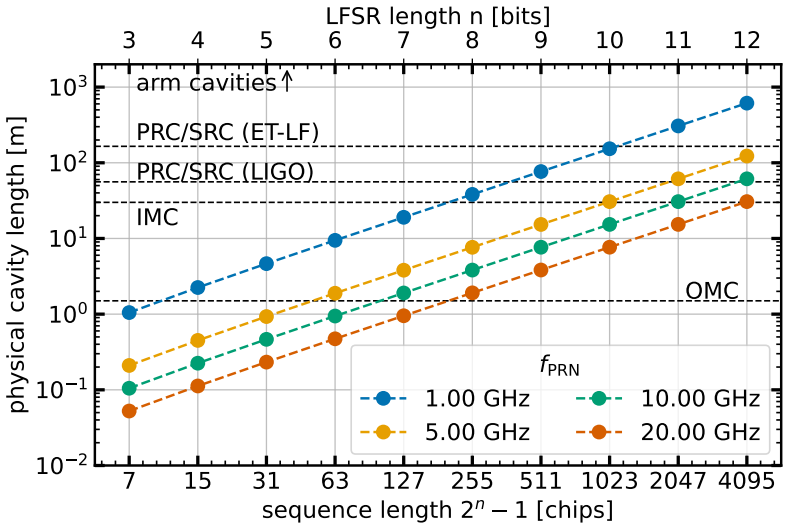

Figure 5.14: The needed physical cavity lengths in order for a cavity to be matched to the PRN sequence for *m*-sequences of different lengths and for different PRN frequencies. Additionally indicated are typical length for different types of cavities in GWDs for comparison (arm cavities lie outside the shown range).

5.3.2.a Looking at more complex interactions

In Chapter 6 the interaction between PRN modulated fields and a two-mirror cavity is analytically derived in greater detail. This is then used to simulate deviation from the ideal matching condition. However, even without more detailed analysis, it easily becomes apparent that the simple constraint $d_{\mathrm{rt}} = m\, d_{\mathrm{coh}}$ can have more complex implications in practical implementations. As described, a key feature of a cavity is that the internal field is comprised of fields taking many round-trips in the cavity. The higher the reflectivities of the mirrors, the more round-trips light takes in between them, with the finesse of the cavity being a measure for this. It then easily follows that for an increased number of

round-trips, several aspects become important. As each round-trip corresponds to at least one additional sequence in delay, the requirements in stability and consistency of the PRN modulation increase.

One aspect of this is the stability of the clock used as time reference for the chips. Any clock jitter introduced by it can negatively impact the auto-correlation between delayed versions of the PRN sequence. Additionally, it can directly impact the length matching between sequence and cavity itself. Further, imperfections in the modulation like changing rise- and fall-times between chips or changes in modulation depth impact the quality of the regained coherence. This is unimportant if beams are interfered after an equal delay as they then carry the same imperfections. In other words, then the imperfections are common-mode. However, any difference in path delay matching to $m\,d_{\mathrm{coh}}$ or the addition of round-trips in a cavity are affected by it.

Another aspect that becomes relevant for high numbers of round-trips or sequence repetitions in general is the precision in matching between cavity and PRN sequence. Over many repetitions, any small mismatch can sum up to a significant deviation. This can lead to the point were a discrepancy between the microscopic tuning, meaning the length offset relative to a wavelength, of a cavity and the macroscopic matching to $m\,d_{\mathrm{coh}}$ can introduce artifacts. In this case, the chip length needs to be tuned so it is an integer multiple of the wavelength or, in other words, the PRN frequency needs to be locked to the laser frequency. A more in depth discussion of these effects is provided in Sec. 11.1.2.

5.4 Conclusion

With this chapter *tunable coherence* was introduced by transferring techniques used in the established field of DI to an all-optical self-demodulation scheme. Thereby the two important parameter chip length $d_{\text{chip}} = c/f_{\text{PRN}}$ and recoherence length $d_{\text{coh}} = n_{\text{chip}}\, d_{\text{chip}}$ were introduced. It was motivated how the modulation reduces the coherence length and thereby effectively widens the linewidth of a laser. It was further demonstrated how phase modulation of the laser following a PRN sequence creates a pseudo-white-light interferometer that is almost fully insensitive to scattered light. By modulating the laser's phase at GHz frequencies, the coherence length is reduced to the cm-scale, allowing for parasitic beams even with small relative delays to be suppressed. These short lengths also allow *tunable coherence* to be implemented in tabletop experimental setups and especially on the scale of GWDs. Additionally, the use of periodic sequences to regain coherence after each repetition allows optical cavities to function if additional constraints are met. Lastly, factors influencing the functionality of cavities with *tunable coherence* were considered. To further deepen the understanding of the here introduced interactions, the next chapter presents more detailed simulation results.

Using the provided relations, one can compare the newly created effective linewidth resulting from 1 GHz PRN frequency of $\Delta\lambda_{\text{TC}} \approx 3.78\,\text{pm}$ to the sub-fm linewidth of stabilized continuous-wave lasers. On the other side, pulsed lasers easily have a linewidth on the nm-scale and true *white light* reaches hundreds of nm. This is showcasing that a PRN modulated laser resembles somewhat of a hybrid by preserving the ultra narrow linewidth for perfect delay matching but artificially adding a tunable one. Due to the control that is gained through the implementation, discussed in detail in Chapter 7, these parameters can be dynamically tuned with *tunable coherence*.

6 | Simulating *Tunable Coherence*

The previous chapter introduced the new characteristics a laser gains when modulated with a PRN sequence. To gain a better understanding of the resulting interactions, especially outside of simplified assumptions like perfect matching, *tunable coherence* was simulated. One focus of these simulations was *tunable coherence*'s interaction with optical resonators, but also its straylight suppression capabilities were investigated. For this, a simulation tool was needed that could handle both the PRN modulation and the nonlinear coupling of scattered light. A first approach was to numerically solve analytical calculations for different parameters. The results of these simulations were published in Voigt et al. [23], titled *Simulating tunable coherence for scattered light suppression in laser-interferometric gravitational wave detectors* (doi: 10.1063/5.0148790), and are taken from this publication for the relevant parts of this chapter. Additionally, the work on a subsequently developed, more flexible simulation tool is summarized in this chapter.

6.1 Simulation tools

Due to the complexity of the optical layout used for modern gravitational wave detectors (GWDs) and other high precision laser interferometer and even their subsystems, it is beneficial to simulate these setups to identify problems and optimal parameters. For this purpose, several different simulation tools have been developed. Prime examples for this are e.g. ifoCAD [149, 150] and FINESSE [66, 151]. The latter especially is an often used tool to investigate simple and more complex optical setups due to it being easy to use and producing reliable results quickly. In order to achieve this, it uses a modular input and a matrix formalism to solve the steady state description of a setup. This makes it powerful and fast, however, it does neither support non-linear and time varying effects nor a straight forward implementation of the PRN modulation used in *tunable coherence*. For simulating *tunable coherence*, a simulation tool was needed that not only allowed for the in this context rather unconventional modulation of the laser but also for modeling scattered light. In other words, a simulation tool that, contrary to e.g. FINESSE, runs in time-domain and not frequency-domain. As a first approach, analytical calculations of specific setups were used and investigated for different choices of parameter, later the development of a new simulation tool was started.

6.1.1 Analytical calculations

For the simulations published in Voigt et al. [23], two types of setups were investigated, a Michelson interferometer with scattered light coupling and a cavity without additional scattered light.

6.1.2 Michelson interferometer

For the first part, a Michelson interferometer in which a fraction of the light is scattered out of the main beam in one of the arms, as shown in Figure 6.1 was modeled. For this scattered light creation, a beam splitter with low amplitude reflectivity r_{sc} was used in the model. The light was then back-reflected from a moving surface and re-entered the interferometer so that the field coming from this arm contained the sum of the main and the scattered light.

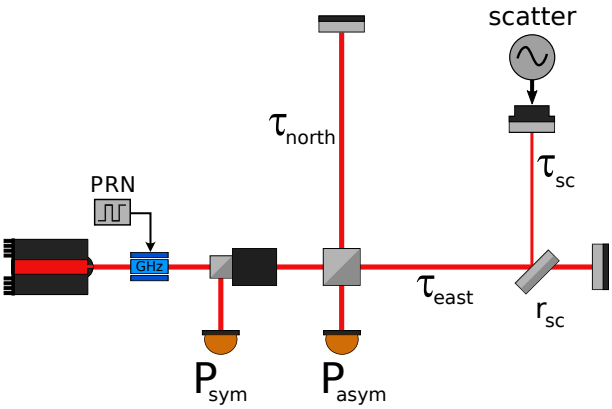

Figure 6.1: Simulated Michelson interferometer topology with scattered light coupled in via a low-reflective beam-splitter and *tunable coherence* realized using PRN modulation. Adapted from Voigt et al. [23].

The electric fields given by eq. 3.8 can be used to calculate the measured power e.g. at the south port of this setup. This power is then given as in eq. 3.9[11] by

$$P_{\text{asym}} = \frac{P_0}{2}\Big[(1-r_{\text{sc}}^2)[1+\cos(\omega\tau+\pi)] + r_{\text{sc}}^2\,[\cos(\omega(\tau+\tau_{\text{sc}})) - \cos(\omega\tau_{\text{sc}})] + r_{\text{sc}}^4\,[1+\cos(\omega\tau_{\text{sc}})]\Big]. \tag{3.9}$$

Here, P_0 is the input power, ω the angular frequency of the laser ($\lambda = 2\pi c/\omega = 1064\,\text{nm}$ was assumed in the simulations), τ the microscopic difference in propagation time between the arms and τ_{sc} the additional delay of the scattered light, which can be time-dependent. In the simulation, a DC-readout scheme was implemented, calculating a time-series of measured phase difference as shown in Figure 6.2a. From this, the amplitude spectral density (ASD) was calculated. Other noise sources like shot noise were omitted for simplicity.

Introducing *tunable coherence*, the electric field carrying the PRN modulation is given by eq. 5.3:

$$E(t) = E_0 e^{i(\omega t+\varphi+s_0(t)\pi)} = s_{\pm1}(t) E_0 e^{i(\omega t+\varphi)}, \tag{5.3}$$

[11] The additional phase shift of π comes from the double transmission through the optic coupling the scattered light

where $s_0(t)$ describes the PRN sequence turning the phase shift of π on and off. If the modulation depth is carefully controlled to be exactly π, the second equality holds with $s_{\pm1}(t) = \pm 1$. With this, the output power from eq. 3.9 then depends on the auto-correlation function (ACF) $R(\tau)$ of the sequence $s_{\pm1}(t)$. This is, as described in Section 5.1, an ideal two-level ACF for the used *m*-sequence, as long as the measurement by the PD is averaged over full sequences:

$$\begin{aligned} P_{\text{asym}} = \frac{P_0}{2} \Big[& (1-r_{\text{sc}}^2)\,[1 + R(\tau)\cos(\omega\tau+\pi)] \\ & + r_{\text{sc}}^2\ [R(\tau+\tau_{\text{sc}})\cos(\omega(\tau+\tau_{\text{sc}})) - R(\tau_{\text{sc}})\cos(\omega\tau_{\text{sc}})] \\ & + r_{\text{sc}}^4\ [1 + R(\tau_{\text{sc}})\cos(\omega\tau_{\text{sc}})] \Big] \end{aligned} \tag{6.1}$$

All parasitic oscillating terms are suppressed by the value of $R(\tau)$ at the delay of the scattered light. Designing the two interferometer arms nearly equally long keeps the delay between them small enough for $R(\tau)$ to still be close to unity. Thus the former non-linearly coupled noise is now reduced to a constant offset term scaling with scattered power.

6.1.3 Optical cavity

In a Michelson interferometer only the differential delay between the two arms is relevant, however, optical resonators face more drastic constraints. Here, coherence between multiple round-trips is required to achieve e.g. a high power buildup in the cavity. By calculating the reflected field from a cavity with PRN modulation using the incoming field given by eq. 5.3 (also restated above), one gets

$$E_{\text{refl}}(t) = r_1 E_0 e^{i(\omega t+\varphi)} \left[s_{\pm1}(t) - \frac{t_1^2}{r_1^2} \sum_{n=1}^{\infty} s_{\pm1}(t-n\tau) \left(r_1 r_2 e^{-i\omega\tau} \right)^n \right]. \tag{6.2}$$

Here τ is the round-trip delay of the cavity and $r_{1,2}$ and $t_{1,2}$ the amplitude reflectivity and transmittance of the first (input) and second mirror respectively. In the same manner, one can obtain equations for the transmitted and circulating fields.

As expected for reduced coherence lengths, the random modulation suppresses stable constructive and destructive interference around the cavity mirrors for an arbitrary macroscopic cavity length, inhibiting power buildup in the cavity. In all cavity field equations, such as Equation 6.2, the PRN term $s_{\pm1}$, causes the sum to converge randomly around zero. It is therefore not trivial to understand the interaction of the PRN modulation and a two-mirror-resonator for arbitrary lengths. Thus the area studied more closely is the one, where the length of the cavity is close or equal to the recoherence length d_{coh} of the PRN sequence, or an integer multiple of it.

In the case of ideal matching of a sequence repetition to a round-trip delay, the equations for the fields of the cavity can be rewritten such that no modulation terms appear anymore. Then $s_{\pm1}(t-n\tau)=s_{\pm1}(t)\ \forall n,t$ and therefore, the for example reflected field, becomes:

$$\begin{aligned} E_{\text{refl}}(t) &= r_1 s_{\pm1}(t) E_0 e^{i(\omega t+\varphi)} \left[1 - \frac{t_1^2}{r_1^2}\sum_{n=1}^{\infty}\left(r_1 r_2 e^{-i\omega\tau}\right)^n\right] \\ &= s_{\pm1}(t) E_0 e^{i(\omega t+\varphi)} \left[r_1 - t_1^2 r_2 e^{-i\omega\tau}\sum_{n=0}^{\infty}\left(r_1 r_2 e^{-i\omega\tau}\right)^n\right] \\ &= E_{in}(t)\left[r_1 - \frac{r_2 t_1^2 e^{-i\omega\tau}}{1 - r_1 r_2 e^{-i\omega\tau}}\right] \end{aligned} \tag{6.3}$$

In a similar fashion, $s_{\pm1}$ also drops out for all other fields.

This shows that cavities in principle can be operated in the same way as without PRN modulation. However, operation close to, but not exactly at this ideal macroscopic length is much more practical and is investigated in more detail in the simulations. In complex interferometer topologies, such as in GWDs, optical cavities fulfill several different tasks, which means different configurations of cavities are used. Therefore the simulation was used to demonstrate, that the requirements needed for the detector to work as without PRN modulation can still be met.

In order to properly simulate *tunable coherence* in this cavity setup it was necessary to assume that the repetition of the PRN sequence was always also an integer multiple of the wavelength as otherwise numerical precision was not good enough to avoid artifacts. In other words, the assumption was made that the real PRN frequency was locked to the laser frequency to simplify calculations, similar as is often done with macroscopic length and microscopic tuning in regards to the wavelength [66, p. 20].

6.2 Simulation results

The following results were obtained from the simulations used for the publication Voigt et al. [23] and are summarized here.

6.2.1 Michelson interferometers

Figure 6.2a shows simulation result of scattered light coupling into the interferometer without PRN modulation as given by eq. 3.9. Two main features of scattered light noise can be observed, the frequency up-conversion and scatter shoulder – extended for increased sinusoidal dynamics – in the amplitude spectral density (ASD) and the constant envelope due to fringe-wrapping in the time-series.

The scattered light effects now with and without PRN modulation present are shown in

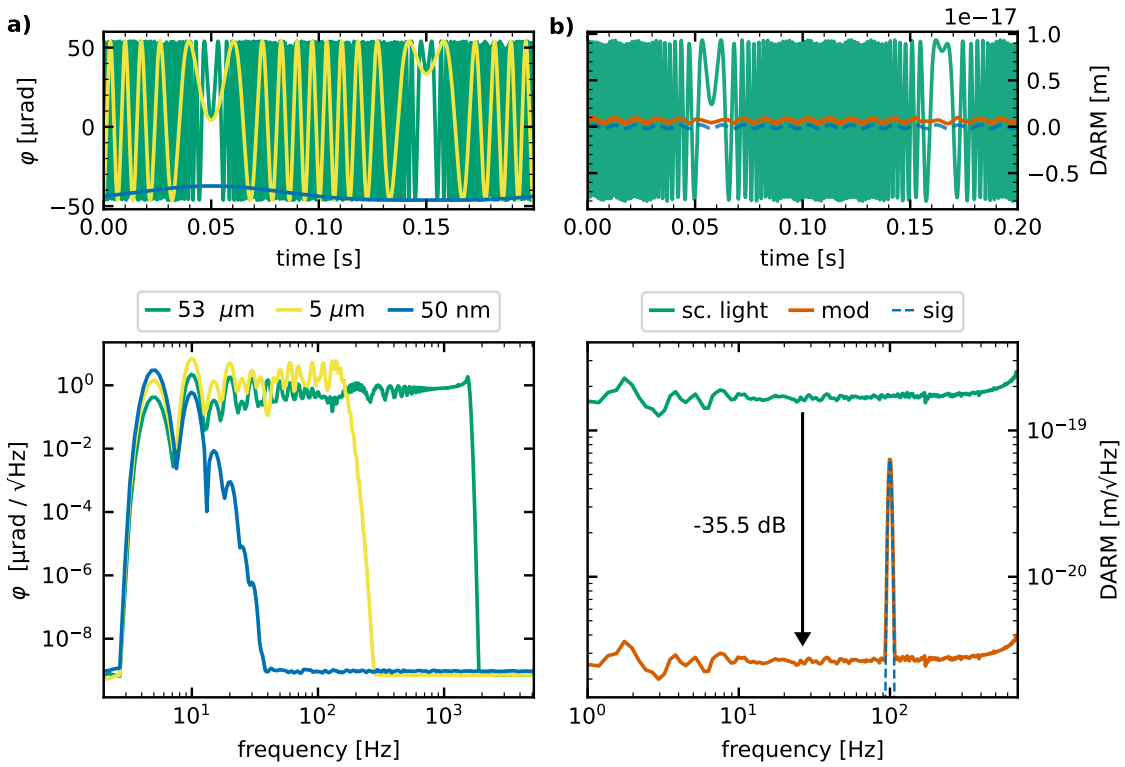

Figure 6.2: Simulation of scattered light coupling into a Michelson interferometer. a) time-series (top) of the measured phase for different movements (53 µm green, 5 µm yellow and 50 nm blue) of the scattering object at 5 Hz and corresponding ASD (bottom). b) Example of scattered light noise suppression with *tunable coherence*. The upper plot shows a time-series of a differential arm length change (DARM) measurement of an example signal of 2×10^{-19} m oscillation at 100 Hz (dashed, blue) and the same signal masked by scattered light (movement of 40 µm at 0.2 Hz and 30 µm at 4.5 Hz and $r_{sc} = 1 \times 10^{-5}$, $P_0 = 1$ W) without PRN modulation (green). The same signal and same noise as measured when *tunable coherence* is used (orange). The plot below shows the ASD of the pure signal (dashed, blue), with scattered light noise (green) and *tunable coherence* (orange). Note that the vertical scaling between a) and b) differs by several orders of magnitude as a) shows general scattered light examples with signals in µrad and b) follows more realistic parameters and signals of an interferometer used for gravitational wave detection. Adapted from Voigt et al. [23].

Figure 6.2b. For this, a strain signal of 2×10^{-19} m in amplitude with 100 Hz was simulated, which is masked by the sum of two scatter sources with some µm scale movement range. The two adjustable parameters of the PRN modulation were chosen to be 63 chips for the sequence length l_{seq}, and 1 GHz for the modulation frequency f_{PRN}.

In the example depicted in Figure 6.2b a suppression of 35.45 dB was reached and further results are shown in Figure 6.3. There, results using different sequences length and their simulated suppression are presented. They show nicely the expected dependence of the reachable suppression on the ACF's minimum value. This expectation in decibel is given by $20 \log_{10}(1/l_{seq})$, only depending on the sequence length as discussed in Chapter 5.

6.2.2 Optical resonators

First, the simulations were verified by comparing the reflected, circulating and transmitted fields in an overcoupled cavity of ideal length (finesse $\mathcal{F} \approx 57$) with PRN modulation (63 chips, 1 GHz) for microscopic detuning to the known response without modulation. This is shown in Figure 6.4. To study the field in the simulation an additional PRN demodulation of the fields was used to recover the phase response, which in a Michelson, is expect to be achieved with optical demodulation by delay matching. The resulting field amplitudes and phases corresponded exactly to the well-known case without PRN modulation [66], indicating that microscopic detuning on the order of one wavelength behaves as expected. Hence, both operation on resonance and anti-resonance or at other detunings should in principle be possible with *tunable coherence*, as is required for arm-cavities, power and signal recycling. Further, overcoupled, undercoupled and impedance-matched cavities responded analogously to the operation with PRN modulation.

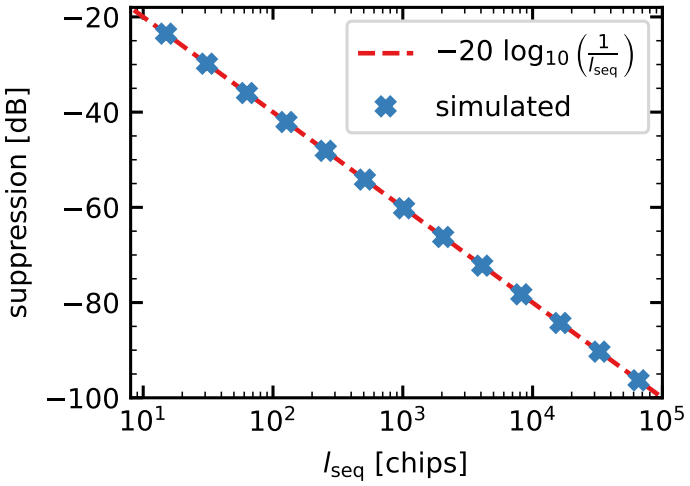

Figure 6.3: Achievable suppression for increasing modulation sequence length, simulated (blue cross) and theoretical prediction (red line). Adapted from Voigt et al. [23, Supplements].

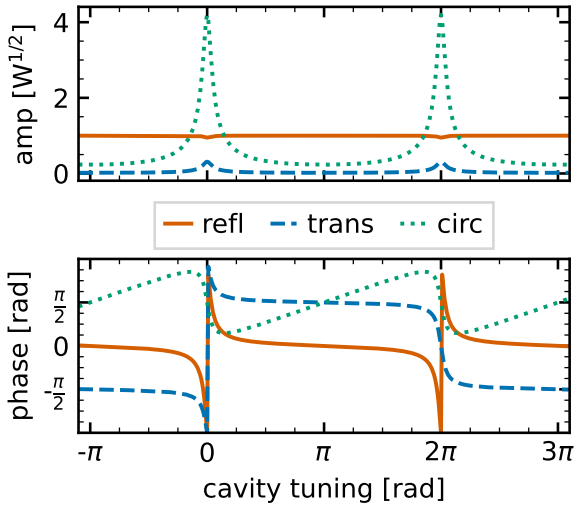

Figure 6.4: Reflected (orange), transmitted (blue) and circulating (green) field and phase of an over-coupled ($r_1 = 0.898$, $r_2 = 0.997$) cavity matched to the modulation sequence length ($l_{\mathrm{seq}} = 63$ chips, with an inbound electric field with $E_0 = 1$ and $f_{\mathrm{PRN}} = 1\,\mathrm{GHz}$). The modulation sequence length and thus also the round-trip length are about 18.89 m. The fields are demodulated with a delay matched copy of the modulation sequence to measure the phase relative to the inbound electric field. Adapted from Voigt et al. [23, Supplements].

The most critical aspect in the simulation was to investigate how far off-resonance a cavity can be tuned before the PRN modulation interacts negatively, assuming that the

macroscopic cavity length is matched to an integer multiple of the recoherence length. As discussed, for high modulation frequencies – and thus short coherence lengths – it is also relevant, that the chip-length is an integer multiple of the laser wavelength, as this determines the achievable overlap of microscopic tuning and macroscopic coherence.

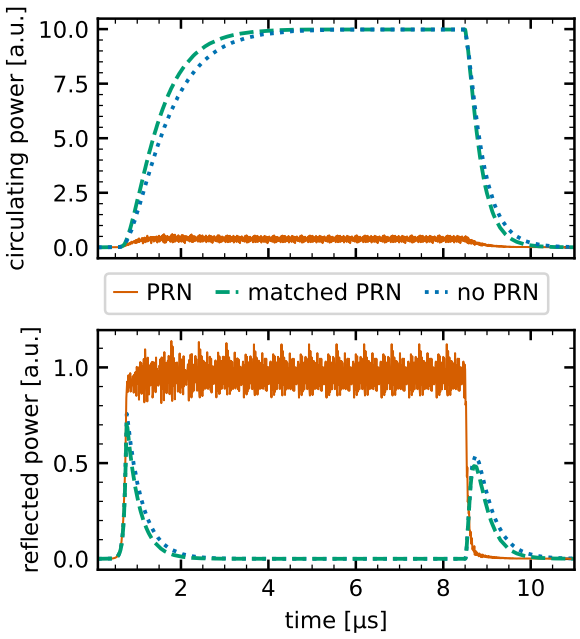

Figure 6.5: Time-series of circulating (upper plot) and reflected (lower plot) power of an impedance-matched ($r_{1,2}^2 = 0.9$) cavity tuned on resonance. In blue: unmodulated inbound laser light. In orange: inbound laser phase modulated with a 63 chip long PRN sequence at 1 GHz, the cavity length is mismatched by 0.234 sequence lengths. In both cases the incoming field is switched on at 0.75 µs and off at 8.5 µs. Additionally, the circulating and reflected power for a length-matched resonator (green) is shown. Since this resonator has a shorter macroscopic length (9.4 m compared to 11.7 m), the buildup and decay happen slightly quicker, which is observable on the timescale chosen with a simulated measurement bandwidth of roughly 50 MHz. Adapted from Voigt et al. [23, Supplements].

To investigate these effects the power buildup in the cavity and the Pound-Drever-Hall (PDH) error signals, which are suitable metrics for the operation of cavities, were simulated. A simulation depicting the time-dependent behavior of circulating and reflected power in a cavity with a length unmatched to the recoherence length is shown in Figure 6.5. Here, one can observe that the resonator in combination with the PRN modulation is producing a very different behavior than what is known from unmodulated light. The resonator was impedance-matched and tuned to be on resonance for unmodulated light. However, it shows in Figure 6.5 (PRN, orange curve), that most of the power is reflected with an average reflectivity slightly above an individual mirror. The conventionally observed power buildup (no PRN, blue, dashed) is strongly suppressed with the intensities of reflected, transmitted and circulating light randomly fluctuating due to the random nature of the PRN modulation in the case of a length mismatch.

On the other hand, for a slight mismatch of modulation sequence length and cavity length, the power buildup should not decrease in the presence of PRN modulation. This was investigated by simulating the power buildup in an impedance matched cavity for varying cavity length and three modulation frequencies. For a modulation frequency of about 10 GHz, one chip has a length of about 2.99 cm, resulting in a minimum cavity length matched to the recoherence length of a 63 chip sequence of about 1.88 m. The results, depicted in Figure 6.6, show a clear repeating pattern, with the maximum power

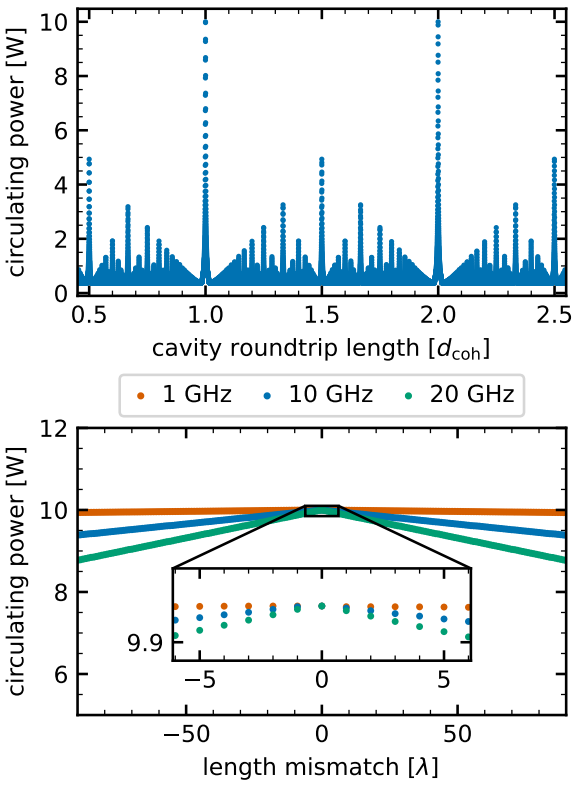

Figure 6.6: Circulating power in an impedance-matched ($r_{1,2} = 0.9$) cavity with $E_0 = 1$ for different mismatches between cavity and modulation sequence length. The modulation is kept at a length of 63 chips at about 10 GHz (blue). In the lower half, the peak around a cavity length that equals a multiple of the sequence length is resolved in more detail with mismatches of up to ±90 fringes ($\lambda = 1064$ nm). Here, the same curve is shown for a modulation frequency of 1 GHz (orange), 10 GHz (blue) and 20 GHz (green). The insert shows an excerpt of ±6 fringes mismatch.
Adapted from Voigt et al. [23].

buildup repeating at integer multiples of the matched cavity length. Additionally, for various ratios a fraction of the power build-up can be observed. For instance, at a cavity length of 1.5 sequence lengths, only half of the build-up is realized, since for only every second round-trip (equaling a shift of exactly three sequences) the PRN modulation allows for coherent interference. The peak around a length matched cavity has a FWHM of only around 1.89 mm for a modulation frequency of about 10 GHz, equaling around 1776 wavelengths. Further, a higher dependency of the power buildup on the length-matching for a higher cavity finesse was observed but not shown here. Physically, this is due to the higher number of cavity field round-trips of which for many, a slight mismatch adds up to a wrong modulation phase. Thus, depending on the PRN frequency and cavity finesse, this FWHM can correspond to not only far less than a centimeter but down to µm of offset. Nevertheless, Figure 6.6 shows that, on a microscopic scale, the cavity can still be tuned through several fringes, the number depending on cavity finesse and modulation frequency, before the build-up starts to drop significantly. It must be stressed again, that for this simulations the PRN frequency was chosen such, that one chip-length always equaled exactly an integer multiple of a wavelength for zero code mismatch, the before mentioned ideal situation.

Highly precise readout of the cavity detuning is critical, especially for the arm cavities, and should ideally be possible even if one of the mirrors moved through several fringes before lock is acquired. To verify this, the response of the Pound-Drever-Hall (PDH)

locking scheme to the PRN modulation was investigated by adding another MHz phase modulation onto the modulated electric field to simulate the error signal. For this, a modulation depth of $\delta = 0.01$ and a modulation frequency of $f_{\mathrm{PDH}} = 50\,\mathrm{MHz}$ were assumed. The field reflected from an impedance-matched cavity ($r_{1,2}^2 = 0.9$) was then computed while scanning the tuning and thus extracting the PDH error signal. To investigate the influence of sequence mismatch, this was repeated for various cavity lengths at a fixed PRN sequence length of 63 chips at about 1 GHz. Here it is to note, that the local oscillator phase was not newly optimized for unmatched cavities. As the shape of the PDH signal varies for different phases, this opened another degree of freedom not further investigated. The result is shown in Figure 6.7 where it shows that again a length matched cavity works without limitations. However, for a mismatch in length, the error signal shows some unexpected behavior. In addition to a shift of the zero crossing away from the resonance condition with increasing mismatch a slight increase in the slope can be observed as well. This was not observed in later measurements discussed in Sec. 9.1.1 and is thus likely to be an artifact of the simulation. Thereby, it indicates limitations in the underlying simulation, which are further discussed in Sec. 6.3.1. These limitations need to be considered when drawing conclusions from the simulation results. All in all, they prohibited understanding the impact on the interferometer layouts caused by the PRN modulation in full detail. For this, experimental demonstrations as presented in the following chapters were more useful.

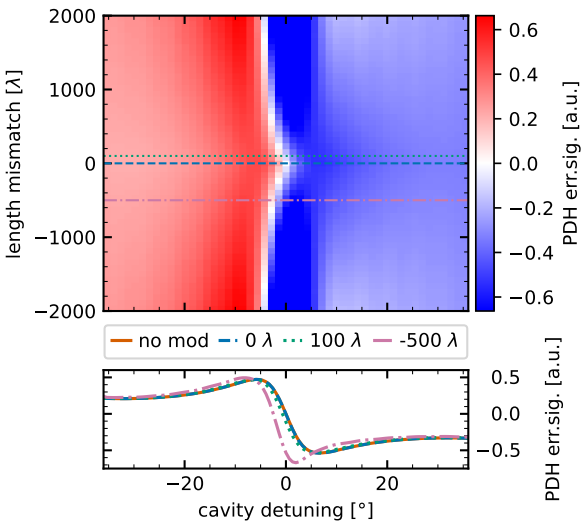

Figure 6.7: Pound-Drever-Hall error signal for different mismatches between round-trip length (about 18.89 m) and PRN sequence length. The modulation is kept fixed with 63 chips at 1 GHz modulation frequency, while the length of the impedance-matched ($r_{1,2}^2 = 0.9$) cavity is changed. The upper plot depicts the error signals for mismatches between $\pm 2000\lambda$. The lower plot shows four example PDH signals: no PRN modulation at all (orange), a perfectly matched cavity (blue, dashed), a cavity with a mismatch of $100\,\lambda$ (green, dotted) and one with a mismatch of $-500\,\lambda$ (pink, dashed). Adapted from Voigt et al. [23].

6.2.3 Simulation conclusions

The simulations showed how *tunable coherence* using PRN phase modulations of the laser can significantly reduce the scattered light induced noise in the readout of GWDs. As expected, the suppression only depends on the length of the PRN sequence, with the

here used *m*-sequences being a suitable choice also for an experimental demonstration in an interferometer or a cavity. Key features of optical resonators were successfully demonstrated to be compatible with *tunable coherence*, encouraging the next step of experimental verification. Further, the simulations give an optimistic outlook that also further advanced topologies, like a dual-recycled Fabry-Perot-Michelson interferometer, can realistically be equipped with *tunable coherence*. Main challenges, however, remain small length differences between cavities used in the layout and in auxiliary functions, such as the Schnupp Asymmetry [152] and mode-cleaners, due to them strongly limiting the usable sequence length. The made assumption of a chip length always being an integer multiple of the wavelength might have to be realized in an experimental setup to avoid small mismatches accumulating to macroscopic differences over many round-trips, especially in high-finesse cavities. In a large scale experiment, this could be done by the use of a frequency comb allowing for stabilization of the GHz PRN frequency relative to the much higher THz laser frequency.

Sagnac interferometers

Simulations to investigate different aspects of scattered light in Sagnac interferometers and the use of *tunable coherence* to suppress it were done by Leonie Eggers as part of her master's project. These used the newly developed tool ifoTDS described in the next section and the results can be found in her thesis [153].

6.3 ifoTDS

The analytical calculations presented in this chapter were used for the simulations published in Voigt et al. [23]. However, during the work on that publication, it became apparent that especially the interferometer setup was not easily adaptable. As the expression for the output power was derived from a specific setup, only the parameters present in the final equation (eq. 6.1) could easily be changed. This was mostly enough to investigate a given set of scattered light and PRN modulation parameters. However, it was not possible to easily simulate a different setup like e.g. a Sagnac or Mach-Zehnder interferometer. The same is true for the cavity, which was already implemented as an object in the simulation code to simplify changing and updating of parameters without introducing errors.

Especially simulations of more complex setups like a recycled interferometer or the use of arm cavities was not easily possible with the approach of implementing analytical calculations. As a next step, the development of a new simulation tool called interferometer Time-Domain Simulation (ifoTDS)[12] was thus started. The idea was to use a modular

[12]The source code for it is currently only available in an internal git-repository

approach like FINESSE but then iterate through the defined setup in time steps such that nonlinear and time dependent effects could be taken into account. Based on this idea, a first implementation of ifoTDS was created by André Lohde as part of his master's project. Some more details about the underlying algorithm can thus be found in his thesis [112]. To summarize the basic working example quickly, the underlying algorithm starts at a specified detector and recursively iterates through the defined setup to neighboring elements until it reaches a source element, the laser. For each timestep the electric field at the detector is calculated by propagating it backwards through the interferometer. Finally the desired quantity (a quadrature or the power) of the field reaching the detector is returned for each step. The implemented elements include lasers with and without PRN modulation, mirrors, beam splitters and isolators as well as spaces to be placed between objects. These spaces can be either fixed in length or change microscopically introducing a phase tuning for e.g. an interferometer arm or cavity.
After these first implementations, some iterations were made to improve computing time and also add more functionality. These include additional functionalities like amplitude and frequency noise for the laser. To improve calculation times, a move towards a symbolic expression algorithm instead of the step wise recursive propagation through the setup, and implementations in C++ instead of python were started. However, the use of the tool, especially with all the later added features, is not yet streamlined and many additional upgrades would be helpful. Nevertheless, other interferometer setups were investigated with ifoTDS like the Sagnac typology as part of the Master's thesis of Leonie Eggers [153]. Additionally, in more recent time, Jan-Niklas Feldhusen started further development on ifoTDS as part of his PhD project by adding the option to include polarization and frequency modulation as new features. Finally, some more notes on what could or should be done next for improvements of ifoTDS are given in section 6.3.2.

6.3.1 Challenges of time-domain simulations

Time-domain simulations face a few challenges that other tools like the **F**requency domain **in**terf**e**rometer **s**imulation **s**oftwar**e** (FINESSE) avoid by solving a steady state setup in frequency domain. The most prominent is calculation times. By including time-depending variations, the simulation has to take this into account for every step in the calculation. To address this issue, two approaches were considered for ifoTDS, the first one being the mentioned recursive iteration algorithm requesting the electric field for each time from neighboring nodes. While this can be fast for simple layouts like a single cavity or interferometer, it quickly becomes time consuming for complex setups like multiple or coupled cavities. As for every time step the field amplitudes at all nodes in the setup have to be taken into account until a certain precision threshold is reached, such setups quickly lead to long iterative loops. Additionally, using this approach, fields have to build

up in parts of the setup like a cavity over the first iteration steps of the simulation before the actual dynamics of interest can be properly investigated. A way around this problem would be to start in the steady state and then investigate the time-dependent effects from there. This would most certainly save computational time but is not straight forward to implement in the current status.
The other investigated approach was the use of symbolic expression that, once found for the whole setup, can be evaluated for every time step instead of iterating through the setup again. Here, the complexity and costly aspect is moved into the first iteration and subsequent construction of the expression for the field reaching the detector from all contributing terms at their relative time delay. First tests showed that this would speed up simulations of complex setups but took longer than the previous approach for simpler setups. In an ideal implementation, the faster approach depending on setup complexity should thus be chosen automatically by the tool to minimize overall simulation times.
Especially in the cavity setup, another problem became apparent, the numerical precision and floating point errors. Even without considering the fast laser oscillations at THz, having the PRN frequencies at GHz requires sampling at several GHz to investigate the properties of the modulation properly. Combining this with reasonable parameters for the investigated setup and, for example in a cavity with higher finesse, enough round-trips taken into account for good precision, this leads to a wide spread of samples and size of involved numbers. For example, it could be observed that for some cases the precision of floating point numbers was not high enough to accurately determine the modulation state at certain delays. This lead to artifacts in the resulting resonance curves caused by this wrongly determined modulation state. In order to avoid this, sampling rates and setup parameter were constricted and attempts using more precise implementation of numbers tested. One assumption stemming from these adaptions was for example the restriction of modulation chip lengths to integer multiples of the used wavelength.
The presented simulations were generally limited to this and other assumptions such as perfect modulation depth and infinite modulation bandwidth. While there are approaches to improve on this, they would require even higher sampling rates and precision, which require more excessive computing than so far used. However, there is no indication that these constraints changed the overall picture of the presented results. Still, this needed to be further confirmed by laboratory experiments, which are discussed in the next chapters.

6.3.2 Future improvements

Besides the already started work, there are some other improvement that could and should be done to improve ifoTDS. Among these are some quality of life updates helping with its usability and others that would expand its functionality and compatibility with other simulation tools.

To name a few, in the current state the setup has to be redefined for even small changes like the used PRN sequence. Meaning something like a phase scan of a cavity can be done in a simulation run, but other parameter can not easily be changed. A first update was made to allow turning the modulation on or off without needing to redefine the setup. Further improvements are possible but more complex to implement. Other rather small but helpful additions would be the implementation of certain setup parts into single objects, like e.g. a BHD. In the current state, options to readout the quadratures of a field do exist, but their implementation is purely mathematical. Thus, a more physical realization that still minimizes complexity compared to a full replication would be beneficial.
On a more general level, to increase compatibility with simulations tools like FINESSE, the implementation of a setup definition input or script which is parsed into an object that can be evaluated would be useful. By following a compatible syntax, this input could be parsed into both simulation tools, making use of their different capabilities. Additionally, this would allow for easier handling of changes to the setup and could implement a function that automatically runs the simulation and properly prepares the output. Currently, execution of the simulation and evaluation of the setup for a time-series has to be programmed manually. Lastly, this would allow for easier integration of the C++ version into the standard python implementation as the parsing could be utilized as a wrapper for the faster C++ code.

6.4 Conclusion

In this chapter, preparatory simulations of *tunable coherence* in a Michelson interferometer and an optical cavity were presented and discussed. These simulation results were published in Voigt et al. [23] and showed promising insights into how *tunable coherence* interacts with the investigated setups. Besides verifying the expected reachable suppression in a Michelson setup presented in Sec 5.3.1, a better understanding of how precise a cavity and the PRN modulation have to be matched in length for undisturbed operation could be gained. While the functionality of cavities with *tunable coherence* was expected, it was nevertheless the most critical aspect of the concept to be verified early on. Lastly, some limitations of the simulations could be observed, for example numerical precision issues and limited customization options for the investigated setup. Therefore, a new simulation tool called ifoTDS was developed. Some more work on it will, however, be necessary to make full use of it in the future.
Nevertheless, with these promising first results, it was time to move towards the experimental realization. In the next chapter, the general PRN modulation implementation with its tunable parameter are presented. Chapter 8 discusses the experiments in Michelson and Sagnac interferometers and Chapter 9 the ones in a table-top sized optical cavity.

7 Experimental Realization of *Tunable Coherence*

After the encouraging results obtained by simulating *tunable coherence* which were discussed in the previous chapter, the next step was to experimentally demonstrate the new concept. In this chapter, the general implementation of *tunable coherence* will be discussed before the next chapters then focus on the demonstration in certain setups, namely interferometer based on the Michelson- and Sagnac-topology, optical resonators or cavities and enhanced interferometer based on the Michelson-topology. While it is not necessary to implement the PRN modulation that is core to *tunable coherence* at GHz-modulation-speeds, the advantages discussed in Chapter 5 motivate to do so. Therefore, besides the laser preparation and modulation setup, this chapter will discuss the challenges and solutions for the implementation of the PRN modulation used in the experiments discussed in this thesis.

7.1 The laser setup

All experiments and setups presented in this thesis are making use of the same laser light provided by a Nd:YAG[13] non-planar ring oscillator (NPRO) laser[14] with a wavelength of 1064 nm and an output power of a little more than 500 mW. These lasers are known for their ultra-narrow linewidth and having high intrinsic stability in their geometry and intensity [154–157]. For improved suppression of residual intensity noise in the used measurement band between 100 and 200 kHz, the internal *"noise eater"* [158] of the NPRO was used. While it is common in the field of GWD to further stabilize these lasers in order to achieve the needed extremely low levels in frequency and amplitude noise [78, 157], the setups used in the scope of this work had no such stabilization implemented yet. First works on additional amplitude stabilization, as well as later also frequency stabilization, were started as part of a supervised Master's Thesis[15] parallel to the last measurements presented in this work, however, neither stabilization was active for these measurements.

[13] neodymium-doped yttrium aluminum garnet (Nd:YAG); $Nd:Y_3Al_5O_{12}$
[14] Coherent: Mephisto 500
[15] Master's Thesis of Lennart Manthey, expected submission in late autumn of 2025

The implementation of *tunable coherence* is based on using phase modulated light, therefore, the core of the laser preparation was dedicated to this modulation. The setup is sketched out in Figure 7.1.

Before most of the laser light is coupled into the fiber setup containing the modulators, its polarization was adjusted with a quarter-wave-retardation plate ($\lambda/4$-plate) and a half-wave-retardation plate ($\lambda/2$-plate) to pass optimally through a Faraday isolator (FI) that was used to protect the laser head from any back-reflection. The beam height was also adjusted to 50 mm above the optical table. After the FI, a combination of a $\lambda/2$-plate and polarizing beam splitter (PBS) was used to adjust the power level going into the fiber setup, which was the beam reflected from the PBS. The transmitted beam was dumped for now but could be used later for stabilization schemes or if the need for a clean (meaning no PRN modulation) beam arises. To optimize the fiber coupling in terms of power and polarization, two lenses were used to match the fiber mode and another combination of $\lambda/2$-plate and $\lambda/4$-plate (to compensate bi-fringing in the fiber coupling optics) to adjust the light's polarization correctly onto the fiber axis.

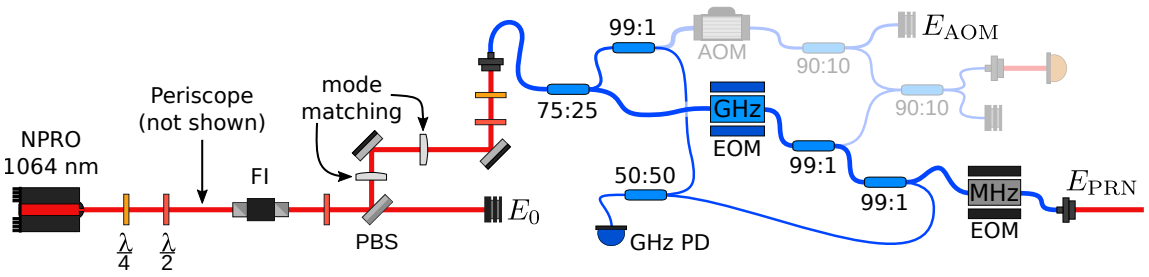

Figure 7.1: Sketch of the used laser preparation and fiber setup, with the latter containing the GHz-EOM used to imprint the PRN modulation onto the laser. Besides the main path through the fiber setup containing the two EOMs, some light was tapped off to construct an eye-diagram measured with a GHz-PD. This could be used to observe the PRN modulation in real-time on a high-bandwidth oscilloscope. The additional path that was supposed to be used for locking the modulation depth θ with the control loop described in Section 7.2.3.a is grayed out as it stayed unused. A new adjusted version of this setup for the use of a new control scheme described in Section 7.2.3.b can be found in the appendix (Fig. A.1). This new setup was implemented after the last measurements were done.

The fiber setup contained not only the GHz-electro-optic modulator (EOM)[16] used to modulate the PRN sequences onto the laser but also another EOM[17] with 150 MHz bandwidth that could be used to add side-bands for e.g. using the PDH technique [159–162]. To observe the PRN modulation in real-time, light tapped off before and after the GHz-EOM was interfered and measured with a high-bandwidth (42 GHz) PD[18]. With this, an eye-diagram (shown in Sec. 7.2.2, Fig. 7.8), which is an in telecommunications commonly

[16]iXblue Photonics: NIR-MPX-LN-20 with exail: DR-DG-20-HO (driver)
[17]iXblue Photonics: NIR-MPX-LN-0.1 with exail: DR-VE-0.1-MO (driver)
[18]Thorlabs: RXM42AF, 42 GHz Photoreceiver

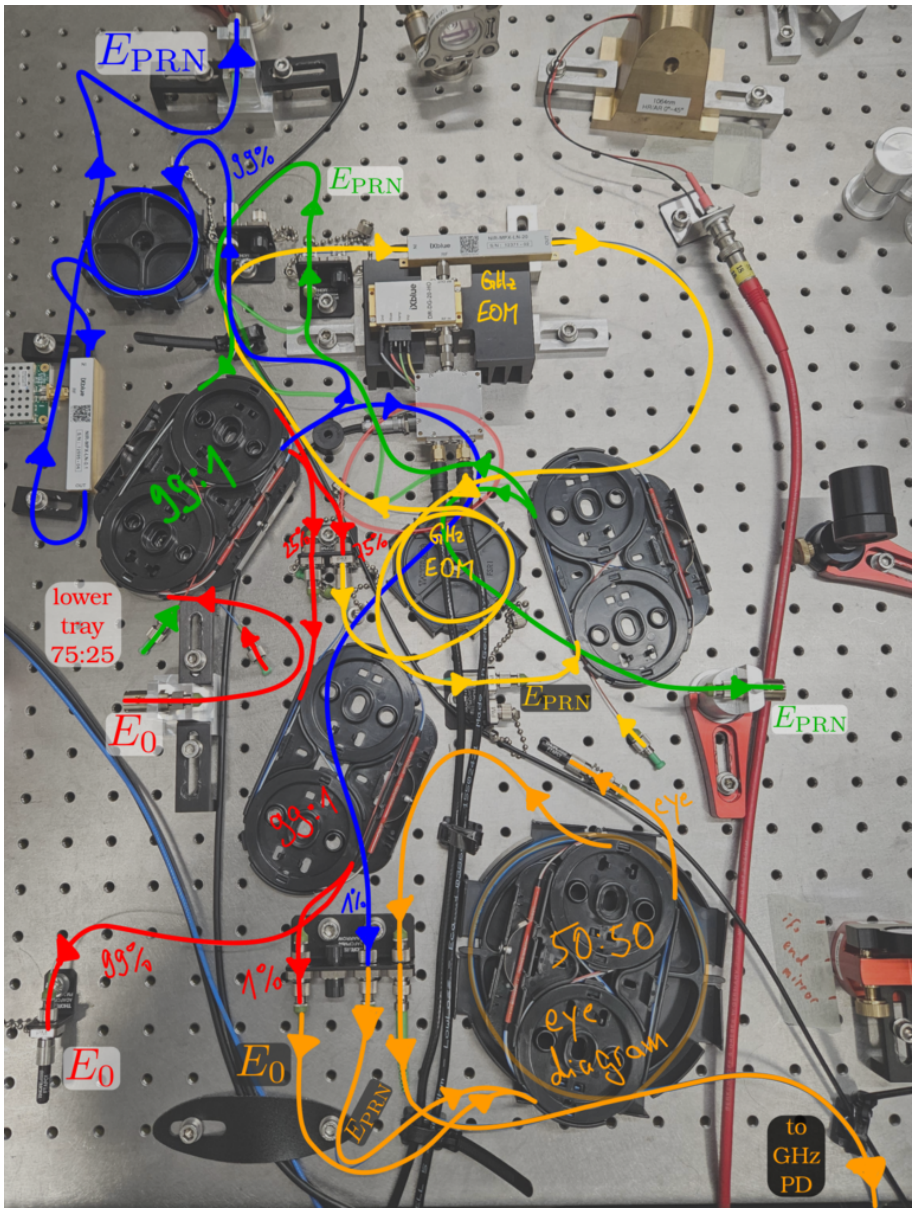

Figure 7.2: Annotated picture of the fiber setup after removing abandoned parts, simplifying the setup. The components handling the input field are shown in red, the part with the GHz-EOM is shown and yellow and the one with the standard EOM in blue. The components transferring the light between them are shown in green and the part to generate the eye-diagram like real-time modulation quality measurement is shown in orange. A simplified sketch of the depicted setup is shown in Figure A.1.

used measure for signal quality, could be constructed on a high-bandwidth oscilloscope[19]. The fiber splitters used in the setup were bought from Thorlabs[20] with different splitting ratios used as needed.

Lastly, a part of the fiber setup was dedicated to an envisioned control-technique to lock the modulation depth of the PRN modulation, described in Section 7.2.3.a. For this, an

[19]Rohde&Schwarz: R&S® RTP084B, 8 GHz analog bandwidth
[20]Thorlabs: PN1064R5A2 (50:50), PN1064R3A2 (75:25), PN1064R2A2 (90:10), PN1064R1A2 (99:1)

acousto-optic modulator (AOM)[21] ($\omega_{\mathrm{AOM}} = 100\,\mathrm{MHz}$) and components to create and read out an interference of the fields passing through the EOM and AOM were added to the setup. Due to the later described problems (see Sec. 7.2.3.a) in its functionality, this part of the fiber setup was later abandoned and is grayed out in Figure 7.1.

After all measurements for this thesis were recorded, the fiber setup was changed to a simplified version in preparation for future work. This new setup is sketched in Figure A.1 in the Appendix and an annotated picture of it is shown in Figure 7.2.

7.2 GHz phase modulation

As described in Chapter 5, at the core of *tunable coherence* is a PRN modulation, preferably at high modulation speeds to optimize its effects on the setup and straylight. In this part, the experimental implementation of this modulation is discussed. The physical setup of this is simple as it only needs an EOM capable of achieving the desired frequencies placed into the setup as shown in Figure 7.1. The challenging part lies in the driving and control of this modulator.

Signaling at GHz frequencies has its challenges mainly in the speed the components need to handle when it comes to rise- and fall-times as well as delays between differential signals and impedance matching. Luckily, due to the use in telecommunications, there are plenty of components available that can be used. On the other hand, the driving signal needs to be generated and provided to the modulator at the desired speeds, which was for now the biggest challenge in implementing *tunable coherence*. While there are commercially available pattern generators that provide a signal usable for the concept, for better flexibility in pattern or PRN sequence length and modulation frequency, an in-house development based on an FPGA was chosen instead. This will be presented in detail in the next section.

One thing to keep in mind in the context of modulation frequencies and bandwidth is that ideally the individual chips of the PRN sequence are as closely resembling an ideal square wave as possible. Thus the needed bandwidth is considerably higher than the used modulation frequency to keep the edges of each chip as sharp as possible.

A balun was needed to properly connect the evaluation board housing the FPGA, which had a differential output, to the driver of the GHz-EOM, which had only a single-ended input. First, some tests, discussed in Sec. 7.2.2.b, with easily available operational amplifiers supposedly capable of handling GHz-bandwidths were done. Finally, the choice fell onto a commercial balun[22] that could be directly connected to the driver. Its input was connected via two identical SMA-cables to the output pins of the evaluation board.

[21] AeroDiode: 1064AOM-1 with RF-AOM-A-100 (driver)
[22] Marki microwave: EBAL-0026 (26 GHz bandwidth)

7.2.1 PRN-sequence generation

The implemented design on the FPGA[23] can be divided into two parts, the generation of PRN sequences and the serial transmission to output SMA-pins, and further to the modulator, at the desired speeds. These parts can be discussed individually as they work independently except for one interface or connection used to provide the needed number of chips in the correct order and with the correct frequency to the transmitting block. This transmitting block is centered around the onboard GTX-transceivers of the FPGA of which one is directly connected to two pairs of SMA-pins on the evaluation board using low-voltage differential signaling (LVDS) via one pair to transmit signals (the other one is for receiving signals which is not needed in this case).

To use the GTX-transceiver of the board, the simplest way is using the software wizard to set it up inside the programming environment Vivado[24] used to create the bitstream for the FPGA. Especially for the use case of *tunable coherence*, most of the available options are not needed as no protocol or other advanced setup is used. Instead, the only requirement is to send the chips as given to this module one at a time in quick succession. The problem in its implementation lied however in the correct use and integration of the intellectual property (IP) core[25] provided by Xilinx. This wizard creates a wrapper for the selected transceiver, setting it up with the given parameters. Here, the first challenge is to determine which is the needed transceiver. It was found that the transceiver labeled "GTX_X0Y9" is the required one which is directly wired to the SMA-pins[26].

While the rest of the setup for the transceiver is relatively straightforward as no further features and only the transceiver (TX)-part is needed, the integration of the created wrapper into the project is not. A summary for the setup of the transceiver-wrapper used for 1 GHz transmission is shown in Table 7.1 while the summaries for other used configurations can be found in the Appendix. The created wrapper cannot be implemented into a

Table 7.1: Setup parameter for the 7 Series FPGAs Transceiver Wizard v3.6 logic core used for the 1 GHz implementation of the PRN generator on the FPGA. The parameter for different frequencies can be found in the Appendix.

1 GHz TX setup summary

Features	GT
Protocol File	Start_from_scratch
TX Line Rate (Gbps)	1
TX reference clock (MHz)	100.000
Encoding	None
TX Internal Data width	16
TX External Data width	16
TXUSRCLK (MHz)	62.5
TXUSRCLK2 (MHz)	62.5
TX Buffer Enabled	true

[23] AMD Artix-7 in Zynq 7000 XC7Z045 SoC on ZC706 Evaluation Board
[24] Xilinx: Vivado 2020.2
[25] 7 Series FPGAs Transceiver Wizard v3.6 (Rev.13)
[26] Package pins Y1 and Y2 of the SoC

block design, meaning all connections and blocks needed for the project to work had to be setup abstractly. This was done by writing it out in several VHSIC Hardware Description Language (VHDL)[27] files. The design wizard did create an example project, which could be used to extract the necessary files and code to set up the wrapper in a custom project. For this, the wrapper needs to be integrated into the top-module directly, not inside another sub-module, and names of all modules and connections need to be transferred properly. Once this was done correctly, the layout could be visualized as elaborated design in Vivado. A screenshot of such a design for the later described sequence generator is shown in the Appendix in Figure A.2. As these designs are quite convoluted, for the more complex projects only parts or simplified recreations will be shown.

The first, from the example project transferred design contained three main modules which were also used in the final PRN generator project. The module used to generate the sequences was, however, exchanged for a more comprehensive one. The other two modules — the wrapper for the GTX-transceiver and the processing system — stayed the same. The latter was needed for the whole evaluation board to function properly and provided clocks used throughout the project. Both modules and their in- and outputs were generated in Vivado by using the corresponding design wizard and then incorporated into the project.

With this first part running, the focus moved to supplying the transceiver with the correct input, which was the second part of the project. As mentioned before, two parameters are important for connecting those two parts with each other, the width and the rate at which the transceiver reads the data. Those are given by the "TX External Data width" and the "TXUSRCLK/TXUSRCLK2" (see Table 7.1) parameters set or determined by the wizard used for setting up the transceiver.

The idea for the PRN sequence generator was to use a state machine controlled by the available push-buttons on the board to cycle between different generated sequences that are then sent to the transceiver. The four buttons were used as "up" and "down", as well as two different types of "reset". They were each connected into the project via a button-debounce logic. For visual information of the generators active state, the four available light emitting diodes (LEDs) were used to display the state's number in binary. For creation of the individual sequences, linear feedback shift registers (LFSRs) were used as described in Chapter 5 and the original idea was to have them generate the sequences in real-time. However, it became quickly apparent that this would require higher frequencies of the driving clock as the FPGA could provide in a stable configuration. While the parallel execution of the FPGA allowed for generation of several chips in one cycle from a given LFSR state, depending on the used tabs[28], this was often not enough to reach the

[27] VHSIC: Very High Speed Integrated Circuit Program

[28] Tabs normally refers to the specific bits, like the first and third, of the LFSR used to generate the new bit by combining them with a XOR-gate

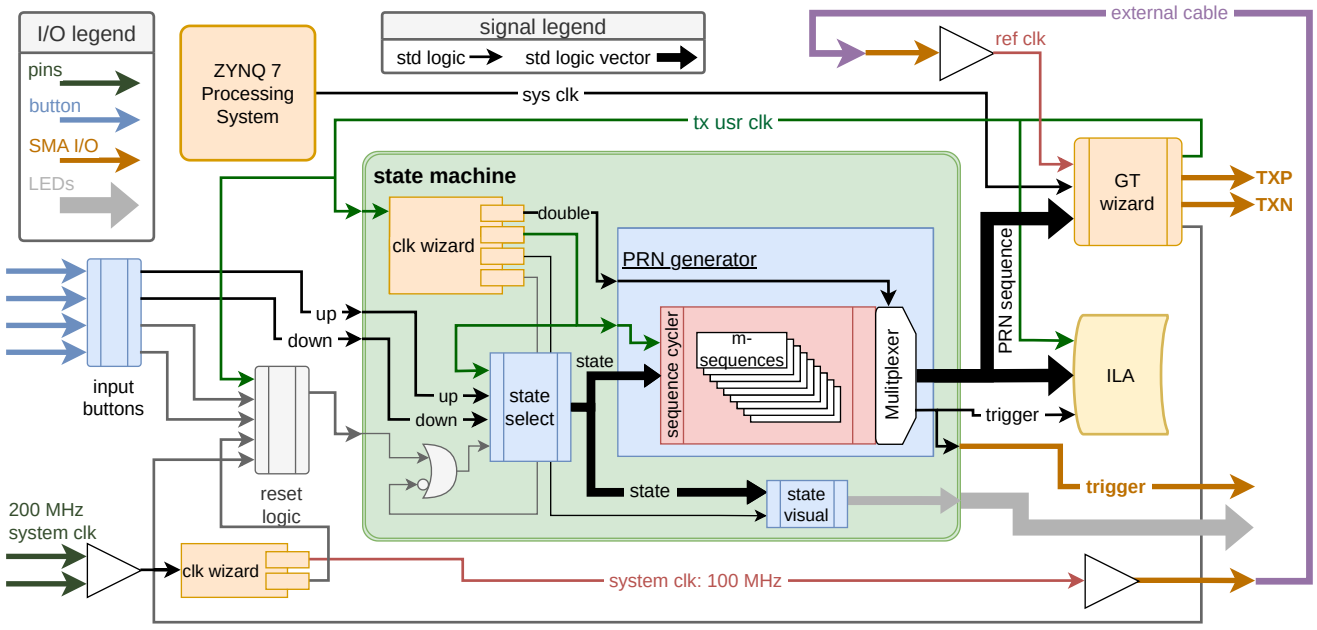

Figure 7.3: Conceptual design of the FPGA setup to generate the PRN sequences as modulation input. On the left, the four user I/O buttons and two pins (package pins G9 and H9 of the SoC) that provide a stable system clock. The reset-logic is simplified here, one of the input buttons can be used to reset everything while the other only resets the state machine and PRN generator. IP-blocks taken from the catalog in Vivado and only configured using their design wizards are marked in orange/yellow. These are often somewhat of a black box. On the right, the SMA-outputs, two for user I/O (connector J67/68, package pins AD18 and AD19) and two connected to the transceiver (connector J34/35, package pins Y1 and Y2) are used for providing the reference clock (connected back to the TX reference clock SMA-input J31, package pin W7) and a sequence repetition trigger as well as the PRN sequence respectively. Additional, a vector carrying the current state is used to display it in binary on the four user configurable LEDs. The constraint file used to define the pins for the used board can be found in the Appendix.

needed chip-rate with the available clock frequencies. Alternatively, several LFSRs could have been run in parallel, however, reconstructing the proper sequence from this would have been challenging and prone to errors. The complication here lies mainly in the fact that the slower running LFSRs will always lag behind the currently needed sequence part until the sequence catches up again due to its repetition. Finding the needed number of LFSRs, their needed starting state and tracking from which LFSR to pull the sequence part at any given time was non-trivial. Further, this would be made even more complicated with the different lengths of PRN sequence and thus LFSR needed. This might be a viable and possibly needed approach for longer sequences at higher frequencies, but it would have been unnecessarily complicated for the here needed setup. Therefore, the sequences were generated once and hard-coded into the individual states of the generator which then only had to rotate the vector containing the sequence by the needed number of chips at the frequency determined by the transceiver.

The conceptual setup of this block is depicted in Figure 7.3 showing the module containing

the logic to handle the state switches commanded by the input buttons, logic to display the current state via four LEDs and finally the sequence generator itself. This last logic block contained an instance of the rotating logic for each available sequence, which was in this implementation the *m*-sequences generated by LFSRs of all length between 3 to 11 bits (meaning sequences of lengths between 7 and 2047 chips). The outputs of all those nine instances were connected to a multiplexer, which forwarded the correct input to the transceiver depending on the current state. The same was done with a "repeat trigger" signal that was activated every time the currently active rotating logic reached the starting configuration again. This trigger was planned to be used for measurement synchronization but not yet needed. It was however useful as a trigger for the high-bandwidth oscilloscope used to measure the eye-diagram. In addition to the states sending PRN sequences, two more states were implemented, one being "idle" and the other one being "test". In the "idle"-state, all outputs were tied to ground, while in the "test"-state simply an alternating sequence of logical 0 and 1 was sent with the transceiver user clock being forwarded as a trigger. The elaborated design of the used sequence generator version for 1 GHz modulation can, as mentioned, be found in the Appendix in Figure A.2, later this was adjusted for higher modulation frequencies by increasing the number of chips transferred to the transceiver to 32 per cycle. The last part of the design then was the four LEDs used for the visual display of the current state.
With the sequence generation and transmission to the EOM, as well as control of the state machine implemented, the only important thing remaining was the reference clock input to the transceiver. For this, no easily working way to route a clock generated by the processing system or other onboard chips directly to the transceiver could be found and due to the importance of this clock, this also seems to be discouraged in general [163]. Further, at a later stage it was required to supply an easily tunable clock as this reference, making the implementation of an input connection necessary in the long run. For this, a 100 MHz clock signal was sent to a user definable SMA-pin which was connected with a short cable to the reference clock SMA-pin. In this way it was either possible to transfer the clock between the two pins or to input a signal from an external clock. A picture of the FPGA is shown in Figure 7.4 and the constraint file used for the setup of the board can be found in the Appendix.

7.2.2 Modulation quality and requirements

In order for *tunable coherence* to work properly and achieve the full potential, three main parameters are important and will be discussed separately. First the integrity of the used PRN sequence to verify the EOM is driven as expected. Next the quality of the signal reaching the EOM driver and subsequently being modulated onto the laser and finally the modulation depth controlled by the driving voltage of the EOM driver.

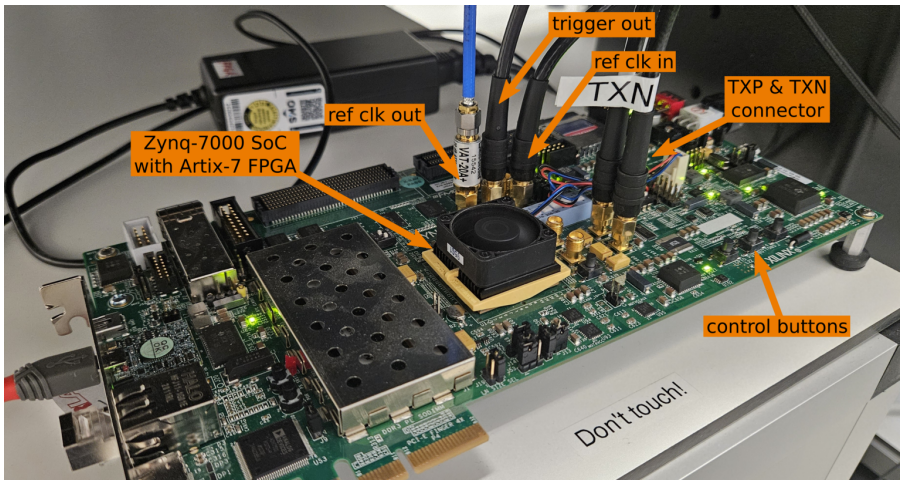

(a) ZC706 Evaluation board with the Zynq-7000 SoC containing the Artix-7 FPGA. In first experiments, the 'ref clk out' pin was directly connected to the 'ref clk in' pin, using an onboard generated reference clock for the transceiver. In order to tune the PRN frequency in later experiments, a signal generator was connected to the 'ref clk in' pin, providing an external clock as depicted in the picture.

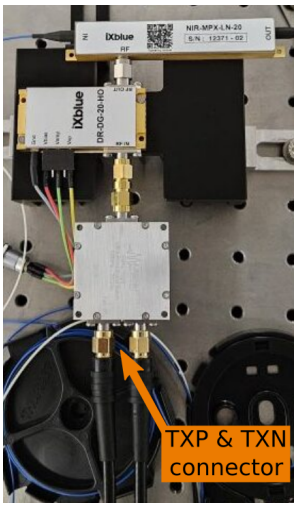

(b) Marki Microwave balun connected directly to the driver, which is connected directly to the high-speed EOM.

Figure 7.4: Pictures of the FPGA evaluation board and the GHz-balun with the EOM driver.

7.2.2.a Sequence integrity

For simplicity and ease of implementation, *m*-sequences were used for the experimental demonstrations in this thesis. The sequences were first generated in real-time on the FPGA and later hard-coded into the state machine. In both cases, they had to be transferred to the onboard transceiver at the correct rate and in the correct partitioning and order. If this would not happen correctly, the properties of the sequence would most likely be lost and the ACF looses its two-level characteristics. The modulation would then introduce artifacts, mainly increasing the noise floor, instead of suppressing scattered light properly. This can be clearly observed in the data shown in Figure 7.5.

Two options were available to check the integrity of the sequences. For all sequences the input to the transceiver could be monitored with an integrated logic analyzer (ILA) core on the FPGA. This logic core was integrated into the FPGA design and could then be used in the programming environment Vivado. Additionally, the shorter sequences could also be verified optically with the eye-diagram setup described in the first section of this chapter. When recorded with high enough bandwidth, the interference of light carrying the PRN modulation and light without it makes the sequence visible. However, the screen size and resolution of the used oscilloscope[29] limited the length of the sequences that could be verified this way. As both methods agreed well with each other, it was assumed that all sequences tested with the ILA core were also correctly modulated onto the laser.

In the beginning some problems with sequence integrity were observed, mainly caused by

[29] Rohde&Schwarz: R&S® RTP084B, 8 GHz analog bandwidth

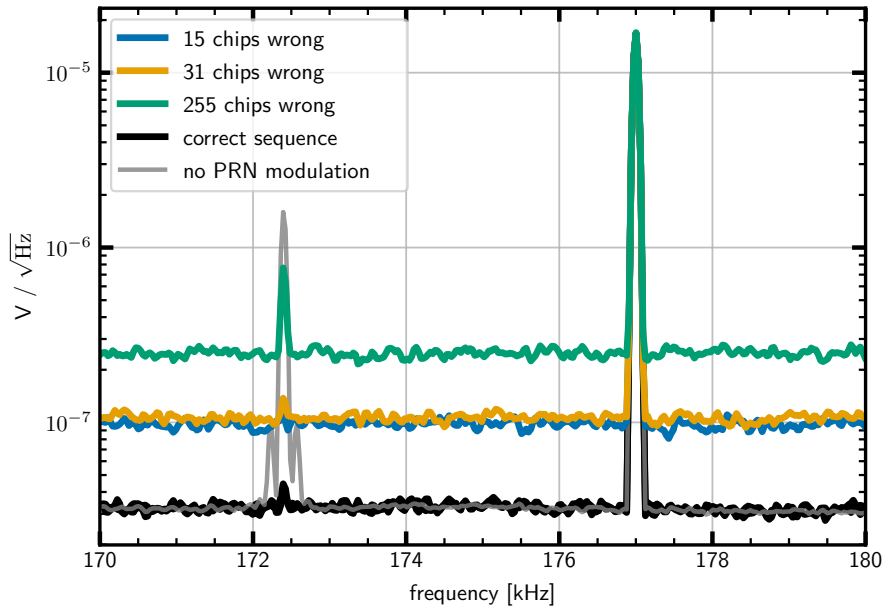

Figure 7.5: The resulting spectra of time-series measurements with different PRN sequences used as modulation input. The three 15, 31 and 255 chips long sequences were tested to be wrong, resulting in an increased noise floor and for the 255 chips long sequence in less suppression.

Figure 7.6: Sequences measured optically with a GHz-PD and oscilloscope. On the left the short 7 chips long sequence with it's expected values written on top, on the right a longer sequence of unknown length.

the real-time generation of the sequences and thus needed high clock frequencies on the FPGA. These were resolved by the switch to the new implementation using rotations of vectors storing the sequences. Examples of these verification are shown in Figure 7.6, due to the needed space to write down all the longer sequences, the parameter to recreate them are summarized in the Appendix instead of showing their verification here.

7.2.2.b Signal quality and conversion

After verifying the correctness of a sequence sent from the FPGA to the EOM driver, the next critical thing is the proper transmission of the GHz-signal without losing too much amplitude or bandwidth. An additional challenge here was the fact that the EOM driver only had a single ended input and the exact internal workings and influences of control voltages were unclear. The signal therefore needed to be properly converted from

differential to single ended to keep its quality optimal. As a short-term solution, only connecting one transceiver output to the driver input was used. However, the integrity and proper voltage levels of the signal could not be guaranteed this way. While details of the driver circuits are unknown, some available data and details can be found in its data sheet and in material of the manufacturer Exail [164]. From these information, it is assumed that the phase-flip of π is technically realized by flips of $\pm\theta$ corresponding to the positive and negative voltage levels of the signal. Thus, ideally the signal would be converted and the driving voltage adjusted such that it leads to flips by $\pm\frac{\pi}{2}$ after amplification in the driver. The importance of and ways to insure this are also discussed in the last section of this chapter (see Sec. 7.2.3).

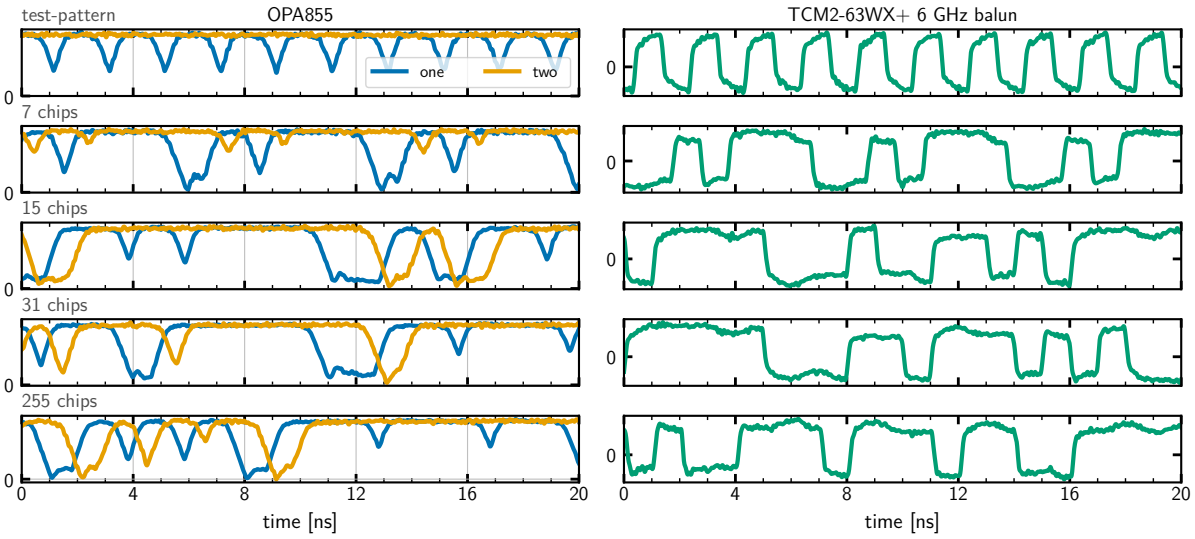

Figure 7.7: Recordings of signal conversion from LVDS to single ended for different sequence length using either up to two OPA855 GHz-OpAmps (left) or the TCM2-63WX+ (mini circuits) 6 GHz balun (right). The sequences are from top to bottom the test-pattern (alternating logical 0 and 1) and then 7, 15, 31 and 255 chips in length. Data was recorded with a GHz-bandwidth oscilloscope.

In a first attempt, the needed signal conversion was tried with the use of two GHz-operational amplifier (OpAmps) on evaluation boards, one for adding the two parts of the signal, the second to add an offset[30]. In parallel, the use of a passive GHz-balun for adding the signals was also investigated. As shown in Figure 7.7, the latter had significantly better results. However, a bandwidth limit between 6 GHz and 8 GHz for both methods was not viable for the planned higher PRN frequency in later experiments of the project. Thus, a commercial high bandwidth (26 GHz) balun from Marki microwave was ordered and tested. This created a good signal as seen in the eye-diagrams in Figure 7.8, and was therefore added to the setup as a permanent solution. However, it could not solve another issue the driver itself caused. While the output of the balun shown in Figure 7.8 showed

[30]This offset was not needed and only thought to be important due to a misconception about the driver circuits which were later clarified.

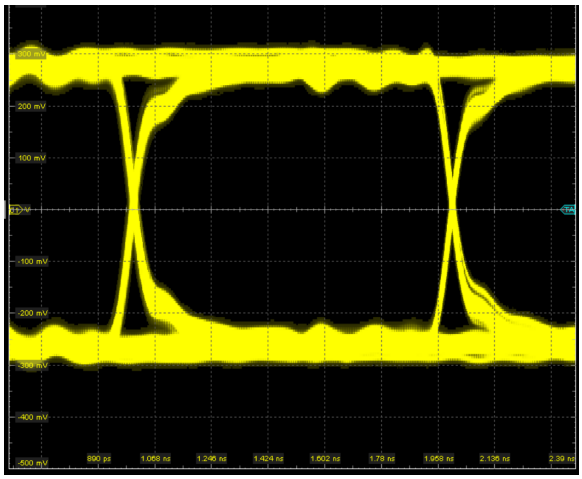

(a) Screenshot of the GHz-oscilloscope used to observe the modulation and construct eye-diagrams showing the eye-diagram of the 255 chips long sequence.

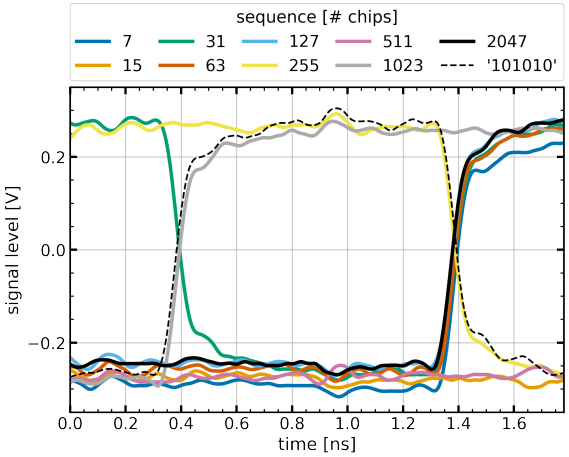

(b) Eye-diagram-like plot constructed by overlaying traces recorded on the same GHz-oscilloscope for all sequence lengths and the test-pattern.

Figure 7.8: Two types of eye-diagram or eye-diagram-like plot recorded after the Marki Microwave GHz balun used to convert the signal from LVDS to single ended. On the left the diagram was constructed on the R&S GHz-oscilloscope directly and then a screenshot was taken. This shows the eye-diagram of the 255 chips long sequence. On the right traces from all sequences recorded with the same oscilloscope are laid over each other. As it was not possible to save the full eye-diagram shown in (a) as a trace but only one of the individual traces forming it, constructing a full eye-diagram for a single sequence this way would be tedious. This alternative approach now instead shows some consistency between sequences. A plot showing how the driver affects this can be found in Figure A.3 in the Appendix.

consistent voltage levels independent of the used PRN sequence, the output of the driver shown in Figure A.3 in the Appendix did not. This, and experiences made during data taking, suggested a sequence dependence of the needed driver gain for optimal operation. The issues resulting from this are discussed further in Section 7.2.2.d.

7.2.2.c Readout bandwidth and sequence average

As detailed in Chapter 5, the concept of *tunable coherence* relies on the averaging of full sequences to achieve its suppression. In that chapter, the consequences of averaging over less than a full sequence were not discussed, however, experimentally it could be observed that this introduces expected artifacts [138]. This is shown in Figure 7.9 where the modulation leads to several noise peaks at different frequencies.
On the other hand, one could consider what a readout with at least the PRN frequency or higher would look like. While so far all experiments and estimations presented in this thesis were limited to a bandwidth below the sequence repetition frequency, a simple argument can be made that the ability to suppress straylight would not be present. When measuring with such high bandwidth, each chip of the sequence can be seen individually as can be seen in data shown so far. As for each chip independently, the scattered light

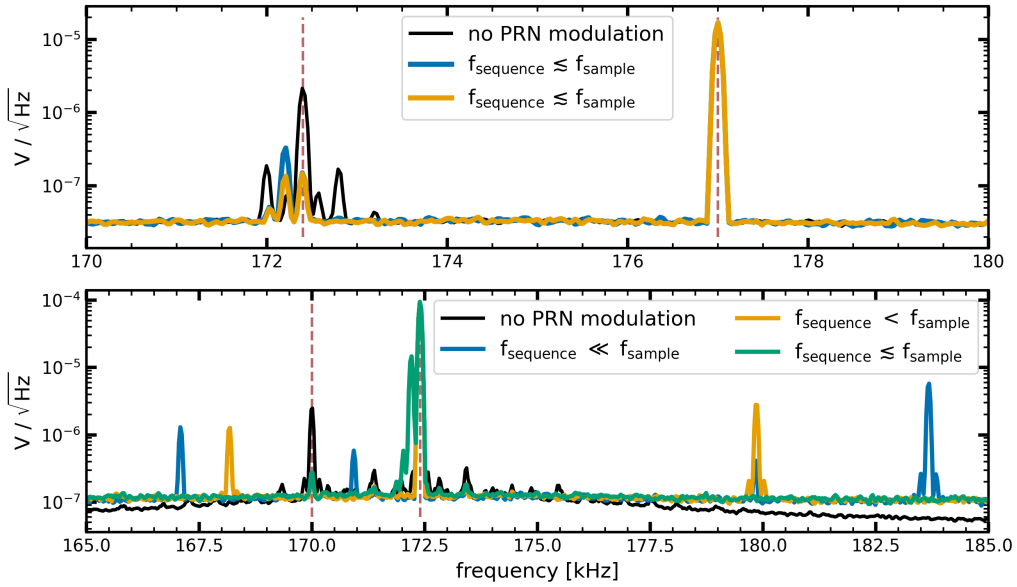

Figure 7.9: Spectra calculated from time-series data taken with two different too high sampling frequencies, exceeding the sequence repetition frequency f_{seq}. In the upper plot both time-series were recorded at 2 MHz while the repetition frequency was around 1.957 MHz. In the lower plot again all time-series were recorded at 2 MHz while the sequence repetition frequencies were around 0.489 MHz (blue), 0.978 MHz (orange) and 1.957 MHz (green). In both plots, a spectrum of a time-series recorded at 2 MHz without PRN modulation is added in black.

does still interfere with the main light, just having a random additional phase offset of 0 or π, the parasitic interference is not suppressed. Only the averaging caused by lower bandwidths leads to the effects mathematically described by the ACF or physically by adding up all of the two possible interference results. These then average out close to zero due to the nearly perfectly balanced distribution of the two possible values which are ideally exactly out of phase by π. This distribution is determined by the way the sequence is set up as described in Section 5.1. Thus, while a readout at these high frequencies should be possible, it must be assumed that the ability to suppress scattered light disappears.

7.2.2.d Modulation depth

The modulation depth can be adjusted and controlled by changing the gain of the amplifier in the EOM driver. This changes the strength of the electric field introduced in the crystal of the GHz-EOM which in turn determines the associated phase delay θ. As described before, it is assumed that technically the positive and negative voltage levels of the signal entering the driver correspond to a phase delay of $\pm\theta$. For simplicity, this is neglected from here on as it is only technical and has no physical effect, except a constant phase offset, on the resulting observations.

While it is not explicitly taken into account or calculated in Chapter 5, again a simple argument can be made why always achieving the proper modulation depth of $\theta = \pi$ is

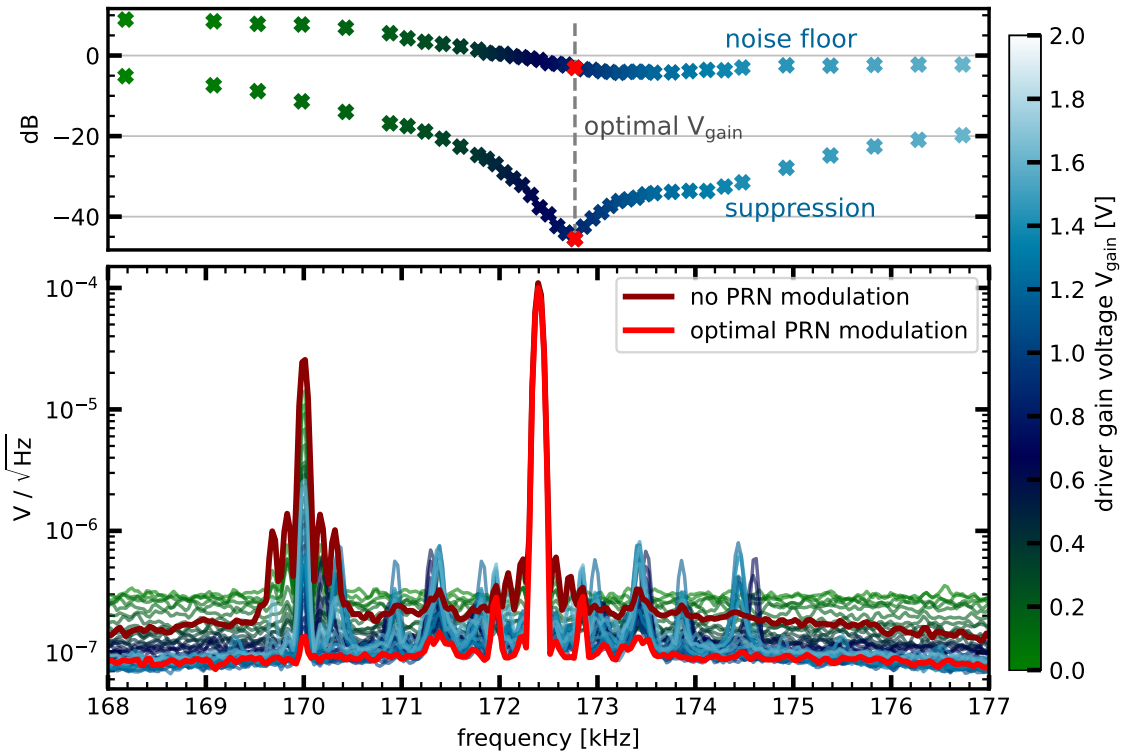

Figure 7.10: Spectra calculated from time-series recorded with different EOM driving voltages, meaning different modulation depths. The color map (green to blue) corresponds to the amplifier gain set by its driving voltage. However, as this voltage is applied to the driver through a set of attenuating and limiting circuits (maximum allowed voltage for the different inputs are either 1 or 2 V) this scale is arbitrary and only an estimate of the actually supplied voltage. While the lower plots show the resulting spectrum for each voltage setting, the upper shows the reached suppression and relative noise floor compared to a time-series without PRN modulation (dark red line) plotted against the driving voltage (also color-coded with the same color bar). Marked in red is the time-series with optimal modulation depth resulting in the highest suppression and no increase in noise-floor.

important. By having the phase-flip introduced by the PRN sequence be exactly π, the values measured for different chips are either in phase or 180° out of phase. Thus, they negate each other and the before mentioned averaging, which sums up the measured interference during individual chips, results in nearly zero. The only remaining contribution is coming from one chip not having an out of phase counterpart due to the sequence composition (see Sec. 5.1). However, if the modulation depth would be less or more than π, the two values would not be negating each other, thus not average to zero and thereby limit the suppression. Of course, the concept also works with uneven multiple of π, however, using this would put unnecessary challenges in the experimental implementation due to the higher voltages needed for the deeper modulation.

Following the same argument, it can also be assumed that longer sequences containing more chips are more sensitive due to more unwanted offsets remaining, however, there was no experimental focus to verify this directly. While experimentally easily observable,

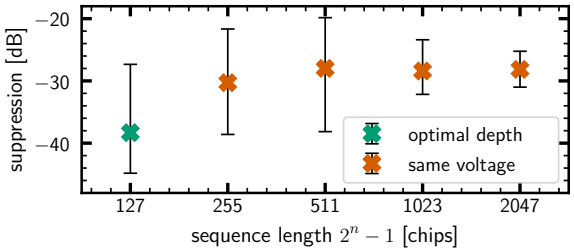

(a) Suppression measured with different sequences but fixed driving voltage for the EOM driver optimized for the 127 chip long sequence.

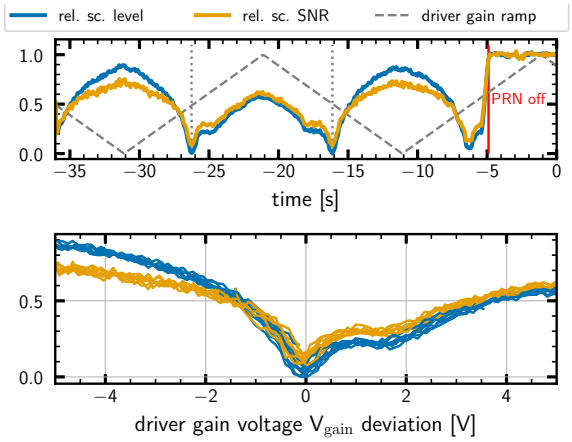

(b) Traces recorded with the measurement function of the Spectrum Analyzer instrument in the Moku:Pro. The upper plot shows the time-series of the recorded scatter level and scatter SNR, normalized to the values without PRN modulation. These were measured by injecting only the scatter signal into the setup and tracking its peak in the spectrum over time while ramping the EOM driver gain voltage (indicated by the gray line). The lower plot shows the same traces now plotted against the driving voltage ramp thus overlaying the values for several recorded cycles of the ramp.

Figure 7.11: Plots showing the influence of the EOM driver gain voltage on the achieved suppression. In (a), the gain voltage was held constant while the sequence was changed, showing loss of suppression and indicating a change in optimal gain voltage for different sequences. In (b), the gain voltage was changed for a given sequence and the achieved suppression of an injected scatter signal into the setup described in Chapter 8 recorded. As the gain voltage controls the modulation depth, a clear loss of suppression can be seen when deviating from the theoretical optimum of π.

Figure 7.10 and 7.11b show explicit measurements of the achieved suppression[31] and noise floor increase depending on the EOM driving voltage which determines the modulation depth.

The control of the EOM driver was handled by custom build analog electronics (see Appendix A.4) that provided the four needed voltages of which two were the supply and the other two influenced the gain[32]. The driving voltage was set by a potentiometer inside attenuating, filtering and limiting circuits that ensured a stable voltage not exceeding the absolute maximum ratings of the driver was supplied. Therefore, in order to drive the gain voltage with a ramp and have more control over the exact voltage set, an external input to these circuits was used for the measurements. This however meant that the recorded voltage is not the real driving voltage. However, as its value is arbitrary in any regard, only a rough conversion was done to take this into account. Both presented measurements show a strong dependence of reached suppression and a slight dependence of the noise-floor on the driving voltage with a clear optimal position.

Besides the direct dependency on the modulation depth and thus driving voltage, another aspect was noticed and hinted at by the shift in voltage levels after the EOM driver for

[31] The setup and experiment used to take this data are described in Chapter 8. There the suppression measurements are discussed in detail, here the focus lies on the influence of the modulation depth.

[32] As of now, it could not be determined how the two voltages V_{gain}, V_{xp} differ in influencing the gain of the driver.

different sequences (shown in Figure A.3). The driving voltage needed to achieve a modulation depth of π seemingly varied between sequence lengths which might be an attribute of how the driver and EOM operated. This could clearly be observed during a measurement in which the driving voltage was optimized for the suppression of a 127 chips long sequence and data for longer sequences, of up to 2047 chips in length, taken subsequently with the same driving voltage. The results as seen in Figure 7.11a show the suppression deteriorating for the longer sequences.

All these observations motivate the implementation of a control loop for locking the modulation depth to π, but *tunable coherence* can function without it. The results obtained for and presented in subsequent parts of this work demonstrate this, yet also hint to first limitations. For these proof-of-concept demonstrations, adjusting and optimizing the modulation depth by hand worked well enough. However, pushing the limits further and reaching long term stability is most likely impossible without proper control of this parameter. Possible options to implement this are discussed in the next section as this can be seen as a crucial step towards proper functionality of *tunable coherence*.

7.2.3 Locking the modulation depth

With the previous sections, especially Sec. 7.2.2.d, motivating the implementation of a control loop for the critical parameter modulation depth θ, two approaches are presented in this section. While it was always planned to have such a control loop in the experimental setup, the original idea for this being described first in Section 7.2.3.a, the implementation did not work. A deeper analysis why this was the case is again described in the same section. For the proof-of-concept demonstrations of this thesis, the lack of a working control loop was not yet critically limiting, however, future experiments and long term implementations of *tunable coherence* will be problematic without it. Data pointing to this problem is presented in later chapters of this thesis, most prominently in Chapter 10. An alternative solution for the failed original scheme is therefore discussed in Section 7.2.3.b as a recommended future improvement.

7.2.3.a Heterodyne interference lock

The original idea for locking the modulation depth was based on heterodyne interference. As the carrier would be suppressed for perfect modulation depth π, the readout of one of the demodulated quadratures could yield an error signal. The advantage of this approach was given by the simplicity of its realization without the need for additional high-speed capable equipment. However, as the following calculations show, this signal would also always be influenced by an additional phase, making it unusable.

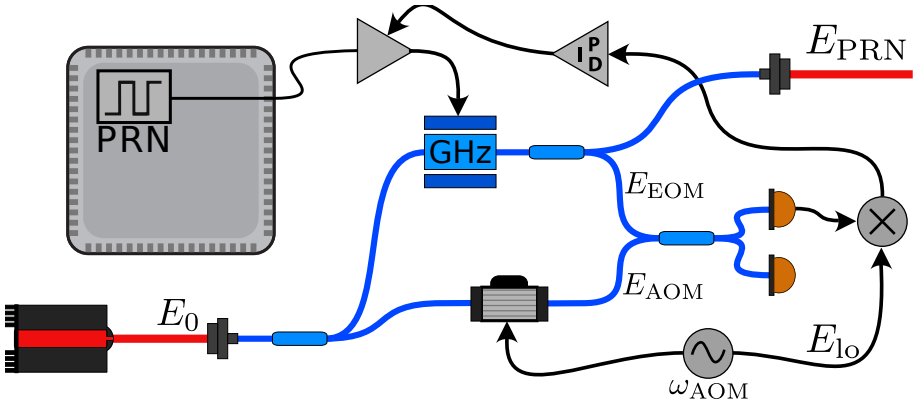

Figure 7.12: Sketch depicting the simplified attempted setup for stabilizing the modulation depth of the GHz-EOM using heterodyne interferometry. The upper path contains the EOM and most of the modulated light is coupled out to be used in the experiment, the lower path contains an AOM to shift the frequency in order to create heterodyne interference. Both paths are recombined and detected with a PD, the recorded signal is demodulated at driving frequency of the AOM ω_{AOM} creating the signals stated in Eq. 7.6.

Starting with a modulated (E_{EOM}) and an unmodulated beam (E_{AOM}) given by

$$\begin{aligned} E_{\mathrm{EOM}}(t) &= E_1 \cdot e^{i(\omega t + s(t)\theta)} \\ E_{\mathrm{AOM}}(t) &= E_2 \cdot e^{i((\omega+\omega_{\mathrm{AOM}})t+\Delta\varphi)} \end{aligned} \tag{7.1}$$

where the subscripts *EOM* and *AOM* stem from the fact that the unmodulated field is shifted in frequency with an AOM while the modulated field is created using an EOM as shown in Figure 7.12. Here E denotes the amplitudes of the various fields, ω the laser frequency with ω_{AOM} being the shift due to the AOM and $\Delta\varphi$ the phase-difference between the two fields. The modultion caused by the EOM follows the PRN sequence $s(t)$ and has a depth of θ[33]. Interfering these beams and detecting the signal on a PD with a standard bandwidth of around 100 MHz then yields

$$\begin{aligned} P(t) = |E_{\mathrm{het}}|^2 &= |E_1 \cdot e^{i(\omega t + s(t)\theta)} + E_2 \cdot e^{i((\omega+\omega_{\mathrm{AOM}})t+\Delta\varphi)}|^2 \\ &\propto 2E_1E_2 \cdot \cos(\omega_{\mathrm{AOM}}t + \Delta\varphi - s(t)\theta) \\ &= 2E_1E_2 \cdot [\cos(\omega_{\mathrm{AOM}}t+\Delta\varphi)\cos(s(t)\theta) + \sin(\omega_{\mathrm{AOM}}t+\Delta\varphi)\sin(s(t)\theta)] \end{aligned} \tag{7.2}$$

Here, terms oscillating at frequencies ω or $\omega \pm \omega_{\mathrm{AOM}}$, above the PD's bandwidth, are averaged over and drop out. Then the transformation to the last line isolates the terms representing the PRN modulation $s(t)\theta$ which also lies in the GHz-frequencies and is thus

[33] As described in the previous section, it is assumed that technically the way the signal is amplified by the driver leads to a phase delay or modulation depth of $\pm\theta/2$ corresponding to the two signal levels of the LVDS-signal, however, as this would only lead to an additional constant phase offset between a modulated and unmodulated beam, which can be absorbed into the already noted one given by $\Delta\varphi$ and has no effect on the phase offset between two modulated beams, this is neglected here and in further calculations.

averaged due to the limited bandwidth of the PD. As $s(t)$ can either be zero or one, this means

$$\cos(s(t)\theta) = \begin{cases} \cos(\theta) & \text{if } s(t)=1 \\ 1 & \text{if } s(t)=0 \end{cases} \quad \& \quad \sin(s(t)\theta) = \begin{cases} \sin(\theta) & \text{if } s(t)=1 \\ 0 & \text{if } s(t)=0 \end{cases} \tag{7.3}$$

and for an *m*-sequence of length 2^n-1 chips, $s(t)=1$ is true for half of them and $s(t)=0$ one time fewer. Thus, averaging over a full cycle yields

$$\begin{aligned} \langle \cos(s(t)\theta)\rangle_{\text{cycle}} &= \alpha + \beta\cos(\theta) \approx \frac{1}{2} + \frac{1}{2}\cos(\theta) \\ \langle \sin(s(t)\theta)\rangle_{\text{cycle}} &= \beta\sin(\theta) \approx \frac{1}{2}\sin(\theta) \end{aligned} \tag{7.4}$$

where $\alpha = (2^{n-1}-1)/(2^n-1)$ and $\beta = 2^{n-1}/(2^n-1)$ both approaching $1/2$ for $n > 5$. Hence, by additionally substituting $\phi = \omega_{\text{AOM}}t + \Delta\varphi$, the power on the PD in eq. 7.2 becomes

$$\begin{aligned} P(t) &\propto 2E_1E_2 \cdot [\cos(\phi)\langle\cos(s(t)\theta)\rangle + \sin(\phi)\langle\sin(s(t)\theta)\rangle] \\ &= 2E_1E_2 \cdot [\cos(\phi)(\alpha+\beta\cos(\theta)) + \sin(\phi)\beta\sin(\theta)] \\ &= 2E_1E_2 \cdot [\alpha\cos(\phi) + \beta\cos(\phi)\cos(\theta) + \beta\sin(\phi)\sin(\theta)] \\ &= 2E_1E_2 \cdot [\alpha\cos(\phi) + \beta\cos(\phi-\theta)] \\ &= 2E_1E_2 \cdot [\alpha\cos(\omega_{\text{AOM}}t+\Delta\varphi) + \beta\cos(\omega_{\text{AOM}}t+\Delta\varphi-\theta)]\,. \end{aligned} \tag{7.5}$$

Here, the conversion $\cos(a)\cos(b)+\sin(a)\sin(b) = \cos(a-b)$ was used and ϕ re-substituted in the last line. Demodulating this power at ω_{AOM} with an arbitrary phase ψ isolates the terms depending on the modulation depth and phase difference

$$\begin{aligned} A(t,\psi) &= P(t)\cdot E_{\text{lo}}\cos(\omega_{\text{AOM}}t+\psi) \\ &= E_1E_2E_{\text{lo}}\,[\alpha\cos(2\omega_{\text{AOM}}t+\Delta\phi+\psi) + \alpha\cos(\Delta\varphi-\psi) \\ &\quad + \beta\cos(2\omega_{\text{AOM}}t+\Delta\varphi-\theta+\psi) + \beta\cos(\Delta\varphi-\theta-\psi)\,] \\ &\approx E_1E_2E_{\text{lo}}\,[\alpha\cos(\Delta\varphi-\psi) + \beta\cos(\Delta\varphi-\theta-\psi)] \end{aligned} \tag{7.6}$$

where the last step is given by using a low-pass filter to remove the fast oscillating terms at $2\omega_{\text{AOM}}$. Setting the demodulation phase ψ to 0° or 90° yields the standard I- and Q-quadratures

$$\begin{aligned} I(\theta,\Delta\varphi) &= E_1E_2E_{\text{lo}}\,[\alpha\cos(\Delta\varphi) + \beta\cos(\Delta\varphi-\theta)] \\ Q(\theta,\Delta\varphi) &= E_1E_2E_{\text{lo}}\,[\alpha\sin(\Delta\varphi) + \beta\sin(\Delta\varphi-\theta)]\,. \end{aligned} \tag{7.7}$$

One can clearly observe, as long as the relative phase $\Delta\varphi$ between the two incoming beams E_{EOM} and E_{AOM} is allowed to fluctuate, it introduces an erroneous influence into the desired error signal for the modulation depth θ. Using this I-Q-demodulation and constructing the amplitude given by $a_0^2 = I^2+Q^2$ would remove the influence of $\Delta\varphi$ as

the ac-term then only depends on $\cos(\theta)$. Thus, for perfect modulation depth $\theta = \pi$ this resulting amplitude would be minimized, however, the locking point would fall in a local minimum, making this unsuitable as a direct error signal. As such, using a dither lock approach might be a working solution, however, adding a dither signal onto the control voltage of the modulation depth could have a degrading influence.
If it were possible to choose the demodulation phase ψ such that $\Delta\varphi - \psi = \pi/2$, a good error signal could be obtained

$$A(\Delta\varphi - \psi = \pi/2) = \beta E_1 E_2 E_{\mathrm{lo}} \sin(\theta). \tag{7.8}$$

It also becomes clear that even though in reality α and β are not perfectly 1/2, they only show up as additional preceding factors (compare also with eq. 7.5), only influencing the steepness of the error signal.
However, to this point, no other possibility to isolate the phase contributions $\Delta\varphi$ and θ to the error signal and thus stabilize them individually could be identified. Further, as the phase difference $\Delta\varphi$ was observed to be varying with time in the experimental setup, no proper lock of the modulation depth could be achieved with this method. Thus no simple and non-interruptive approach to create a usable error-signal this way could be found so far. This does, however, not imply that it is strictly impossible.

7.2.3.b Mach-Zehnder GHz lock

An alternative to the previously described method to lock the modulation depth thus could be favorable as stabilizing it would not only simplify the measurements, but might be unavoidable for proper implementation of *tunable coherence* in the future.
One technique that seems to be implementable in the near future is described in Yang et al. [165] and is based on a Mach-Zehnder (MZ)-topology to compare individual chips of the PRN sequence. From this, an error signal can be constructed and in the use-case of *tunable coherence* this even simplifies compared to their presented case.
As mentioned, the core of the concept is a MZ-interferometer where one arm is delayed by one chip ($\Delta\tau = {f_{\mathrm{PRN}}}^{-1}$) as shown in Figure 7.13. This interferometer is read out with a high-bandwidth (GHz) PD to avoid averaging over several chips. In Yang et al. [165], instead of a MZ-interferometer, a fiber delay-line interferometer (DLI) with splitting ratios $\alpha_1 : (1-\alpha_1)$ and $\alpha_2 : (1-\alpha_2)$ is used and the readout is done with a balanced photodetector (BPD) having responsivities 1 and β for the two individual PDs respectively. The envisioned switch to a free-space setup as shown in Figure 7.13 is mainly for more control and cost-effective testing of the concept. This offers the advantage of more flexibility in adjusting the splitting ratios and locking the interferometer to its desired operating point, but it complicates fine-tuning the delay. The latter might motivate the use of a fiber DLI

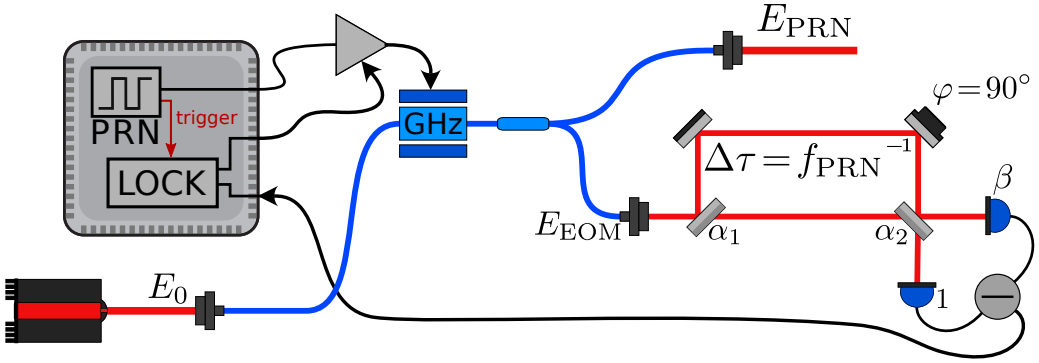

Figure 7.13: Sketch depicting the simplified proposed setup for locking the modulation depth θ by stabilizing the driving voltage of the GHz-EOM. The setup is slightly adapted from Yang et al. [165, Fig.1] with certain denotations kept for easier comparison. For the control scheme, some PRN-modulated light is tapped of and interfered with itself using a MZ-topology with a delay of one chip. The power is detected using a balanced PD (BPD) with GHz-bandwidth and used to construct an error signal digitally. While Yang et al. [165] describes the use of histograms for this, in the case of *tunable coherence* it should be possible to implement a simpler version on the FPGA generating the modulation sequence. The implied changes to the laser preparation setup can be found in the appendix (Fig. A.1).

especially for higher modulation frequencies above a few GHz, even if the locking of this interferometer might not be simplified anymore in that case.
Following Yang et al. [165], the power measured by the BPD is given by

$$\begin{aligned} P_{\mathrm{BPD}} &= \{\alpha_1(1-\alpha_2) + \alpha_2(1-\alpha_1) - \beta[\alpha_1\alpha_2 + (1-\alpha_1)(1-\alpha_2)]\} P_{\mathrm{EOM}} \\ &\quad + 2\sqrt{\alpha_1\alpha_2(1-\alpha_2)(1-\alpha_1)}(1+\beta)\,\mathrm{Re}\left\{E_{\mathrm{EOM}}(t-\Delta\tau)\cdot E^*_{\mathrm{EOM}}(t)\cdot e^{-i\varphi}\right\} \\ &= C_1 P_{\mathrm{EOM}} + C_2\,\mathrm{Re}\left\{E_{\mathrm{EOM}}(t-\Delta\tau)\cdot E^*_{\mathrm{EOM}}(t)\cdot e^{-i\varphi}\right\}. \end{aligned} \tag{7.9}$$

Here E_{EOM} is the field tapped of after the modulator, φ the phase difference in the interferometer and C_1 and C_2 constants depending on the splitting ratios α_1 and α_2 as well as the PD responsitivity β. For at least one ideal splitting ratio of 0.5:0.5 and both responsitivities equaling 1, C_1 vanishes. Further, C_2 becomes 1 if both splitting ratios are ideal, thus motivating the optimization of both of them in the free-beam setup.
As the delay of $\Delta\tau = f_{\mathrm{PRN}}^{-1}$ ensures that always two following chips are compared, $E_{\mathrm{EOM}}(t-\Delta\tau)\cdot E^*_{\mathrm{EOM}}(t)$ can take the values $P_{\mathrm{EOM}}e^{-i\theta}$, P and $P_{\mathrm{EOM}}e^{i\theta}$ leading to three possible expressions for eq. 7.9:

$$\begin{aligned} \mu_1 &= C_1 P_{\mathrm{EOM}} + C_2 P_{\mathrm{EOM}}\cos(\theta+\varphi) \\ \mu_2 &= C_1 P_{\mathrm{EOM}} + C_2 P_{\mathrm{EOM}}\cos(\varphi) \\ \mu_3 &= C_1 P_{\mathrm{EOM}} + C_2 P_{\mathrm{EOM}}\cos(\theta-\varphi). \end{aligned} \tag{7.10}$$

The original concept was proposed for an arbitrary modulation depth θ, for which a combination of these signals, measured with different values for φ, would be needed to

construct an error signal. However, for the here needed case of $\theta = \pi$, this simplifies. By choosing $\varphi = \pi/2$, the three signals reduce to

$$\begin{aligned} \mu_1 &= C_1 P_{\mathrm{EOM}} - C_2 P_{\mathrm{EOM}} \sin(\theta) \\ \mu_2 &= C_1 P_{\mathrm{EOM}} \\ \mu_3 &= C_1 P_{\mathrm{EOM}} + C_2 P_{\mathrm{EOM}} \sin(\theta) \end{aligned} \tag{7.11}$$

where μ_1 and μ_3 yield proper error signals for the desired modulation depth if C_1 vanishes. Alternatively, subtracting μ_2 from either μ_1 or μ_3 could be used to remove the offset. Adjusting at least one splitting ratio to be ideal thus simplifies the needed complexity in properly constructing the error signal.

Besides this advantage in a free-beam setup, there are also two straightforward ways to lock the phase φ of the interferometer in such a setup. Both use a second beam injected from the other input of the first beam splitter (BS) having the splitting ratio $\alpha_1 : (1-\alpha_1)$. This beam can either be frequency-doubled light as shown in Figure 7.14 for clearer visualization or in an orthogonal polarization (which would look similar in Fig. 7.14). The frequency-doubled light would avoid any interference between the two control loops more easily, but the operating point for this would be dark- or bright-port depending on which side is read out. In contrast, avoiding any interference between the two control loops would rely more on the polarization properties of the used optics when using two orthogonal polarizations. However, the operating point could be locked by using a second BPD having a standard bandwidth around a few tens of MHz as it corresponds to mid-fringe, meaning equal power in both outputs. Which option is easier to implement in the future will have to be determined when the experiment progresses.

The more complex part of the control loop for the modulation depth θ lies in properly constructing an error signal, which is proposed to be done digitally, e.g. on the same

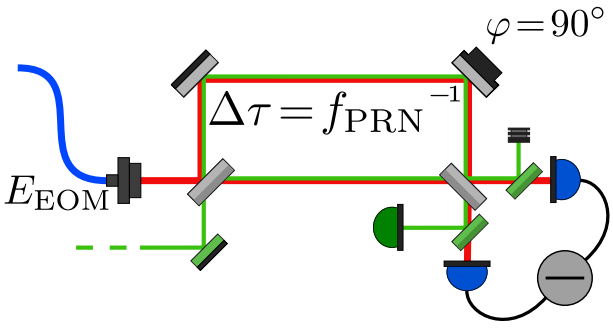

Figure 7.14: Zoomed sketch of the MZ-interferometer used for the proposed modulation depth control loop. Here depicted with a possible addition of frequency-doubled light for creating a second control loop for keeping the interferometer at its needed operating point with a phase shift of $\varphi = 90°$ between the two arms. Instead of frequency doubled light, an orthogonal polarization to the one used for the PRN-modulated light could be used, in this case special care should be taken with the used optics to avoid unwanted interference between the two control loops.

FPGA that generates the PRN sequence driving the GHz-EOM. As seen in eq. 7.11, depending on the type of chip-transition measured ($0 \to 1$, $1 \to 0$ or $0/1 \to 0/1$), three different signals will be obtained. Thus, the logic constructing the error signal needs to either filter out only one of these transitions or construct a new signal by combining them in the correct way. Luckily, all transitions are pre-determined, known and repeating. The first option would therefore be easiest and could be achieved by simply triggering on a certain transition. To avoid exceeding the bandwidth of the control loop locking the MZ-interferometer, values measured from the GHz-BPD on those triggers would then be averaged. The second option would be similar but more complex, it would however also allow for the removal of a possibly present offset in the signals given in eq. 7.11 by combining them. Using the sequence generation on the same FPGA should allow the logic to pair up values with the correct chip-transition easily, e.g. by triggering onto several specific ones with individual triggers. Combining and averaging the obtained values would then allow for the construction of a proper error signal. There are some challenges concerning timing constraints and delays, mainly to make sure the transitions and values are matched correctly, however, solutions to these can be found.

7.3 Conclusion

In this chapter, the experimental realization of the PRN modulation as core part of *tunable coherence* and thus the laser preparation for the experiments discussed in the next chapters has been presented. The parameters influencing the performance of the PRN modulation have been investigated and arising problems discussed. Lastly, the future need for a control loop locking the modulation depth has been motivated and a possible implementation for this presented. Especially in this regard, future optimization is possible and most likely needed, nevertheless, the stage is set for demonstrations of *tunable coherence* in different optical setups, presented in the following chapters.

8 Interferometers with *Tunable Coherence*

This chapter focuses on the experimental demonstration of *tunable coherence* in different interferometer topologies. The main focus lies on the Michelson interferometer as this is the base for the more complex topologies used in current gravitational wave detectors (GWDs). Additionally, the Sagnac topology was investigated as part of the supervised Master's Thesis of Leonie Eggers [153].

Some of the results presented here form parts of two publications, Voigt et al. [24], titled *Tunable coherence laser interferometry: demonstrating 40dB of straylight suppression and compatibility with resonant optical cavities* (doi: 10.1103/PhysRevLett.134.213802), and Eggers et al. [25], titled *Scattered light reduction in Sagnac Speed Meters with tunable coherence* (doi: 10.1103/PhysRevD.112.022001). The former contains most of the 1 GHz proof-of-concept experiment (Sec. 8.1.1). In the latter, results of the Sagnac interferometer experiment (Sec. 8.2) were published. These results are based on the mentioned Master's Thesis [153] with subsequent optimizations for the publication.

8.1 Michelson topology

The motivation for choosing a Michelson interferometer for the initial proof-of-concept experiment had two aspects, its simplicity and possible future iterations. As described in Sec. 2.3.2, all current and currently planned ground-based GWDs are at their core based on a Michelson interferometer with added complexity to enhance their performance. Thus, starting with such an interferometer and adding enhancements in the like of different cavities to it at later stages made sense. Additionally, a Michelson interferometer was easy to build, control and read out for a experimental demonstration of *tunable coherence*.

In this first experiment, the goal was a general proof-of-concept demonstration and investigating two parameters, the sequence length and the scattered light delay. This was first done at a PRN frequency of 1 GHz which was then increased for further experiments.

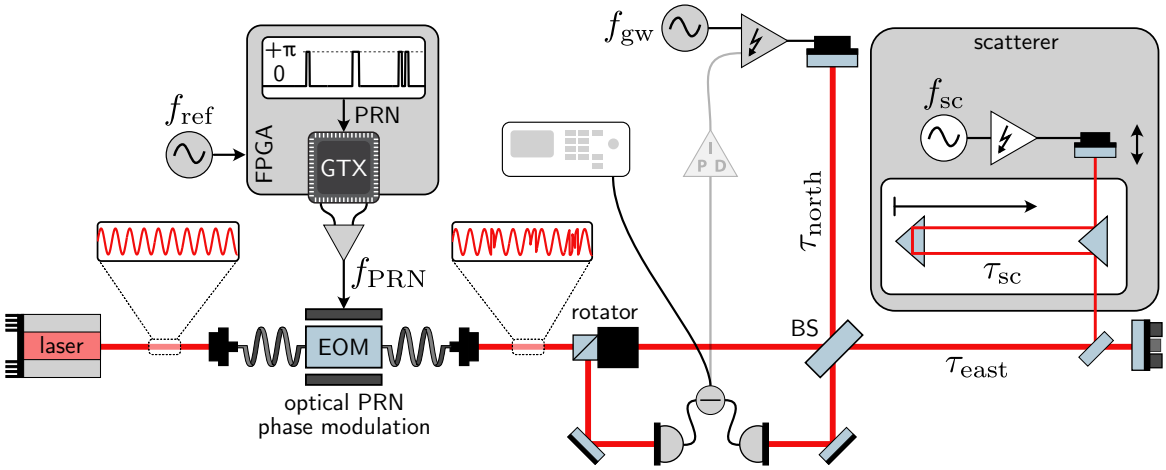

Figure 8.1: The sketch depicts the experimental setup with the fiber-coupled EOM modulating the PRN sequence onto the laser at f_{PRN} and the Michelson interferometer locked at mid-fringe. The north-arm was used to actuate the phase between the two arms and locking the interferometer, in the east-arm some light was reflected out of the arm and coupled back after being reflected from another actuated mirror to simulate scattered light coupling. This scattered light picked up an additional delay τ_{sc} relative to the equal arm-delays τ_{north} and τ_{east}. Taken from Voigt et al. [24].

8.1.1 1 GHz proof-of-concept

The results presented in this section were published as part of Voigt et al. [24]. Thus, the respective parts of the publication form the main body of this section[34], rearranged and complemented with further details where appropriate. First measurements recorded with this setup to generally characterize the implementation of the PRN modulation are discussed in Section 7.2.2. Lastly, some additional measurements were made for verification purposes (Section 8.1.1.a), these were not part of the publication.

Michelson interferometer setup

The proof-of-concept experiment consisted of a Michelson interferometer with matched arm lengths around 1 m, as shown in Figure 8.1. The laser preparation and modulation setup are described in Chapter 7. To create a parasitic beam path, a low power reflectivity ($R \approx 0.2$) mirror was placed in the east-arm to couple some light out and back in. The path of this beam could be actuated with a piezo-electric actuated (PZT) mirror and its optical length changed with a delay-line. This enabled changing the delay τ_{sc} of the straylight relative to the light in the interferometer. Additionally, due the high loss introduced in this arm, the same amount of power was removed from the other arm to keep the power in the arms almost balanced (not shown in Fig. 8.1). This was done to balance the here intentionally but normally unrealistic high loss caused by the straylight. In the

[34] As first and corresponding author of this publication, the text was written by myself and corrected by the co-authors, the final version was then created by me using their input and comments.

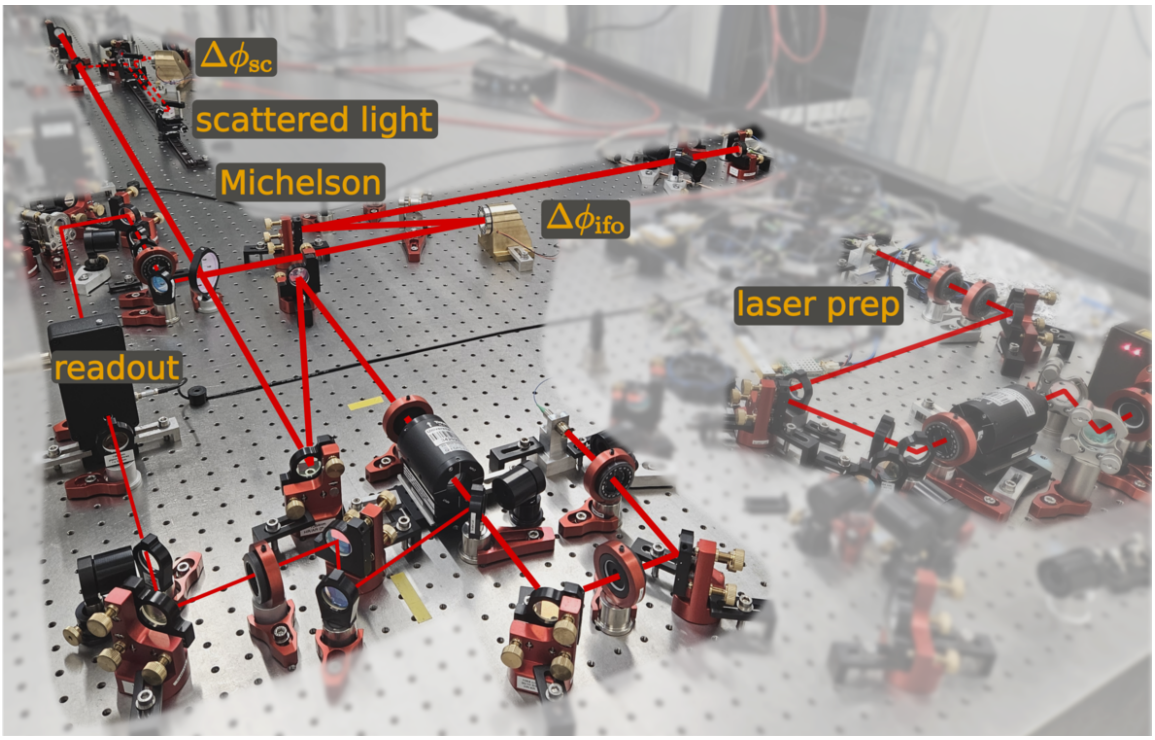

Figure 8.2: Picture of the Michelson setup, showing the interferometer on the upper left side. Below are the input and readout optics for the symmetric port, to the right the laser preparation.

north-arm the end mirror was piezo-actuated for adjusting the relative phase, locking the interferometer and injecting simulated (GW)-signals. The interferometer was locked and read out at mid-fringe by taking the difference between the light power measured at the anti-symmetric and symmetric port. The control-loop for this lock had a unity gain frequency of around 5.5 kHz, resulting in the interferometer being effectively free running at frequencies above 100 kHz. At these kHz frequencies, the measurements were only limited by residual laser amplitude noise, thus omitting the need for additional noise reduction at frequencies more realistic for a GWD. Two different sine-signals were injected, one simulating a gravitational wave (GW) at $f_{\mathrm{gw}} = 172.4\,\mathrm{kHz}$ with the PZT in the north-arm directly into the interferometer and one at $f_{\mathrm{sc}} = 170\,\mathrm{kHz}$ to modulate the phase of the parasitic beam that simulates scattered light coupling into the east-arm. The PZTs were driven on resonance frequencies, identical to the setup described in Sec. 4.2. However, for this and following experiments, new PZTs with a better displacement range and force output were used. This reduced electronic cross-talk in the high voltage (HV) amplifier as lower driving voltages could be used (see Sec. A.4). Needing to relying on the PZT's resonances still limited the strength of the injected scatter dynamics but was less constraining than moving to lower measurement frequencies at this point.

As the coupling of the parasitic beam into the interferometer readout is non-linear [82], the strength of its introduced phase error depends on the DC-phase relative to the main light field, which fluctuates slowly. To ensure that the maximum noise coupling was

always observed, the PZT was ramped slowly through several fringes over each measurement duration. This guaranteed that the strongest possible coupling was present in each measured time-series, thus allowing for comparison between data taken asynchronously.

Recording and treatment of data

Data was recorded as time-series either with or without the PRN modulation. The sampling rate and measurement duration were adjusted to ensure that each sample contained at least one full PRN sequence. This is crucial to avoid artifacts of the modulation showing in the data and it is advisable to have even multiple full sequences in an average to reduce any spurious artifacts [138]. Therefore, the experiments were limited to frequencies below the sequence repetition rate as exceeding f_{PRN} with the sampling frequency was assumed to neglect the effects of the PRN modulation (see Sec. 7.2.2.c).
Each time-series had around four million data points sampled over at least two seconds with a sampling rate of 2 MHz, with the time-series for longer PRN sequences (511 chips and more) being recorded over four and eight seconds at 977 kHz and 488 kHz sampling frequency respectively. From the recorded data, several spectra were computed using Welch's method with a Blackman-Haris window and 50 % overlap.
The average reached suppression was calculated by comparing the peaks at $f_{\mathrm{sc}} = 170\,\mathrm{kHz}$ between two spectra calculated over the full time-series measured with and without PRN modulation respectively. The upper and lower limits to the suppression were calculated by comparing respective minimum and maximum values of the scattered light peak taken from multiple spectra. These were calculated individually for 30 equally long time spans distributed evenly over the whole recorded time-series.

Results

Figure 8.3 shows an example measurement and its spectra for a PRN modulation following a sequence with a length of 255 chips. This measurement demonstrated a noise suppression of about 41 dB for the parasitic tone while maintaining the desired simulated GW signal. Moreover, the surrounding noise floor and side-lobes of the signals were reduced. These were identified to be caused by the parasitic beam path in the interferometer by blocking this path. The measurement also shows that with PRN modulation present the original noise floor could be recovered, except for a residual coupling of the parasitic tone.
Next, the dependency of this suppression on two parameters was investigated, the relative delay of the parasitic beam, tuned with the delay-line, and the length of the PRN sequence, n_{chips}. The results are shown in Figure 8.4.
The suppression for different scatter delays (Figure 8.4a) is shown for two sequence lengths, 15 and 127 chips. The data for the 15 chips sequence follows the theoretical limitations given by the minimal coherence and its dependency on the chip-length. It

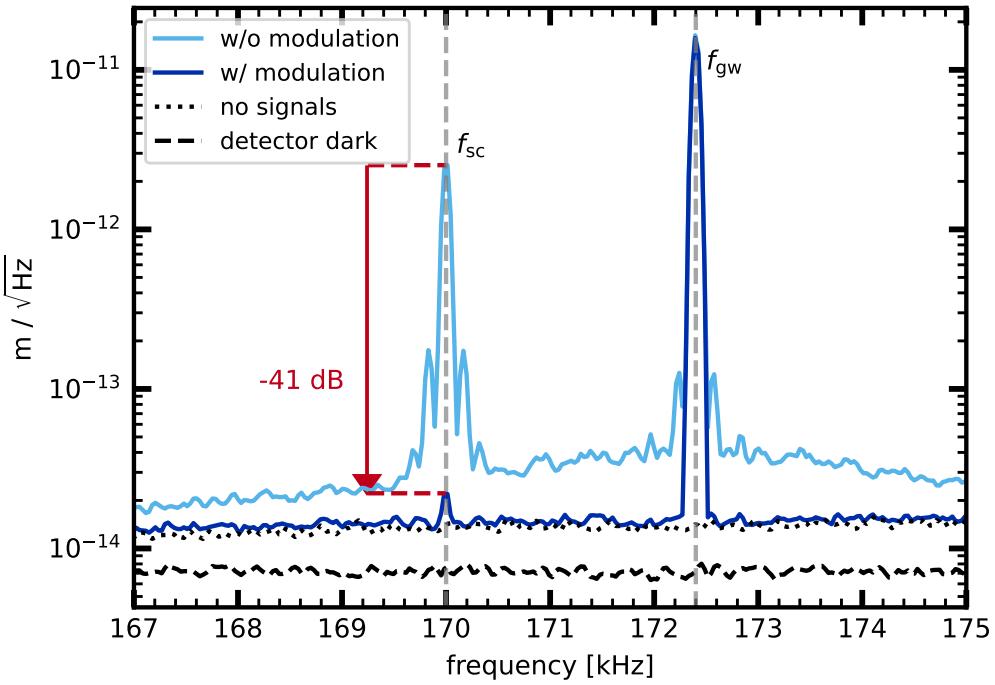

Figure 8.3: ASD of the calibrated interferometer output without and with PRN modulation using a 255-chips long sequence. The peak at 170 kHz corresponds to the injected scattered light modulation, while the peak at 172.4 kHz is from a signal injected directly into the north-arm of the interferometer, simulating a gravitational wave (GW). Using the PRN modulation, the scattered light peak was reduced by 41 dB. Taken from Voigt et al. [24].

reached its maximum possible suppression after a delay exceeding 30 cm, the length of one chip. For the 127 chips long sequence, a fade out of the curve compared to the sharp theoretical estimate can be observed. The maximum suppression is still achieved, but only for longer delays than calculated. The estimate is based on an assumed perfectly binary phase modulation. However, any real modulation shows effects of limited bandwidth and non-flat transfer-functions, which deforms the ideal shape and broadens the coherence length.

The results on measuring the maximum suppression depending on PRN sequence length are shown in Figure 8.4b. The dependence roughly followed the theoretical estimate (see Chapter 5) of $20\log_{10}(\frac{1}{l_{seq}})$ given by the auto-correlation function (ACF) of the sequence with the 63 chips long sequence being a strong outlier. It then saturated at the current experimental limit of suppression levels around 40 dB. This level closely coincided with the limit given by the strength of the parasitic tone in comparison to the measurement noise floor, which fluctuated between measurements (indicated as dashed gray lines in Fig. 8.4). However, for some measurements with long sequences the parasitic tone was still not fully suppressed, which indicates another not yet understood limitation lying in the same range. Nevertheless, except for the 63 chips sequence, the data follows expectations and a maximum of 41.7 dB suppression for the 2047 chips long sequence was reached.

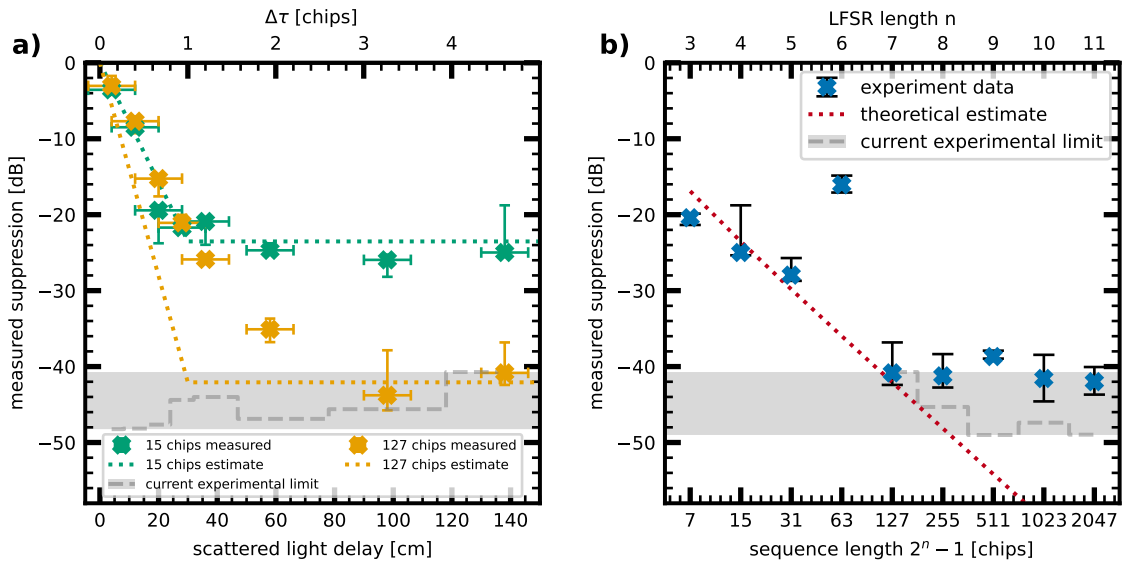

Figure 8.4: Measured suppression of the scattered light depending on its delay relative to the interferometer arms (Figure a) and on the length of the used PRN sequence (Figure b).
(a) The suppression for the 15-chip sequence follows the theoretical estimates, while the 127 chip sequence is not dropping off as sharply as theoretically predicted. The latter still achieves the maximum expected suppression for longer spatial delays.
(b) The dependence of the suppression on the PRN sequence length mostly follows the theoretical estimate until the maximum suppression level achieved in this setup is reached. Just the 63-chips long sequence showed unexpectedly low suppression. Adapted from Voigt et al. [24].

Discussion

The presented measurements showed that the coherence length could be reduced to the 10 cm scale and parasitic phase noise suppression was verified up to 41 dB without introducing any additional noise within the current measurement precision.

The current limitation to the suppression measurement was close to the experimental limitations to generate parasitic tones, however, other effects are suspected to also be relevant in this range, mainly deviations from perfect phase-flips in the PRN modulation. As discussed in Section 7.2.2.d, only for ideal phase-flips of π maximal suppression of the carrier tone can be achieved. Otherwise it can still contain significant power, reducing the achieved suppression as it competes with the PRN modulated fields. With the ability to handle these effects, one could push for stronger suppression using longer PRN sequences in the future. An option to actively stabilize the PRN modulation depth following Yang et al. [165] is discussed in Section 7.2.3.

The deficiency in reaching full suppression after one chip-length relative delay also indicates an influence of limited bandwidth in the PRN generation and application. This imperfection degrades the ACF of the used sequence, limiting the reachable suppression for delays close to the length of one chip. Optimizing electronics and cabling could help to push this limit further, with various high-speed equipment available from telecommu-

nication technology. Additionally, using PRN modulation in the GHz-range ensures good separation of radio frequency (RF) signal modulations from the sequence repetition rate (500 kHz for 2047 and 140 MHz for 7 chips here), even for moderate sequence lengths. As this repetition frequency poses as an upper limit to the used sampling frequency (see Sec. 7.2.2.c), pushing the PRN frequency higher also enables higher signal bandwidths.
However, there are some open challenges in the data that need addressing. One sequence did not perform as expected while the very short 7 chips long sequence often outperformed expectations. This is currently not understood, but the correctness of the used *m*-sequence was verified in various ways (see Sec. 7.2.2), leaving it open to be another, yet unknown effect. The used theoretical estimate is rather rudimentary and might not take into account all details of the more complex nature accompanying the experimental implementation. Direct investigation of the used sequences, including its spectrum and the longest runs[35], did, however, not show any irregularities. Especially the concern that a long section without a flip could fall outside of the AC-coupled driver's bandwidth could be discarded. No sequence falls below 100 MHz in this context while the driver's lower cut-off lies in the kHz-range.

8.1.1.a Additional measurements

One important question is not answered by the so far presented results. In almost all measurements, some residual scattered light remained and it was inconclusive whether this is a general limitation or coincidental. In the current setup, it could be a coincident that the strength of the scattered light lies in a range where first limitations for the suppression become visible. However, it could also be that a small portion of scattered light always remains, indicating a limitation to a minimal proportion of scattered light that cannot be suppressed. Further measurements were thus conducted to verify that the latter is not the case. For these measurements, the scattered light strength was reduced, with the expectation that it can be fully suppressed once its strength is less than the achievable suppression limited by the other discussed factors.
The results are shown in Figure 8.5 and verified the independence of current suppression limitations and scattered light strength. For the two shortest sequences, the suppression was still limited by the theoretical estimation following the ACF of the sequences. Thus, here remaining scattered light was expected. While the 63 chips long sequence was again an outlier, all other sequences capable of achieving full suppression reduced the scattered light down to the noise floor in this measurement. This is shown in Figure 8.5 for measurements using spectra calculated from recorded time-series data and directly recorded spectrum analyzer traces. For all spectra, the peak at the frequency used to modulate the scattered light was measured in relation to the average of the surrounding noise floor,

[35] sections without any flip between the two binary states

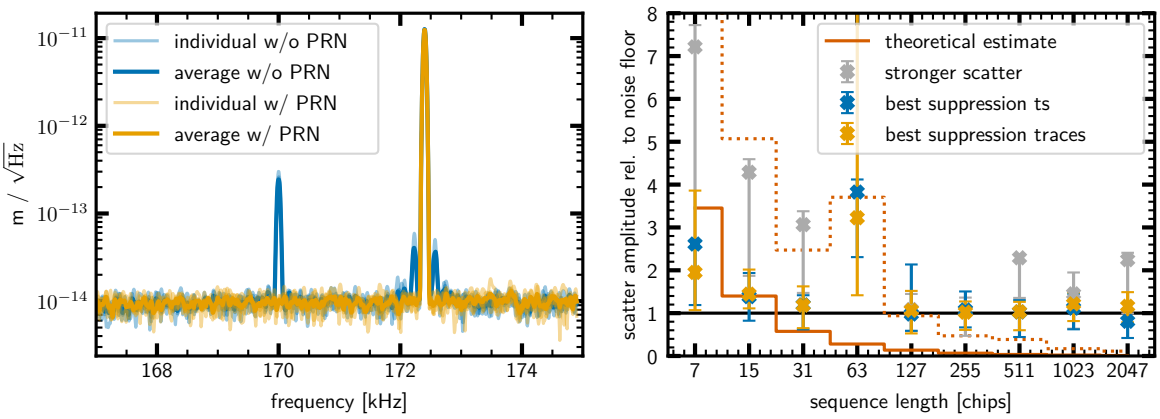

Figure 8.5: Plots showing suppression with reduced scattered light. On the left an example spectrum recorded with the Moku:Pro spectrum analyzer using a 511 chips long sequence as PRN sequence, on the right the remaining scattered light amplitude relative to the noise floor without PRN modulation for different measurements. The data in gray was taken for the publication Voigt et al. [24] and is shown for comparison. The data in blue was recorded as time-series (ts) and the data in yellow was recorded as traces of the Moku:Pro spectrum analyzer, with the suppression in the latter optimized in real-time. The theoretical estimate was calculated in relation to the reduced scatter (solid line) and the stronger scatter (dotted line) separately by using the strength of the scattered light and the estimate given by the ACF of the sequences.

leading to an expected result of 1 for full suppression. The theoretical estimate was calculated from the height of this peak without the PRN modulation and the reachable suppression of a given sequence given by $20\log_{10}(\frac{1}{l_{seq}})$ (see eq. 5.6), the dotted line then corresponds to the stronger scattered light which could only be fully suppressed for longer sequences. The results showed that there is no general constraint limiting the suppression to a remaining fraction of the injected scattered light. Comparing it to the data taken with stronger scattered light, it becomes clear that the remaining scattered light amplitude in those measurements was coincidentally close to the noise floor but caused by limitations independent of the scattered light strength.

8.1.2 Effects of higher PRN-frequencies

The next step in this layout was to push to higher frequencies for the PRN modulation. For this, the implementation on the FPGA was adjusted to feature either 2 GHz, 5 GHz or 10 GHz chip rate for the modulation in addition to the 1 GHz used so far. However, for these higher frequencies, the two arms need to be matched more precisely in length. This was achievable for most measurements up to 5 GHz PRN frequency with the setup used so far. Mostly for measurements at 10 GHz, the precision was not enough, thus they needed to be done in a revised setup, also used to transition into more complex topologies (see Chapter 10).

Revised Michelson setup

To achieve the needed precision in the length matching of the interferometer arms, especially for 10 GHz PRN frequency, the setup was changed. The revised setup is depicted in Figure 8.6. As moving towards power-recycling in the Michelson interferometer (see Chapter 10) was the next step following these experiments, a PZT delay-line was added to one of the arms. This was necessary as the constraints on the length matching of the arms were even stricter once inside the power-recycling cavity (PRC). With this delay-line in place, the arms could be matched in length to the point were the PRN modulation showed no impact on the contrast of the interferometer when the relative phase was ramped. To have more control and better fine-adjust also the delay of the injected scattered light, a linear-translation stage replaced the manual delay-line in the scattered light path. This could be used to move a reflecting prism, making the optical delay of the scattered light adjustable by up to 10 cm. During the re-alignment of the two Michelson arms, the low-reflectivity mirror dumping light from the second arm was removed in preparation for adding a power-recycling cavity (discussed in Sec. 10.1).

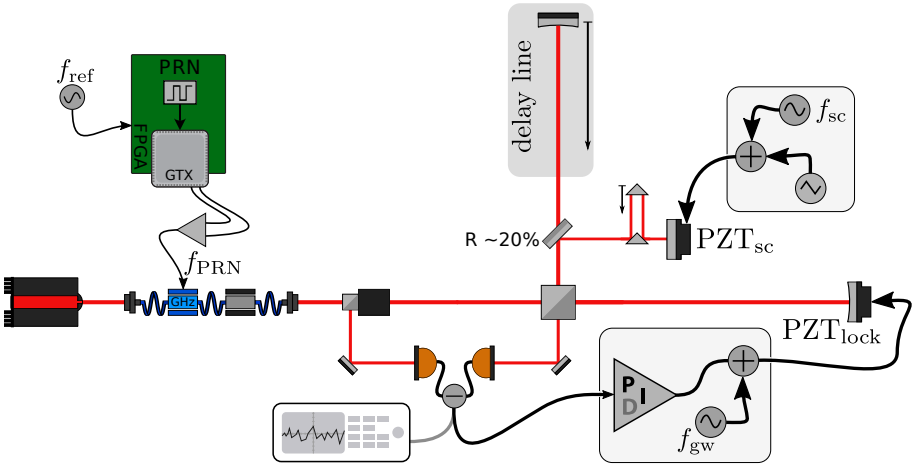

Figure 8.6: Sketch of the altered Michelson setup in order to match the arm length precise enough for the 10 GHz PRN frequency demonstration. As this setup was supposed to be iterated further to the PRMI setup shown in Fig. 10.1, the end-mirrors were replaced as well. In this experiment the interferometer was again locked to mid-fringe as described before.

Results

In this section, results of the measurements recorded at higher PRN frequencies are presented and compared to the results at 1 GHz PRN frequency. A discussion of the observations follows after.

For a PRN frequency of 2 GHz, the expected remaining coherence length of around 15 cm was long enough for all measurements to be done in the original setup. However, moving to a PRN frequency of 5 GHz, shrinks the remaining coherence down to around 6 cm.

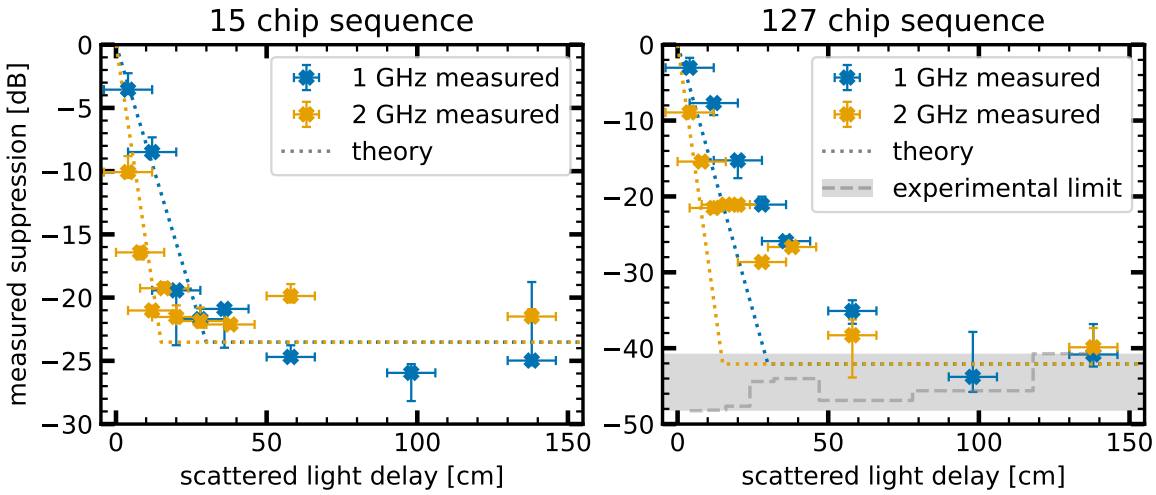

Figure 8.7: Plots showing the measured suppression depending on the scattered light delay relative to the interferometer arms. On the left the suppression reached with the 15 chips long sequence at $f_{\mathrm{PRN}} = 1\,\mathrm{GHz}$ and $f_{\mathrm{PRN}} = 2\,\mathrm{GHz}$. On the right the same measurement for a 127 chips long sequence, again at the same PRN frequencies. For the shorter sequence, the data points follow the theoretical estimate for both frequencies with some small outliers. For the longer sequence a washing out of the curve compared to the sharp estimate can be observed for both frequencies. The maximum suppression is therefore only reached for longer delays than the expected length of one chip.

Even though the two arms of the Michelson in the original setup were still matched well enough to be relatively unaffected by the PRN modulation (see also Figure 8.13), the setup allowed only for measurements with an arbitrary scattered light delay outside the remaining coherence. The reason for this was the delay line used originally to scan the scattered light delay, which was not precise enough anymore for these higher PRN frequencies. Thus, Figure 8.7 shows measurements comparing the remaining coherence length between 1 GHz and 2 GHz PRN frequency. The same measurements at higher frequencies, taken in the revised setup, are shown in Figure 8.8.

Similar to the results at 1 GHz modulation frequency, the shorter sequence (15 chips) shown on the left of Figure 8.7 again followed the theoretical estimate quite closely and leveled off after one chip. This now corresponded to a shorter delay of only around 15 cm for this higher PRN frequency. However, the achieved suppression was slightly less than at 1 GHz. The same similarities could be observed for the longer sequence of 127 chips length shown on the right of Figure 8.7. While the coherence decreased faster in the beginning compared to the measurement at 1 GHz, it also took more than the length of one chip to approach the theoretical estimate. For two data points close to the length of one chip the suppression even stagnated around −21 dB (not shown in the figure) before the suppression increased again for the next data point. After another outlier around 40 cm, the sequence approached the estimate at a delay close to 60 cm or around 4 chips. The reason for measurements exceeding the theoretical estimate is again not fully understood

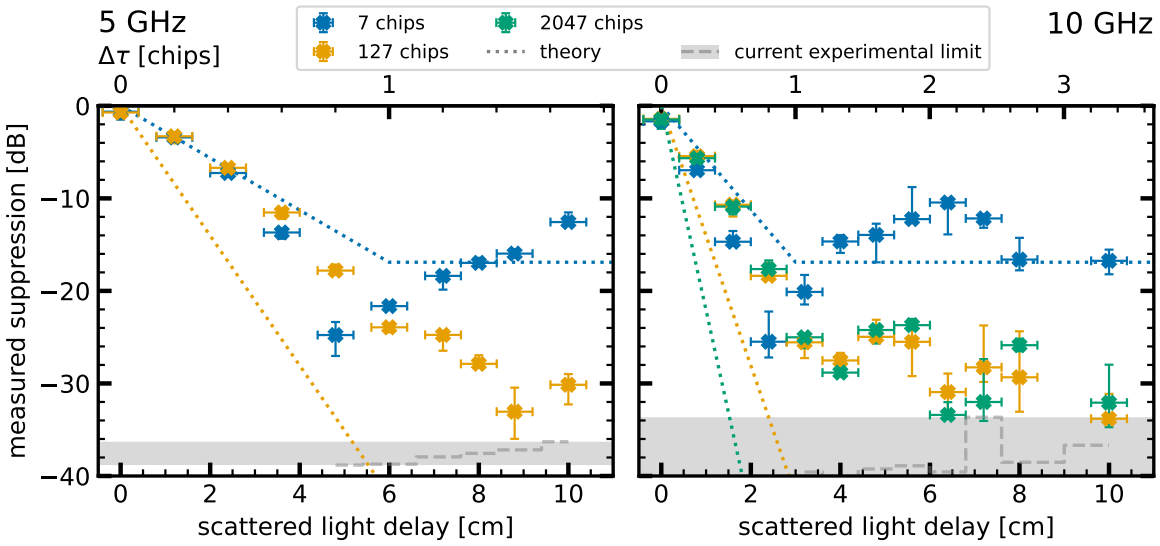

Figure 8.8: Measurements showing the dependence of reached suppression on the relative delay of the scattered light for $f_{\mathrm{PRN}} = 5\,\mathrm{GHz}$ (left) and $f_{\mathrm{PRN}} = 10\,\mathrm{GHz}$ (right) and several different sequence length at each frequency. At 5 GHz PRN frequency on the left, the 7 and 127 chips long sequences are shown, with the latter showing a steady but slower increase in suppression for longer delays. It comes close to the experimental limit but the maximum achievable delay of less than two chips was not enough to reach it. The shorter 7 chips sequence loosely follows the prediction in the beginning before exceeding it for some data points around the length of one chip*. Afterwards the suppression decreases towards the longest achievable delay. On the right side in the data taken at 10 GHz PRN frequency, the 7 chips long sequence shows similar behavior but starts following the theoretical estimate for the two delays longer than 2.5 chips. In addition to the 127 chips long sequence, the 2047 chips long one is also shown. Both exhibit a steady but slower than expected increase in suppression, reaching the experimental limit after a delay of two to three chip-lengths.

*Figure with a theoretical estimate corrected post submission added in Appendix.

but might be attributed to limitations in the complexity of the estimate itself.

Figure 8.8 shows the measured suppression depending on the scatter delay for 5 GHz and 10 GHz PRN frequency in the revised setup with the new delay-line. On the left, side the suppression of the 7 and 127 chips long sequences are plotted for $f_{\mathrm{PRN}} = 5\,\mathrm{GHz}$. Due to the limited range of the translation stage, the maximum reachable delay in the revised setup for this PRN frequency was only close to two chips. Thus, especially the behavior of the longer sequence could not be fully investigated at long delays. Its suppression capability again lacked behind the theoretical estimate. In the observable range, the suppression steadily increased but at a slower rate than predicted. Towards the maximum delay, a flattening of this increase might be observable, however, more data points would be needed to see a clear trend at longer delays. Especially for the longest realizable delay of 10 cm, the suppression was less than predicted and generally only exceeded 30 dB for the delays longer than 8 cm or around 1.5 chips. The shorter 7 chips long sequences behaved somewhat oddly starting shortly before a delay of one chip. While the first three data

points followed the prediction nicely, the reached suppression then increased faster and further than predicted. However, after it reached a maximum of about 25 dB – around 7 dB better than the prediction[36] – close to a delay of 5 cm, a steady weakening of the suppression towards longer delays was observed.

The results for the measurements at $f_{\mathrm{PRN}} = 10\,\mathrm{GHz}$ showed a similar pattern, however, due to the reduced chip-length, at this PRN frequency a delay of more than three chips was realizable. The behavior of the shortest 7 chips long sequence is very similar to the 5 GHz measurement, but now longer delays could be investigated. Here the suppression increased again before following the theoretical prediction after around 2.5 chip-lengths. The longer 127 chips long sequence, together with the here additionally measured longest 2047 chips long sequence, also showed a similar steady increase in suppression with increasing scatter delay. However, this was again less steep than predicted. For delays longer than 4 cm, or a little over one chip-length, the suppression started to increase slower and fluctuated before it approached the experimental limit at around 34 dB for both sequences at a delay of 10 cm. Already for a delay of around 6 cm or two chips, where the longest sequence reached its best suppression, both sequences also approached this experimental limit. The deficit in suppression of the data points in between seemed to have been caused by instabilities in the experiment. This is indicated as the error range of all but one of them puts them reasonably within the trend towards the experimental limit. Additional data taken with reduced scattered light coupling due to the use of an optic with lower reflectivity in preparation for a power-recycling setup can be found in the Appendix.

The dependency of the suppression on the sequence length for PRN frequencies up to 5 GHz recorded in the original Michelson setup is shown in Figure 8.9 on the left side. Here again, the suppression at 2 GHz behaved similar to the data at 1 GHz. However, the shortest sequence (7 chips) now performed worse compared to the other PRN frequencies. The formerly problematic 63 chips long sequence on the other hand performed better but still not as expected at 2 GHz. It did, however, perform almost as anticipated for $f_{\mathrm{PRN}} = 5\,\mathrm{GHz}$. In the 2 GHz measurements, two more outlier at a sequence length of 511 and 2047 chips should be noted. No definitive reason is known for the underperformance of these two sequences, but it is noteworthy that the 511 chips sequence already showed performance problems at 1 GHz. These could finally be counteracted with repeated optimization of the PRN modulation for those measurements. Further, as discussed in the previous chapter (see Sec. 7.2.2) with increasing length of the used sequence, the opti-

[36] In further considerations after submission of this thesis, it became apparent that the here used theoretical estimate was oversimplified and missing a crucial feature caused by the zero-crossing of the ACF close to the length of one chip. When taking this into account, the data points follow that estimate well if a static offset of 2 mm is added to the base length of the physical straylight path. Such an offset can be reasonably attributed to a systematic error in the calibration of the zero-delay point. An updated plot with the corrected estimate is used in the submitted publication (10.48550/arXiv.2508.00503) and provided in the Appendix.

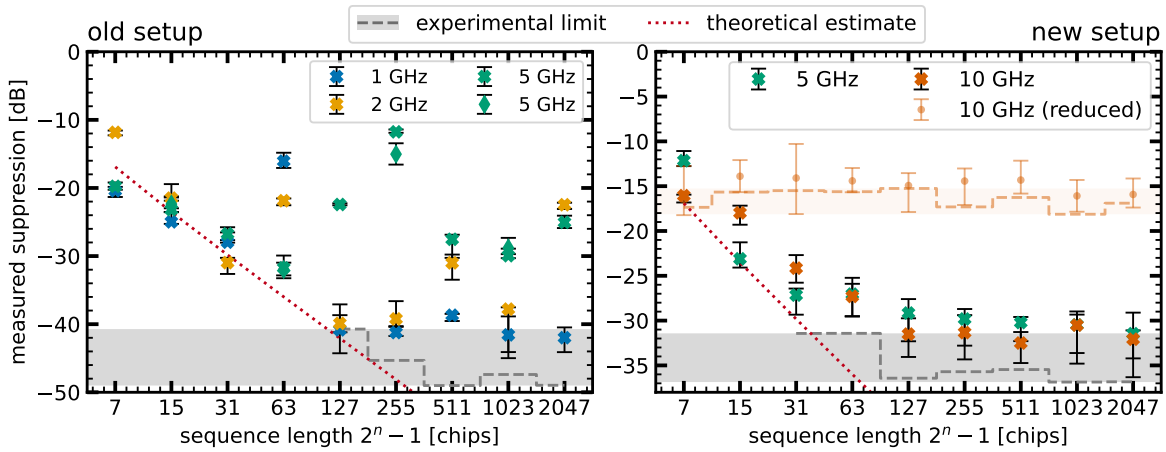

Figure 8.9: Measured suppression for different sequence length at different frequencies. Data for the left plot was taken in the first experimental setup described in Sec. 8.1.1. The data for the right plot was taken in the setup optimized for higher PRN-frequencies described in this section. For the measurements using a PRN frequency of $f_{\mathrm{PRN}} = 5\,\mathrm{GHz}$ in the first setup, data was recorded as time-series (crosses) and spectrum analyzer-traces (diamonds), for all other frequencies, data was recorded as time-series. On the right, in addition to the data taken with maximized scattered light coupling, a measurement at 10 GHz PRN frequency and reduced scattered light is also shown. Data taken in the first setup shows some outliers and weaker suppression at $f_{\mathrm{PRN}} = 5\,\mathrm{GHz}$; these discrepancies are not present in the data shown for the revised setup on the right. Even though the scattered light is not fully suppressed, the values approach either the theoretical estimate or experimental limit in almost all cases. The data with weaker scattered light shows consistently close to full suppression, although on a lower level of only around 15 dB compared to the slightly above 30 dB for the stronger straylight.

mization of the modulation parameter becomes more difficult.

For the higher PRN frequency of 5 GHz, all data points up to the 63 chips long sequence followed the theoretical estimate. Notably, here the 63 chips long sequence performed almost as expected at this frequency. All longer sequences showed deficits in the suppression they reached. The longest 511, 1027 and 2047 chips long sequences reached between 25 and 30 dB suppression, which coincides roughly with the level the longest sequence reached at 2 GHz. Interestingly, at 5 GHz modulation frequency, the 127 chips long and the 255 chips long sequences underperform noticeably by only reaching around 20 dB and 10 dB of suppression respectively.

The length dependency of the reached suppression for 5 GHz and 10 GHz PRN frequency measured in the previously described revised setup (Figure 8.6) is shown on the right side of Figure 8.9. Especially for a PRN frequency of 10 GHz, the more precise fine-adjustment ability of the arm lengths in this setup was needed. At 10 GHz PRN frequency specifically for the matching of the two Michelson arms (see also Figure 8.13), but also for the scattered light delay adjustment at both PRN frequencies. In general, the results followed the expected shape, notably with no obvious outlier at any specific sequence length. However, the performance was slightly worse than at the lower PRN frequencies as

the suppression stayed about 4 dB above both the theoretical prediction and experimental limit, with only a few exceptions. The shorter sequences often reached or approached the theoretical estimate, even though showing some instability through their errors. However, for the three shortest sequences this was always just for either 5 GHz or 10 GHz but never for both. Only the 63 chips and longer sequences performed mostly similar at both frequencies, with all longer ones approaching the experimental limit. For comparison, data taken at 10 GHz with lower scattered light coupling using a less reflective optic is also shown in Figure 8.9. For this case, the suppression always approached the lower experimental limit, with some sequences like the 127 chips long one fully suppressing the injected straylight. In both setups, some instability in the experiment concerning the straylight creation and modulation stability are apparent.

Generally, the noise-floor was higher in the setup used for the measurements at 5 and 10 GHz limiting the maximum achievable suppression by around 10 dB compared to the setup used before. There are two suspected reasons for this, one being the power-imbalance due to removing significant power (around 30 %) only from one arm for the scattered light coupling. The other one being the stability of the used PZT delay-line. While the latter is less likely, it cannot be excluded. The former can and should be checked by adding the second low-reflectivity mirror back into the other arm.

Discussion

In all data shown in Figure 8.7 and 8.8 it can be observed that longer delays are needed to reach full suppression and this is approached asymptotically compared to the expected sharp triangular shape of the remaining coherence width. The probable cause for this is the limited bandwidth of the PRN signal leading to a smoothed and washed out shape instead of perfectly rectangular PRN signal and thus a degradation of the auto-correlation function (ACF). This was also observed for $f_{\mathrm{PRN}} = 1\,\mathrm{GHz}$ and current data suggests it is similarly present at all investigated PRN frequencies as shown in Figure 8.10. Nevertheless, it might become more prominent and thus more problematic at even higher modulation frequencies. Improvements and reduction of needed cabling for connecting the PRN generator to the EOM driver could certainly reduce these negative impacts, as well as more refined electronics for transmitting and amplifying the signal. These deficiencies certainly limit the effectiveness of *tunable coherence* at relative delays close to the chip-length d_{chip}. They do not necessarily explain, however, the lower achieved suppression measured in some data at longer delays shown in Figure 8.9a. Overall, most data at long delays shows suppression reaching the theoretical estimate or experimental limitations, however, some sequences with more than 500 chips are outlier to this in the first setup. In general, as discussed in Sec. 7.2.2, without the stabilization and control of the PRN modulation's depth, each measurement can be negatively influenced by im-

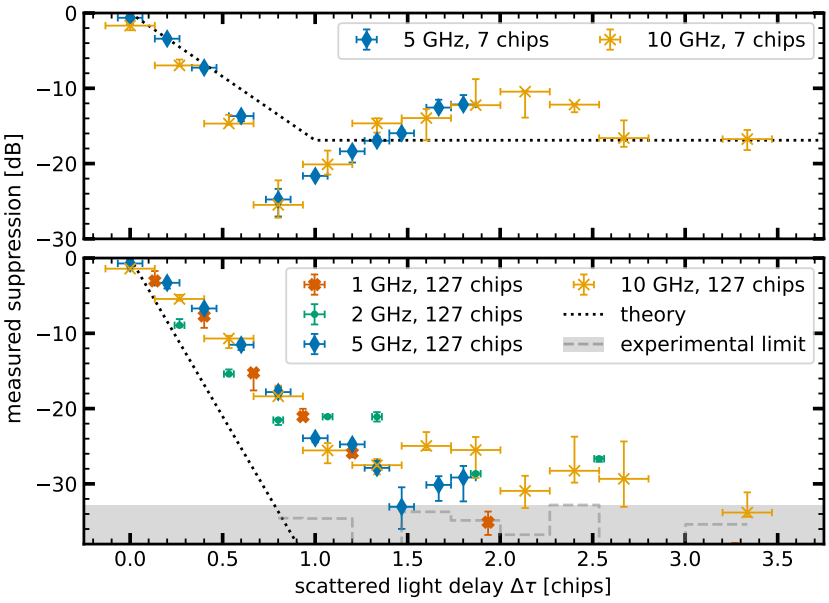

Figure 8.10: Plots showing the measured scattered light suppression depending on its relative delay in length of the chips d_{chip} forming the PRN sequence. In the upper part for the 7 chips long sequence at 5 and 10 GHz PRN frequency, in the lower part for the 127 chips long sequence at $1, 2, 5$ and 10 GHz PRN frequency. All sequences show a similar behavior.*

*Figure corrected post submission added in Appendix.

perfections arising from drifts or sub-optimal manual adjustment of it. This is especially critical for the longer sequences or at high suppression levels as here the sensitivity to such imperfections is highest. Most data at $f_{\text{PRN}} = 1\,\text{GHz}$ was taken several times with optimizations in between or repeated with more fine-tuning of parameters like the modulation depth. For data at higher PRN frequencies, this was only done to a limited degree due to necessary changes in the setup and complications in the laboratory. It is therefore reasonable to assume that the suppression reached with the three longest sequences at higher frequencies could be optimized. In further studies, it should also be investigated why the short sequences (7 and 15 chips) are surpassing the prediction repeatedly and if this can be exploited consistently. No probable cause could be determined yet, so a first step would be identifying the reason for this phenomenon.

Most deficits in the measurements can be attributed to imperfections in the PRN modulation and limits in the ability to inject strong scattered light tones consistently. However, the underperformance of the 63 chips long sequence at lower modulation frequencies and the next two longer sequences at 5 GHz modulation frequency seem to have a different cause. It was verified that all sequences were correct and they were the same regardless of the value for f_{PRN}, thus the consistent underperformance raises questions. Further, the distribution of the occurrences between sequence length and PRN frequencies could hint to an unknown ghostbeam in the setup. If such a beam had a delay close to the recoherence lengths of the affected sequences, it could limit the reached suppression. This is even further supported by the fact that in the revised setup, the same limitations could not be seen for the 5 GHz measurement.

Thus, by converting the length in chips of the sequences to their recoherence lengths d_{coh}, it might be possible to get a hint at which relative delay such straylight could occur.

However, with the available data this is very speculative as many parameters like the exact multiple of d_{coh} are unknown. Further, a likely looking physical path length of around 12.5 m could not be associated with any relevant feature of the setup at this point. With an easily adjustable sequence length in smaller steps than the almost doubling or halving in the present implementation and additional fine tuning by detuning the PRN frequency, one could however try to narrow down this length and possibly identify the source.

8.2 Sagnac topology

Parallel to the demonstrations in Michelson topologies, investigations of *tunable coherence* in Sagnac topologies, more precisely a Sagnac Speed Meter (SSM), were done as part of a supervised Master's project. These experiments were done by Leonie Eggers and detailed results can be found in her Master's Thesis [153]. The accomplishing publication Eggers et al. [25] is summarized in this section. The following text thus closely follows the publication[37] , with some rearrangement and addition of context where applicable done for the adaption into this thesis.

Difference to the Michelson topology

For future GW observatories, SSMs are a possible alternative topology [166–168] as they offer advantages for quantum noise reduction due to speed being a quantum non-demolition observable [166]. However, among other things, their bigger footprint and need for additional suspensions make their implementation more challenging. The Sagnac topology is also used in e.g. gyroscopes [169–171] and in more general in instruments aiming for measuring speed or rotation. In all these applications, it suffers in the same way from scattered light noise as the Michelson topology. Additionally, as it features two counter-propagating beams, it is also affected by light scattering from one propagation direction into the other. This, often referred to as back-scatter [172, 173], introduces even more phase noise and a power imbalance and is especially problematic in associated ring resonators [174–177]. Currently, this impact is reduced with post-processing techniques but no general solution exists [178, 179]. Especially baffles cannot be employed to solve this issue (see also Sec. 3.2.1.a). As it is still a major hurdle for applications of SSMs in e.g. GWDs, investigating *tunable coherence* as a possible solution is of great interest.
In contrast to a Michelson topology, in a Sagnac topology both clockwise $\tau_{+\mathrm{c}}$ and counter-clockwise $\tau_{-\mathrm{c}}$ propagating beams are inherently length matched. However, as the asymmetric port is also inherently dark, a balanced-homodyne-detector (BHD) is used for the

[37] I am second and corresponding author for this publication; the experimental work was done by L. Eggers under my supervision and the draft co-authored by us. The version which parts of this chapter closely follow was in large parts refined by me from the initial draft.

readout. This means that now the local oscillator (LO) needs to be delay-matched to the interferometer beam (see Sec. 5.3). One option is the use of the symmetric port as LO, as per default all light leaves through this output port back towards the laser. This is called "co-moving LO" and has the benefit that the light already traveled nearly the same total path as the other, asymmetric output. The other commonly used approach is to pick off the light for the LO before the interferometer, the "pick-off LO", as shown in Figure 8.11. The delay-matching for this is more challenging due to the bigger difference in the optical paths. Here, a heterodyne demodulation with a second PRN modulated laser as used in de Vine et al. [146, 147] could be an alternative option. Simulations from the thesis of Leonie Eggers [153] indicated that the choice of LO described before should not influence the suppression of scattered light in the readout. However, experimental data presented in the thesis showed limits in the reached suppression, which might have been caused by the choice of using a co-moving LO. This choice of LO potentially allows scattered light to interfere with itself by traveling into the readout via the two matched paths respectively. Thus, the more reliable approach is to use a pick-off LO as this way, any matched paths for scattered light from inside the interferometer to the readout are avoided. The data for the publication Eggers et al. [25] was therefore taken in a setup using a pick-off LO as shown in Figure 8.11. The results and an analytical analysis of backscatter suppression in ring-cavities are summarized in the following.

8.2.1 Experimental demonstration

Sagnac interferometer Setup

The setup used for this experiment consisted of a Sagnac interferometer with a circumference of around 343 cm. A regular Sagnac instead of a zero-area was used for simplicity as any rotational effects picked up by the interferometer would be outside of the measurement bandwidth. The layout of the setup can be found in Figure 8.11.
Similar to the Michelson setup, one of the mirrors inside the interferometer was a PZT mirror to inject a simulated signal into the interferometer at f_{gw}. The location for this in the interferometer could be chosen at random as the positioning did not change the relative delay between the interfering main beams and was therefore not influenced by the PRN modulation. Scattered light noise was created in the same way as in the Michelson setup, with a low-reflectivity mirror ($R \approx 0.2$), a delay-line to change its relative delay τ_{sc} and a PZT mirror to modulate it at f_{sc}. This resulted in a maximal phase error of 0.04 rad introduced by the scattered light (see eq. 3.7). In this setup, it was picked off the counter-clockwise $\tau_{-\mathrm{c}}$ and coupled back into the clockwise $\tau_{+\mathrm{c}}$ propagating beam. The position for this was chosen such that τ_{sc} could be varied between 0 cm and 50 cm, thereby exceeding the length of one chip at $f_{\mathrm{PRN}} = 1$ GHz which is around 30 cm.

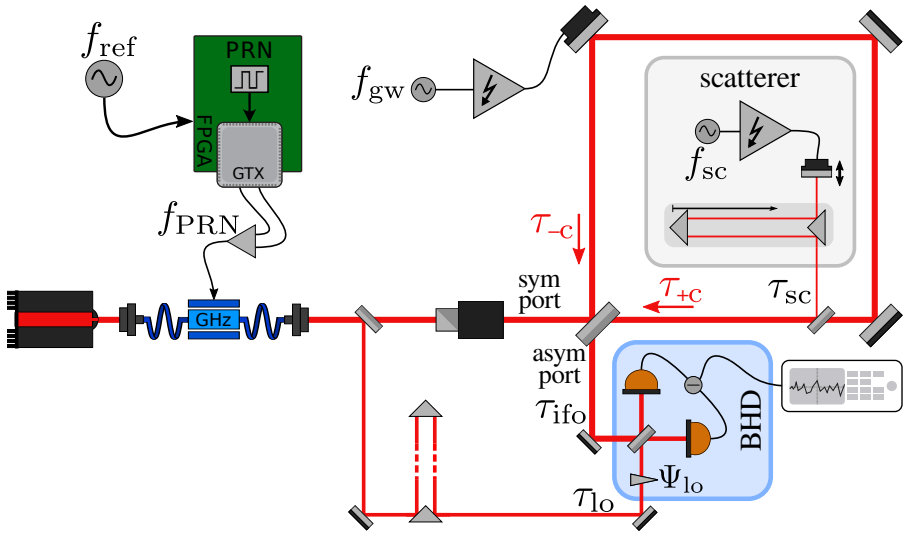

Figure 8.11: Sketch of the experimental setup with the laser being PRN modulated by a fiber-coupled EOM at f_{PRN} and the Sagnac interferometer including the BHD for the readout with the signal recorded as time-series by an oscilloscope. One of the mirrors in the interferometer was used to actuate the phase of the beams and through this inject a signal. Some light from the counter-clockwise propagating beam was reflected out and coupled back into the clockwise propagating beam after being reflected from another actuated mirror and going through an optical delay-line. From this, the scattered light picks up an additional delay τ_{sc} relative to the delays τ_{+c} and τ_{-c}. Adapted from Eggers et al. [25].

To read out the interferometer signal, here a BHD at the asymmetric port was used. For the LO part of the light was picked off before the interferometer and delay matched to the beam coming from the interferometer. Another PZT mirror was used to lock the phase of the LO for the interferometer readout. As in the Michelson experiments, the driving voltage for the EOM was optimized to the suppression of the injected scattered light tone in a live spectrum view.

As before, the control loop for locking the LO phase had a corner frequency of around 5.5 kHz. Thus, at the used frequency of $f_{\mathrm{gw}} = 172.4\,\mathrm{kHz}$ and $f_{\mathrm{sc}} = 170\,\mathrm{kHz}$ the readout was again effectively free-floating and the experiment limited by residual laser amplitude noise. The PZT mirror modulating the scattered light was again additionally ramped through several fringes during each measurement to ensure recording of the strongest possible coupling.

Further, the same laser preparation and modulation setup as for the Michelson interferometer experiment were used, both are described in Chapter 7.

Recording and treatment of data

The data was recorded and analyzed in the same way as for the Michelson interferometer experiments described before. However, as a decrease in signal amplitude was observed (see Figure 8.13) when using the PRN modulation, the reached straylight suppression

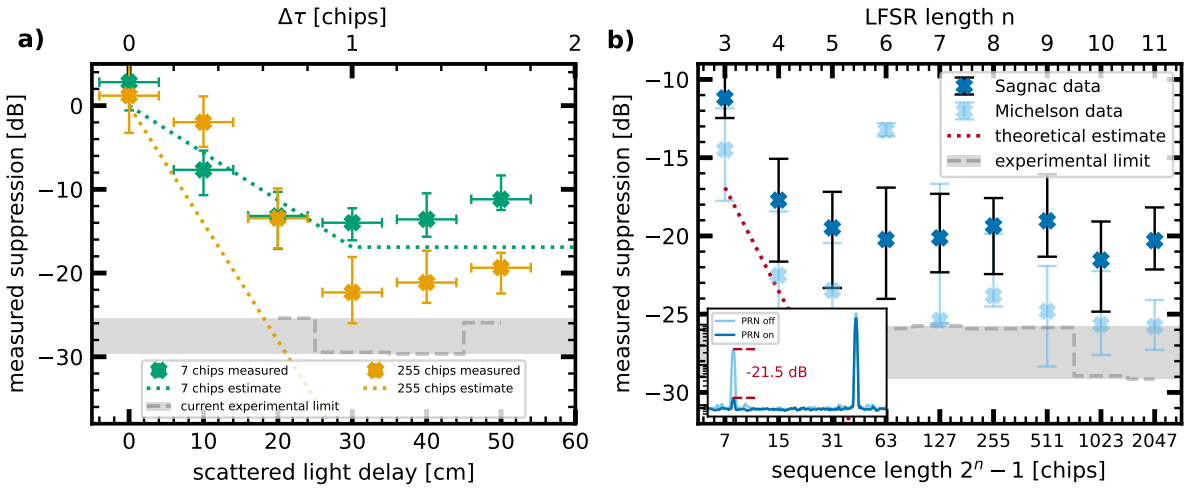

Figure 8.12: Measured suppression of the scattered light depending on a) the delay of the scattered light relative to the interferometer beam and b) the PRN sequence length.
Figure a) shows the achieved scattered light signal suppression using 7 and 255 chip long PRN-sequences for different scattered light delays between 0 cm and 50 cm compared to the theoretical expectation and current experimental limit within the setup.
Figure b) shows the achieved suppression of the scattered light signal compared to the theoretical expectation and the current experimental limit within the setup for PRN sequence lengths between 7 and 2047 chips. For comparison, data from the Michelson setup with reduced scattered light (see Sec. 8.1.1.a) is added. Adapted from Eggers et al. [25], complemented with Michelson data.

needed to be calculated differently. This effect was most likely caused by a slight length mismatch between the LO and signal path[38]. Thus, the measured straylight suppression here was taken as the improvement of signal-to-noise-ratio (SNR) between the two spectra with and without PRN modulation. This SNR was calculated as the ratio between the signal peak at f_{gw} and the scatter peak at f_{sc}. The upper and lower limits were again found by using minimum and maximum values from several spectra calculated for evenly distributed parts of the respective time-series.

Results

Again, two different types of measurements were done: one with changing the length of the PRN sequence and one with changing the relative delay τ_{sc} of the scattered light. The results are shown in Figure 8.12 for both measurements.
For the varied relative delay the results are shown in Figure 8.12a for the 7 and 255 chips long sequences. The shorter sequence followed the estimate quite well and stagnated close to the maximum possible suppression of this sequence for delays exceeding the length of one chip. However, towards and especially for the last data point at 50 cm a slight decrease

[38] The relative tolerance of the optical path mismatch was around three times smaller in this setup compared to the Michelson setup.

in suppression was observed. On the other hand, the longer sequence exhibited a slightly slower increase in suppression stretching towards longer delays than expected. It further leveled off before reaching maximum suppression. A major reason for this lied, however, also in the experimental limitation in creating stronger scattered light tones.
The results for the sequence length dependence of the suppression shown in Figure 8.12b followed but did not reach the expected dependence for the first three sequence lengths. Then the suppression saturated close to 20 dB. The maximal achieved suppression in this setup was 21.5 dB for the 1023 chips long sequence. This early saturation is partly caused by the experimental limitations in the strength of the injected scattered light tone, which was weaker than in the Michelson setup. However, all measurements clearly show some residual scattered light as they did not fully reach the experimentally possible suppression. For comparison, the data taken with reduced scattered light in the Michelson setup (see Sec. 8.1.1) is also shown. It can clearly be seen that for similar levels of scattered light strength, the suppression in the Michelson performed far better, nearly fully suppressing the scattered light. However, the 63 chips long sequence is no outlier in the Sagnac data at $f_{\mathrm{PRN}} = 1\,\mathrm{GHz}$ and reached the same suppression as other sequences. Compared to the Michelson it even is the only sequence that reached higher suppression in the Sagnac setup. This strengthens the assumption that the sequence worked as intended but some unidentified ghostbeam might have limited its performance in the Michelson setup.

Discussion

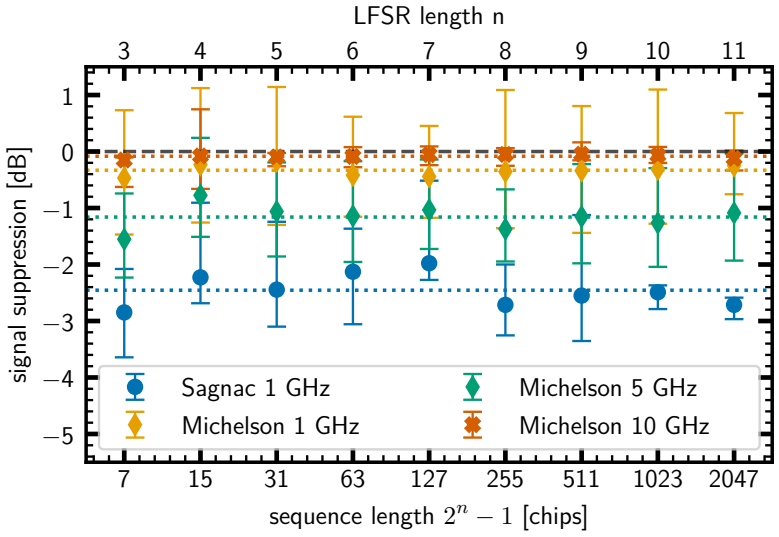

Figure 8.13: Plot showing the suppression caused by *tunable coherence* on the signal directly injected into the different interferometer setups. Shown as blue dots for the Sagnac topology at 1 GHz PRN frequency, as diamond shapes in yellow and green for the Michelson topology without delay-line at 1 and 5 GHz respectively and in orange for the revised Michelson (crosses) at 10 GHz. Dotted lines indicate the mean of each set.

As already mentioned, the Sagnac setup faced some additional suppression of the (GW) signal injected directly into the interferometer of around 2.5 dB as shown in Figure 8.13. This suppression was not observed in the Michelson interferometer. There, only the 5 GHz data set taken in the first setup without a delay-line to fine-tune the length matching

showed some similar but less drastic effects. Especially for the revised Michelson setup using a fine-adjustable delay-line in one of the arms, this effect could be minimized to be almost non-existent. The spurious suppression in this data was most likely caused by other measurement instabilities like fluctuations of the signal strength caused by the PZTs themselves. This is indicated by the observable errors stemming from the fluctuations in measured signal power at 172.4 kHz. Nevertheless, the results obtained in the Sagnac interferometer show that *tunable coherence* can suppress scattered light in a simple SSM topology. However, while encouraging, the data also opens some further questions. It is not fully understood why the residual scattered light cannot be fully suppressed in this setup. While the setup faced the same limitations in the PRN modulation as the previously discussed Michelson setup, there were additional challenges present due to the more complex readout and weaker scattered light coupling. Especially the latter might have caused electronic cross-talk to be present in the high voltage amplifier used to drive the PZTs. The signal strength needed to create a significant scattered light tone was stronger than in the previous setup, reaching levels more prone to induce cross-talk. This was checked for and mostly excluded by blocking the scattered light path, however, as it was also observed to be non-stationary, it can not be fully excluded. Additional simulations were done using ifoTDS (see Sec. 6.3) to verify that the power imbalance resulting from both arms loosing power at the scatter optic but only one gaining around 4 % were not influencing the results negatively.
The limit in injected scattered light prohibits a clear observation of the relation between relative delay of the scattered light and achieved suppression. Nevertheless, a similar trend as in the Michelson topology is visible. Especially for longer sequences, a strong suppression is only reached after longer delays than estimated. For this again the limited bandwidth of the PRN modulation setup is the probable cause.

8.2.2 Backscatter analysis

Additional to the experimental demonstration, suppression of back-scatter was analytically discussed in both the thesis [153] and publication [25]. For the publication, a refined and rewritten version with new sketches for better visualization was created. This version[39] is summarized here by adapting the corresponding part from Eggers et al. [25]:
The effect of *tunable coherence* on back-scatter is analyzed by comparing the delay difference between the two beams in the setup at a point of possible back-scatter. All delays are taken in relation to the PRN sequence, treating integer multiple as the same delay. A complex Sagnac layout consists of the central interferometer and adjacent ring-cavities that share one mirror with the central interferometer each as depicted in Figure 8.14a. It can be seen as a similar layout to the Fabry-Perot Michelson interferometer (FPMI) which

[39] The rewritten form and the new sketches used here were done by me for the publication.

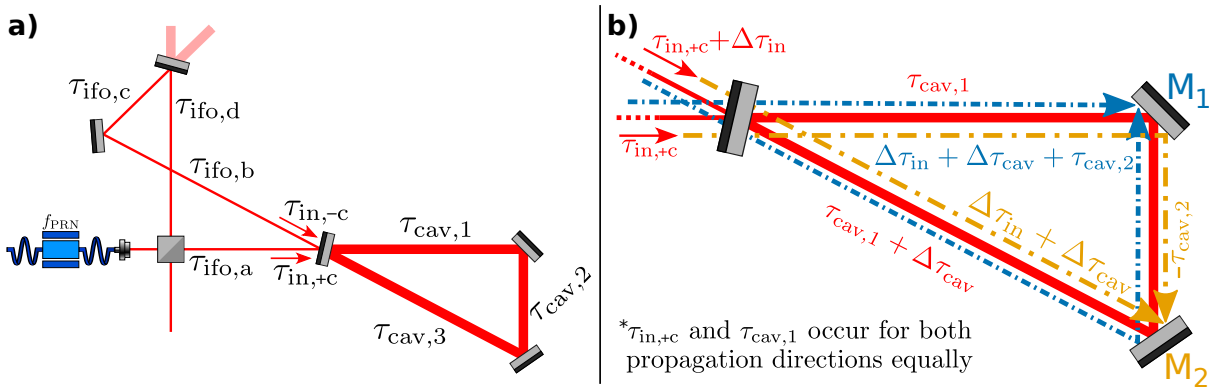

Figure 8.14: Sketches for the analytic back-scatter discussion. In Figure a) the designation for the variables is shown in a Sagnac Speed Meter (SSM) with ring cavities. The second ring cavity (towards the top) is omitted, as it is analogous to the one shown to the right of the central interferometer. In Figure b) the needed relative delay between the two counter-propagating beams at the mirrors in a ring-cavity is visualized. The two counter-propagating beams meeting at mirrors M_1 or M_2 accumulate delays before meeting. The common delays $\tau_{\mathrm{in,c+}}$ and $\tau_{\mathrm{cav,1}}$ are omitted as they cancel when looking at the relative delay between the two beams. In red, the new defined delays taking into account intentional mismatches in the central Sagnac and cavity. For the beam paths meeting at mirror M_1 (indicated in blue), the counterclockwise beam accumulates the additional delays $\Delta\tau_{\mathrm{in}}$ and $\Delta\tau_{\mathrm{cav}}$ in this reference frame plus the delay $\Delta\tau_{\mathrm{cav,2}}$. For the beam paths meeting at mirror M_2 (indicated in yellow), the counterclockwise beam accumulates only the additional delays $\Delta\tau_{\mathrm{in}}$ and $\Delta\tau_{\mathrm{cav}}$, while the clockwise beam travels the delay $-\Delta\tau_{\mathrm{cav,2}}$ as it goes in the opposite direction compared to the beam indicated in blue. Adapted from Eggers et al. [25].

connects two FPCs by an inner Michelson interferometer (see also Sec. 2.3.2), however, transferred to ring-topologies.

Starting the analysis at the ring-cavities, a general requirement for the use of cavities with *tunable coherence* is the matching of the cavity's round-trip length to an integer multiple n of the sequence's recoherence length (see Ch. 6 & 9 and [23, 24]):

$$\sum_i \tau_{cav,i} = n \cdot t_{\mathrm{seq}} = n \cdot d_{\mathrm{coh}}/c. \tag{8.1}$$

Here, $d_{\mathrm{coh}} = c \cdot t_{\mathrm{seq}}$ and $t_{\mathrm{seq}} = n_{\mathrm{chips}}/f_{\mathrm{PRN}}$ were used (see Sec. 5.3). A sketch of the setup with all variables included can be found in Figure 8.14a.

To suppress back-scattered light, the two counter-propagating beams have to be mismatched in the delay between each other at surfaces where back-scatter can occur. For the input mirror this means

$$\tau_{\mathrm{in,+c}} \neq \tau_{\mathrm{in,-c}} \tag{8.2}$$

as a round-trip in the cavity does not change the relative delay due to the matching of the cavity to an integer multiple of the sequence length. From this, it follows for the central Sagnac interferometer

$$\tau_{\mathrm{ifo,a}} \neq \tau_{\mathrm{ifo,b}} + \tau_{\mathrm{ifo,c}} + \tau_{\mathrm{ifo,d}} \tag{8.3}$$

or for the input in the other ring-cavity

$$\tau_{\text{ifo,d}} \neq \tau_{\text{ifo,a}} + \tau_{\text{ifo,b}} + \tau_{\text{ifo,c}}. \tag{8.4}$$

From here on only one ring-cavity (shown in Figure 8.14b) is considered, as the requirements for the other follow analogous. To suppress back-scatter at the two mirrors inside the cavity, the following requirements have to be met:

$$\tau_{\text{in,+c}} + \tau_{\text{cav,1}} \neq \tau_{\text{in,-c}} + \tau_{\text{cav,3}} + \tau_{\text{cav,2}} \tag{8.5}$$

for the mirror M_1 where the blue arrows meet in Figure 8.14b and

$$\tau_{\text{in,-c}} + \tau_{\text{cav,3}} \neq \tau_{\text{in,+c}} + \tau_{\text{cav,1}} + \tau_{\text{cav,2}} \tag{8.6}$$

for the mirror M_2 where the orange arrows meet. The difference in delay at the input mirror can be written as $\tau_{\text{in,-c}} - \tau_{\text{in,+c}} = \Delta\tau_{\text{in}}$ such that

$$\tau_{\text{cav,1}} \neq \Delta\tau_{\text{in}} + \tau_{\text{cav,3}} + \tau_{\text{cav,2}} \tag{8.7a}$$

$$\Delta\tau_{\text{in}} + \tau_{\text{cav,3}} \neq \tau_{\text{cav,1}} + \tau_{\text{cav,2}} \tag{8.7b}$$

By defining the difference between the two cavity beams reaching the input mirror as $\Delta\tau_{\text{cav}} = \tau_{\text{cav,3}} - \tau_{\text{cav,1}}$, where $\Delta\tau_{\text{cav}} = 0$ is possible, this becomes

$$n \cdot t_{\text{seq}} \neq \Delta\tau_{\text{in}} + \Delta\tau_{\text{cav}} + \tau_{\text{cav,2}} \tag{8.8a}$$

$$n \cdot t_{\text{seq}} \neq \Delta\tau_{\text{in}} + \Delta\tau_{\text{cav}} - \tau_{\text{cav,2}} \tag{8.8b}$$

with $n \in \mathbb{N}_0$ as any integer repetition of the sequence is regarded as zero relative delay. Finally, with the total difference in delay $\Delta\tau_{\text{in}} + \Delta\tau_{\text{cav}} = \Delta\tau$, the restriction reduces to

$$n \cdot t_{\text{seq}} \neq \left|\Delta\tau - \tau_{\text{cav,2}}\right|. \tag{8.9}$$

The results of this calculation are visualized in Figure 8.14b in detail by showing the two counter-propagating beams with their difference in relative delay at both mirrors.

Equation 8.9 gives the restriction for the placement of the cavity mirrors to achieve a delay mismatch. When following this, *tunable coherence* can in principle be used to suppress back-scatter. For it to work, the distance $\tau_{\text{cav,2}}$ between the two mirrors of the cavity must not compensate the two intended mismatches; $\Delta\tau_{\text{cav}}$ between the cavity mirrors and $\Delta\tau_{\text{ifo}}$ inside the central Sagnac. With the same approach, restrictions on ring-cavities with more mirrors could be worked out, and on the mirror placement in the central Sagnac interferometer by using a relative input delay of $\Delta\tau_{\text{in}} = 0$ and the delays $\tau_{\text{ifo,i}}$.

Like regular scattered light, back-scatter faces strongly reduced coherence for delay mismatches exceeding the chip-length d_{chip} of the PRN modulation and is thus suppressed. While this also applies to power fluctuations caused by interference of back-scattered light, it does not affect the power imbalance due to loss of power in one propagation direction.

8.3 Conclusion

In this chapter, results were presented that experimentally demonstrate *tunable coherence* in both a Michelson and a Sagnac topology. The focus here was on the Michelson interferometer with more excessive measurements conducted in this setup. Both topologies showed encouraging results with *tunable coherence* being able to suppress scattered light by up to 41 dB at 1 GHz PRN frequency in the Michelson setup. Further, the coherence length was reduced to the cm scale by using PRN frequencies up to 10 GHz. Experimental limitations stemming from the performance deficits of the PZTs at the used measurement frequencies were identified, motivating the move towards a lower measurement bandwidth. Further discussion on this follows in Sec. 10.2.2. Additionally, limitations in the implementation of the PRN modulation were identified to cause a diminishing in performance especially close to the length of a single chip. These observations experimentally support the future implementation of additional control loops for the PRN modulation as suggested in Section 7.2.3. Besides the very promising results obtained in the Michelson setup, the Sagnac interferometer also showed straylight suppression of around 20 dB. Even though the performance was more limited due to less extensive optimizations, it demonstrated the successful use of a BHD with *tunable coherence*. Lastly, an analytical analysis led to the conclusion that *tunable coherence* could be used to suppress backscatter in ring-topologies like ring-cavities used in complex Sagnac layouts.
With this, it becomes time to verify that *tunable coherence* does indeed function with optical cavities in the first place. The experimental verification of this is the topic of the next chapter.

9 Optical Resonators with *Tunable Coherence*

The focus of this chapter is the compatibility of *tunable coherence* with optical resonators or cavities. As described in Chapter 1, the optical layout of gravitational wave detectors (GWDs) contains a multitude of optical cavities for different purposes. These are most prominently used for increasing circulating power in the likes of power-recycling and arm cavities, but other implementations are also used for e.g. mode-cleaning or signal extraction. With the former being operated on resonance, the latter, also called signal-recycling cavity (SRC), is operated off-resonant. All of these cavities must be compatible with *tunable coherence* in order for the concept to work in GWDs.

Normally, optical cavities rely on the high coherence of laser light to function. With the long arms or arm cavities of a stable interferometer being kept resonant, the laser is effectively stabilized, increasing its coherence length. Thus, using phase-modulation to break this coherence would intuitively make cavities non-functional with *tunable coherence*. In this lies the motivation to use PRN modulation which follows a repeating sequence. As discussed in detail in Chapter 5, this introduces a recoherence length d_{coh} at which in the ideal case the modulated light regains coherence with any light traveling a relative delay that is a multiple of this length. Using this, cavities work again as long as their round-trip length matches an integer multiple of this recoherence length of the used sequence.

In this chapter, results using a stand-alone cavity to demonstrate general compatibility of *tunable coherence* with optical resonators are presented. Parts of these results, most measurements done with $f_{\mathrm{PRN}} = 1\,\mathrm{GHz}$, are also part of the publication Voigt et al. [24][40]. Data at higher PRN frequencies is planned to be included in an upcoming publication.

9.1 Proof-of-principle demonstration using a stand-alone cavity

This section contains the results of Voigt et al. [24] and thus consists of the respective parts of the publication, rearranged and complemented with further details where appropriate.

[40] As described, I am first and corresponding author of it, doi: 10.1103/PhysRevLett.134.213802

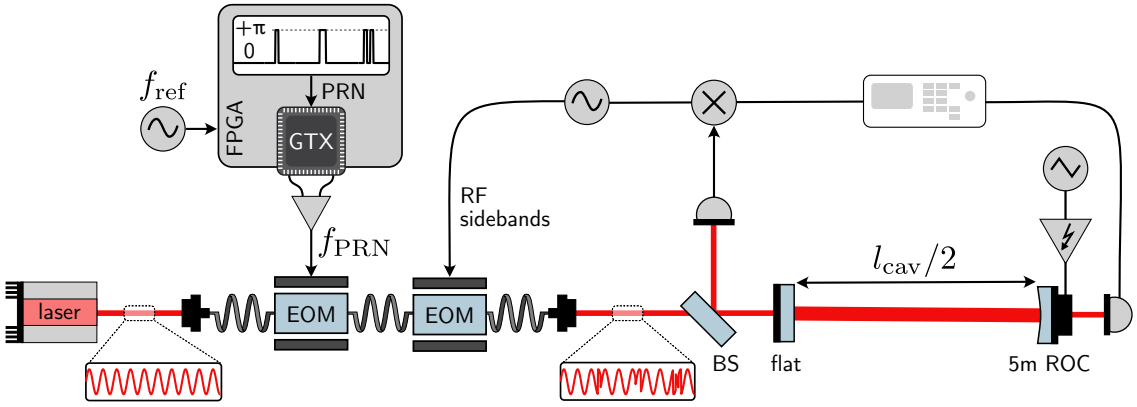

Figure 9.1: The sketch depicts the second experimental setup with the fiber-coupled EOM modulating the PRN sequence onto the laser at f_{PRN} and another EOM for RF sideband generation. Coming from the fiber setup, the light was coupled into a linear optical cavity. The actual cavity was folded, but is depicted here on one axis for simplicity. The round-trip length of the cavity l_{cav} was fixed in each measurement, instead the PRN sequence repetition length was tuned by adjusting the reference clock frequency f_{ref} provided to the evaluation board of the FPGA, which is proportional to the PRN frequency f_{PRN}. Taken from Voigt et al. [24].

Linear cavity setup

The experimental setup to demonstrate compatibility of *tunable coherence* and optical resonators consisted of a folded, linear cavity, as sketched in Figure 9.1. This cavity was microscopically tuned in length with a PZT mirror, the folding mirror. It was set up using two mirrors with 99.5 % power reflectivity as input and end mirrors, the input mirror was flat, the end mirror had a radius of curvature (ROC) of 5 m. With two PDs, the laser power in transmission and reflection was measured. The finesse of the cavity was measured to be 696.074 ± 180.297 while the calculated prediction was 626.7.

The cavities round-trip length, l_{cav}, was chosen to be 4.496 m in order to match the recoherence length of a 15 chips long sequence at 1 GHz PRN frequency. To achieve this, the original idea was to use a PZT delay-line with a retro-reflector on it to fine-tune the round-trip length of the cavity. However, this combination of delay-line and retro-reflector had a beam-height higher than the otherwise used one. Thus, periscopes were used in first attempts to adjust the beam-height such that it matched the one of the delay-line. Due to lacking options for adjusting the periscopes and too many mirrors inside the cavity leading to too much loss, these were unsuccessful. Also mounting the delay line differently to avoid the periscopes did not succeed. As only the retro-reflector and the two needed adjustment mirrors alone added up to almost 10 % one-way loss, using the delay-line was finally scrubbed. In the used setup, the recoherence length was therefore matched to l_{cav} by tuning the PRN frequency. This tuning was done by changing the reference clock frequency supplied to the GTX-transceiver on the FPGA's evaluation board, which is simply proportional to f_{PRN}. However, this is only possible as long as there is but

one optical feature determining the needed length present in the setup. In more complex layouts, one has to fine-tune the macroscopic cavity length to a given d_{coh}, preferably with a low-loss fine-adjustable opto-mechanic to sustain optical contrast. Such layouts are also discussed in Chapter 10. On the other hand, by tuning the PRN frequency, assuming it is well known, it is possible to precisely measure the absolute cavity length, in multiples of d_{coh}. Here, the cavity was resonant for a frequency of $f_{\mathrm{PRN}} = 0.998\,495\,\mathrm{GHz}$, meaning a length deviation of 3.388 mm or 0.15 % from the geometrically measured length.

In addition to the so far described combination, two other cases were investigated. In these and further measurements at higher PRN frequencies, the ratio of recoherence length and cavity length becomes more relevant, thus it will from now on be denoted as

$$\alpha = \frac{l_{\mathrm{cav}}}{d_{\mathrm{coh}}}. \tag{9.1}$$

For one case the cavity length was matched to half the recoherence length, meaning $\alpha = 0.5$. This was achieved by tuning the PRN frequency such that a 31-chip long sequence had a recoherence length of 9.0047 m and thus double the optical cavity length. In the other case the cavity was matched to twice the recoherence length ($\alpha = 2$) to demonstrate the possibility of using any integer multiple relation. For this case a shorter, 7-chip long sequence with a recoherence length around 2.098 m was combined with a shortened cavity of twice the lengths. This was necessary due to limitations in the tuning range of the reference clock frequency supplied to the FPGA's evaluation board as the phase-locked loop (PLL) of the transceiver could not follow a too far detuned reference frequency.

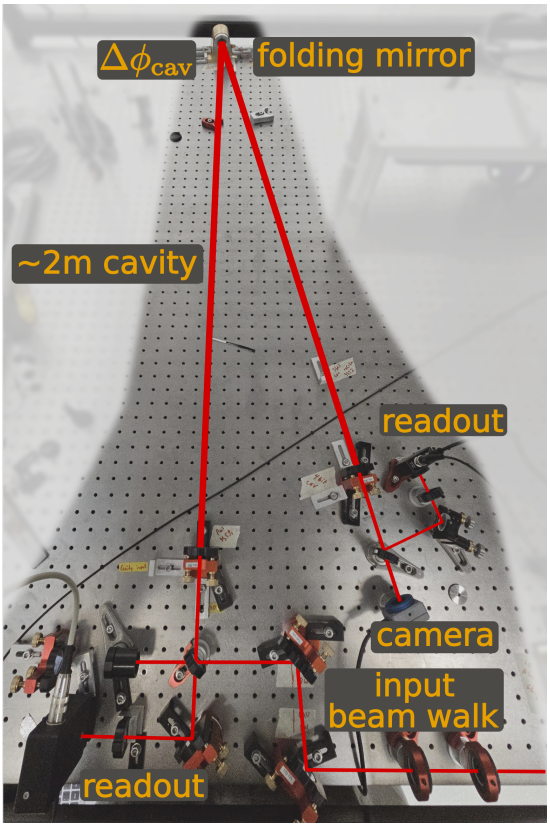

Figure 9.2: Picture of the cavity setup with the input beam walk in the lower center, the readout in reflection to the left of it and in transmission above it. On the top is the folding mirror which can microscopically tune the phase.

For an additional RF phase modulation of the injected light field, a second fiber-coupled EOM[41] with a bandwidth of 150 MHz was introduced. This EOM was driven by a second dedicated EOM driver[42] and was used to implement the Pound-Drever-Hall (PDH) locking scheme. It is depicted in both sketches of the setup shown in Figure 7.1 and Figure 9.1.

[41] iXblue Photonics: NIR-MPX-LN-0.1
[42] iXblue Photonics (exail): DR-VE-0.1-MO

Recording and treatment of data

The first scans over the resonances of the cavities were recorded as oscilloscope traces with and without PRN modulation and then compared. For the step-wise measurements of the PRN frequency detuning, a different method was used to gather more data quicker. For these measurements time-series were recorded containing around 200 scans over the cavity's resonance with a saw-tooth ramp on the PZT mirror. In these time-series, the maximum transmitted power reached in each individual scan was identified and an average taken. This average was then compared with the same measurement done without PRN modulation active. For the continuous measurement of the PRN modulation resonance, the transmitted power and the current frequency of the transceiver-reference clock were recorded synchronously. From these recordings, the transmitted power in relation to PRN frequency detuning could be recovered. This was done in a state in which the cavity was locked to resonance using the PDH-techinque. The PDH error signals which were also used as a demonstration of its compatibility with *tunable coherence* were again recorded as oscilloscope traces.

Direct effects of *tunable coherence* on the cavity

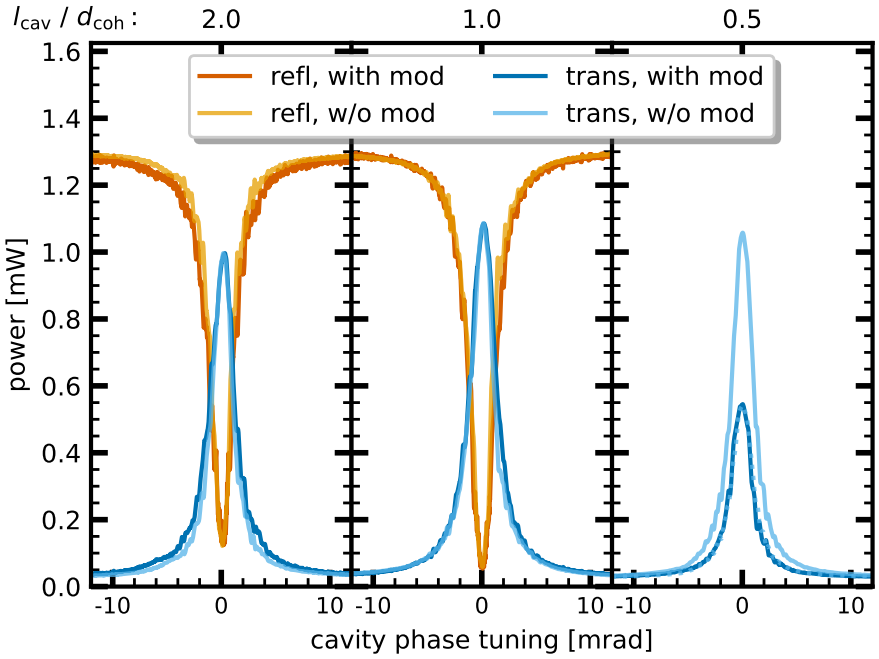

Figure 9.3: Measured cavity transmission and reflection without and with modulation using three different sequence lengths (left: 7 chips, middle: 15 chips, right: 31 chips). The longer 2.252 m cavity allowed for the 15-chips long sequence to be resonant with a real modulation frequency of $f_{\mathrm{PRN}} = 0.998\,495\,\mathrm{GHz}$ and the 31-chips long sequence at $f_{\mathrm{PRN}} = 1.031\,77\,\mathrm{GHz}$. The 7-chips long sequence was resonant in the shorter 2.100 m long cavity at $f_{\mathrm{PRN}} = 0.998\,94\,\mathrm{GHz}$. As this was a physically different cavity, the finesse is slightly worse due to alignment inaccuracies. Adapted from Voigt et al. [24].

The first measurement was a scan over the resonance of the cavity for each case ($\alpha = 0.5, 1, 2$) with and without PRN modulation while recording the power in transmission and reflection. These measurements, with example time-series shown in Figure 9.3, indicated no measurable differences in the resonant behavior for integer relations between the lengths. Only for the half-integer relation, a reduction in transmitted or reflected power to half the nominal value without PRN modulation was observed in the data. This is expected from simulation results as described in Chapter 6.

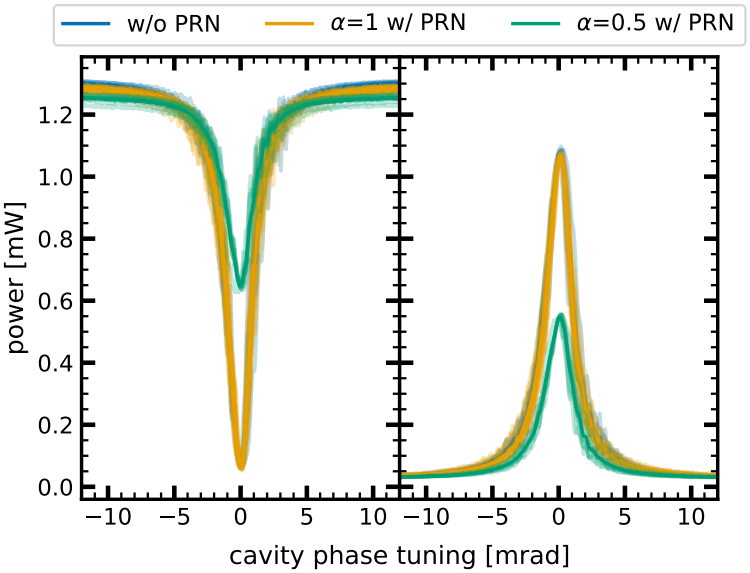

Figure 9.4: Scan over the cavity resonance recorded between 10 and 20 times in reflection (left) and transmission (right) without PRN modulation and with PRN modulation for the cases $\alpha = 1$ and $\alpha = 0.5$. All traces are plotted together with their respective average. For the case $\alpha = 1$ both data nearly perfectly matches the reference without PRN-modulation, for the case $\alpha = 0.5$ both reflected and transmitted power reach only half of it, as expected.

In Figure 9.3 chosen example traces are shown; Figure 9.4 on the other hand shows exemplary for two α-values several traces recorded with and without PRN modulation. The respectively resulting average has no significant deviations caused by the PRN modulation.

9.1.1 Locking cavities while using *tunable coherence*

To investigate the effect of *tunable coherence* on RF-sidebands, this was tested by adding a phase modulation at $f_{\mathrm{PDH}} = 5\,\mathrm{MHz}$. The power recorded in reflection was demodulated to generate the well known Pound-Drever-Hall (PDH) [161, 162][43] error signal. Again the cavity was scanned over its resonance and the PDH error signal characterized for different detunings of the PRN modulation, as shown in Figure 9.5b. As these error signals were again recorded as example traces, Figure 9.5a shows recordings of several traces with and without PRN modulation and how their averages align in the case of the PRN frequency being resonant in the cavity.

These measurements demonstrated that the error signal was again preserved for perfect

[43] An introduction in the technique can be found in [162], the original publication is [161]

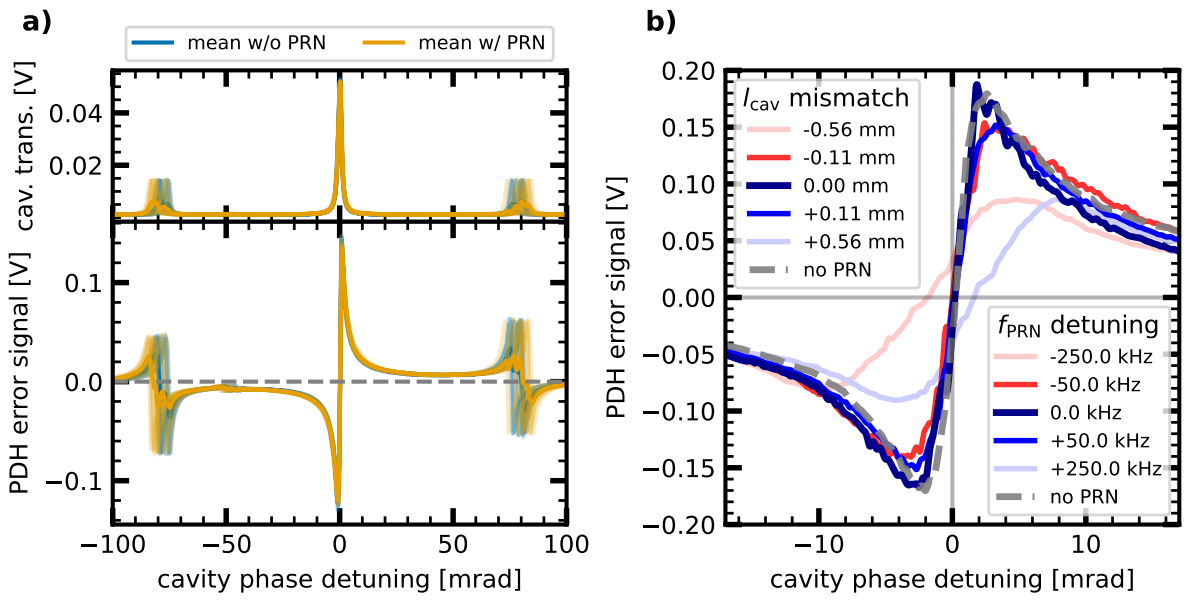

Figure 9.5: The PDH error signal behavior measured in reflection with different detunings of the PRN-frequency f_{PRN} and thus mismatch between round-trip and recoherence length. Figure a) shows several scans and PDH error signals with their average for the matching case and Figure b) shows example error signals recorded for different mismatches.
a) Ten individual recordings of the error signal and cavity transmission with and without PRN modulation each, and their respective resulting average, showing good agreement, especially in the relevant range close to the cavity resonance.
b) PDH error signals measured with a matched, and a just slightly (±50 kHz) detuned PRN sequence showing no meaningful deviation from the case without *tunable coherence*. Only the farther detuned (±250 kHz) PRN modulation deteriorates the error signal significantly. Figure b) taken from Voigt et al. [24]

matching between sequence and cavity. Furthermore, for slight detunings of the lengths neither the zero-crossing, nor the slope of the error signals changed in a meaningful way, indicating general compatibility of PDH locking and *tunable coherence*. Another demonstration of this can also be seen in the measurements done for the continuous PRN frequency detuning scan discussed in Sec. 9.1.2. Only for larger mismatches, a significant deviation making the error signal unusable could be observed. Especially for detunings reaching minimal transmitted power, no usable error signal could be obtained. However, once acquired, a lock did withstand farther detuning as seen in Figure 9.6 where the PRN frequency was detuned by up to 1 MHz from the nominal 1 GHz in a locked cavity.

9.1.2 Introducing a new linewidth with *tunable coherence*

To further investigate the interaction of *tunable coherence* with a cavity, the scan over its microscopic resonance as described earlier was repeated. This time for different detunings of the PRN frequency, equaling length mismatches between cavity and PRN sequence. For the two longer sequences (15 and 31 chips) this measurement was done in steps for several

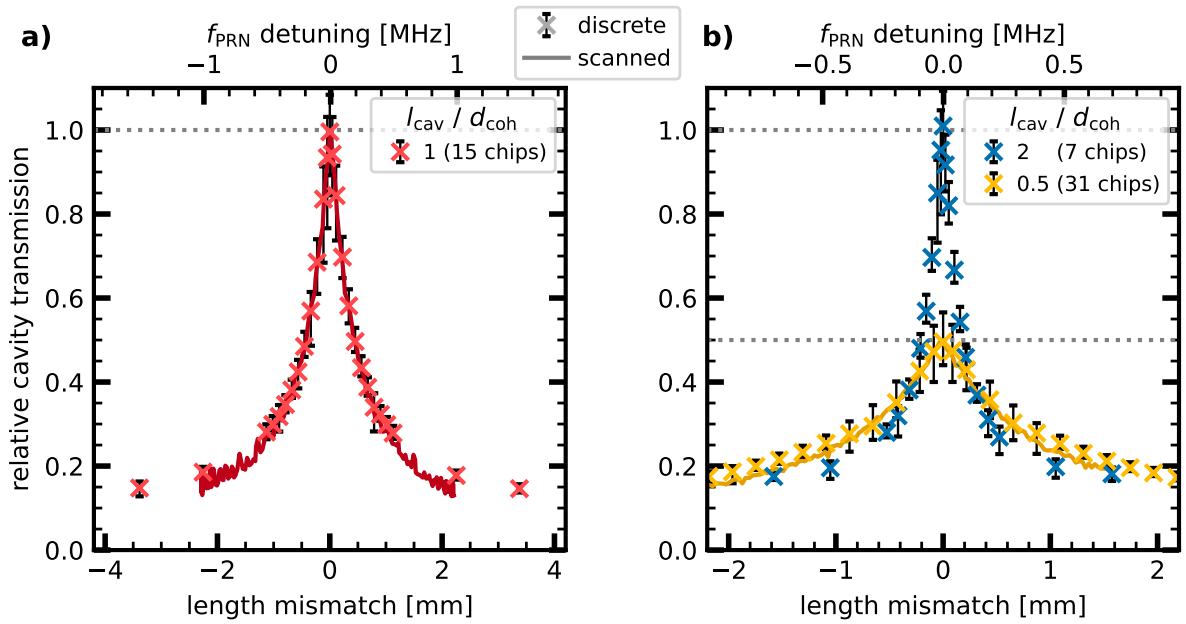

Figure 9.6: Cavity behavior measured with different detunings of the PRN-frequency f_{PRN} and thus mismatch between round-trip and recoherence length. Figure a) shows the relative transmitted power as a measure for power build-up inside the cavity for $\alpha = 1$ with the 15 chips long sequence. Figure b) shows the same measurement for $\alpha = 2$ and $\alpha = 0.5$ with the 7 and 31 chips long sequence respectively.
a) Step-wise detuning and scanning the PRN frequency while the cavity is locked on microscopic resonance show a new resonance depending on macroscopic length matching to the PRN sequence having a FWHM of around 710 µm for 1 GHz PRN modulation and a cavity finesse of around 696. Figure a) taken from Voigt et al. [24].
b) The same measurement for a shorter 7 chips and a longer 31 chips long sequence showing the expected behavior of regaining full transmission for the matched case with a FWHM of around 315 µm when the sequence fits twice in the cavity and only regaining half the transmission with a FWHM around 1162 µm for the sequence having $\alpha = 0.5$.

different detunings and continuous by recording the transmitted power while the PRN frequency was scanned. For the shorter 7 chips long sequence, only the step-wise detuned measurement was conducted as the setup was already altered to the longer cavity once a lock of the cavity could be obtained. With this, the compatibility of *tunable coherence* and PDH locking could also be further demonstrated as now not only an error signal was created but also used to keep the cavity on microscopic resonance. Both measurements are displayed in Figure 9.6a for the case where l_{cav} and d_{coh} were equal ($\alpha = 1$). The two other cases ($\alpha = 0.5$ and $\alpha = 2$) also showed the expected behavior of full resonance regained for $\alpha = 2$ and only half of it for $\alpha = 0.5$. Both are presented in Figure 9.6b.
From this measurement, it was possible to determine a new FWHM for the cavity being resonant depending on its macroscopic length additionally to the microscopic phase tuning. In the case here with 1 GHz modulation in the given cavity, this FWHM lied around 710 ± 86 µm for the 15 chips long sequence. For the same conditions but with the shorter 7 chips long sequence having twice the number of round-trips, the FWHM

was roughly half the previous at $315 \pm 158\,\mu m$. Here, the bigger error results from the discrete measurement instead of the continuous one which was not recorded for this sequence. The 31 chips long sequence reached half the maximum transmission as expected and had a FWHM of around $1162 \pm 60\,\mu m$. This sequence behaved differently due to its half-integer length matching of $\alpha = 0.5$. However, the former indicates a dependency on the PRN frequency f_{PRN} as it determines the remaining coherence length (see eq. 5.4) and also the number of repetitions in the cavity. This suggests a dependency on the sequence length relative to the cavity (α-value) and the cavities finesse due to higher number of round-trips summing up a mismatch. The dependency on f_{PRN} was also observed in the simulation discussed in Chapter 6 and then further investigated in additional measurements discussed in Sec. 9.2. The dependency on finesse or relative sequence length due to their influence on the number of round-trips was so far only speculated. While the finesse of the cavity was not changed in this setup, the influence of the relative sequence length was also investigated in the additional measurements at higher PRN frequencies.

With the introduction of this new FWHM it also becomes apparent that for parasitic beams traveling with round-trips not matching the cavity mode, especially bouncing back from some exterior surface, the resonance is reduced. Thus the remaining coherence length of straylight could be drastically reduced from, in the best case, d_{chip} in a simple interferometer layout to already the mm-scale in a cavity using a PRN frequency of only 1 GHz.

9.2 Effects of higher PRN frequencies

After reprogramming the FPGA, the setup could also be used for demonstrations and measurements at a higher PRN frequency. As the increase in PRN frequency makes the sequence length shorter, all sequences used so far still fit in the same cavity but with higher values for α. The additional frequencies were chosen to be 2 GHz, 5 GHz and 10 GHz thus allowing for values of α up to 22. This highest α-value was achieved with the 7 chips long sequence at $f_{PRN} = 10\,GHz$ now fitting in the same physical cavity as the two longer sequences. With different combinations of the 7 and 15 chips long sequences at the three PRN frequencies several integer values for α were realizable. Additionally, the longest 31 chips long sequence had a half-integer value of $\alpha = 2.5$ at 5 GHz and an integer value of $\alpha = 5$ at 10 GHz. For some, but not all, combinations of sequence length and modulation frequency measurements were again taken in discrete detuning steps additionally to the continuous scan of the PRN frequency with a locked cavity.

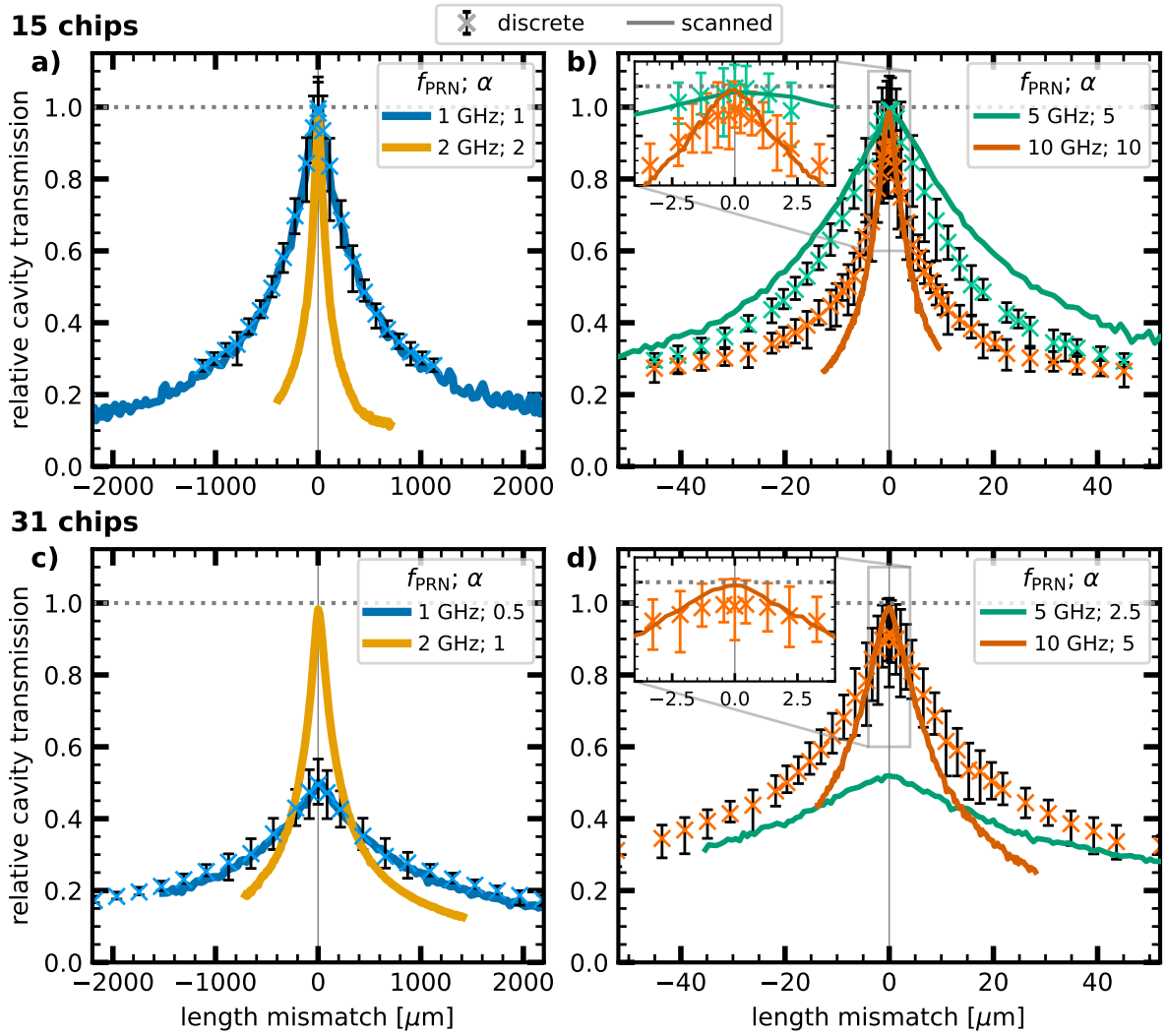

Figure 9.7: Cavity behavior measured with different detunings of the PRN-frequency f_{PRN} and thus mismatch between round-trip and recoherence length. The first row shows data for the 15 chips long sequence at different modulation frequencies, the second row shows the same for the longer 31 chips long sequence. All figures show the relative transmitted power as a measure for power build-up inside the cavity for the different combinations of sequences length and f_{PRN}.
a) Discrete detuning at 1 GHz and scanning the PRN frequency while the cavity is locked on microscopic resonance for the 15 chips sequence at 1 GHz and 2 GHz giving α-values of 1 and 2.
b) The same measurements at 5 GHz and 10 GHz modulation frequency with the same sequence, equaling α-values of 5 and 10. The FWHM is considerably smaller in these measurements and discrete and continuous measurement deviate more for farther detunings.
c) Same measurements as in a) but with the longer 31 chips sequence, again at 1 GHz and 2 GHz PRN frequency resulting in α-values of 0.5 and 1 with the former only reaching 50 % relative transmission as expected.
d) Measurements with the same longer sequence as in Figure c) now at 5 GHz and 10 GHz modulation frequency, giving α-values of 2.5 and 5. Again the former reached only half of the original transmission and the FWHM was considerably smaller than at lower f_{PRN}. The discrete and continuous measurements again deviate more for farther detunings.

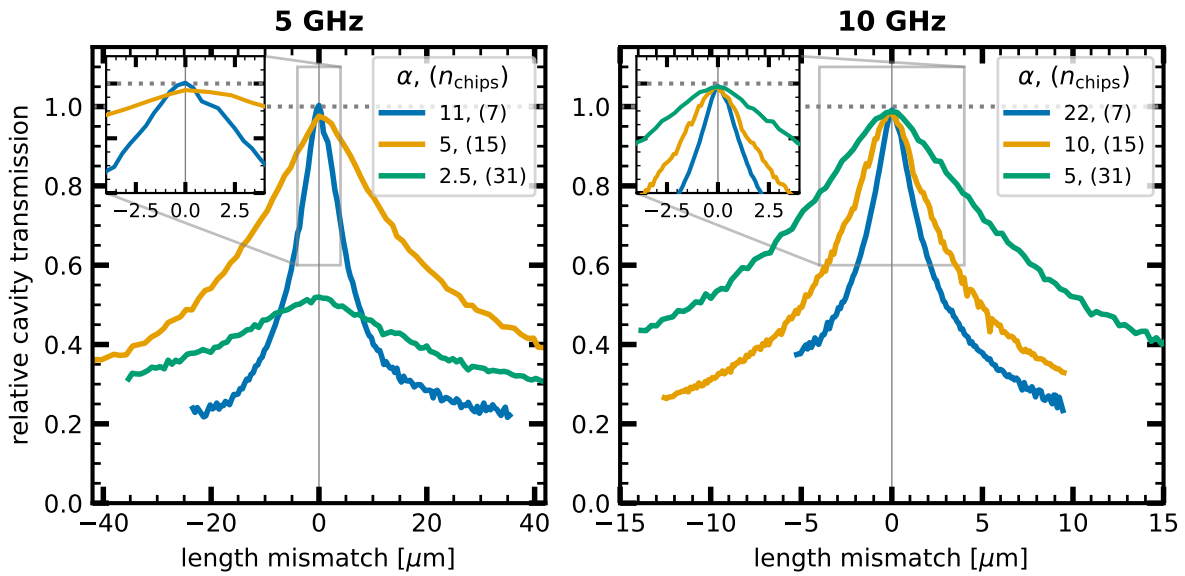

Figure 9.8: Comparison of the FWHM induced by the PRN-modulation at a PRN frequency of 5 GHz (left) and 10 GHz (right). In both cases the 7 chips long sequence is shown in blue, the 15 chips long sequence in yellow and the 31 chips long sequence in green. Depending on the modulation frequency this corresponds to α-values of either 11, 5 and 2.5 for 5 GHz or 22, 10 and 5 for 10 GHz. While at 5 GHz the values for the FWHM are 9.7 µm, 35.7 µm and 54.2 µm, they decrease to 3.9 µm, 7.4 µm and 15.5 µm for 10 GHz. An overview of these and other measured values can also be found in Table 9.1.

Results

Figure 9.7 shows the measured curves for the 15 and 31 chips long sequences at all used PRN frequencies. This gives values for α of 0.5, 1, 2, 2.5, 5 and 10. All of these showed the expected behavior of full transmission on resonance for integer values and half the nominal transmission for half-integer values. The FWHM induced by the PRN modulation narrowed with increasing modulation frequency, which was expected and simulated before (see Chapter 6). Additionally, one can start to observe an influence of the number of sequence repetitions fitting in the cavity, given by α, on the FWHM as well. This is even more clearly observable in Figure 9.8 where the resonance curves are shown for different sequence lengths at a fixed PRN frequency.

When directly comparing the curves for different numbers of repetitions fitting into the given cavity at the same PRN frequency, one can directly observe a narrowing of the FWHM for increasing number of repetitions. This is best shown in the data presented in Figure 9.8, especially on the right for $f_{\mathrm{PRN}} = 10\,\mathrm{GHz}$ and α-values of 5, 10 and 22. The values of the FWHM for all measured combinations of α and f_{PRN} are also summarized in Table 9.1. While the widest FWHM recorded with a integer value for α lies around 710 µm for the before mentioned 1 GHz-measurement, this goes down to only around 4 µm, meaning less than four wavelengths, for the highest α-value of 22 at $f_{\mathrm{PRN}} = 10\,\mathrm{GHz}$.

Table 9.1: FWHM-values calculated from the resonance scans of the PRN modulation at different PRN frequencies with the three sequences of length 7, 15 and 31 chips resulting in α-values between 0.5 and 22.

	FWHM introduced by *tunable coherence*			
α	1 GHz	2 GHz	5 GHz	10 GHz
0.5	$1133.6 \pm 62.8\,\mu m$	-	-	-
1	$709.6 \pm 86.0\,\mu m$	$318.1 \pm 32.2\,\mu m$	-	-
2	$210.2 \pm 157.6\,\mu m$	$156.1 \pm 16.0\,\mu m$	-	-
2.5	-	-	$54.2 \pm 1.4\,\mu m$	-
5	-	-	$35.7 \pm 2.4\,\mu m$	$15.5 \pm 0.6\,\mu m$
10	-	-	-	$7.4 \pm 0.2\,\mu m$
11	-	-	$9.7 \pm 0.8\,\mu m$	-
22	-	-	-	$3.9 \pm 0.2\,\mu m$

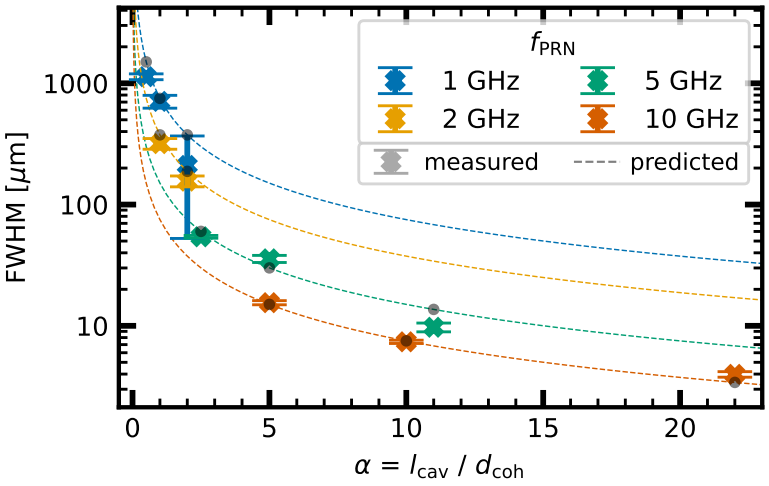

Figure 9.9: Measured FWHMs of the PRN resonance as given in Table 9.1 plotted against the α-value of the corresponding measurement. The PRN frequencies used for reaching these α-values are color-coded. The gray dots represent fitted values using Eq. 9.4 with the finesse $\mathcal{F}$ as a free parameter resulting in a value of $\mathcal{F} = 696$.

Discussion

As the simulations discussed in Chapter 6 already showed, the measurements confirmed a dependence of the FWHM introduced by *tunable coherence* on the remaining coherence length, given by the length of a chip d_{chip} and determined by the PRN frequency f_{PRN}. While the dependence on the finesse can still not be verified with these measurements, its existence follows from the same reasoning as the α-dependency, which can be observed in the data. Figure 9.9 shows the measured FWHMs in relation to the α-values of the corresponding measurement. Using these dependencies as parameter, the FWHM can be described by

$$\text{FWHM}_{\text{PRN}} \propto \frac{d_{\text{chip}}}{\alpha \cdot \mathcal{F}} = \frac{c}{\alpha \cdot f_{\text{PRN}} \cdot \mathcal{F}} \tag{9.2}$$

with $\mathcal{F}$ being the finesse of the cavity and c the speed of light. As $\alpha \propto f_{\text{PRN}}$, this can also be seen as an inverse quadratic dependency on either of these parameters. Thus explaining the shape of the curve seen in Figure 9.9. Using the given description, the data can be fitted to the equation

$$\text{FWHM}_{\text{PRN}}(\alpha, f_{\text{PRN}}, \mathcal{F} = 696) = b \cdot \frac{c}{\alpha \cdot f_{\text{PRN}} \cdot 696} \tag{9.3}$$

where b is the free parameter to be fitted. With this simple approach, the fit results to $b = 1.617 \pm 0.065$ which equals approximately $\pi/2$. Fixing b therefore to this value of $\pi/2$ and fitting the cavities finesse instead, the result is $\mathcal{F} = 696.000 \pm 29.375$ when using the measured finesse of 696.074 ± 180.297 as input. Using the calculated finesse of 626.7 instead, the fit results in $\mathcal{F} = 626.700 \pm 27.377$. It should be mentioned that fits were also tested with exponential dependencies in the form of α^{b1} and f_{PRN}^{b2} with $b1$ and $b2$ as additional fit parameter. However, these resulted in values close to unity with errors on the order of 10^5. Further, while the cavity finesse is fitted with a comparatively small error, it is obvious that the input estimate is kept and similar input values also work. Thus, additional investigations using more data points, also including changes in the finesse, should be completed to verify this relation. Nevertheless, to the current understanding, the FWHM induced by *tunable coherence* can, in good agreement with available data, preliminarily be described by

$$\mathrm{FWHM}_{\mathrm{PRN}}(\alpha, f_{\mathrm{PRN}}, \mathcal{F}) = \frac{\pi}{2} \cdot \frac{c}{\alpha \cdot f_{\mathrm{PRN}} \cdot \mathcal{F}} \,. \tag{9.4}$$

9.3 Conclusion

In this chapter, the compatibility of *tunable coherence* with optical resonators was experimentally demonstrated. First, results were discussed that showed no impact of the PRN modulation on the functionality of a cavity as long as its round-trip length was matched to the recoherence length of the PRN sequence. While these measurements were done at 1 GHz modulation frequency, they were further complemented with measurements at higher PRN frequencies. The used cavity was successfully locked with PRN modulation present using the PDH technique and a new linewidth induced by *tunable coherence* was investigated. This new linewidth is caused by a detuning of the PRN frequency leading to mismatches adding up over several round-trips or repetitions of the sequence. In the current setup, a FWHM of only around 4 µm or four wavelength could be achieved this way, thus significantly reducing the remaining coherence length. After these successful individual demonstrations presented here and in the previous chapter, the next step was to combine interferometer and cavity to investigate a more complex setup closer resembling a GWD. This part is presented in the next chapter.

10 | Complex Topologies with *Tunable Coherence*

The previous chapters 8 and 9 discussed the demonstration of *tunable coherence* in basic interferometer topologies and optical resonators individually. Now it is time to combine the two, so this chapter presents the first results of using *tunable coherence* to suppress scattered light in a power-recycled Michelson interferometer (PRMI). The new setup and its complications are explained, as well as demonstrations showing the functionality of the power-recycling cavity (PRC) and scattered light suppression presented. Additionally, it is discussed how the use of arm-cavities in a Fabry-Perot Michelson interferometer (FPMI) would interact with *tunable coherence*. Finally, possible next experimental steps using the current setup are outlined.

10.1 Power-recycled Michelson interferometer

To use *tunable coherence* in a PRMI, the PRN sequence needs to fit in the PRC that is created by adding a power-recycling mirror (PRM) between the Faraday rotator (FR) and the central beam splitter (BS) of the interferometer. The round-trip length of this cavity is given by twice the arm length of the interferometer plus twice the distance between the BS and PRM. As before, the two arms of the interferometer need to be matched in length to avoid any negative impacts of *tunable coherence*. As a result of this length constraint and the available space on the optical table, the demonstration of *tunable coherence* in a PRMI was planned to be done at higher PRN frequencies than 1 GHz. Using higher frequencies and thus shortening the cavity's length was also intended to increase the stability of the setup. The highest possible PRN frequency using the current modulation generation was 10 GHz and a little over 1 m distance could easily be realized on the table. With this, the longest PRN sequence usable was the 63 chips long one with a recoherence length of around 1.888 m at 10 GHz.

10.1.1 PRMI setup

As described in the previous chapter, the length of a PRN sequence can be tuned to a degree by adjusting the reference clock supplied to the FPGA's evaluation board. Thus,

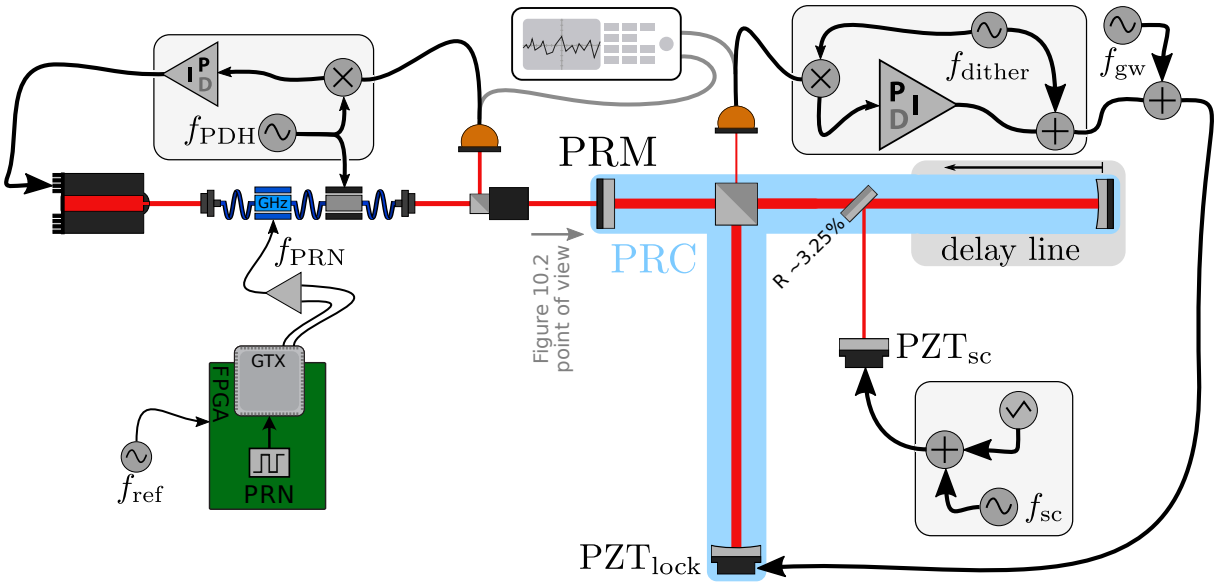

Figure 10.1: Sketch showing the PRMI setup used to demonstrate *tunable coherence*. A piezo-driven delay line in one of the interferometer arms was used to match it in length to the other arm. The same arm contained a scatter window to demonstrate scattered light suppression.

the exact length of the cavity was chosen to be 0.922 m such that shorter sequences at lower modulation frequencies would also lie within the tuning range. The revised setup discussed in Section 8.1.2, from which the PRMI was iterated, already contained a PZT optical delay-line in one of the arms of the Michelson interferometer. As it was used to demonstrate *tunable coherence* at up to 10 GHz, described in Chapter 8, the interferometer arms were already precisely matched to a length of 82.2 cm. However, placing the interferometer inside the cavity, increases the needed accuracy for the length matching. With the given arm length, the PRM thus needed to be placed 10 cm in front of the central BS. The new PRMI setup is sketched in Figure 10.1 and the lengths of the used PRN sequences at the used frequencies summarized in Table 10.1. A picture of the PRMI can be found in Figure 10.2. In order to match the laser mode coming out of optical fiber to the mode of the cavity, two lenses were used for this mode-matching.[44] For the end-mirrors of both arms a reflectivity of 99.5 % with a ROC of 2 m was chosen. The PRM mirror was chosen to have a reflectivity of only 90 % due to expected losses inside the interferometer. Most prominent here was the scatter window (R≈3.25 %) inserted in one arm for the scattered light demonstration. The round-trip loss in this arm was measured to be around 6 %. The PRM was also chosen to be flat to simplify mode-matching and alignment. Only one of the interferometer arms was microscopically tunable with a PZT mirror, the other arm could only be adjusted macroscopically with the PZT delay-line.

[44] The setup was actually done the opposite way around, the mode matching determined the position of the PRM and the BS was already at a given position, which was kept in order to reuse the readout optics without needing readjustments. From this, the arm length was determined and used in the 10 GHz demonstration setup described in Chapter 8.

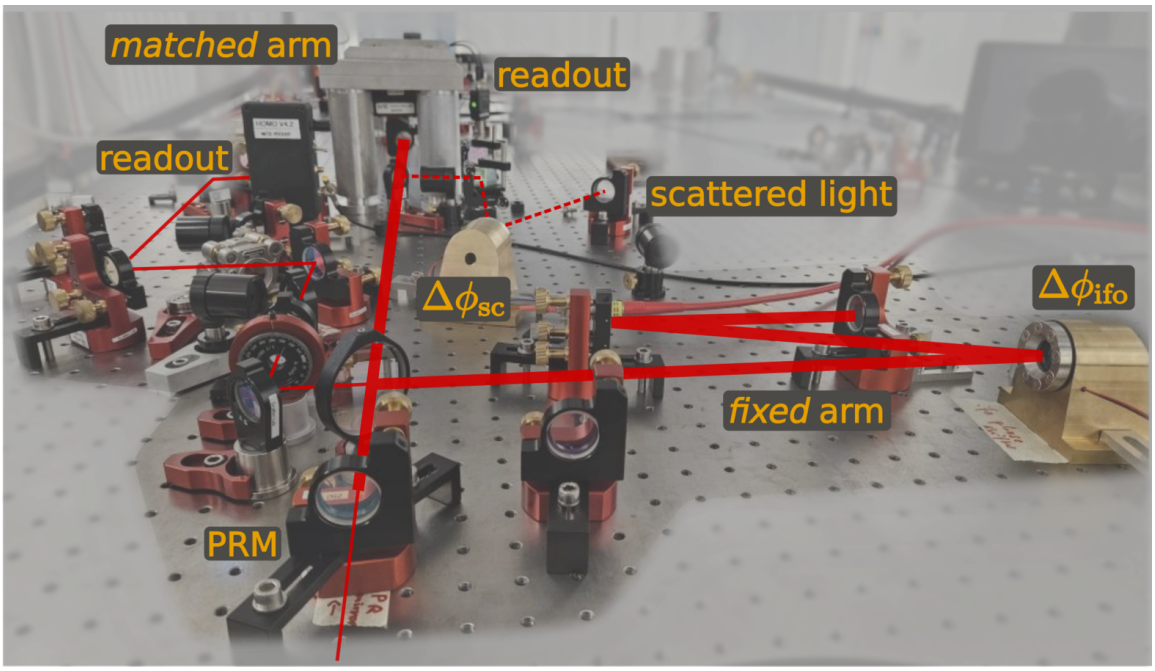

Figure 10.2: Picture of the PRMI setup with the readout on the left side and the PRM in the front slightly to the left. The macroscopically adjustable arm of the interferometer runs from front to back, the microscopically adjustable one from left to right. The scattered light injection (fixed length) is visible slightly above the center of the image.

Table 10.1: Overview of PRN sequences fitting in the PRC (see Fig 10.1) at the available modulation frequencies. The length given in the first row is the maximal recoherence length of a sequence at the lowest used PRN frequency (for which $\alpha = 1$). The 7 chips sequence is an exception due to its non-intuitive multiple, thus the relevant used length with $\alpha = 9$ at 10 GHz is given.

	PRN-sequence			
	7 chips	15 chips	31 chips	63 chips
l_{cav} [m]	1.888	1.798	1.858	1.888
PRN -freq	α-value (number of repetitions fitting the PRC)			
2.5 GHz	-	1	-	-
5 GHz	-	2	1	-
10 GHz	9	4	2	1

The PRM was fixed, thus the PRC could not be microscopically tuned. Instead the laser frequency was tuned to achieve resonance conditions in the cavity.

10.1.2 Locking the PRMI

To properly operate a PRMI, two control loops are needed. One that keeps the interferometer itself at its desired operating point, the dark-fringe, and one to keep the PRC on resonance. These control loops are planned to be implemented in analog electronics as much as possible in the long term. However, a quicker approach was to handle them with a Moku:Lab[45] and a Moku:Pro[46] by using their *Laser Lock Box* instrument.
In order for power-recycling to properly work, the interferometer has to be kept at the

[45]Liquid Instruments, Moku:Lab, Moku: v3.3.2.2 (build 3251), Firmware Version 601.0
[46]Liquid Instruments, Moku:Pro, Moku: v3.3.2.2 (build 3251), Firmware Version 601.0

dark-fringe such that all light is reflected back to the laser, thus effectively forming the end-mirror of the PRC. In the current setup, the easiest way to accomplish a lock that kept the interferometer at the dark-fringe was the use of dithering. This could be easily implemented by adding the needed signal to the PZT mirror controlling the relative phase between the interferometer arms. In the existing setup, a signal could be added inside the used HV amplifier, however, using the Moku:Lab instrument even simplified this further as here the dither-signal could be internally added to the output signal. When dithering the relative phase of the interferometer arms at a higher frequency (here above 100 kHz), the resulting signal in the interferometer response can be isolated by demodulating it at the same frequency. This generates an error signal capable of locking to the dark-fringe due to the phase-dependency of the demodulation and subsequent integration done by low-pass filtering the mixed signal. As the power response to the dithering reverses when crossing the dark-fringe point of the interferometer, the constructed signal is sensitive to this and its sign changes. In other words, with the signal processing done to the measured power at the interferometer output its derivative is extracted and this has a zero-crossing at the dark-fringe.

The challenging part of implementing this locking technique was finding a frequency outside the measurement bandwidth at which the dither signal was strong enough to achieve a stable lock. This was especially complicated as in the next step the scanning and locking of the PRC introduced dynamics into the system that the lock needed to withstand. The most promising options for this were resonance frequencies of the PZT mirror, of which several were identified in the hundreds of kHz-range. However, only the one previously used for simulating a GW-signal at 172.4 kHz was strong enough for constructing a resilient error-signal. The parameters used for the control loop are summarized in Figure 10.3 and the Moku:Lab *Laser Lock Box* setup is sketched in Figure A.8 in the Appendix.

Once the interferometer is controlled to stay at the dark-fringe, the PRC can be locked like any other cavity as long as the increased power in the interferometer does not lead to the loss of its lock. Similar to the locking scheme in the previous stand-alone cavity demonstration, the PDH technique was used to lock the PRC. The only change was, that in this case the laser frequency was scanned and controlled while the cavity had a fixed length. The parameters used for the PDH lock and the instrument setup for this control loop are depicted in Figure 10.3.

10.1.3 First results

At the time of writing, first measurements were already obtained, showing the general functionality of a PRMI with *tunable coherence*. These results can be split in two parts, the scan over the normal and newly induced resonances of the PRC and the suppression of scattered light in the PRMI. The measurements scanning the PRC resonances were

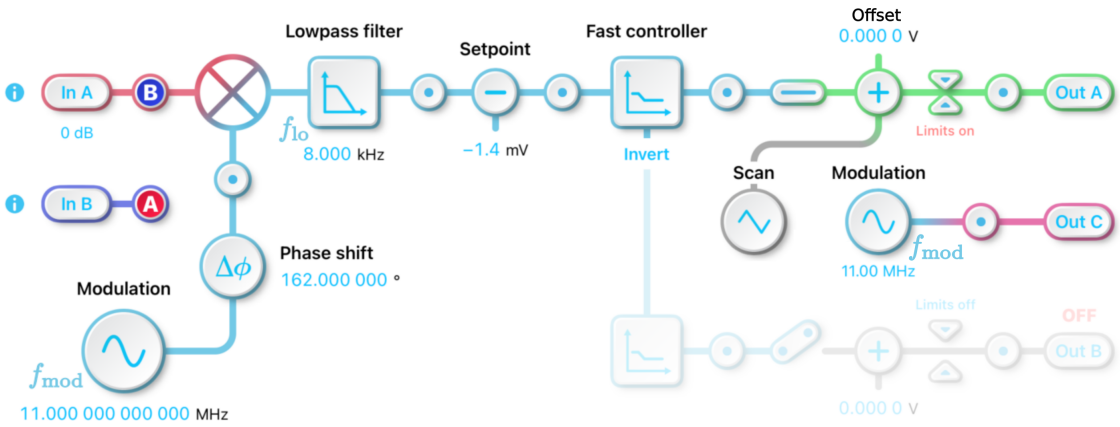

	f_{mod}	$\Delta\phi$	f_{lo}	setpoint	P-value	I-value	IS-value	invert	offset
ifo lock	172.4 kHz	172.0°	5 kHz	−500 µV	−5.0 dB	692.8 Hz	49.9 dB	yes	8 mV
PRC lock	11 MHz	162.0°	8 kHz	−1.4 mV	−17.0 dB	2.034 kHz	39.3 dB	no	0 mV

Figure 10.3: Screenshot of the Moku *Laser Lock Box* instrument used to lock the interferometer to its operation point and the PRC onto its resonance. Below a list of all parameters set for the respective locks in the instrument. For the interferometer part: Input 1 (In A) was the voltage from an in-house designed and built variable gain PD (HomoV4 without mixer). As this circuit was designed for a BHD, it had two PDs of which one was blocked. Output 1 (Out A) was connected to an in-house build HV amplifier driving the piezo-controlled mirror in one of the interferometer arms. In this setup, the modulation was added to Out A internally (see also Fig. A.8). For the PRC part: Input 1 (In A) was the voltage measured by an in-house build PD (HomoV3, one PD of the two in the design was used, the other blocked) in reflection of the cavity, Input 2 (In B) was the voltage measured in transmission by a commercial PD (Thorlabs: PDA20CS2). Output 1 (Out A) was connected to a commercial HV amplifier (Falco Systems: WMA-005 HV Amplifier DC-20 kHz) used to drive the frequency modulation input of the laser head, Output 3 (Out C) was connected to the driver of the MHz-EOM used to add side-bands to the laser.

effectively the same as done with a stand-alone cavity described in Chapter 9 and the demonstration of scattered light suppression was similar to the experiments described in Chapter 8. For both, some successful measurements could be recorded and are presented in the following sections.

10.1.3.a Setup iterations

Even though the data obtained first showed the best performance, there was room for improvement and thus some optimization of the setup was attempted. In total, there were three iterations at which data was taken. The first was the original setup which had instabilities in the laser frequency and used control loops. One major factor for these instabilities was the temperature set for the laser crystal. This had the laser running in an unstable range with the PRC resonance at the edge of the available tuning range. Under these conditions, only the the resonance for the 15 chips long sequence was identified. The

second was after changing the laser crystal temperature, leading to a more stable operation condition and therefore also better performance of the control loops. For this, also the resonance of the 31 chips long sequence could be identified and thus two PRN sequences were available. The last was a reconstruction of the whole setup. Due to changes in the laboratory environment, the whole interferometer had to be realigned. Additionally, a band-pass amplifier was used to amplify the measured signal between 100 kHz and 200 kHz in an attempt to reach shot-noise limited performance for this measurement band. However, due to problems with measurement devices and the laboratory environment, the here recorded data showed degraded performance in regards of noise-level and suppression induced by the PRN modulation. Even though all available PRN sequences could be made resonant in the PRC, time constraints made it unfeasible to further optimize this setup and reach full performance.

10.1.3.b Scanning the power-recycling cavity

After locking the interferometer to its dark fringe operating point, the first measurements done were focused on investigating the PRC and scan over its microscopic and, by *tunable coherence* induced, macroscopic resonances.

Microscopic resonance The first scan was done over the microscopic resonance of the PRC to demonstrate its functionality and measure its finesse, which was roughly 79 ± 21. Additionally, the free spectral range (FSR) of the cavity was calculated from this scan to be 128.36 ± 5.40 MHz while the theoretical estimate was 162.58 MHz. These and further parameters of the PRC are also summarized in Table 10.2. Due to the large FSR of the cavity, the scan had to be done by modulating the crystal temperature of the laser head. While the frequency of the used NPRO laser can be scanned either by using a PZT to mechanically change the crystal properties or by changing the crystal temperature, the former has a guaranteed range of only around 130 MHz. Thus, using the PZT was not enough to cover the full FSR of the cavity. The quicker response and therefor higher bandwidth (up to 100 kHz) of this option was, however, needed for the PRC control loop. As no dedicated laser frequency stabilization was used, it was possible that the laser drifted in frequency and thereby moved the cavity resonance out of the PZT tuning range. This lead to some instability in the experiment but could be worked around manually for the most part. While this scan was done for all setup iterations, the data shown was recorded in the last configuration.

To find the resonance frequencies of the PRN sequences in the PRC, repeating scans over the cavities resonance using the PZT with the PRN modulation active were used. During those scans the PRN frequency was adjusted by changing the reference clock supplied to the transceiver until the cavity resonance was regained.

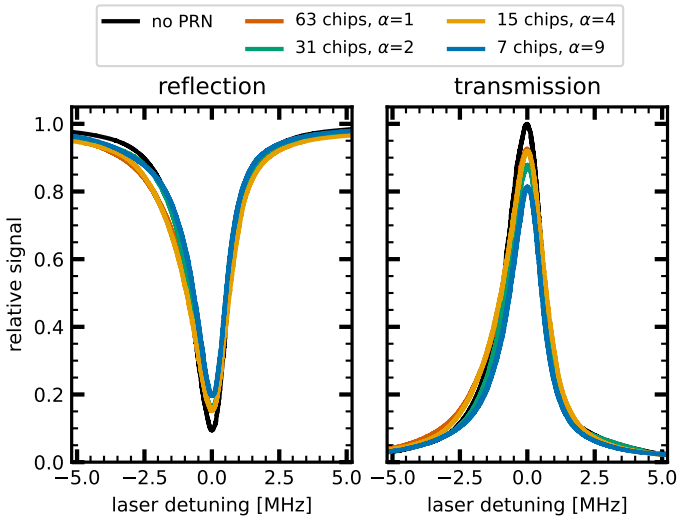

Figure 10.4: Power reflected (left) and transmitted (right) from the PRC recorded while scanning the laser frequency over the cavity resonance. In black recorded without PRN modulation active, in color for the four sequences fitting the PRC at 10 GHz PRN frequency.

	estimated	measured
R_{PRM}	0.9	-
R_{ifo}	0.995	~ 0.94
RoC_{PRM}	flat	-
RoC_{ifo}	2 m	-
FSR	162.58 MHz	~ 128 MHz
Finesse	56.9	$\sim$ 79
FWHM	2.86 MHz	~ 1.63 MHz
P_{refl}	6.76 %	~ 9.4 %

Table 10.2: Parameter of the PRC, calculated or given values on the left and measured values on the right.

The resonant curves for all four PRN sequences specified in Table 10.1 are shown in Figure 10.4 for the case of $f_{PRN} = 10$ GHz. Additionally, a curve without PRN modulation is shown, which had a measured FWHM of 1.63 ± 0.30 MHz. Compared to scans in the stand-alone cavity (see Ch. 9), some deterioration can be observed in these scans, especially for higher values of $\alpha = l_{cav}/d_{coh}$. This hints to imperfect matching of the sequences length and cavity length, which now had an additional degree of freedom in the length matching of both arms. As the shown curves already correspond to an optimized matching of the PRN frequency to the cavity length, a slight mismatch of the interferometer arms was the most likely cause of the degradation. Additionally to this influence of *tunable coherence*, the performance of the control loop keeping the interferometer on the dark-fringe might also have impacted the quality of the scans shown in Figure 10.4. Nevertheless, a contrast of up to ~ 90 % was still observed.

Macroscopic resonance Once the resonance frequency of a PRN sequence was known, a scan of this macroscopic resonance newly introduced by *tunable coherence* was measured. The setup for this was similar as for the stand-alone cavity in Chapter 9. The multi-instrument mode of the Moku:Pro could be used to lock the PRC, modulate and record the reference clock frequency and measure the transmitted power. The setup of the *Multi Instrument* is shown in the Appendix in Figure A.9. In the first slot, the *Laser Lock Box* was used to lock the cavity as described in Sec 10.1.2. The second slot was used for a *Waveform Generator* that provided the reference clock for the transceiver and thus controlled the exact PRN frequency. The sinusoidal wave it generated was modulated in

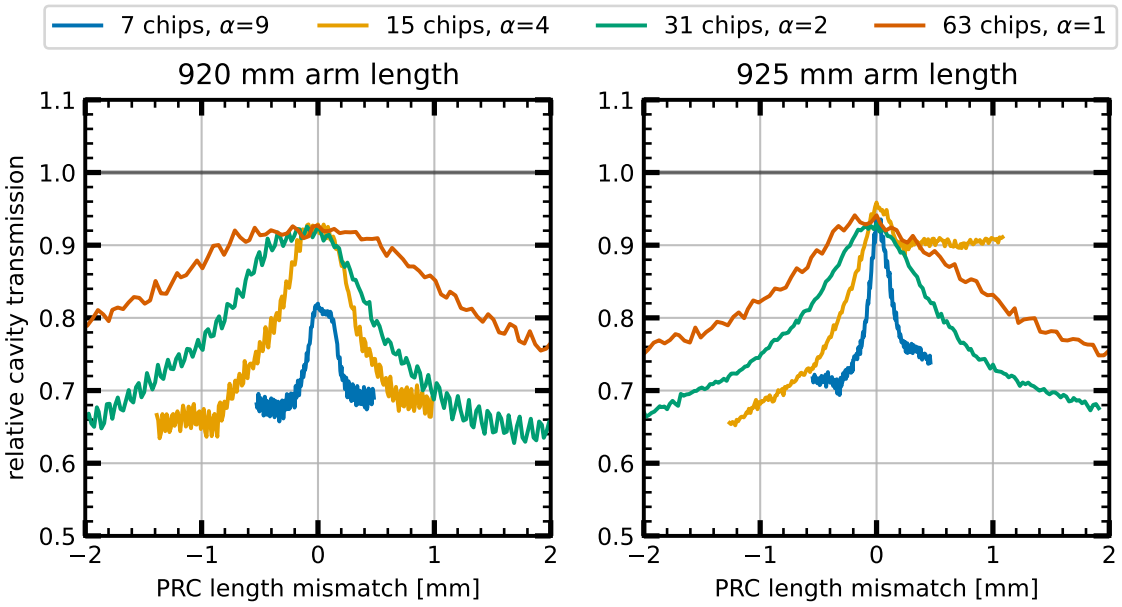

Figure 10.5: Scans over the by the PRN modulation newly introduced resonance at $f_{\mathrm{PRN}} = 10\,\mathrm{GHz}$, recorded for all four sequences fitting the PRC. On the left the adjustable interferometer arm was set to a length of 920 mm resulting in less optimal scans. On the right the same scans for the arm length set to 925 mm. This corresponded to the length for which the shortest sequence reached its best transmission, indicating best matching of the arm lengths. For this setting, the 15 chips long sequence shows some one-sided stagnation for which no explanation could be found so far.

frequency with a ramp. This could be either internally generated or driven by an external signal generator for more customization options. The frequency of this sine-wave was in turn tracked by a *Phasemeter* placed in the third slot. With this, data was recorded using the integrated *Data Logger* and later synchronized to the recorded power in transmission and reflection of the PRC. To make this easier, the ramp driving the modulation of the reference clock was one-sided and had an offset, leading to a jump in the recorded power after one cycle. Once the cavity was locked, the PRN modulation was turned on and the power recorded with the integrated oscilloscope of the *Laser Lock Box*. Traces from this were saved such that multiple ramps and sections without PRN modulation were recorded in one measurement. The results of these measurements are shown in Figure 10.5 and Figure 10.6.

The resonance scans at 10 GHz PRN frequency for two different arm length matchings and all four used sequences are shown Figure 10.5. This was recorded for the last setup configuration in which all four sequences were available and their resonance frequencies identified. However, in this setup, the best results could be obtained for an arm length of 925 mm instead of the from previous measurements expected 922 mm. And even for this length, the resonance could not be fully regained with the PRN modulation active. The main cause for the decrease in performance was most likely misalignment of the setup,

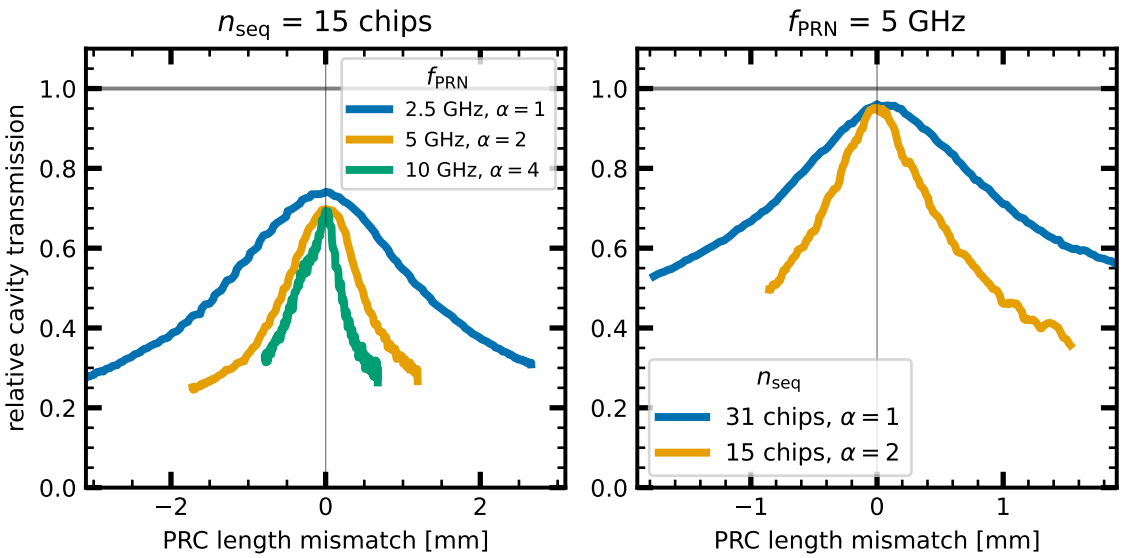

Figure 10.6: First measurements of the scan over the resonance newly introduced with *tunable coherence* in the PRC. On the left side before first optimizations regarding the stability of the laser and control-loops. These scans showed only partial regaining of the full transmitted power compared to the scan without PRN modulation. For these measurements, only the resonant frequency for the 15 chips long sequence was identified. Data was taken for three different PRN frequencies and the behavior between them was similar to the stand-alone cavity, only with lower relative transmission. Data shown on the right was recorded in a more stable configuration allowing to achieve higher relative transmitted power for both the 15 and 31 chips long sequences. This data was recorded at $f_{PRN} = 5\,\text{GHz}$ and showed FWHMs of 985 µm and 1776 µm for the shorter and longer sequence respectively.

possible mode-changes and resulting misalignment caused by changes in temperature and overall deterioration of the laboratory environment.

Nevertheless, the comparison of the scans taken with different lengths of the controllable arm showed an influence of the length matching on the resonance. While for most sequences a set arm length of 925 mm showed a cleaner scan, narrower width and slightly higher maximum values, the 15 chips long sequence showed unusual behavior. Towards one side of the scan, the transmitted power stagnated around 90 % relative power even when the length mismatch was increased. So far, no explanation could be found for this phenomenon which occurred consistently for this but only this sequence at all tested PRN frequencies, but only in the reworked setup. As can be seen in comparison between the two lengths shown in Figure 10.5 and in further data shown in the Appendix, it was also dependent on the arm lengths matching of the interferometer. It cannot, for example, be observed for a set length of 920 mm as shown on the left of Figure 10.5. However, at this length the shortest 7 chips long sequence having the highest α-value of 9 performed significantly worse, indicating that the arms are not optimally matched in length.

Figure 10.6 shows data recorded with the original setup, on the left the first data taken with only the 15 chips long sequence at different PRN frequencies. On the right, data

recorded after the first optimizations of laser stability and control loops is shown. Here, the resonances for the 15 and 31 chips long sequences at $f_{\mathrm{PRN}} = 5\,\mathrm{GHz}$ were recorded. The behavior of these measurements was similar to the stand-alone cavity but the resonances were wider and the maximum transmission did not fully reach the value without PRN modulation. While the wider resonances are expected due to the lower finesse of the PRC compared to the stand-alone cavity, the shortcoming in transmitted power again hints to some remaining mismatch, probably in the arm length matching. For the optimized measurements at 5 GHz the FWHMs were around $1776 \pm 56\,\mu\mathrm{m}$ and $985 \pm 29\,\mu\mathrm{m}$ for the 31 chips (α=1) and 15 chips (α=2) long sequences respectively. When calculated with Equation 9.4, the expected values are 1192 µm and 596 µm, meaning both measured FWHMs are wider than estimated and would indicate a finesse of only around 50 for the cavity. However, as both sequences do not reach the same transmitted power as without PRN modulation, this sub-optimal matching also influences the width slightly.

10.1.3.c Suppressing scattered light

Finally, the suppression of scattered light injected into one of the interferometer arms of the PRMI was tested. For this, the interferometer and PRC were both locked to their operating points and several spectra, as well as time-series data were recorded at the interferometers asymmetric port. Data recorded as spectrum analyzer traces was analyzed by taking the mean of five spectra which were saved from the Moku:Pro *Spectrum Analyzer*. One trace was averaged over 10 frames and used 8 spectra per frame, resulting in an average over 80 calculated spectra per recorded trace. The data recorded as time-series was analyzed by calculating spectra as described in Chapter 8.

Two new frequencies were chosen to modulate the scattered light and simulate a GW-signal as the resonance at 172.4 kHz was now used for the dither-lock. Due to the added power-recycling and the strength needed for a stable lock, it was dominant in the surrounding frequency range, making a shift to frequencies further separated necessary. Thus, for the scattered light a frequency of $f_{\mathrm{sc}} = 135\,\mathrm{kHz}$ and for the simulated GW-signal a frequency of $f_{\mathrm{gw}} = 145\,\mathrm{kHz}$ were chosen. This second tone at f_{gw} was not injected into the interferometer for all measurements. However, for the ones without it, the peak at the dither frequency $f_{\mathrm{dither}} = 172.4\,\mathrm{kHz}$ could also be used to gauge the impact of *tunable coherence* on the interferometer itself.

Again, data was taken for all three described iterations of the setup. While most parameters could be investigated in this last configuration, the quality of the recorded data was poor in comparison. The results from these measurements are therefore presented in the Appendix (see Figure A.10 and A.11). The data presented in Figure 10.7 and 10.8 was taken during the first two iteration with only the slight improvements described previously made in between. This data was measured at 5 GHz PRN frequency with the

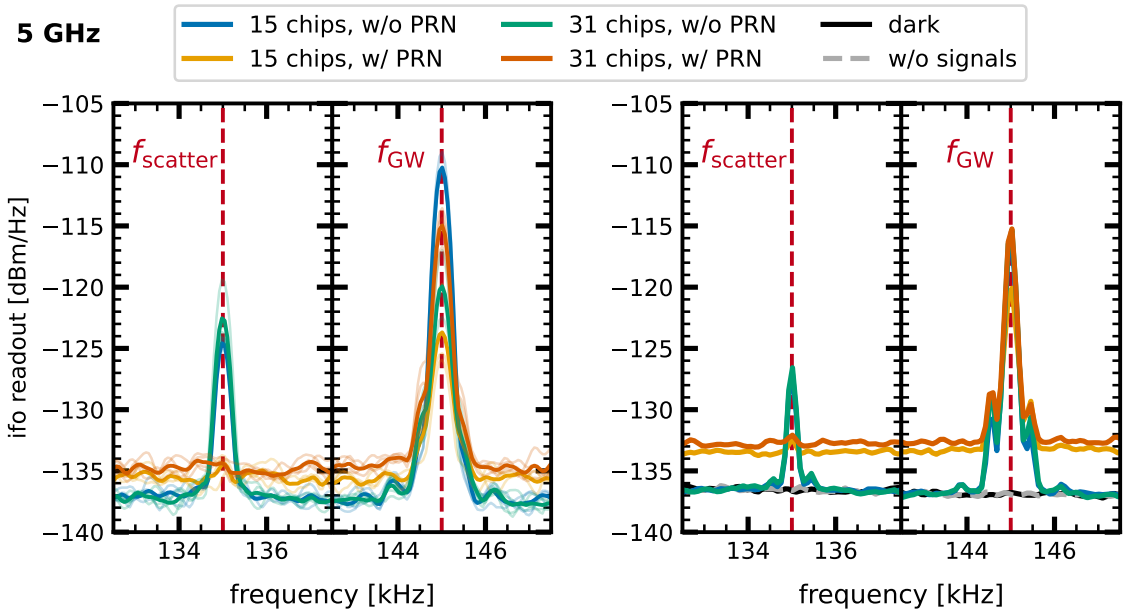

Figure 10.7: Suppression of scattered light measured in the PRMI with 5 GHz PRN frequency after stability optimizations resulted in a lowered noise-floor. On the left side, measurements recorded as spectrum analyzer traces are shown. On the right, measurements recorded as time-series are shown. Because the spectrum was observed to be not fully stationary on the timescales between sequence changes which also needed PRN frequency adjustments, data with and without PRN modulation is labeled with the respective sequence used for the measurement. The noise-floor increase with active PRN modulation is smaller for the live-optimized data recorded as traces compared to the time-series measurement, but the signal peak fluctuates more in this data. This could be caused by the PRN modulation but also by instabilities in the power-recycling gain and interferometer readout. For both data sets, the scattered light peak is suppressed down to the noise-floor resulting in suppression values of around 10 dB on the left and around 5 dB on the right if the reduced scatter peak is assumed to be purely caused by *tunable coherence*.

two sequences of length 15 and 31 chips fitting the PRC at this frequency.

The data shown in Figure 10.7 shows the suppression of scattered light in a PRMI with the 15 and 31 chips long sequences, recorded as spectrum analyzer-traces (left) and time-series (right). This measurement featured a lower dark-noise at only around 136 dBm/Hz calculated from the time-series data, mainly due to the improved stability reached for these measurements. For both sets of measurements, the sensitivity was limited by this dark-noise with clear peaks at the injected frequencies at 135 and 145 kHz. The former caused by the scattered light was weaker due to the low amplitude of the beam coupled back into the interferometer. All data showed suppression of this peak when the PRN modulation was used, however, also an increase in the noise-floor. In the live-optimized data recorded as traces, this was slightly less prominent. As discussed in Chapter 7, the PRN modulation can cause such an increase for imperfect modulation depths which is the most likely cause in these measurements. Additionally, the peak at the simulated GW-signal frequency directly injected into the interferometer at 145 kHz fluctuated, especially

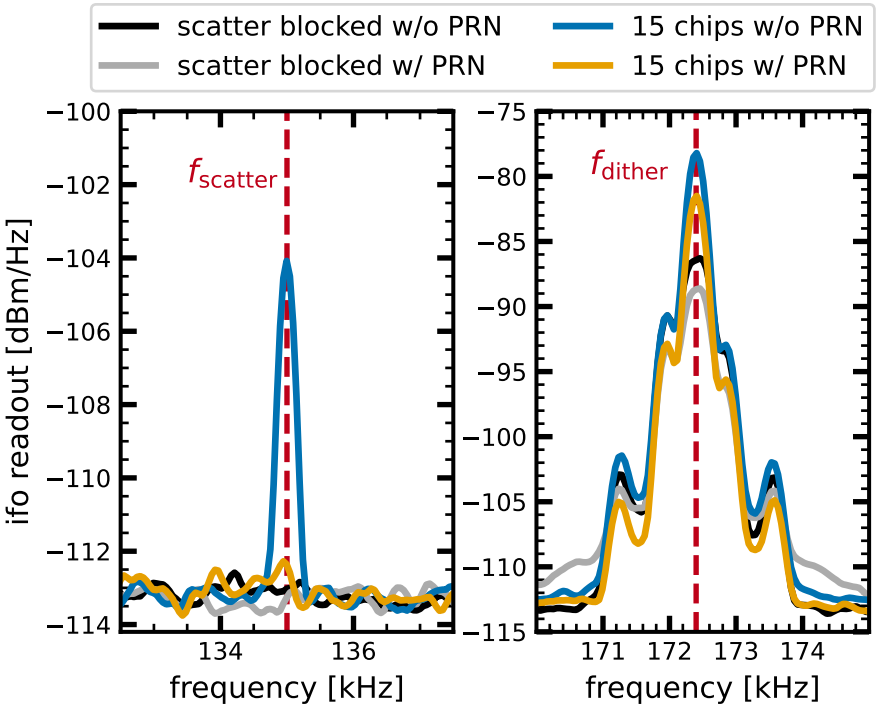

Figure 10.8: Best measured suppression in the PRMI recorded before first optimizations were done and thus having a higher noise-floor than later measurements. On the left, the change of the scattered peak between measurements using the PRN modulation and not using it. This showed a change in peak height of around 8 dB with the peak suppressed to the noise-floor levels when the PRN modulation is active. On the right, the strength of the peak stemming from the dither-signal for comparison. Its height is reduced by around 3 dB which could be caused by the PRN modulation as well. Thus, the increase in SNR is around 5 dB for this measurement. A slight decrease in the dither-signal peak can also be observed for the case where the scattered light was blocked. However, in this measurement it is in general lower, indicating some instability in the power-recycling gain and interferometer readout.

for the data recorded as traces. This could partially be caused by imperfect matching of the arms, leading to partial suppression of the interferometer signal. However, also instabilities in the setup, mainly the control-loops keeping the operating points, could have caused fluctuations in the power-recycling gain and interferometer readout. Even though not perfect, a clear suppression and increase of SNR can be seen when using *tunable coherence* compared to the recordings without the PRN modulation.

The overall best data regarding the performance of *tunable coherence* in a PRMI was recorded in the first iteration and is shown in Figure 10.8. This data was only recorded as spectrum analyzer traces and the noise-floor was higher at around 113 dBm/Hz. Overall, this measurement was done with the first configuration and thus least stable condition of the setup in which additional frequency noise might have coupled into the readout. These unstable conditions also prevented successful measurements with the second sequence of 31 chips length as its resonance was not identified at this point. Data was therefore only available for the shorter 15 chips long sequence and without the additionally injected

simulated GW-signal at 145 kHz. Instead, the peak stemming from the dither signal at 172.4 kHz is shown to get an impression of the influence directly on the interferometer. The scatter peak shown on the left of Figure 10.8 vanished almost completely when using the PRN modulation with the remaining part nearly indistinguishable from other noise fluctuations. Calculating the suppression of the scatter peak directly resulted in 8.28 dB. However, also the peak of the dither-signal experienced some suppression. This varied between 2.25 and 3.29 dB for the suppression measurement and the measurement with blocked scattered light respectively. The change in ratio between the dither and scatter peak is therefore a better estimate for the real suppression of scattered light. An improvement in SNR of about 5 dB could be measured by using this approach.

Discussion

Both, the scans of the PRC and the first demonstration of scattered light suppression in a PRMI are encouraging results. However, improvements and optimizations are possible and necessary. Especially at the used higher PRN frequencies up to 10 GHz, the constraints on the length matching of the interferometer arms and between PRN sequence and cavity reach levels that require careful alignment and high precision of the setup. While the successful implementation is certainly possible, it is unclear how much effort would be necessary to avoid any negative influence of *tunable coherence*. Especially the failings of the realigned last configuration of the setup showed that the additional parameters and degrees of freedom needed to be optimize for the use of *tunable coherence* can pose significant challenges. In general, with this reworked setup experiencing multiple problems that could have influenced the performance negatively, this data is inconclusive and needs to be investigated further. While the data taken during the first iterations of the setup does show better results, it also suffered from instabilities causing fluctuations in the power-recycling gain and interferometer readout. For the most part it was therefore problematic to distinguish between influences of these instabilities and *tunable coherence*. All data showed some degradation of the intended signal or decrease in transmitted power, the most probable cause for this are persistent length mismatches in the setup. This shows how the increasing complexity of an optical setup leads to more challenges in its alignment and precise length adjustments needed for *tunable coherence*. Having coupled features like the interferometer and PRC in this case makes it especially challenging as they cannot be easily length matched individually but only as a whole. The here presented demonstrations can only be a first proof-of-concept, showing that *tunable coherence* can work and suppress scattered light in a complex layout like a PRMI. Due to time constraints and problems with the laboratory infrastructure, all necessary improvements for better performance could not yet be done. In the future, the demonstrations should be repeated using a more stable setup and stronger scattered light to achieve improved results reaching

higher suppression. Further, these future measurements need to show that any negative impacts present in the first results here can be avoided once the setup is properly optimized. Nevertheless, demonstrating already 5 dB improvement in SNR with the imperfect setting available is highly encouraging. It thus paves the way for further experimentation, moving towards lower, for GWDs more realistic measurement frequencies. Here, the expected better performance of e.g. the used PZTs then directly helps in increasing stability of the locking relying on it and allows for more consistent and stronger straylight injection.

10.2 Additional thoughts

10.2.1 Fabry-Perot Michelson interferometer

Contrary to the previously discussed demonstration of *tunable coherence* in a PRMI, adding Fabry-Perot cavities into the arms of a Michelson interferometer to form a FPMI does not yield additional fundamental insights into the use of *tunable coherence* in more complex topologies. The reason for this lies in the clear separation of the parameters influenced by *tunable coherence* between the three parts of the topology. Or in other words, the two cavities and the interferometer between them can be viewed individually regarding *tunable coherence*.

As shown in eq. 6.2 and demonstrated in the experiments described in Chapter 9, the field reflected from a cavity behaves the same with the PRN modulation as without it but still carries the modulation. Thus the two Fabry-Perot cavities need to be length matched to the PRN sequence individually while each is expected to behave like the stand-alone cavity demonstrated in the previous chapter. A sketch of a possible setup, highlighting the separation, is depicted in Figure 10.9. Ideally, one would fix one of the cavities in length, then probe the other one for its length by tuning the PRN frequency. Its length would then need to be adjusted with a high precision opto-mechanic until both cavities reach full resonance for the same PRN frequency. The Michelson interferometer between them then also behaves like a simple Michelson as demonstrated in Chapter 8, meaning its arms have to be matched in length. Interestingly, there is no reason for the cavities to have the same length in regards to *tunable coherence*, however, they still need to match an integer multiple of the PRN sequence each.

This said, from the point of demonstrating compatibility of *tunable coherence* with a FPMI, there is no additional fundamental complexity expected. However, how the coupling of scattered light is suppressed depending on the point where it couples back into the layout, is more interesting. Thus the sketch in Fig. 10.9 includes several scattered light paths coupling into different parts of the topology, for example into the interferometer or the arm-cavities. Also, once any type of recycling is added to a FPMI, the complexity

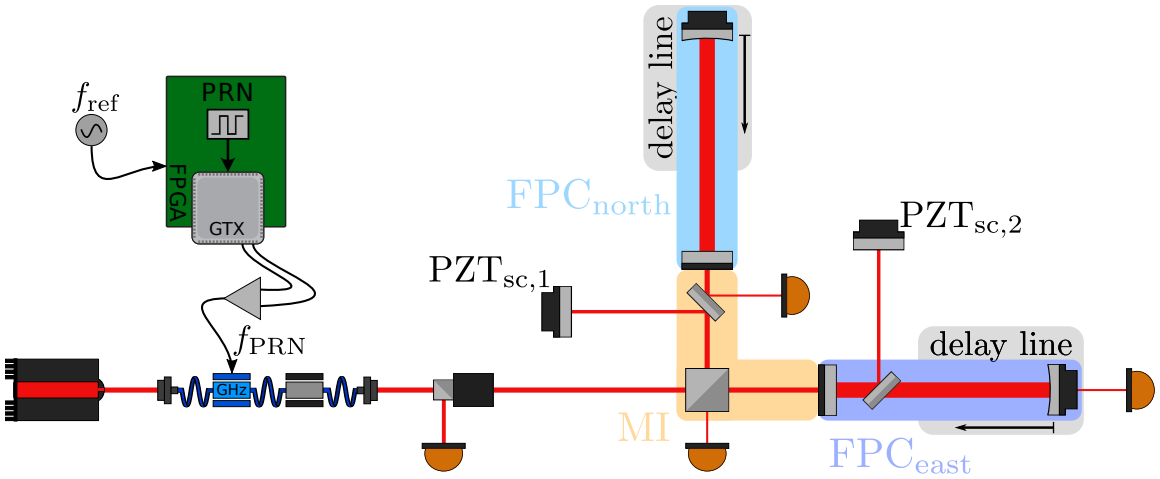

Figure 10.9: Sketch showing a simplified possible setup for a FPMI to demonstrate *tunable coherence* and its ability to suppress straylight coupling into the layout at different positions. This could be either inside or outside the FPCs that form the arm cavities in the north and east arm. The colored parts show how each layout component can be treated individually in regard to *tunable coherence*, contrary to the PRMI-setup shown in Fig. 10.1 which needed to be configured for *tunable coherence* as a whole.

drastically increases.

10.2.2 Next steps

Taking the so far mentioned results and considerations into account, the next steps can be laid out. The obvious first step is finalizing the demonstrations with the PRMI by tackling the remaining problems and repeat the measurements under optimized conditions. Further, demonstrating shot noise limited performance in general and at frequencies closer to the actual sensitivity band of GWDs is already in preparation. For this, additional stabilization of the laser in amplitude and frequency is needed. Schemes for both stabilizations are being worked on and will be implemented in the near future. For the frequency stabilization, a stable reference cavity will be added to the setup and possibly further isolated to increase performance. To avoid complications stemming from *tunable coherence*, this is planned to be implemented in front of the fiber setup containing the modulators. As can be seen in Figure 7.1, a currently unused beam is available for this which was blocked so far. Being able to move the measurements to lower frequencies might then also simplify the setup as a whole by removing the reliance on the few, and often weak piezo resonances above 100 kHz.

Once this demonstration is done, a change in setup should be considered, moving to a FPMI for investigating the scattered light coupling and suppression in more detail. This could then later be extended to include power or signal-recycling forming a power-recycled Fabry-Perot Michelson interferometer (PRFPMI) or signal-recycled Fabry-Perot Michelson interferometer (SRFPMI), leading to the first demonstration of *tunable coherence* in

coupled cavities and an interferometer combined. Alternatively, the demonstration of signal-recycling in a basic Michelson setup could be done first to demonstrate both types of recycling before moving on to the FPMI and eventually adding recycling cavities to it. In any case, moving to a FPMI setup will increase the number of degrees of freedom needing to be controlled to keep the interferometer and the cavities at the desired operating point. This will be more difficult to handle and might introduce the need for a frequency-doubled laser and more complex control-schemes.
Generally, the addition of macroscopic length constraints complicates any control scheme, especially if dependencies between different degrees of freedom exist. Being able to adjust and fine-tune the relevant length degrees of freedom, possibly simultaneously to the fast and also highly precise microscopic tuning, is challenging. A good example is the used PRMI setup where the arm lengths could only be matched to a limited precision without the cavity being added. However, once it was added, operating with *tunable coherence* not only relied on more precise readjustment of this matching but also identifying the exact needed recoherence length or PRN frequency. If the fine-tuning can be decoupled like in an FPMI, this simplifies but is by no means trivial. Taking it a step further to suspended interferometer where the position of all optics needs to be kept stable, this can become even more challenging. On the other hand, as long as the optimal positions fall within the range of used actuators, this at least allows for more flexibility in moving the optics. All in all, additional challenges will be added with *tunable coherence*, however, once the macroscopic length is optimized, the microscopic stability can be expected to revert back to its previous performance.

10.3 Conclusion

In this chapter, a first demonstration of *tunable coherence* in a complex topology was presented. Even though the data measured for this demonstration shows room for improvement, an increase in SNR between a signal injected directly into a PRMI and scattered light of 5 dB was achieved. The scattered light signal was suppressed by more than 8 dB in the best data recorded, however, the setup suffered from instabilities and suboptimal alignment. Thus, to properly investigate the impact of *tunable coherence*, this demonstration should be repeated after future optimizations. Additionally, the prospects of investigating *tunable coherence* in a FPMI were discussed and options for the next experimental steps pondered. Even though not yet fully satisfactory, the overall promising outcome of this chapter motivate the detailed discussion of options for an improved implementation and application possibilities in the next chapter.

11 Discussion

In this chapter, the findings, results and individual conclusion of the previous chapters are combined to discuss *tunable coherence* as a whole. With the premise of this thesis, the leading aspect is its use for straylight suppression in interferometers and more specifically gravitational wave detectors (GWDs). However, other aspects are considered as well.

11.1 Implementation of *tunable coherence* and its effects

The ideas on which *tunable coherence* is based have been around for several decades. However, the needed hardware was not available or not good enough until recently. Pushing the phase modulation into the GHz-range is crucial to minimize the remaining coherence and achieve reasonable recoherence lengths while still reaching high suppression.
Modern phase modulators are now reaching several tens of GHz in bandwidth, thus allowing the coherence lengths to be reduced to the centimeter scale and below. As presented in Chapter 8, the coherence was strongly reduced for delays of only a few centimeter in a Michelson interferometer using a PRN frequency of 10 GHz. Moreover, such short chips enable the use of longer sequences that significantly suppress unwanted fields. With chip lengths of only around 3 cm, their recoherence lengths stay in the order of a few meter. They therefore realistically fit optical resonators of lengths usable in table top experiments, as discussed in Chapter 9. In such cavities, the number of round-trips needed for resonance enhancement further reduces the tolerable deviation from the intended lengths. Thus a new resonance condition is introduced. The experiments presented in Chapter 9 demonstrated that in these setups, only a few µm path length deviation can significantly reduce coherence. It is as such realistic that the remaining coherence can be reduced below a wavelength under the correct circumstances. At this point a whole new set of implications might arise. Some of them are discussed more detailed in Sec. 11.1.2.
The experimental parts of this work demonstrated that *tunable coherence* works in simple interferometer topologies like the Michelson and Sagnac. Compatibility with stand-alone cavities was also demonstrated. Lastly, the combination of both was investigated, showing first impressions of *tunable coherence* in a power-recycled Michelson interferometer (PRMI). Very promising results were obtained for the Michelson interferometer and cavity individually. However, the Sagnac topology and especially the combination in the

PRMI revealed some room for improvement. For the complex PRMI setup, instabilities in the laboratory environment and setup itself were primarily causing these problems. In addition to short comings in the implementation of *tunable coherence* as used for this work. It is, however, likely that with improved stability, better results can be obtained in the near future. For the deficiencies in the Sagnac topology no definite cause could be identified but probable aspects are discussed in Sec. 8.2.1.

Generally, all measurements showed two important aspects for the implementation of *tunable coherence*, the proper depth of the PRN phase modulation and the bandwidth of the modulation setup. The switching between chips in the PRN sequence is not instant but has a finite rise- or fall-time. This leads to a non-rectangular shape of the modulation, as observed here and in other experiments using GHz-PRN modulations [134]. In turn, the ACF of the sequence is degraded, limiting suppression close to the length of one chip. Generalizing this, *tunable coherence* has limited to no effect on scattered light having a relative delay that falls into the chip length d_{chip}. Allowing such scattered light to couple back into the interferometer thus needs to be avoided. Alternatively, optimization of cables and the electronics setup to increase the bandwidth can help to improve the modulation shape. Other methods of transferring the sequence to the modulator could also be investigated. Improving the signal shape and resulting auto-correlation function (ACF) would help in realizing higher suppression for shorter delays.

In the here presented experiments, the modulation depth was only manually adjusted. While this worked to a satisfactory degree, it complicated measurements. Further, especially in more complex setups it can introduce an additional degree of freedom which can negatively influence the performance. It would thus be beneficial to implement a control loop as suggested in Sec. 7.2.3 or similar.

Another aspect that could be problematic in a setup having specific length constraints is the flexibility in PRN sequence length. For this work, *m*-sequences were used as a fast and easy way to generate and implement a form of PRN sequence and the setup was designed around their lengths. However, other sequences are possible and it could even be considered to generate custom sequences for a desired length. Combining a good sequence length with fine-tuning the PRN frequency would then cover a wide range of possible lengths.

A long term implementation of *tunable coherence* might even move towards designing a fully integrated single device to handle all the parts of PRN modulation. In a first iteration, this could simply be combining sequence generation and modulation depth control into a single FPGA which is located close to the GHz-EOM. However, one might consider implementing the phase modulation into an on-chip design [180–183], as for example investigated for squeezed light sources [184]. This could then be directly combined with the FPGA generating the PRN sequence and controlling the modulation. By doing this,

signals could be routed directly on the chip, making cables in between components obsolete. Additionally, voltage levels needed to generate a phase shift of π decrease and drop below 5 V even for GHz-modulation frequencies. Dedicated electronics therefore become less complex and important. Thus, combining everything from PRN sequence generation to transmission, amplification and phase modulation together with needed control loops into a single device would not only simplify the setup. It can also optimize each individual step to avoid negative influences as present in the current implementation.
Another complication currently is the complex fiber setup as shown in Figure 7.1. Here, several fiber to fiber connections introduce loses and polarization instabilities. These in turn lead to amplitude fluctuations due to polarizing optics. Combining all needed components into a single device would also solve most of this problem. Especially if the possibility to add lower frequency sidebands is also integrated. However, independent of that, a short term solution should be pursued by simplifying the setup, only keeping and optimizing the essential connections. This would benefit the experimental setup, helping to reduce the noise floor at lower frequencies and thus allow for better demonstrations of *tunable coherence*.

11.1.1 Straylight noise mitigation

Noise caused by scattered light can be divided into two aspects, the phase coupling noise and the radiation pressure noise caused by it. While only the former has been investigated in this work, a few aspects about the latter can be inferred.

11.1.1.a Phase coupling noise

In a Michelson interferometer, suppression levels of 40 dB were demonstrated consistently at a PRN frequency of 1 GHz and for some occasions at 2 GHz. Further, for a PRN frequency of up to 10 GHz, suppression levels of 30 dB were shown. The needed minimal delay of the scattered light relative to the interferometer was thus reduced to the 10 cm-scale and below. Thus showing that *tunable coherence* can suppress scattered light from sources with short relative delays to a significant degree. Other previous experiments achieved around one order of magnitude suppression without further post-processing [103]. The here demonstrated suppression therefore considerably shifts the state-of-the-art. It additionally removes the need to identify individual scatter-sources. As identifying these sources is not a trivial task, especially in advanced GWDs [18, 21], this is another major advantage of *tunable coherence* compared to other mitigation techniques.
The reached suppression can be negatively influenced by imperfect modulation depth. Further, the needed minimum scattered light delay was shown to be higher than expected. This can, however, be solved by the optimizations discussed before and an increased PRN frequency. Suppression of effects from spurious beams scales linearly with the number of

chips in the sequence n_{chips} [130]:

$$\varphi_{\text{res,err}} = \frac{\varphi_{\text{err}}}{n_{\text{chips}}}, \tag{11.1}$$

with $\varphi_{\text{res,err}}$ as the residual phase error. Thus the tolerable parasitic beam power scales quadratic with sequence length, which strongly motivates longer sequences. In order for these to still fit reasonably into the setup, higher PRN frequncies to shorten the recoherence length are again beneficial.

Experimental limitations of this work limited the scattered light strength to similar levels as the reached suppression. With the available data it can therefore not be determined how feasible higher suppression levels are. Whether the theoretical potential of very long sequences exceeding 40 dB of suppression can realistically be achieved thus remains to be investigated. As this might require equally high levels of precision on the modulation depth control, an optimized setup including this is most likely needed for such demonstrations. Nevertheless, as the phase errors φ_{err} scale proportionally with the straylight power P_{sc}, the achieved 40 dB translate to an increase in tolerable parasitic power by a factor $10,000$. The use of *tunable coherence* thus could significantly simplify efforts to reduce straylight phase noise in ground-based GWDs and other interferometers.

11.1.1.b Radiation pressure noise

The additional radiation pressure noise caused by straylight can stem from two aspects. The loss of photons or light power due to scattering if this is caused by a non-stationary scatter process. And the recoupling and time varying interference of the straylight into the cavity. The latter is especially at low frequencies, where the optomechanical coupling becomes more relevant, generally the dominant coupling mechanism for straylight noise [88, 111]. Against the former, there is not much one can do besides avoiding the loss of light power due to scattering altogether. This is more challenging than the mostly done mitigation to avoid its recoupling. For this loss of light power, like most other techniques, the use of *tunable coherence* also does not help. However, it reduces any time-varying interference between the scattered light and the main interferometer, or in this case the arm-cavity. Therefore, it would in principle be able to reduce this aspect of the radiation pressure noise. Even additional noise stemming from non-permanent coupling and not only a time-varying phase might be suppressed to a degree as *tunable coherence* hinders its constructive or destructive interference. Instead, an almost constant offset would be added for the moments the straylight reaches the cavity again. Thus, not fully avoiding radiation pressure fluctuations but limiting them. Both these mitigations could not yet be demonstrated with the available experimental setup. They should instead be considered for future work as another probably beneficial aspect of using *tunable coherence*.

11.1.2 Sub-wavelength coherence length

The experiments discussed in Chapter 9 demonstrated, high PRN frequency and many sequence repetitions in a cavity can bring the remaining coherence very close to a wavelength. The high number of repetitions in this case can be either due to high finesse or a short PRN sequence or both. However, with the currently feasible modulation frequencies, this is only true inside optical resonators. Without these, even for a PRN frequency of 100 GHz the chips would still be in the mm-range. This distinction might be important for the resulting effects. Still, remaining coherence lengths on the scale of a wavelength will in any case cause some new interesting aspects to become relevant.

At such short coherence lengths, the tuning of the cavity can cause a significant mismatch between cavity round-trip and recoherence length. Especially in high finesse cavities when using high PRN frequencies, this can happen, if the recoherence length is not an integer multiple of the wavelength. Then, the cavity is microscopically resonant at a different round-trip length than the one perfectly matching the recoherence length. This aspect was relevant even above the wavelength-scale for the simulations discussed in Chapter 6 and generally requires new, refined simulation tools for further investigations. So far, no experimental evidence for such a condition could be seen, however, the parameters investigate here were still relatively moderate. To avoid problems in the future, locking the chip length to the wavelength could be considered by e.g. using a frequency comb.

By reaching sub-wavelength coherence lengths, further issues besides these needed high precision adjustments might arise. One of them is the very limited tuning range of especially cavities. Again, no influence of the PRN modulation on the power or PDH error signal behavior for a slight detuning of the cavity could so far be observed. Therefore, a cavity remained operable also off-resonant if desired even with *tunable coherence* in the here presented experiments. The same is, however, almost certainly not true anymore in the case of sub-wavelength coherence lengths. The PRN frequency would then have to be fine-tuned such that the recoherence length matches with this cavity tuned to the needed operating point. However, if this very short coherence length is caused by the number of repetitions inside the cavity in the first place, their influence could be less dramatic. In this case, the most mismatched round-trips are contributing the least to the intra-cavity field as their amplitude decreases with every round-trip. Thus, the largest contributions should still be mainly constraint by the chip length d_{chip} as the limiting length.

Another aspect that should be considered are the interactions with highly reflective mirrors or more specific the used coatings to give them this property. These work by utilizing several layers of quarter wavelength thickness, each reflecting most of the light not reflected by the previous layer. Thus, every additional reflection collects a full wavelength in phase[47] and interferes constructively with the others. If the coherence is reduced close

[47] optical path through the layer plus two transmissions when entering and leaving the layer

or even below a wavelength, more and more layers would not contribute anymore, degrading the reflectivity of the mirror. Here again, if the chip length is still much longer than a wavelength, this should not be as critical. The parts experiencing longer round-trip lengths inside the cavity due to reflection on deeper layers again contribute very little to the overall intra-cavity field. This effect could, however, still become a limiting factor in very high finesse cavities when using *tunable coherence*. By reducing effective reflectivity, it could lead to a reduction in finesse even when the standard round-trip length is perfectly matched. Mirror coatings are another important research field for GWD development as their thermal noise is another limiting noise source [17, 18]. A proposed answer to this problem is the use of anti-resonant, so-called Khalili cavities [185, 186], to replace single high reflective mirrors by a cavity. This would reduce thermal noise levels [186] and might also help solving complications induced by *tunable coherence* due to more control over the distance between mirrors.
Even though these effects are challenging in many regards, the resulting precise and well defined absolute lengths might also be beneficial for e.g. reducing other associated noise sources like for example (angular) control or suspension noise.

11.2 *Tunable coherence* in gravitational wave detectors

The demonstrated ability of *tunable coherence* to suppress scattered light to levels equivalent to four orders of magnitude reduction in straylight power strongly motivates its application in high precision interferometers like GWDs. However, for the incorporation of *tunable coherence* into a GWD, some important other factors are to be considered. Practical aspects related to the functionality and optical layout of a GWD are discussed in later parts of this section. Besides those, it must be certain that the incredible sensitivity of the detector will not be compromised by *tunable coherence*. So far, the experimental demonstrations did not show a degradation in overall sensitivity of the used interferometer, on the contrary, additional side lopes and raised noise floor caused by the scattered light were also suppressed for optimized modulation parameters. Yet, these experiments did not demonstrate shot noise limited performance at this point and their sensitivity was of course far from a GWD. Thus, the need for demonstrating the sustainability of high sensitivities in the presence of the PRN modulation remains an important aspect.
Additionally, the lasers used for GWD interferometers have considerably higher power than the here used one. Currently, the input power provided by the pre-stabilized laser systems used in the LIGO detectors is around 60 W [18], around a factor 200 higher than in the experiments described here. For future detectors, this is even planned to be increased up to 700 W for e.g. the Einstein Telescope High-Frequency detector (ET-HF) [19]. On the other hand, ET-LF is planned to have around 5 W laser power [19]. Nevertheless,

demonstrating good PRN modulation quality on the used narrow-linewidth laser at such power levels needs to be done. PRN modulation is commonly used in fiber amplifiers to suppress Brillouin scattering [187–189], realizing power levels of several kW [190, 191], however, with a linewidth in the GHz-range [191]. Nevertheless, this is a promising indication that high quality PRN modulation at high powers is feasible. Additionally, similar approaches for fiber based amplifiers are also investigated for GWDs [192–194].

11.2.1 A pseudo-white-light DRFPMI

The optical layout of GWDs, as described in Sec. 2.3.2, consist of a Michelson interferometer enhanced with several cavities. One in each arm, one for power-recycling and one for signal-recycling, forming a dual-recycled Fabry-Perot-Michelson interferometer (DRFPMI). The complexity of using *tunable coherence* in a GWD thus moves from a simple white light interferometer to creating a *pseudo-white-light* DRFPMI. In order to achieve this, all cavity lengths have to be matched to the recoherence length of the used PRN sequence. So a common minimal length has to be found or created of which all lengths of the setup are integer multiples of. This implies that all cavity lengths and the arms of the interferometer need to be equally long up to multiples of the chosen recoherence length. Thus, the shortest cavity or asymmetry determines the longest possible sequence, even though the several kilometers long arms would allow for very long sequences. In many layouts, this shortest length would be the Schnupp Asymmetry. As it therefore has the most implications for *tunable coherence*, it is discussed separately in Sec. 11.2.3.

Using the LIGO detectors as am example, the two recycling cavities are already close in length. With the SRC at 56 m and the PRC at 57.7 m [17], they have a mismatch of 3.4 m in round-trip length. Adjusting this by only 6 mm would yield a usable recoherence length of $d_{\mathrm{coh}} \approx 3.394\,\mathrm{m}$ which would fit $\alpha_{\mathrm{SRC}} = 33$ and $\alpha_{\mathrm{PRC}} = 34$ times (eq 9.1: $\alpha = l_{\mathrm{cav}}/d_{\mathrm{coh}}$) into the respective cavities. Thus by lengthening the SRC by 1 mm and shortening the PRC by 2 mm, they could be matched to the same PRN sequence. However, keeping these lengths would still reduce the usable sequence length considerably compared to the cavity length. It would thus be more beneficial if the two cavities could either be identical in length or their relative offset increased. For such changes, important considerations are, however, also the implications on the bandwidth and Gouy-phase of the cavities.

The arm cavities are already identical in length at 3994.5 m [17], thus they fit the same PRN sequence automatically. However, they are around 23.8 cm too short to be matched with the recycling cavities. If lengthened, they would fit $\alpha_{\mathrm{FPC}} = 2354$ multiples of the same 3.394 m recoherence length. Excluding the Schnupp-Asymmetry, only slight adjustments would be needed to turn the LIGO detectors into a *pseudo-white-light* DRFPMI using *tunable coherence*. This would allow for strong straylight suppression needing only relative delays on the low cm-scale ($d_{\mathrm{chip}} \approx 3\,\mathrm{cm}$) to be effective.

11.2.2 Mode-cleaner and auxiliary optics

More constraining than the cavities in the main interferometer are the input mode cleaner (IMC) and output mode cleaner (OMC), as well as auxiliary optics, which also have to comply with the length constraints added by *tunable coherence*.

For the auxiliary optics excluding the mode cleaner, the concept is relatively simple. If interference is needed, for example to measure a signal in reference to a local oscillator (LO), length matching is needed. However, especially for recoherence lengths on the order of meter, this is not a simple, but also not an impossible task. More challenging could be the needed precision in the length matching of the LO for a balanced-homodyne-detector (BHD) readout scheme. This is planned to be implemented during the next interferometer upgrades at LIGO [18, 108] and also for ET [19]. In this part of the detector, it is crucial to not loose any sensitivity. Thus, extra effort might have to be put into highly precise control of the LO's relative delay to the readout. This readout scheme would also add a second OMC for the LO, however, this would give the same constraints as the existing OMC. The presented Sagnac interferometer results (Sec. 8.2.1) showed that a BHD scheme does work with *tunable coherence*. Even though, it is likely that this demonstration did suffer from a length mismatch of the LO. However, in this case, so far no additional effort was put into precisely matching or controlling the relative delay microscopically.

For the mode cleaners, the situation is a little more complicated, at least for the OMC. An overview of the relevant lengths and described changes can be found in Figure 11.1. The IMC has an optical path length of $\sim$32.945 m and is thus quite close to be matchable with the other cavities. Using the aforementioned recoherence length of 3.394 m, the IMC would need to be roughly a meter longer to match it tenfold. If the recoherence length would, alternatively, be set to a tenth of the IMC length, the other cavities would have to be adjusted slightly differently. This new length would fit $\alpha_{\mathrm{SRC}} = 34$ and $\alpha_{\mathrm{PRC}} = 35$ times into the recycling cavities if they are 6.5 mm longer and 4.625 cm shorter respectively. The arm cavities would fit $\alpha_{\mathrm{FPC}} = 2425$ multiples of the length, if they are 8.125 cm longer.

A different story is the OMC, as it is significantly shorter. The purpose of the OMC is to isolate the carrier mode and audio-frequency sidebands carrying the GW signal from any higher order modes and the RF sidebands used for interferometer control. Its design is a non-trivial combination of different parameters to optimize it for this purpose [195]. To optimize frequency spacing between carrier and unwanted modes, a specific ROC is used for the mirrors, which are bonded onto a glass breadboard to increase stability. From the choice of mirrors, the optimal length is chosen by minimizing the transmission of the unwanted sidebands and higher order modes [195]. This length is 1.132 m [195] and as the OMC is a bow-tie cavity, this also gives the maximal recoherence length fitting it. While such a length is not impossible to realize, it would reduce the expected suppression for a PRN frequency of 10 GHz to around 31.6 dB. The IMC would then need to be 11.7 cm

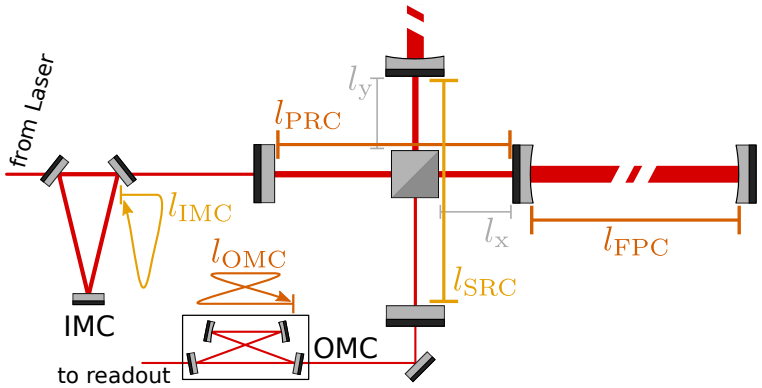

	l_{OMC} (α_{OMC})	l_{IMC} (α_{IMC})	l_{SRC} (α_{SRC})	l_{PRC} (α_{PRC})	l_{FPC} (α_{FPC})	suppression ~10 GHz
currently	1.132 m	32.945 m	56 m	57.7 m	3994.5 m	-
excluding OMC $d_{coh} = 3.394$ m	-	33.94 m +995 mm (10)	56.001 m +1 mm (33)	57.698 m -2 mm (34)	3994.738 m +238 mm (2354)	41 dB
excluding OMC $d_{coh} = 3.2945$ m	-	32.945 m (10)	56.0065 m +6.5 mm (34)	57.653 75 m -46.25 mm (35)	3994.581 25 m +81.25 mm (2425)	41 dB
current OMC $d_{coh} = 1.132$ m	1.132 m (1)	32.828 m -117 mm (29)	56.034 m +34 mm (99)	57.732 m +32 mm (102)	3994.262 m -238 mm (7057)	31.6 dB

Figure 11.1: Sketch of the for *tunable coherence* relevant lengths in the LIGO detectors. The table below summarizes needed adjustments and length changes to make the full layout compatible with *tunable coherence*. For this, it is assumed that the inner Michelson arms are equal, $l_x = l_y$, meaning there is no Schnupp Asymmetry. Therefore, the PRC and SRC lengths are also simplified as sketched instead of taking the average inner Michelson arm length.

shorter to fit 29 multiples of it and the recycling cavities would fit to $\alpha_{SRC} = 99$ and $\alpha_{PRC} = 102$ multiples if 3.4 cm and 3.2 cm longer respectively. Finally, the arm cavities would need to be 23.8 cm shorter, to fit $\alpha_{FPC} = 7057$ multiples. An alternative would be to change the length of the OMC to fit a longer recoherence length. However, to which degree this is possible without sacrificing its performance would need to be determined.
With these α-values of d_{coh} multiples fitting the different cavities, a quick estimate of remaining coherence width in the cavities can be done using eq. 9.4. For the arm cavities with a finesse of ~200, this FWHM already shrinks down to around a tenth or less of the wavelength. While it is not clear how well the equation is holding up for such high α-values, it is likely that especially the arm cavities would have to be controlled in macroscopic length with a precision of a single wavelength. The high numbers of repetitions also put very strict requirements on the modulation quality. Whether these are possible to achieve will need to be verified beforehand.
Nevertheless, even when considering both mode cleaner, the needed changes to make the LIGO detectors compatible with *tunable coherence* are minor. With changes on the cm-scale, a suppression of more than 30 dB for unmatched straylight could be realizable.

11.2.3 The elephant in the room - the Schnupp Asymmetry

The most obvious problem when it comes to the implementation of *tunable coherence* in a gravitational wave detector (GWD) is the Schnupp Asymmetry [152]. This intentional macroscopic arm length difference ($l_x \neq l_y$) in the inner Michelson interferometer[48] is too large to be ignored and too small to allow reasonable sequence lengths to fit. For the LIGO detectors it is 8 cm long [1, 17], implying a needed recoherence length of 16 cm. To make a 15 chips long PRN sequence fit into this, the PRN frequency would have to be about 28.1 GHz for a theoretical suppression of around 23.5 dB. This is certainly not unfeasible but technically more challenging than what was demonstrated here. Additionally, having a short recoherence length allows straylight at all multiples of it to couple coherently again. It further limits the achievable PRN sequence length considerably, keeping the shape of its auto-correlation function (ACF) farther from the ideal δ-peak. It might therefore be beneficial to omit the Schnupp Asymmetry when using *tunable coherence*, not least to reduce the risk of accidentally delay-matched straylight.

A full analysis whether this is feasible under all circumstances is beyond the scope of this work, a brief assessment of possible options is, however, considered. The Schnupp Asymmetry was proposed by Lise Schnupp in the 1980s [152] and allows modulation sidebands to reach the asymmetric port of an interferometer while it is microscopically at dark-fringe. This is due to the sidebands frequency-shift allowing them to slightly diverge from the microscopic phase-tuning of the carrier. Thus while the carrier is at dark-fringe, the sidebands are not. In the locking sequence of the LIGO detectors, the sideband at $f_{sb} = 45\,\text{MHz}$ is leaking into the SRC due to the asymmetry [1, 196]. Error signals derived from it are then used to keep the inner Michelson and the SRC on their respective operating points [93, 196]. Thus, without the Schnupp Asymmetry, other methods would be needed to generate error signals for these two degrees of freedom.

Locking the inner Michelson using a different signal independent from the Schnupp Asymmetry is in general possible [197]. An option would be the other modulation sideband (at 9 MHz) which is not leaking into the SRC. However, the currently used approach making use of the asymmetry has the highest SNR [197]. Nevertheless, further optimization could be considered and locking of the inner Michelson is a solvable problem.

An alternative for locking the SRC can not as easily be found within the currently employed error signal generation. However, other approaches are possible, even though they require additions to the setup. Adya [198] proposed a technique using an additional laser beam which is frequency shifted to the main carrier and injected from the readout side. This sub-carrier beam can then be used to lock the SRC by employing the PDH technique, similar to the locking of the PRC from the interferometer input side. Principle functionality of this technique was shown in experimental demonstrations at GEO600 [199].

[48] the interferometer formed between the beam splitter and the two arm cavities

In the case that removing the Schnupp Asymmetry is impossible or undesirable after all, an alternative solution would be needed. Choosing a PRN sequence short enough to fit the current length scale of implemented asymmetries would be one option. However, this has all the aforementioned drawbacks regarding suppression and PRN frequency, as well as the higher likelihood of straylight accidentally having a delay fitting any integer multiple of such a short recoherence length. It could therefore be more beneficial to increase the Schnupp Asymmetry such that a longer sequence would fit into it. Alternatively, the parameter space of usable modulation sequence is not limited to the here used *m*-sequences such that the possibility of more suitable sequences could be investigated.
On a general note, it might be beneficial to separate the employed locking schemes from the modulated laser beam to decouple degrees of freedom. This could be done by using secondary beams analogous to the mentioned sub-carrier approach for the SRC. Currently, the arm cavities of the LIGO detector are already locked using frequency doubled auxiliary lasers injected from behind the ETMs [1, 196]. Extending this to the other cavities would allow to separate the locking of them from any PRN modulation influence before bringing them into resonance with the modulation.

11.2.4 *Tunable coherence* and squeezed light

Lastly, all GWDs employ squeezed light in order to reduce quantum noise. It is therefore indispensable that *tunable coherence* can be combined with this technique.
According to the Heisenberg uncertainty principle, the two observables of the EM field cannot surpass the standard quantum limit. Thus, the two quadratures of the field, or amplitude and phase of an EM wave, cannot be measured simultaneously with unlimited precision. This gives rise to the quantum noise of the detector, of which shot noise is the relevant noise source at higher and radiation pressure noise at lower frequencies [64]. While precise measurement of both observables simultaneously is not possible, the precision for one can be increased on the expense of the other. This is called squeezing as the formerly equal uncertainty is "squeezed" in one parameter as depicted in Figure 11.2 [8, 63]. The

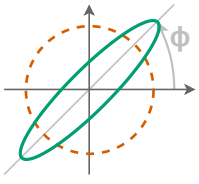

Figure 11.2: Depiction of a squeezed vacuum state in the quadrature plane. In green the squeezing ellipse and in orange the unsqueezed vacuum state for comparison. The phase Φ determines the squeezed quadrature (relative to the carrier field).

resulting elliptical shape illustrates how one quadrature can be determined more precisely while the precision in the orthogonal one is reduced. The rotation or phase of this ellipse determines which observable is squeezed [64].
For a GWD, the noise couples through fluctuations in the the vacuum field entering the detector via the output path [67, 68]. Thus, squeezed vacuum states are injected at the

output Faraday isolator (FI) to reduce the quantum noise. The squeezed quadrature, or noise component, is determined by the phase of the squeezing ellipse in relation to the carrier field in the interferometer [64]. As *tunable coherence* introduces phase flips of 180°, the phase between carrier and squeezed field undergoes the same flips. However, a rotation of the squeezing ellipse by 180° results in the same quadrature being squeezed. Therefore, the critical part in combining *tunable coherence* with squeezing is the finite time in which the phase is changed between the chips. Even though this happens at frequencies far above the measurement bandwidth, it introduces additional phase noise relative to the squeezed field. Any phase noise degrades the squeezing, also when stemming from higher frequencies. Stabilizing the modulation depth to minimize phase noise is thus important. Even then, further investigations to what degree *tunable coherence* negatively impacts squeezing are needed. Especially relevant here are these switching times between chips, as they can constitute significant phase errors if not instantaneous. Thus, deeper analysis of this effect and slew-rate optimization as discussed in Sec. 11.1 should be prioritized.

Another aspect is the squeezing angle control. This is done using a heterodyne control field that co-propagates with the squeezed light through the detector and is then interfered with the carrier [63, 64]. Similar as in digitally enhanced heterodyne interferometry (sec. 5.2.1), this control signal would have to be demodulated when using *tunable coherence*.

In conclusion, assuming that *tunable coherence* can be combined with the use of squeezed light seems reasonable. Nevertheless, further studies need to be done to verify this. Additionally, the approach of imprinting the same PRN sequence onto the squeezed light could be investigated.

11.3 Planning *tunable coherence* for ET

Contrary to the existing detectors which would need to be altered, future detectors could be planned so that they are compatible with *tunable coherence*. A prime candidate is the Einstein Telescope Low-Frequency detector (ET-LF) as it is the part of ET that needs to be most sensitive at low frequencies. Additional, its relatively low laser power of 5 W [19] simplifies the implementation of *tunable coherence*.

A rough estimate of how *tunable coherence* could be implemented in ET-LF can be done by taking currently available data from the ET design report [19] and optical layout proposals [200, 201]. In the current planning phase, the precision scale is not yet on the level where a Schnupp Asymmetry needs to be considered. However, for the reasons discussed in Sec. 11.2.3 it is likely that one will be implemented. As also discussed in that section, to make *tunable coherence* work, the asymmetry would either have to be large enough to fit a reasonable PRN sequence, meaning on the scale of at least 0.5 to 1 m. Or, alternatively, be omitted with other locking schemes implemented that do not rely on it.

Assuming the layout does not have a Schnupp Asymmetry, the most stringent restriction is again given by the OMC. If a Schnupp Asymmetry is needed, it would ideally match the round-trip length of the OMC. At the time of writing, no specific length for the OMC is determined besides it being table-top size. Even though, adjusting it to $\sim$10 m or even $\sim$30 m is categorized to fall only into "*small*" to "*medium*" impact changes to the current design. However, conservatively it should be expected that the length will be similar to the LIGO OMC, due to similar requirements influencing its design (see Sec. 11.2.2). The next shortest round-trip length is then again the IMC, however, for ET-LF this is currently assumed to be 240 m, possibly going up to 300 m. Both recycling cavities are planned with a length of 165 m for the "10 km-Δ (triangle)" configuration [200], giving them identical round-trip lengths of 330 m. The arm cavities are also identical in length with 20 140 m round-trip length in the "10 km-Δ" configuration of ET-LF.

Dropping the assumption of a short OMC, the currently planned "10 km-Δ" layout would allow for significantly longer PRN sequences due to its longer IMC and matched recycling cavities. Shortening the arm cavities by 5 m makes a recoherence length of 30 m realizable in the "10 km-Δ" configuration. This could even be done with the "*medium*" impact change to the OMC. At $f_{\mathrm{PRN}} = 10$ GHz, it would theoretically allow for 60 dB of scattered light suppression, with α-values of 8 or 10 for the IMC, 11 for PRC and SRC and 671 for the arm cavities. And even using only $d_{\mathrm{coh}} = 10$ m, reducing the impact of the OMC length change to "*small*", would still give 50 dB suppression at the same PRN frequency. This latter length would fit all other cavities without adjustments, tripling their α-values. Both these recoherence lengths could also be adjusted to be a multiple of a shorter OMC length of around 1.5 m. This would again reduce the suppression to $\sim$30 dB but also the needed length increase of the arms to only 25 cm, while again increasing the α-values.

For the "15 km-L" configuration the recycling cavities are planned to be slightly longer at 168.6 m, thus 337.2 m round-trip length [201]. The arms are also longer and have 30 100 m round-trip length in this layout. The length matching is thus less straight forward. To avoid changes on the order of tens of meters, choosing a recoherence length of around 3.24 m seems more reasonable. This would fit 74 times into a 239.76 m long IMC and 104 times into recycling cavities of 168.48 m. Thus, changes of 24 cm and 12 cm would be necessary. The arm cavities would fit to 9290 times this length if adjusted by 40 cm. For the assumption of a short OMC, the chosen recoherence length could be halved to around 1.62 m, still fitting with the previously described adjustments but doubled α-values.

For all considered options, the α-value of the arm cavities comes close to or easily exceeds 1000 in both layouts. This puts even higher requirements on the modulation consistency and is expected to reduce the coherence length down to a wavelength or even below ($\lesssim$140 nm, see eq. 9.4 and Sec. 11.1.2). For comparison, the minimal scattered light delay in the arms for a baffle to beam clearance of 5 cm would be around half a wavelength.

However, this would not be the primarily by *tunable coherence* targeted straylight.
In general, a properly fitting recoherence length would need to be determined once more concrete design parameters are started to be fixed, especially for the OMC. As this is the most critical length constraint and if bonded not easily changeable, other cavity lengths should be derived from it. Adopting the ET-LF layout to be compatible with *tunable coherence* could be relatively straight forward due to the currently planned symmetrical recycling cavities and an IMC at a similar length. However, the immense numbers of repetitions needing to properly interfere without artifacts make a clean implementation of *tunable coherence* in ET even more challenging than it would already be for LIGO.

11.4 Other applications of *tunable coherence*

While the focus of this work is on the use of *tunable coherence* in GWDs, there are other applications that could benefit from it. The obvious ones are other interferometric setups encountering scattered light. Examples of this are gyroscopes [170] and ring laser [169, 171] used to e.g. measure Earths rotation. For these, especially the ability of *tunable coherence* to suppress backscatter as discussed in Sec. 8.2.2 could be very beneficial. This additional noise source, relevant in ring resonators specifically [174–177], is so far only reducible in post-processing [178, 179]. Further, it is also one of the reasons Sagnac-like topologies are currently not a realistic alternative for GWDs, even though they have certain advantages regarding quantum noise reduction [166–168].
Another aspect of *tunable coherence* that could be of interest is the ability of determining an absolute length of e.g. a cavity, up to multiples of the used recoherence length. As the power build-up inside a resonator is sensitive to only slight mismatches between round-trip and recoherence length, these can be measured with good precision. Thus, given a well known PRN frequency or reference clock for it, cavity lengths or mirror positions could be measured and adjusted precisely also on a macroscopic scale.
Lastly, it is worth mentioning that *tunable coherence* introduces a new controllable parameter to the cavity operation. By creating the new resonance condition depending on macroscopic length, cavity behavior like power build-up can be changed without altering the physical cavity setup. Thus, the effective finesse of a cavity can be changed without having to e.g. divert from optimal operating points by simply employing a different PRN sequence. Data obtained in the experiments described in Ch. 9 and simulations described in Ch. 6 demonstrate, that choosing the ratio of cavity and sequence length can allow for reduction of effective finesse by a wide range of values. Further, as the modulation depth can be tuned in real-time, the ratio between PRN modulated and unmodulated carrier can thus be changed likewise. How useful these aspects can be in various applications of optical resonators in different research areas remains to be seen.

12 | Conclusion

Since the first detection of gravitational waves in 2015, the network of currently existing detectors has initiated the new field of gravitational wave astronomy. Thereby, they expanded the field of multi-messenger astronomy with an important new contributor. Increasing the detectors sensitivity now towards low frequencies (below 10 Hz) not only allows for the detection of more and new sources, it also enables earlier detection of them. Thus, this technically challenging endeavor is immensely beneficial for future observations and the scientific impact of future observatories like the Einstein Telescope (ET).
A major limiting noise sources in this frequency region is scattered or straylight. Already at current sensitivity levels, this becomes increasingly apparent and is expected to become an even bigger challenge as sensitivities increase. Just projecting the currently known straylight noise contributions to design parameters of planned third-generation detectors raises major concerns. Including the possibility of additional straylight noise contributions that might be unveiled when pushing sensitivities further, it becomes unmistakable that currently used approaches are more of a Band-Aid. Further improving existing mitigation techniques, but especially finding and investigating new ones is thus an essential risk reduction, potentially yielding a more fundamental and permanent solution.
This work successfully demonstrates the experimental implementation of a technique for straylight reduction that was already considered at the beginning of gravitational wave detection. While technically unfeasible at that time, it is now a viable concept reaching strong straylight suppression. By creating a *pseudo-white-light* interferometer with the use of GHz-phase modulation, it allows for precise coherence control. Thus, the incredible coherence achieved by the science laser of a gravitational wave detector can be sustained when needed but strongly reduced otherwise. In turn, this hinders the coherent interference of scattered or straylight with the detector's readout.
In the presented work, this technique called *tunable coherence* was first successfully simulated, with a special focus on its interaction with optical resonators. Following these promising results, experimental proof-of-concept demonstrations for different optical layouts were achieved. In a Michelson interferometer, straylight suppression of more than 40 dB was shown with a PRN frequency of 1 GHz. In this case, the remaining coherence was reduced to significantly below a meter. Further increasing the PRN frequency to 10 GHz then resulted in remaining coherence lengths below 10 cm and straylight suppression of more than 30 dB.

Similarly, straylight suppression in a Sagnac interferometer was demonstrated. These results were, however, more constraint by experimental limitations. After successful verification of *tunable coherence* in these interferometer topologies, its compatibility with optical resonators was shown. In a cavity matched in length to the repetition of the PRN sequence, meaning to the newly introduced recoherence length, the known, undisturbed cavity behavior was demonstrated. This was done at PRN frequencies between 1 GHz and 10 GHz. A clear dependency of the newly introduced macroscopic resonance on remaining coherence length and number of repetitions fitting the cavity was observed. By using a PRN frequency of 10 GHz and the shortest available sequence, a resonance width of only 4 µm was achieved. With the available data, a preliminary empirical description of this resonance was found. From it, indications were seen that reaching a regime of wavelength and even sub-wavelength scale coherence is likely realizable, especially in long cavities. Challenges induced by such short coherence lengths were outlined and interesting implications for further studies identified.

A further experimental step towards enhanced layouts like the ones used in gravitational wave detectors was eventually taken. By using a power-recycled Michelson setup, an initial demonstration of *tunable coherence* in a more complex layout was achieved. Here, however, new challenges and current experimental limitations hindered a fully satisfactory demonstration. General compatibility could be shown, still, further work will need to be done to fully demonstrate *tunable coherence* in more demanding setups.

Finally, the implications and examples for implementations of *tunable coherence* were discussed. Focusing on gravitational wave detectors, needed changes like removal or lengthening of the so-called Schnupp Asymmetry and adjustments to the different cavity lengths were considered. The output mode cleaner could be identified as the most probable minimal length defining component of the layout. It was estimated that needed adjustments for its length to be more favorable would, however, constitute just a "*medium impact*" change in the case of the ET design. Other needed changes for making detector layouts compatible with *tunable coherence* were identified to be only of at most around half a meter or "*small impact*" changes for the layout of ET. Further, other needed verification steps like compatibility with squeezed light injection and general stability and sensitivity requirements were discussed and outlined. A final thought was given on opportunities of using *tunable coherence* in other fields than gravitational wave detection. In this regard, its ability to introduce a new controllable parameter into the operation of optical cavities that is tunable without needing changes to the physical setup can be highlighted.

Ultimately, this work achieved a first experimental demonstration of a long envisioned straylight suppression technique. While further work needs to be done, this opens new prospects for dealing with one of the major technical challenges in high-precision laser interferometry, potentially immediately benefiting table-top scale experiments of this kind.

Acronyms

$\lambda/2$-plate	half-wave-retardation plate 86
$\lambda/4$-plate	quarter-wave-retardation plate 86
m-sequence	maximum-length sequence 56–58, 62, 64, 65, 67, 73, 80, 92, 93, 102, 113, 160, 169
ACF	auto-correlation function ix, 55, 57, 58, 60–62, 64, 66, 73, 75, 93, 97, 111–114, 118, 120, 160, 168
AOM	acousto-optic modulator 88, 101
AR	anti-reflective 34
ASD	amplitude spectral density 48, 49, 72, 74, 75, 111
BD	balanced-detector 46, 48, 49
BHD	balanced-homodyne-detector x, 43, 45–50, 83, 122, 124, 130, 147, 166
BPD	balanced photo-detector 103–106
BRDF	bidirectional reflectance distribution function 33
BS	beam splitter 105, 143, 144
CE	Cosmic Explorer 14, 26, 42
DARM	differential arm length change 35, 75
DBR	*dual balanced readout* 45–47, 51, 52
DI	digital interferometry 15, 53, 55, 58–61, 69
DLI	delay-line interferometer 103
DRFPMI	dual-recycled Fabry-Perot-Michelson interferometer 27, 165
EM	electro-magnetic 18, 20, 22–24, 169
EOM	electro-optic modulator i, v, vii, x, 86–88, 92–94, 97–101, 104, 106, 108, 120, 124, 132, 133, 147, 160
ESD	electrostatic drive 33, 35, 40
ET	Einstein Telescope 14, 24, 26, 29, 37, 42–44, 166, 170, 172–174

ET-HF	Einstein Telescope High-Frequency detector 164
ET-LF	Einstein Telescope Low-Frequency detector 37, 164, 170–172
ETM	end test mass 33, 34, 40, 44, 169
FI	Faraday isolator 40, 86, 170
FINESSE	**F**requency domain **in**terf**e**rometer **s**imulation **s**oftwar**e** 71, 81, 83
FPC	Fabry-Perot cavity 26, 29, 32, 128, 157
FPGA	field programmable gate array i, 58, 88–94, 104, 106, 114, 132, 133, 138, 143, 160
FPMI	Fabry-Perot Michelson interferometer 127, 143, 156–158
FR	Faraday rotator 48, 50, 143
FSR	free spectral range 148
FWHM	full-width-half-maximum 55, 78, 137–142, 149, 151, 152, 167
GPS	global positioning system 59
GR	General Theory of Relativity 17, 20, 29
GW	gravitational wave xii, 15, 18–27, 29, 31, 34, 43, 49, 52, 67, 109–111, 122, 126, 146, 152, 153, 155, 166
GWD	gravitational wave detector 13, 15, 24, 25, 27, 31, 37, 43, 45, 50, 51, 53, 61, 66, 67, 69, 71, 74, 79, 85, 107, 109, 122, 131, 142, 156, 157, 159, 161, 162, 164, 165, 168, 169, 172
HV	high voltage vii, x, 109, 146, 147
ifoTDS	interferometer Time-Domain Simulation 80–83, 127
ILA	integrated logic analyzer 93
IMC	input mode cleaner 27, 30, 42, 166, 171, 172
IP	intellectual property 89, 91
KAGRA	Kamioka Gravitational Wave Detector 13, 22, 23
LED	light emitting diode 90–92
LFSR	linear feedback shift register v, 56–58, 90–92
LHO	LIGO Hanford Observatory 27, 28, 34–36
LIGO	Laser Interferometer Graviational-Wave Observatory vi, 13, 22, 23, 25–28, 30, 33–35, 39–41, 44, 164–169, 171, 172, 176, 177

LISA	Laser Interferometer Space Antenna 22, 43, 59
LLO	LIGO Livingston Observatory 27, 35
LO	local oscillator vii, 48, 50, 52, 59, 61, 123–125, 166
LSB	least significant bit 56
LVDS	low-voltage differential signaling 89, 95, 96, 101
MSB	most significant bit 56, 57
MZ	Mach-Zehnder 103–106
Nd:YAG	neodymium-doped yttrium aluminum garnet 85
NPRO	non-planar ring oscillator 85, 148
O3	observation run 3 22, 23, 27, 35, 36
O4	observation run 4 25, 27, 28, 39
OMC	output mode cleaner 27, 39, 166, 167, 171, 172
OpAmp	operational amplifier 95
PBS	polarizing beam splitter 86
PD	photo-detector i, vii, x, 28, 44, 53, 73, 86, 94, 101–104, 132, 147
PDH	Pound-Drever-Hall x, 77–79, 86, 133–137, 142, 146, 163, 168
PLL	phase-locked loop 133
PRC	power-recycling cavity x–xii, 26, 51, 115, 143, 145–153, 155, 165, 167, 168, 171
PRFPMI	power-recycled Fabry-Perot Michelson interferometer 157
PRM	power-recycling mirror 26, 51, 52, 143–145
PRMI	power-recycled Michelson interferometer x–xii, 15, 115, 143–146, 152–160
PRN	pseudo-random-noise i–iii, v, viii, xii, xiii, 14, 53–69, 71–83, 85–99, 101, 103–108, 110–127, 130–145, 148–156, 158–166, 168–174
PTA	pulsar timing array 22–24
PZT	piezo-electric actuated x, 46, 48–50, 108–110, 115, 120, 123, 124, 127, 130, 132, 134, 144, 146, 148, 156
RF	radio frequency 113, 132, 133, 135, 166
RMS	root-mean-square 36, 38
ROC	radius of curvature 132, 144, 166

SNR	signal-to-noise-ratio 27, 28, 39, 49, 99, 125, 154–156, 158, 168
SoC	system on a chip 89, 91, 93
SRC	signal-recycling cavity 26, 131, 165, 167–169, 171
SRFPMI	signal-recycled Fabry-Perot Michelson interferometer 157
SRM	signal-recycling mirror 26, 39
SSM	Sagnac Speed Meter 122, 127, 128
TX	transceiver 89
VHDL	VHSIC Hardware Description Language iii, 90
XNOR	exclusive NOR 56
XOR	exclusive OR 56

List of Figures

List of Publications

[23] **Daniel Voigt**, André Lohde, and Oliver Gerberding. Simulating tunable coherence for scattered light suppression in laser-interferometric gravitational wave detectors. *Applied Physics Letters*, 123, July 2023. doi: 10.1063/5.0148790.

[22] André Lohde, **Daniel Voigt**, and Oliver Gerberding. Dual balanced readout for scattered light noise mitigation in Michelson interferometers. *Physical Review D*, 111: 022004, Jan 2025. doi: 10.1103/PhysRevD.111.022004.

[24] **Daniel Voigt**, L. Eggers, K.-S. Isleif, S. M. Koehlenbeck, M. Ast, and O. Gerberding. Tunable coherence laser interferometry: demonstrating 40dB of straylight suppression and compatibility with resonant optical cavities. *Physical Review Letters*, 134:213802, May 2025. doi: 10.1103/PhysRevLett.134.213802.

[25] Leonie Eggers, **Daniel Voigt**, and Oliver Gerberding. Scattered light reduction in Sagnac Speed Meters with Tunable Coherence. *Physical Review D*, 112:022001, July 2025. doi: 10.1103/PhysRevD.112.022001.

In addition to the listed publications, the following is submitted for publication:

Daniel Voigt and Oliver Gerberding. Using tunable coherence for reaching micrometer coherence lengths and suppressing stray light in a power-recycled Michelson interferometer. Submitted to: *Physical Review D*, doi: 10.48550/arXiv.2508.00503

Bibliography

[1] J. Aasi, B. P. Abbott, R. Abbott *et al.* Advanced LIGO. *Classical and Quantum Gravity*, 32:074001, 4 2015. doi: 10.1088/0264-9381/32/7/074001.

[2] B. P. Abbott, R. Abbott, T. D. Abbott *et al.* Observation of Gravitational Waves from a Binary Black Hole Merger. *Phys. Rev. Lett.*, 116:061102, Feb 2016. doi: 10.1103/PhysRevLett.116.061102.

[3] B. P. Abbott, R. Abbott, T. D. Abbott *et al.* GW150914: The Advanced LIGO Detectors in the Era of First Discoveries. *Phys. Rev. Lett.*, 116:131103, 2016. doi: 10.1103/PhysRevLett.116.131103.

[4] B. P. Abbott, R. Abbott, T. D. Abbott *et al.* Prospects for Observing and Localizing Gravitational-Wave Transients with Advanced LIGO, Advanced Virgo and KAGRA. *Living Reviews in Relativity*, 23:3, 12 2020. doi: 10.1007/s41114-020-00026-9.

[5] F. Acernese, M. Agathos, K. Agatsuma *et al.* Advanced Virgo: A Second-Generation Interferometric Gravitational Wave Detector. *Classical and Quantum Gravity*, 32: 24001, 1 2015. doi: 10.1088/0264-9381/32/2/024001.

[6] T. Akutsu, M. Ando, K. Arai *et al.* Overview of KAGRA: Detector design and construction history. *Progress of Theoretical and Experimental Physics*, 2021, 5 2021. doi: 10.1093/ptep/ptaa125.

[7] H. Lück, C. Affeldt, J. Degallaix *et al.* The upgrade of GEO 600. *Journal of Physics: Conference Series*, 228:12012, 5 2010. doi: 10.1088/1742-6596/228/1/012012.

[8] J. Abadie, B. P. Abbott, R. Abbott *et al.* A Gravitational Wave Observatory Operating Beyond the Quantum Shot-Noise Limit. *Nature Physics*, 7:962–965, 9 2011. doi: 10.1038/nphys2083.

[9] D. Kasen, B. Metzger, J. Barnes *et al.* Origin of the Heavy Elements in Binary Neutron-Star Mergers from a Gravitational-Wave Event. *Nature*, 551:80–84, 2017. doi: 10.1038/nature24453.

[10] R. Abbott, T. D. Abbott, S. Abraham *et al.* GW190521: A Binary Black Hole Merger with a Total Mass of $150\,M_{\odot}$. *Phys. Rev. Lett.*, 125:101102, Sep 2020. doi: 10.1103/PhysRevLett.125.101102.

[11] B. P. Abbott, R. Abbott, T. D. Abbott *et al.* Multi-messenger Observations of a Binary Neutron Star Merger. *The Astrophysical Journal Letters*, 848:L12, 10 2017. doi: 10.3847/2041-8213/aa91c9.

[12] D. Reitze, R. X. Adhikari, S. Ballmer *et al.* Cosmic Explorer: The U.S. Contribution to Gravitational-Wave Astronomy beyond LIGO. *Bulletin of the AAS*, 51(7), 9 2019. URL https://baas.aas.org/pub/2020n7i035.

[13] E. D. Hall, K. Kuns, J. R. Smith *et al.* Gravitational-Wave Physics with Cosmic Explorer: Limits to Low-Frequency Sensitivity. *Phys. Rev. D*, 103:122004, 6 2021. doi: 10.1103/PhysRevD.103.122004.

[14] M. Punturo, M. Abernathy, F. Acernese *et al.* The Einstein Telescope: A Third-Generation Gravitational Wave Observatory. *Classical and Quantum Gravity*, 27 (19):194002, 9 2010. doi: 10.1088/0264-9381/27/19/194002.

[15] Einstein Telescope Steering Committee and Science Team. Einstein Telescope: Science Case, Design Study and Feasibility Report. Technical report, ET-0004A-20, 8 2020. URL https://apps.et-gw.eu/tds/ql/?c=15284.

[16] A. Abac, R. Abramo, S. Albanesi *et al.* The Science of the Einstein Telescope. *unpublished*, 15, 3 2025. URL http://arxiv.org/abs/2503.12263.

[17] A. Buikema, C. Cahillane, G. L. Mansell *et al.* Sensitivity and Performance of the Advanced LIGO Detectors in the Third Observing Run. *Phys. Rev. D*, 102, 2020. doi: 10.1103/PhysRevD.102.062003.

[18] E. Capote, W. Jia, N. Aritomi *et al.* Advanced LIGO Detector Performance in the Fourth Observing Run. *Phys. Rev. D*, 111:062002, Mar 2025. doi: 10.1103/PhysRevD.111.062002.

[19] Einstein Telescope Steering Committee Editorial Team. Design Report Update 2020 for the Einstein Telescope. Technical report, ET-0007B-20, 9 2020. URL https://apps.et-gw.eu/tds/?content=3&r=17245.

[20] P. Nguyen, R. M. S. Schofield, A. Effler *et al.* Environmental Noise in Advanced LIGO Detectors. *Classical and Quantum Gravity*, 38, 2021. doi: 10.1088/1361-6382/ac011a.

[21] S. Soni, J. Glanzer, A. Effler *et al.* Modeling and Reduction of High Frequency Scatter Noise at LIGO Livingston. *Classical and Quantum Gravity*, 41:135015, 7 2024. doi: 10.1088/1361-6382/ad494a.

[22] A. Lohde, D. Voigt and O. Gerberding. Dual Balanced Readout for Scattered Light Noise Mitigation in Michelson Interferometers. *Phys. Rev. D*, 111:022004, 1 2025. doi: 10.1103/PhysRevD.111.022004.

[23] D. Voigt, A. Lohde and O. Gerberding. Simulating Tunable Coherence for Scattered Light Suppression in Laser-Interferometric Gravitational Wave Detectors. *Applied Physics Letters*, 123, 7 2023. doi: 10.1063/5.0148790.

[24] D. Voigt, L. Eggers, K.-S. Isleif *et al.* Tunable Coherence Laser Interferometry: Demonstrating 40dB of Straylight Suppression and Compatibility with Resonant Optical Cavities. *Phys. Rev. Lett.*, 134:213802, May 2025. doi: 10.1103/PhysRevLett.134.213802.

[25] L. Eggers, D. Voigt and O. Gerberding. Scattered Light Reduction in Sagnac Speed Meters with Tunable Coherence. *Phys. Rev. D*, 112:022001, Jul 2025. doi: 10.1103/PhysRevD.112.022001.

[26] Albert Einstein. Die Grundlage der allgemeinen Relativitätstheorie. *Annalen der Physik*, 354:769–822, 1 1916. doi: 10.1002/andp.19163540702.

[27] Albert Einstein. Zur Elektrodynamik bewegter Körper. *Annalen der Physik*, 322 (10):891–921, 1905. doi: 10.1002/andp.19053221004.

[28] Hermann Minkowski. Die Grundgleichungen für die elektromagnetischen Vorgänge in bewegten Körpern. *Nachrichten von der Gesellschaft der Wissenschaften zu Göttingen, Mathematisch-Physikalische Klasse*, pages 53–111, 1908.

[29] C. W. Misner, K. S. Thorne and J. A. Wheeler. *Gravitation*. W. H. Freeman, 1973. ISBN 9780716703440.

[30] J. A. Wheeler and K. Ford. *Geons, Black Holes, and Quantum Foam: A Life in Physics*. W. W. Norton, 2010. ISBN 9780393079487.

[31] Karl Schwarzschild. Über das Gravitationsfeld eines Massenpunktes nach der Einsteinschen Theorie. *Sitzungsberichte der Königlich Preussischen Akademie der Wissenschaften*, pages 189–196, January 1916.

[32] J. R. Oppenheimer and G. M. Volkoff. On Massive Neutron Cores. *Physical Review*, 55:374–381, 2 1939. doi: 10.1103/PhysRev.55.374.

[33] J. R. Oppenheimer and H. Snyder. On Continued Gravitational Contraction. *Physical Review*, 56:455–459, 9 1939. doi: 10.1103/PhysRev.56.455.

[34] Roger Penrose. Gravitational Collapse: The Role of General Relativity. *Nuovo Cimento Rivista Serie*, 1:252, January 1969. doi: 10.1023/A:1016578408204.

[35] Albert Einstein. Näherungsweise Intergration der Feldgleichungen der Gravitation. *Sitzungsberichte der Königlich Preussische Akademie der Wissenschaften*, pages 688–696, January 1916. doi: 10.1007/978-3-662-57411-9_13.

[36] É. É. Flanagan and S. A. Hughes. The Basics of Gravitational Wave Theory. *New Journal of Physics*, 7:204–204, 9 2005. doi: 10.1088/1367-2630/7/1/204.

[37] Peter R. Saulson. *Fundamentals of Interferometric Gravitational Wave Detectors*. World Scientific Publishing Co. Pte. Ltd., second edition, 1994. ISBN 9789814350235. doi: 10.1142/9789814350235.

[38] Kip S. Thorne. Multipole Expansions of Gravitational Radiation. *Reviews of Modern Physics*, 52:299–339, 4 1980. doi: 10.1103/RevModPhys.52.299.

[39] Albert Einstein. Über Gravitationswellen. *Sitzungsberichte der Königlich Preussischen Akademie der Wissenschaften*, pages 154–167, January 1918. URL http://echo.mpiwg-berlin.mpg.de/MPIWG:8HSP60BU.

[40] R. A. Hulse and J. H. Taylor. Discovery of a pulsar in a Binary System. *The Astrophysical Journal*, 195:L51, 1 1975. doi: 10.1086/181708.

[41] J. M. Weisberg and Y. Huang. Relativistic Measurements from Timing the Binary Pulsar PSR B1913+16. *The Astrophysical Journal*, 829:55, 9 2016. doi: 10.3847/0004-637X/829/1/55.

[42] C. J. Moore, R. H. Cole and C. P. L. Berry. Gravitational-Wave Sensitivity Curves. *Classical and Quantum Gravity*, 32:015014, 1 2015. doi: 10.1088/0264-9381/32/1/015014.

[43] The LIGO Scientific Collaboration, The Virgo Collaboration and The KAGRA Collaboration. Search for Iintermediate-Mass Black Hole Binaries in the Third Observing Run of Advanced LIGO and Advanced Virgo. *Astronomy & Astrophysics*, 659:A84, 3 2022. doi: 10.1051/0004-6361/202141452.

[44] Aaron Geller. Masses in the Stellar Graveyard LIGO-Virgo-KAGRA, accessed: 28-04-2025. URL https://ligo.northwestern.edu/media/mass-plot/index.html.

[45] R. W. Hellings and G. S. Downs. Upper Limits on the Isotropic Gravitational Radiation Background from Pulsar Timing Analysis. *The Astrophysical Journal*, 265:L39–L42, February 1983. doi: 10.1086/183954.

[46] G. Agazie, A. Anumarlapudi, A. M. Archibald *et al.* The NANOGrav 15 yr Data Set: Evidence for a Gravitational-Wave Background. *The Astrophysical Journal Letters*, 951:L8, 7 2023. doi: 10.3847/2041-8213/acdac6.

[47] The LIGO Scientific Collaboration and The Virgo Collaboration. An Upper Limit on the Stochastic Gravitational-Wave Background of Cosmological Origin. *Nature*, 460:990–994, 8 2009. doi: 10.1038/nature08278.

[48] P. Binétruy, A. Bohé, C. Caprini *et al.* Cosmological Backgrounds of Gravitational Waves and eLISA/NGO: Phase Transitions, Cosmic Strings and other Sources. *Journal of Cosmology and Astroparticle Physics*, 2012:027–027, 6 2012. doi: 10.1088/1475-7516/2012/06/027.

[49] Nelson Christensen. Stochastic Gravitational Wave Backgrounds. *Reports on Progress in Physics*, 82:016903, 1 2019. doi: 10.1088/1361-6633/aae6b5.

[50] Andrew Liddle. *An Introduction to Modern Cosmology*. Wiley, 3rd edition, 6 2015. ISBN 978-1-118-50214-3.

[51] N. Aggarwal, O. D. Aguiar, A. Bauswein *et al.* Challenges and Opportunities of Gravitational-Wave Searches at MHz to GHz Frequencies. *Living Reviews in Relativity*, 24:4, 12 2021. doi: 10.1007/s41114-021-00032-5.

[52] B. P. Abbott, R. Abbott, T. D. Abbott *et al.* GW170817: Observation of Gravitational Waves from a Binary Neutron Star Inspiral. *Phys. Rev. Lett.*, 119:161101, 10 2017. doi: 10.1103/PhysRevLett.119.161101.

[53] M. L. Chan, C. Messenger, I. S. Heng *et al.* Binary Neutron Star Mergers and Third Generation Detectors: Localization and Early Warning. *Phys. Rev. D*, 97, 6 2018. doi: 10.1103/PhysRevD.97.123014.

[54] Joseph Weber. Detection and Generation of Gravitational Waves. *Phys. Rev.*, 117: 306–313, Jan 1960. doi: 10.1103/PhysRev.117.306.

[55] T. Schmirander, V. Miltchev, S. Rao *et al.* Concept Study of a Storage Ring-Based Gravitational Wave Observatory: Gravitational Wave Strain and Synchrotron Radiation Noise. *Phys. Rev. D*, 110:082002, Oct 2024. doi: 10.1103/PhysRevD.110.082002.

[56] C. Fabry and A. Perot. Theorie et applications d'une nouvelle methode de spectroscopie interferentielle. *Ann. Chim. Phys.*, 16:115–144, 1899.

[57] D. Fattaccioli, A. Boulharts, A. Brillet *et al.* Sensitivity of Multipass and Fabry-Perot Delay Lines to Small Misalignments. *Journal of Optics*, 17:115–127, 5 1986. doi: 10.1088/0150-536X/17/3/001.

[58] H. Billing, W. Winkler, R. Schilling *et al.* *The Munich Gravitational Wave Detector Using Laser Interferometry*, pages 525–566. Springer US, 1983. ISBN 978-1-4613-3712-6. doi: 10.1007/978-1-4613-3712-6_23.

[59] R. W. P. Drever, J. Hought, A. J. Munley *et al.* *Gravitational Wave Detectors Using Laser Interferometers and Optical Cavities: Ideas, Principles and Prospects*, pages 503–514. Springer US, 1983. doi: 10.1007/978-1-4613-3712-6_21.

[60] Brian J. Meers. Recycling in Laser-Interferometric Gravitational-Wave Detectors. *Phys. Rev. D*, 38:2317–2326, 10 1988. doi: 10.1103/PhysRevD.38.2317.

[61] G. Heinzel, K. A. Strain, J. Mizuno *et al.* Experimental Demonstration of a Suspended Dual Recycling Interferometer for Gravitational Wave Detection. *Phys. Rev. Lett.*, 81:5493–5496, 12 1998. doi: 10.1103/PhysRevLett.81.5493.

[62] Gerhard Heinzel. *Advanced Optical Techniques for Laser-Interferometric Gravitational-Wave Detectors*. PhD thesis, Leibniz Universität Hannover, 2 1999. URL https://repo.uni-hannover.de/handle/123456789/5674.

[63] D. Ganapathy, W. Jia, M. Nakano *et al.* Broadband Quantum Enhancement of the LIGO Detectors with Frequency-Dependent Squeezing. *Phys. Rev. X*, 13:041021, 10 2023. doi: 10.1103/PhysRevX.13.041021.

[64] W. Jia, V. Xu, K. Kuns *et al.* Squeezing the Quantum Noise of a Gravitational-Wave Detector Below the Standard Quantum Limit. *Science*, 385:1318–1321, 9 2024. doi: 10.1126/science.ado8069.

[65] D.V. Martynov, E.D. Hall, B.P. Abbott *et al.* Sensitivity of the Advanced LIGO Detectors at the Beginning of Gravitational Wave Astronomy. *Phys. Rev. D*, 93: 112004, 6 2016. doi: 10.1103/PhysRevD.93.112004.

[66] C. Bond, D. Brown, A. Freise *et al.* *Interferometer Techniques for Gravitational-Wave Detection*, volume 19. Springer International Publishing, 2016. ISBN 4111401600. doi: 10.1007/s41114-016-0002-8.

[67] Carlton M. Caves. Quantum-Mechanical Noise in an Interferometer. *Phys. Rev. D*, 23:1693–1708, 4 1981. doi: 10.1103/PhysRevD.23.1693.

[68] Carlton M. Caves. Quantum-Mechanical Radiation-Pressure Fluctuations in an Interferometer. *Phys. Rev. Lett.*, 45:75–79, 7 1980. doi: 10.1103/PhysRevLett.45.75.

[69] S. M. Aston, M. A. Barton, A. S. Bell *et al.* Update on Quadruple Suspension Design for Advanced LIGO. *Classical and Quantum Gravity*, 29:235004, 12 2012. doi: 10.1088/0264-9381/29/23/235004.

[70] S. Wen, R. Mittleman, K. Mason *et al.* Hydraulic External Pre-Isolator System for LIGO. *Classical and Quantum Gravity*, 31:235001, 12 2014. doi: 10.1088/0264-9381/31/23/235001.

[71] J. C. Driggers, J. Harms and R. X. Adhikari. Subtraction of Newtonian Noise Using Optimized Sensor Arrays. *Phys. Rev. D*, 86:102001, 11 2012. doi: 10.1103/PhysRevD.86.102001.

[72] M.W. Coughlin, J. Harms, J. Driggers *et al.* Implications of Dedicated Seismometer Measurements on Newtonian-Noise Cancellation for Advanced LIGO. *Phys. Rev. Lett.*, 121:221104, 11 2018. doi: 10.1103/PhysRevLett.121.221104.

[73] J. Harms, L. Naticchioni, E. Calloni *et al.* A Lower Limit for Newtonian-Noise Models of the Einstein Telescope. *The European Physical Journal Plus*, 137:687, 6 2022. doi: 10.1140/epjp/s13360-022-02851-z.

[74] K. Janssens, G. Boileau, N. Christensen *et al.* Impact of Correlated Seismic and Correlated Newtonian Noise on the Einstein Telescope. *Phys. Rev. D*, 106:042008, 8 2022. doi: 10.1103/PhysRevD.106.042008.

[75] K. Somiya, Y. Chen, S. Kawamura *et al.* Frequency Noise and Intensity Noise of Next-Generation Gravitational-Wave Detectors with RF/DC Readout Schemes. *Phys. Rev. D*, 73:122005, 6 2006. doi: 10.1103/PhysRevD.73.122005.

[76] C. Cahillane, G. L. Mansell and D. Sigg. Laser Frequency Noise in Next Generation Gravitational-Wave Detectors. *Optics Express*, 29:42144, 12 2021. doi: 10.1364/OE.439253.

[77] P. Fritschel, R. Bork, G. González *et al.* Readout and Ccontrol of a Power-Recycled Interferometric Gravitational-Wave Antenna. *Applied Optics*, 40:4988, 10 2001. doi: 10.1364/AO.40.004988.

[78] P. Kwee, C. Bogan, K. Danzmann *et al.* Stabilized High-Power Laser System for the Gravitational Wave Detector Advanced LIGO. *Optics Express*, 20:10617, 5 2012. doi: 10.1364/OE.20.010617.

[79] E. Morrison, B. J. Meers, D. I. Robertson *et al.* Automatic Alignment of Optical Interferometers. *Applied Optics*, 33:5041, 8 1994. doi: 10.1364/AO.33.005041.

[80] Guido Mueller. Beam Jitter Coupling in Advanced LIGO. *Optics Express*, 13:7118, 2005. doi: 10.1364/OPEX.13.007118.

[81] Edoardo Amaldi. Summary of Workshop on Gravitational Radiation. *Annals of the New York Academy of Sciences*, 336(1):322–333, 1980. doi: https://doi.org/10.1111/j.1749-6632.1980.tb15941.x.

[82] R. Schilling, L. Schnupp, W. Winkler *et al.* A Method to Blot Out Scattered Light Effects and its Application to a Gravitational Wave Detector. *Journal of Physics E: Scientific Instruments*, 14:65–70, 1981. doi: 10.1088/0022-3735/14/1/018.

[83] L. Schnupp, W. Winkler, K. Maischberger *et al.* Reduction of Noise due to Scattered Light in Gravitational Wave Antennae by Modulating the Phase of the Laser Light. *Journal of Physics E: Scientific Instruments*, 18:482–485, 1985. doi: 10.1088/0022-3735/18/6/005.

[84] E. Flanagan and K. S. Thorne. Noise due to Backscatter off Baffles, the Nearby Wall and Objects at the Far End of the Beam Tube; and Recommended Actions. Technical report, LIGO-T940063-00, 1994. URL https://dcc.ligo.org/public/0028/T940063/000/T940063-00.pdf.

[85] J.-Y. Vinet, V. Brisson and S. Braccini. Scattered Light Noise in Gravitational Wave Interferometric Detectors: Coherent Effects. *Phys. Rev. D*, 54:1276–1286, 7 1996. doi: 10.1103/PhysRevD.54.1276.

[86] J.-Y. Vinet, V. Brisson, S. Braccini *et al.* Scattered Light Noise in Gravitational Wave Interferometric Detectors: A Statistical Approach. *Phys. Rev. D*, 56: 6085–6095, 11 1997. doi: 10.1103/PhysRevD.56.6085.

[87] Stefan Hild. *Beyond the first Generation: Extending the Science Range of the Gravitational Wave Detector GEO600*. PhD thesis, Leibniz Universität Hanover, 1 2007. URL https://gwic.ligo.org/assets/docs/theses/Hild_Thesis.pdf.

[88] B. Canuel, E. Genin, G. Vajente *et al.* Displacement Noise from Back Scattering and Specular Reflection of Input Optics in Advanced Gravitational Wave Detectors. *Optics Express*, 21:10546, 2013. doi: 10.1364/oe.21.010546.

[89] D. J. Ottaway, P. Fritschel and S. J. Waldman. Impact of Upconverted Scattered Light on Advanced Interferometric Gravitational Wave Detectors. *Optics Express*, 20:8329, 2012. doi: 10.1364/OE.20.008329.

[90] S. S. Y. Chua, S. Dwyer, L. Barsotti *et al.* Impact of Backscattered Light in a Squeezing-Enhanced Interferometric Gravitational-Wave Detector. *Classical and Quantum Gravity*, 31, 2014. doi: 10.1088/0264-9381/31/3/035017.

[91] T. Accadia, F. Acernese, F. Antonucci *et al.* Noise from Scattered Light in Virgo's Second Science Run Data. *Classical and Quantum Gravity*, 27:194011, 10 2010. doi: 10.1088/0264-9381/27/19/194011.

[92] S. Soni, C. Austin, A. Effler *et al.* Reducing Scattered Light in LIGO's Third Observing Run. *Classical and Quantum Gravity*, 38:1–24, 2021. doi: 10.1088/1361-6382/abc906.

[93] Denis Martynov. *Lock Acquisition and Sensitivity Analysis of Advanced LIGO Interferometers*. PhD thesis, California Institute of Technology, January 2015.

[94] J. Marque and G. Vajente. *Stray Light Issues*, pages 275–290. Springer International Publishing, 2014. ISBN 978-3-319-03792-9. doi: 10.1007/978-3-319-03792-9_10.

[95] J. Glanzer, S. Soni, J. Spoon *et al.* Noise in the LIGO Livingston Gravitational Wave Observatory due to Trains. *Classical and Quantum Gravity*, 40:195015, 10 2023. doi: 10.1088/1361-6382/acf01f.

[96] L. K. Nuttall. Characterizing Transient Noise in the LIGO Detectors. *Philosophical Transactions of the Royal Society A: Mathematical, Physical and Engineering Sciences*, 376(2120):20170286, 2018. doi: 10.1098/rsta.2017.0286.

[97] Craig Cahillane. LIGO Hanford Noisebudget Interactive, accessed: 27-05-2025. URL https://ccahilla.github.io/lho_noisebudget.svg.

[98] O. Ballester, O. Blanch, L. Cardiel *et al.* Measurement of the Stray Light in the Advanced Virgo Input Mode Cleaner Cavity Using an Instrumented Baffle. *Classical and Quantum Gravity*, 39:115011, 6 2022. doi: 10.1088/1361-6382/ac6a9d.

[99] M. Andrés-Carcasona, O. Ballester, O. Blanch *et al.* Instrumented Baffle for the Advanced Virgo Input Mode Cleaner End Mirror. *Phys. Rev. D*, 107:062001, 3 2023. doi: 10.1103/PhysRevD.107.062001.

[100] M. Andrés-Carcasona, M. Martínez, L.M. Mir *et al.* Performance of an Instrumented Baffle Placed at the Entrance of Virgos End Mirror Vacuum Tower During O5. *Phys. Rev. D*, 111:042001, 2 2025. doi: 10.1103/PhysRevD.111.042001.

[101] M. Andrés-Carcasona, A. Macquet, M. Martínez *et al.* Study of Scattered Light in the Main Arms of the Einstein Telescope Gravitational Wave Detector. *Phys. Rev. D*, 108:102001, Nov 2023. doi: 10.1103/PhysRevD.108.102001.

[102] A. Romero-Rodríguez, M. Martínez, L. M. Mir *et al.* Determination of the Stray Light-Induced Noise from the Baffle in the Cryogenic Trapping Area of Advanced Virgo in O5. *Galaxies*, 10:86, 8 2022. doi: 10.3390/galaxies10040086.

[103] H. Lück, J. Degallaix, H. Grote *et al.* Opto-Mechanical Frequency Shifting of Scattered Light. *Journal of Optics A: Pure and Applied Optics*, 10:85004, 2008. doi: 10.1088/1464-4258/10/8/085004.

[104] S. Steinlechner, J. Bauchrowitz, M. Meinders *et al.* Quantum-Dense Metrology. *Nature Photonics*, 7:626–629, 2013. doi: 10.1038/nphoton.2013.150.

[105] M. Meinders and R. Schnabel. Sensitivity Improvement of a Laser Interferometer Limited by Inelastic Back-Scattering, Employing Dual Readout. *Classical and Quantum Gravity*, 32, 2015. doi: 10.1088/0264-9381/32/19/195004.

[106] M. Ast, S. Steinlechner and R. Schnabel. Reduction of Classical Measurement Noise via Quantum-Dense Metrology. *Phys. Rev. Lett.*, 117:180801, 2016. doi: 10.1103/PhysRevLett.117.180801.

[107] Melanie Ast. *Quantum-dense metrology for substraction of back-scatter disturbances in gravitational-wave detection.* PhD thesis, Leibniz Universität Hannover, 2017. URL https://repo.uni-hannover.de/handle/123456789/8981.

[108] P. Fritschel, M. Evans and V. Frolov. Balanced Homodyne Readout for Quantum Limited Gravitational Wave Detectors. *Optics Express*, 22:4224, 2 2014. doi: 10.1364/oe.22.004224.

[109] Frank Steier. *Interferometry Techniques for Spaceborne Gravitational Wave Detectors.* PhD thesis, Leibniz Universität Hannover, 2008. URL https://repo.uni-hannover.de/handle/123456789/7197.

[110] R. Fleddermann, C. Diekmann, F. Steier *et al.* Sub-pm$\sqrt{\text{Hz}}^{-1}$ Non-Reciprocal Noise in the LISA Backlink Fiber. *Classical and Quantum Gravity*, 35:75007, 4 2018. doi: 10.1088/1361-6382/aaa276.

[111] M. Wąs, R. Gouaty and R. Bonnand. End Benches Scattered Light Modelling and Subtraction in Advanced Virgo. *Classical and Quantum Gravity*, 38:75020, 4 2021. doi: 10.1088/1361-6382/abe759.

[112] André Lohde. Advanced Scattered Light Noise Supression Techniques in Interferometric Gravitational Wave Detection. Master's thesis, University of Hamburg, 8 2023.

[113] Mark Fox. *Quantum Optics: An Introduction.* Oxford University Press, 04 2006. doi: 10.1093/oso/9780198566724.001.0001.

[114] Peter D. Welch. The Use of Fast Fourier Transform for the Estimation of Power Spectra: A Method Based on Time Averaging Over Short, Modified Periodograms. *IEEE Transactions on Audio and Electroacoustics*, 15:70–73, 6 1967. doi: 10.1109/TAU.1967.1161901.

[115] T. Westphal, G. Bergmann, A. Bertolini *et al.* Design of the 10 m AEI Prototype Facility for Interferometry Studies. *Applied Physics B*, 106:551–557, 3 2012. doi: 10.1007/s00340-012-4878-z.

[116] H. Vahlbruch, D. Wilken, M. Mehmet *et al.* Laser Power Stabilization Beyond the Shot Noise Limit Using Squeezed Light. *Phys. Rev. Lett.*, 121:173601, 10 2018. doi: 10.1103/PhysRevLett.121.173601.

[117] M. Trad Nery, J. R. Venneberg, N. Aggarwal *et al.* Laser Power Stabilization via Radiation Pressure. *Optics Letters*, 46:1946, 4 2021. doi: 10.1364/OL.422614.

[118] F. Acernese, M. Agathos, A. Ain *et al.* Calibration of Advanced Virgo and Reconstruction of the Detector Strain h(t) During the Observing Run O3. *Classical and Quantum Gravity*, 39:045006, 2 2022. doi: 10.1088/1361-6382/ac3c8e.

[119] Daniel Dewey. *A Search for Astronomical Gravitational Radiation with an Interferometric Borad Band Antenna*. PhD thesis, Massachusetts Institute of Technology, 1986. URL https://hdl.handle.net/1721.1/123081.

[120] Pat. No. US2292387, *Secret communication system*, Hedy Kiesler Markey and George Antheil, 8 1941, USPTO. URL https://patents.google.com/patent/US2292387A/en.

[121] J.G. Proakis and M. Salehi. *Communication Systems Engineering*. Prentice Hall International Editions. Prentice Hall, 2002. ISBN 9780130617934. URL https://books.google.se/books?id=ydi1QgAACAAJ.

[122] Ronald Hugh Barker. Group Synchronization of Binary Digital System. *Communication theory*, pages 273–287, 1953.

[123] Robert Gold. Optimal Binary Sequences for Spread Spectrum Multiplexing. *IEEE Transactions on Information Theory*, IT-3:619–621, 1967. doi: 10.1109/TIT.1967.1054048.

[124] Tadao Kasami. Some Lower Bounds on the Minimum Weight of Cyclic Codes of Composite Length. *IEEE Transactions on Information Theory*, 14:814–818, 11 1968. doi: 10.1109/TIT.1968.1054233.

[125] M. G. Parker, K. G. Paterson and C. Tellambura. *Golay Complementary Sequences*. John Wiley & Sons, Ltd, 2003. ISBN 9780471219286. doi: 10.1002/0471219282.eot367.

[126] Solomon. W. Golomb. *Shift Register Sequences*. Aegean Park Press, 1982. ISBN 9780894120480.

[127] Solomon W. Golomb. On the Classification of Balanced Binary Sequences of Period $2^n - 1$; (Corresp.). *IEEE Transactions on Information Theory*, 26:730–732, 11 1980. doi: 10.1109/TIT.1980.1056265.

[128] D. V. Sarwate and M. B. Pursley. Crosscorrelation Properties of Pseudorandom and Related Sequences. *Proceedings of the IEEE*, 68:593–619, 1980. doi: 10.1109/PROC.1980.11697.

[129] A. J Sutton, K. McKenzie, B. Ware *et al.* Improved Optical Ranging for Space Based Gravitational Wave Detection. *Classical and Quantum Gravity*, 30:075008, 3 2013. doi: 10.1088/0264-9381/30/7/075008.

[130] Daniel A. Shaddock. Digitally Enhanced Heterodyne Interferometry. *Optics Letters*, 32:3355, 11 2007. doi: 10.1364/ol.32.003355.

[131] D. M. R. Wuchenich, T. T.-Y. Lam, J. H. Chow *et al.* Laser Frequency Noise Immunity in Multiplexed Displacement Sensing. *Optics Letters*, 36:672, 3 2011. doi: 10.1364/OL.36.000672.

[132] G. de Vine, D. S. Rabeling, B. Slagmolen *et al.* Picometer Level Displacement Metrology with Digitally Enhanced Heterodyne Interferometry. *Optics Express, Vol. 17, Issue 2, pp. 828-837*, 17:828–837, 1 2009. doi: 10.1364/OE.17.000828.

[133] O. P. Lay, S. Dubovitsky, D. A. Shaddock *et al.* Coherent Range-Gated Laser Displacement Metrology with Compact Optical Head. *Optics Letters*, 32:2933, 10 2007. doi: 10.1364/OL.32.002933.

[134] K.-S. Isleif, O. Gerberding, S. Köhlenbeck *et al.* Highspeed Multiplexed Heterodyne Interferometry. *Optics Express*, 22:24689, 2014. doi: 10.1364/oe.22.024689.

[135] A. J. Sutton, O. Gerberding, G. Heinzel *et al.* Digitally Enhanced Homodyne Interferometry. *Optics Express*, 20:22195, 9 2012. doi: 10.1364/oe.20.022195.

[136] A. Dey, P. G. Sibley, J. Wong *et al.* Hybrid Homodyne Digital Interferometry. *Optica Sensing Congress 2023 (AIS, FTS, HISE, Sensors, ES) (2023), paper SW3B.3*, page SW3B.3, 7 2023. doi: 10.1364/SENSORS.2023.SW3B.3.

[137] Andrew J. H. Sutton. *Digital Techniques for Coherent Optical Metrology*. PhD thesis, Australian National University, 2013. URL http://hdl.handle.net/1885/151725.

[138] P. G. Sibley, R. L. Ward, L. E. Roberts *et al.* Crosstalk Reduction for Multi-Channel Optical Phase Metrology. *Optics Express*, 28:10400, 2020. doi: 10.1364/oe.388381.

[139] A. Dey, Y. Zhang, J. Wong *et al.* Algebraic Cancellation of Inter-Channel Crosstalk in Multiplexed Heterodyne Interferometry. *Optics Letters*, 10 2021. doi: 10.1364/OL.444116.

[140] J. T. Spollard, L. E. Roberts, P. G. Sibley *et al.* Improved Cross-Talk Suppression for Digitally Enhanced Interferometry Using Golay Complementary Pairs. *Optics Letters*, 47:1570, 4 2022. doi: 10.1364/ol.448668.

[141] C. P. Bandutunga, Y. Zhang, T. G. Mcrae *et al.* Coherent Rayleigh Backscatter Phase Noise in Digitally Enhanced Fiber Interferometers. *Journal of Lightwave Technology*, 39:2625–2630, 4 2021. doi: 10.1109/JLT.2021.3049567.

[142] A. Dey, P. G. Sibley, J. Wong *et al.* Common-Mode Phase Noise Suppression with an Open-Loop Differential Phasemeter. *Optics Express*, 32:48276, 12 2024. doi: 10.1364/OE.545972.

[143] J. Wong, C. P. Bandutunga, Y. Zhang *et al.* Digitally Enhanced Molecular Dispersion Spectroscopy. *Optics Letters*, 45:6290, 11 2020. doi: 10.1364/OL.409721.

[144] J. Wong, C. P. Bandutunga, P. Singh *et al.* Molecular Dispersion Spectroscopy Using a Code-Division-Multiplexed Optical Carrier. *Physical Review Applied*, 19: 044027, 4 2023. doi: 10.1103/PhysRevApplied.19.044027.

[145] J. Wong, C. P. Bandutunga, M. Gray *et al.* Dispersion Spectroscopy Using a Code Division Multiplexed Re-Entrant Delay Line. *Optica Sensing Congress 2023 (AIS, FTS, HISE, Sensors, ES) (2023), paper SW3B.5*, page SW3B.5, 7 2023. doi: 10.1364/SENSORS.2023.SW3B.5.

[146] G. de Vine, K. McKenzie, B. Ware *et al.* Simplified Optical Payload with Digital Interferometry. Technical report, Jet Propulsion Laboratory, 11 2011. URL https://pcos.gsfc.nasa.gov/studies/architecting/grav-wave/submissions/GWRFI-0006-Vine.pdf.

[147] G. de Vine, D. Wuchenich, B. Ware *et al.* High-Speed Digital Interferometry, NASA Tech Briefs NPO-47886. Technical report, NASA's Jet Propulsion Laboratory, 1 2012. URL https://www.techbriefs.com/component/content/article/12685-npo-47886.

[148] Eugene Hecht. *Optics*. Pearson Deutschland, 5th edition, 2016. ISBN 9781292096933.

[149] IfoCAD, accessed: 27-05-2025. URL https://www.aei.mpg.de/ifocad.

[150] G. Wanner, G. Heinzel, E. Kochkina *et al.* Methods for Simulating the Readout of Lengths and Angles in Laser Interferometers with Gaussian Beams. *Optics Communications*, 285:4831–4839, 11 2012. doi: 10.1016/j.optcom.2012.07.123.

[151] D. Brown, A. Freise, H. T. Cao *et al.* FINESSE, March 2025. URL https://finesse.ifosim.org/.

[152] Lise Schnupp. Presentation at European Collaboration Meeting on Interferometric Detection of Gravitational Waves. Sorrent, Italy, 1988.

[153] Leonie Christin Eggers. Suppression of Scattered Light Noise through Tunable Coherence in Sagnac-Speed-Meters. Master's thesis, University of Hamburg, 5 2024.

[154] T. J. Kane and R. L. Byer. Monolithic, Unidirectional Single-Mode Nd:YAG Ring Laser. *Optics Letters, Vol. 10, Issue 2, pp. 65-67*, 10:65–67, 2 1985. doi: 10.1364/OL.10.000065.

[155] I. Freitag, A. Tünnermann and H. Welling. Power Scaling of Diode-Pumped Monolithic Nd:YAG Lasers to Output Powers of Several Watts. *Optics Communications*, 115:51–515, 1995. doi: 10.1016/0030-4018(95)00020-9.

[156] Mephisto Lasers Ultra-Low Noise and Narrow Linewidth | Coherent, accessed: 27-05-2025. URL https://www.coherent.com/web-resources/white-paper/mephisto-lasers-wp.

[157] M. Heurs, V. M. Quetschke, B. Willke *et al.* Simultaneously Suppressing Frequency and Intensity Noise in a Nd:YAG Nonplanar Ring Oscillator by Means of the Current-Lock Technique. *Optics Letters*, 29:2148, 9 2004. doi: 10.1364/OL.29.002148.

[158] C. C. Harb, M. B. Gray, H. A. Bachor *et al.* Suppression of the Intensity Noise in a Diodepumped Neodymium:YAG Nonplanar Ring Laser. *IEEE Journal of Quantum Electronics*, 30:2907–2913, 1994. doi: 10.1109/3.362718.

[159] R. V. Pound. Electronic Frequency Stabilization of Microwave Oscillators. *Review of Scientific Instruments*, 17:490–505, 11 1946. doi: 10.1063/1.1770414.

[160] R. W. P. Drever, G. M. Ford, J. Hough *et al.* A Gravity-Wave Detector Using Optical Cavity Sensing. In *General Relativity and Gravitation 1980*, page 265, 1983.

[161] R. W. P. Drever, J. L. Hall, F. V. Kowalski *et al.* Laser Phase and Frequency Stabilization Using an Optical Resonator. *Applied Physics B Photophysics and Laser Chemistry*, 31:97–105, 6 1983. doi: 10.1007/BF00702605.

[162] Eric D. Black. An Introduction to Pound-Drever-Hall Laser Frequency Stabilization. *American Journal of Physics*, 69:79–87, 1 2001. doi: 10.1119/1.1286663.

[163] avrumw. GTX reference clock (using internal clock), 4th answer, accessed: 13-04-2025. URL https://adaptivesupport.amd.com/s/question/0D52E00006hpgHHSAY/gtx-reference-clock-using-internal-clock?language=en_US.

[164] Exail. Introduction to Exail RF Drivers and Amplifiers for Optical Modulators, 3 2024. URL https://www.exail.com/media-file/7732/tn-introducing-exail-rf-drivers.pdf.

[165] Y. Yang, C. Lu, A. P. T. Lau *et al.* A Robust and Dither-Free Technique for Controlling Driver Signal Amplitude for Stable and Arbitrary Optical Phase Modulation. *Optics Express*, 19:26353, 2011. doi: 10.1364/oe.19.026353.

[166] Yanbei Chen. Sagnac Interferometer as a Speed-Meter-Type, Quantum-Nondemolition Gravitational-Wave Detector. *Phys. Rev. D*, 67:122004, 6 2003. doi: 10.1103/PhysRevD.67.122004.

[167] P. Purdue and Y. Chen. Practical Speed Meter Designs for Quantum Nondemolition Gravitational-Wave Interferometers. *Phys. Rev. D*, 66:122004, 12 2002. doi: 10.1103/PhysRevD.66.122004.

[168] M. Wang, C. Bond, D. Brown *et al.* Realistic Polarizing Sagnac Topology with DC Readout for the Einstein Telescope. *Phys. Rev. D*, 87:96008, 5 2013. doi: 10.1103/PhysRevD.87.096008.

[169] H. Igel, K. U. Schreiber, A. Gebauer *et al.* ROMY: A Multicomponent Ring Laser for Geodesy and Geophysics. *Geophysical Journal International*, 225:684–698, 2 2021. doi: 10.1093/gji/ggaa614.

[170] W. Z. Korth, A. Heptonstall, E. D. Hall *et al.* Passive, Free-Space Heterodyne Laser Gyroscope. *Classical and Quantum Gravity*, 33:35004, 1 2016. doi: 10.1088/0264-9381/33/3/035004.

[171] K. U. Schreiber, J. Kodet, U. Hugentobler *et al.* Variations in the Earths Rotation Rate Measured with a Ring Laser Interferometer. *Nature Photonics*, 17:1054–1058, 12 2023. doi: 10.1038/s41566-023-01286-x.

[172] Teng Zhang. *Advanced Techniques for Future Generation Gravitational Wave Detectors*. PhD thesis, University of Glasgow, 7 2019. URL https://theses.gla.ac.uk/75096/.

[173] Daniela Pascucci. *On Optics Surface Imperfections and their Effects on the Sensitivity of Speed Meters*. PhD thesis, University of Glasgow, 2019. URL https://theses.gla.ac.uk/40989/.

[174] F. Giovinetti, C. Altucci, F. Bajardi *et al.* GINGERINO: A High Sensitivity Ring Laser Gyroscope for Fundamental and Quantum Physics Investigation. *Frontiers in Quantum Science and Technology*, 3:1363409, 2 2024. doi: 10.3389/frqst.2024.1363409.

[175] K. Liu, F. Zhang, Z. Li *et al.* Noise Analysis of a Passive Resonant Laser Gyroscope. *Sensors*, 20:5369, 9 2020. doi: 10.3390/s20185369.

[176] A. D.V. Di Virgilio, F. Bajardi, A. Basti *et al.* Noise Level of a Ring Laser Gyroscope in the Femto-Rad/s Range. *Phys. Rev. Lett.*, 133:13601, 7 2024. doi: 10.1103/PhysRevLett.133.013601.

[177] E. Maccioni, N. Beverini, G. Carelli *et al.* High Sensitivity Tool for Geophysical Applications: A Geometrically Locked Ring Laser Gyroscope. *Applied Optics*, 61: 9256, 11 2022. doi: 10.1364/AO.469834.

[178] R. B. Hurst, N. Rabeendran, K. U. Schreiber *et al.* Correction of Backscatter-Induced Systematic Errors in Ring Laser Gyroscopes. *Applied Optics*, 53:7610, 11 2014. doi: 10.1364/AO.53.007610.

[179] E. A. Petrukhin, I. N. Khokhlov and N. I. Khokhlov. Correlation Relationship Between the Dissipative and Conservative Backscattering Components in the Ring Resonator of a Laser Gyroscope. *Quantum Electronics*, 51:359–364, 4 2021. doi: 10.1070/QEL17466.

[180] T. Nagatsuma, G. Ducournau and C. C. Renaud. Advances in Terahertz Communications Accelerated by Photonics. *Nature Photonics*, 10:371–379, 6 2016. doi: 10.1038/nphoton.2016.65.

[181] Y. Kurosaka, K. Hirose, T. Sugiyama *et al.* Phase-Modulating Lasers Toward On-Chip Integration. *Scientific Reports*, 6:30138, 7 2016. doi: 10.1038/srep30138.

[182] Y.-D. Wang, Z.-N. Tian, Y.-C. Li *et al.* Phase Customization in Photonic Integrated Circuits with Trimmed Waveguides. *Optics Letters*, 47:5889, 11 2022. doi: 10.1364/OL.474179.

[183] P.-N. Ni, P. Fu, P.-P. Chen *et al.* Spin-Decoupling of Vertical Cavity Surface-Emitting Lasers with Complete Phase Modulation Using On-Chip Integrated Jones Matrix Metasurfaces. *Nature Communications*, 13:7795, 12 2022. doi: 10.1038/s41467-022-34977-0.

[184] Y. Zhang, M. Menotti, K. Tan *et al.* Squeezed Light From a Nanophotonic Molecule. *Nature Communications*, 12:2233, 4 2021. doi: 10.1038/s41467-021-22540-2.

[185] Farit Yavdatovich Khalili. Reducing the Mirrors Coating Noise in Laser Gravitational-Wave Antennae by Means of Double Mirrors. *Physics Letters A*, 334: 67–72, 1 2005. doi: 10.1016/j.physleta.2004.10.078.

[186] A. G. Gurkovsky, D. Heinert, S. Hild *et al.* Reducing Thermal Noise in Future Gravitational Wave Detectors by Employing Khalili Etalons. *Physics Letters A*, 375:4147–4157, 11 2011. doi: 10.1016/j.physleta.2011.07.063.

[187] M. Shi, Z. Wu, J. Li *et al.* High-Power Narrow-Linewidth Fiber Lasers Using Optical Spectrum Broadening Based on High-Order Phase Modulation of Inversion Probability-Tuning Sequence. *Optics Express*, 30:8448, 3 2022. doi: 10.1364/OE.449779.

[188] A. Flores, C. Robin, A. Lanari *et al.* Pseudo-Random Binary Sequence Phase Modulation for Narrow Linewidth, Kilowatt, Monolithic Fiber Amplifiers. *Optics Express*, 22:17735, 7 2014. doi: 10.1364/OE.22.017735.

[189] C. Robin, I. Dajani, C. Zernigue *et al.* Pseudo-Random Binary Sequency Phase Modulation in High Power Yb-Doped Fiber Amplifiers. In *Fiber Lasers X: Technology, Systems, and Applications*, volume 8601, page 86010Z, 3 2013. doi: 10.1117/12.2004486.

[190] M. Liu, Y. Yang, H. Shen *et al.* 1.27 kW, 2.2 GHz Pseudo-Random Binary Sequence Phase Modulated Fiber Amplifier with Brillouin Gain-Spectrum Overlap. *Scientific Reports*, 10:629, 1 2020. doi: 10.1038/s41598-019-57408-5.

[191] D. J. Kim, J. Koo, S. W. Jun *et al.* A 2 kW, 8 GHz-Linewidth Yb-Doped Polarization-Maintained Fiber Laser with Quasi-Flat-Top Pseudo Random Binary Sequence Phase Modulation for SBS Suppression. *Nanomaterials*, 13:1329, 4 2023. doi: 10.3390/nano13081329.

[192] F. Wellmann, M. Steinke, F. Meylahn *et al.* High Power, Single-Frequency, Monolithic Fiber Amplifier for the Next Generation of Gravitational Wave Detectors. *Optics Express*, 27:28523, 9 2019. doi: 10.1364/OE.27.028523.

[193] A. Buikema, F. Jose, S. J. Augst *et al.* Narrow-Linewidth Fiber Amplifier for Gravitational-Wave Detectors. *Optics Letters*, 44:3833, 8 2019. doi: 10.1364/OL.44.003833.

[194] F. Thies, N. Bode, P. Oppermann *et al.* Nd:YVO_4 High-Power Master Oscillator Power Amplifier Laser System for Second-Generation Gravitational Wave Detectors. *Optics Letters*, 44:719, 2 2019. doi: 10.1364/OL.44.000719.

[195] K. Arai, S. Barnum, P. Fritschel *et al.* LIGO Output Mode Cleaner Design. Technical report, LIGO-T1000276-v5, 1 2013. URL http://www.ligo.caltech.edu/.

[196] A. Staley, D. Martynov, R. Abbott *et al.* Achieving Resonance in the Advanced LIGO Gravitational-Wave Interferometer. *Classical and Quantum Gravity*, 31, 12 2014. doi: 10.1088/0264-9381/31/24/245010.

[197] K. Izumi and D. Sigg. Advanced LIGO: Length Sensing and Control in a Dual Recycled Interferometric Gravitational Wave Antenna. *Classical and Quantum Gravity*, 34, 1 2017. doi: 10.1088/0264-9381/34/1/015001.

[198] Vaishali Badrish Adya. *Ways to Stop Mirrors From Moving Unnecessarily: Design of Advanced Gravitational Wave Detectors*. PhD thesis, Leibniz Universität Hannover, 2018. URL https://repo.uni-hannover.de/handle/123456789/3460.

[199] Fabio Bergamin. *Development of a Squeezing-Compatible Signal Recycling Cavity Control at GEO600*. PhD thesis, Leibniz Universität Hannover, 4 2024. URL https://repo.uni-hannover.de/handle/123456789/17572.

[200] D. Bersanetti, D. D. Brown, J. Casanueva *et al.* ET Optical Layout Update 2024. Technical report, ET-0443A-24, 6 2024. URL https://apps.et-gw.eu/tds/?r=19083.

[201] D. D. Brown, J. Casanueva, A. Chiummo *et al.* ET 2L Optical Layout Update 2024. Technical report, ET-0695A-24, 12 2024. URL https://apps.et-gw.eu/tds/?r=19352.

[202] E. Sanchez and C. Torrie. Layout of SLC Baffles with New 2017 SLiC Baffles. Technical report, LIGO-D1700361-V3, 2017. URL https://dcc.ligo.org/LIGO-D1700361/public.

A | Appendix

A.1 Improvements for the fiber setup

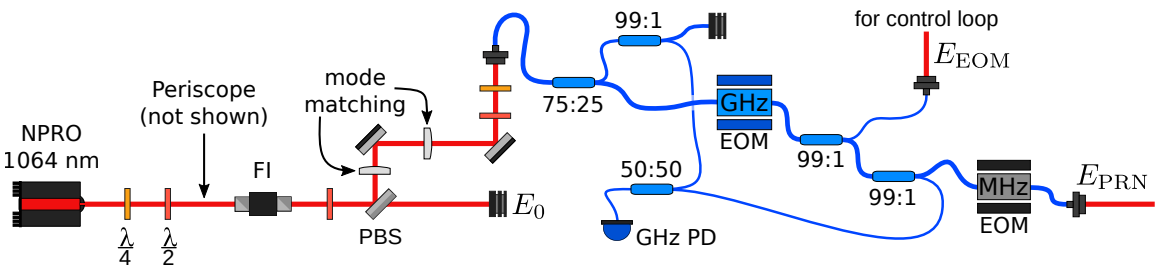

Figure A.1: Sketch showing the updated laser preparation and fiber setup with the non-functioning Heterodyne interference lock-part replaced. The proposed new setup for making use of a Mach-Zehnder GHz lock-scheme is not depicted but can be found in Fig. 7.14. In the fiber setup, only the EOM path containing both the GHz-modulator and a second modulator for adding side-bands was kept, together with the GHz-PD to measure an eye-diagram by interfering an unmodulated and a modulated beam. The for the experiments of this thesis implemented setup can be found in Fig. 7.1.

A.2 GHz modulation data

FPGA setup parameters and designs

Transceiver wizard setup summaries

2 GHz TX setup summary

Features	GT
Protocol File	Start_from_scratch
TX Line Rate (Gbps)	2
TX reference clock (MHz)	100.000
Encoding	None
TX Internal Data width	32
TX External Data width	32
TXUSRCLK (MHz)	62.5
TXUSRCLK2 (MHz)	62.5
TX Buffer Enabled	true

2.5 GHz TX setup summary

Features	GT
Protocol File	Start_from_scratch
TX Line Rate (Gbps)	2.5
TX reference clock (MHz)	100.000
Encoding	None
TX Internal Data width	32
TX External Data width	32
TXUSRCLK (MHz)	78.125
TXUSRCLK2 (MHz)	78.125
TX Buffer Enabled	true

Table A.1: Parameter used to set up the GTX transceiver wizard in Vivado for the PRN sequence generation and transmission at 2 and 2.5 GHz.

5 GHz TX setup summary	
Features	GT
Protocol File	Start_from_scratch
TX Line Rate (Gbps)	5
TX reference clock (MHz)	100.000
Encoding	None
TX Internal Data width	32
TX External Data width	32
TXUSRCLK (MHz)	156.25
TXUSRCLK2 (MHz)	156.25
TX Buffer Enabled	true

10 GHz TX setup summary	
Features	GT
Protocol File	Start_from_scratch
TX Line Rate (Gbps)	10
TX reference clock (MHz)	100.000
Encoding	None
TX Internal Data width	32
TX External Data width	32
TXUSRCLK (MHz)	312.5
TXUSRCLK2 (MHz)	312.5
TX Buffer Enabled	true

Table A.2: Parameter used to set up the GTX transceiver wizard in Vivado for the PRN sequence generation and transmission at 5 and 10 GHz.

PRN sequence generator design

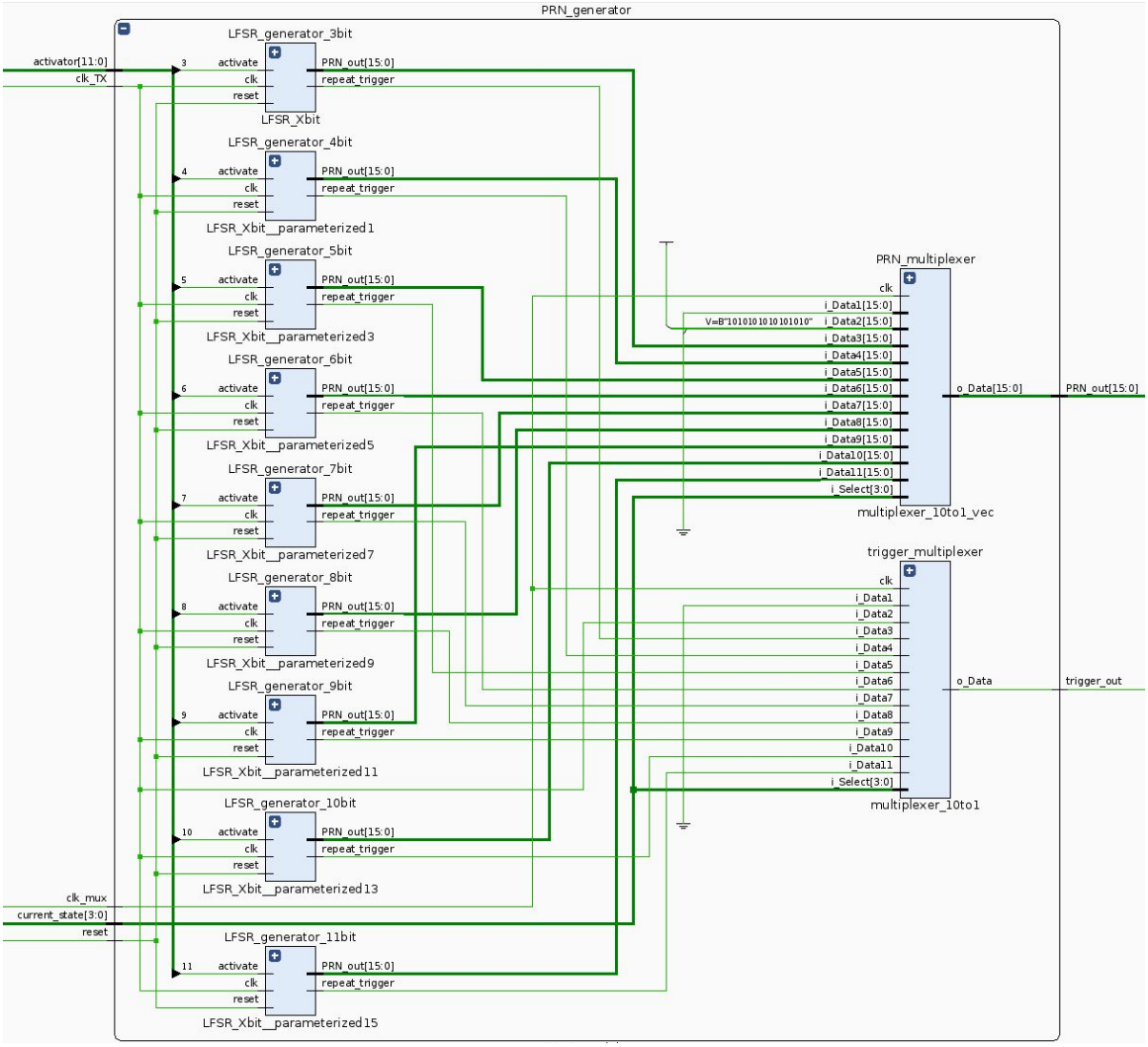

Figure A.2: Elaborated design of the PRN sequence generator used to cycle the selected sequence and send it to the transceiver with the correct width and rate for the used PRN frequency. The code describing the cycler initiated for each sequence is given below.

PRN cycler VHDL-file

Code block describing the sequence cycler, initiated in the design in Figure A.2 as "LFSR_generator_*bit".

```
library IEEE;
use IEEE.STD_LOGIC_1164.ALL;
use IEEE.NUMERIC_STD.ALL;

entity LFSR_Xbit is
  Generic (
    outputWidth                 : integer                                   := 32;
    sequenceLength              : integer;
    sequence                    : std_logic_vector
    );
  Port (
    clk                         : in std_logic;
    reset                       : in std_logic;
    activate                    : in std_logic;

    repeat_trigger              : out STD_LOGIC;
    PRN_out                     : out std_logic_vector ( outputWidth - 1 downto 0 )
  );
end LFSR_Xbit;

architecture RTL of LFSR_Xbit is

    constant vec_length         : integer                                   := sequenceLength - 1;
    constant ZERO               : std_logic_vector ( vec_length downto 0 )  := (others => '0');

    signal fullSequence         : std_logic_vector ( vec_length downto 0 );
    signal internalSequence     : unsigned ( vec_length downto 0 )          := (others => '0');
    signal start_state          : unsigned ( vec_length downto 0 );

begin

    fullSequence                <= ZERO ( vec_length downto sequence'length ) & sequence;
    start_state                 <= unsigned(fullSequence);

    PRN_out                     <= std_logic_vector(internalSequence ( outputWidth - 1 downto 0 ));

    rotate_sequence :  process ( clk, reset, activate ) begin
        if reset = '1' then
            internalSequence    <= start_state;
        elsif rising_edge(clk) and activate = '1' then
            internalSequence    <= internalSequence ror outputWidth;
        end if;

        if internalSequence = start_state and reset = '0' then
            repeat_trigger      <= '1';
        else
            repeat_trigger      <= '0';
        end if;

    end process;

end RTL;
```

ZC706 constraint file

```
# ============================================================================ #
## Constraints for ZC706 with Zynq-7000 XC7Z045 SoC (xc7z045ffg900-2)    ##
##    using GTX transceiver connected to SMA pins J35 and J34 as output ##
# ============================================================================ #

## I/O ports defintion -------------------------
# ============================================================================
# Push buttons
# SW7
set_property PACKAGE_PIN AK25       [get_ports resetButtonExternal]
set_property IOSTANDARD LVCMOS25    [get_ports resetButtonExternal]
# SW8
set_property PACKAGE_PIN R27        [get_ports toggleRightExternal]
set_property IOSTANDARD LVCMOS25    [get_ports toggleRightExternal]
# SW9
set_property PACKAGE_PIN K15        [get_ports toggleLeftExternal]
set_property IOSTANDARD LVCMOS15    [get_ports toggleLeftExternal]
# SW13
set_property PACKAGE_PIN A8         [get_ports PL_CPU_RESETExternal]
set_property IOSTANDARD LVCMOS15    [get_ports PL_CPU_RESETExternal]

# LEDs
# DS8 (left, L)
set_property PACKAGE_PIN Y21        [get_ports LEDs[3]]
set_property IOSTANDARD LVCMOS25    [get_ports LEDs[3]]
# DS9 (center, C)
set_property PACKAGE_PIN G2         [get_ports LEDs[2]]
set_property IOSTANDARD LVCMOS15    [get_ports LEDs[2]]
# DS10 (right, R)
set_property PACKAGE_PIN W21        [get_ports LEDs[1]]
set_property IOSTANDARD LVCMOS25    [get_ports LEDs[1]]
# DS35 (0, meaning furthest right)
set_property PACKAGE_PIN A17        [get_ports LEDs[0]]
set_property IOSTANDARD LVCMOS15    [get_ports LEDs[0]]

# SMA pins (not GTX)
# J67
set_property PACKAGE_PIN AD18       [get_ports SMA_PIN_P]
set_property IOSTANDARD LVCMOS25    [get_ports SMA_PIN_P]
#J 68
set_property PACKAGE_PIN AD19       [get_ports SMA_PIN_N]
set_property IOSTANDARD LVCMOS25    [get_ports SMA_PIN_N]

## clock setup ---------------------------------
# ============================================================================
create_clock -period 10.0           [get_ports Q2_CLK0_GTREFCLK_PAD_P_IN]

# GTX refrence clock SMA pins
# J31
set_property LOC W7                 [get_ports  Q2_CLK0_GTREFCLK_PAD_N_IN ]

# Add fixed 200 MHz system clock (U64)
create_clock -period 5.0            [get_ports SYSCLK_P]
set_property PACKAGE_PIN H9         [get_ports {SYSCLK_P}]
set_property IOSTANDARD LVDS        [get_ports {SYSCLK_P}]

# User Clock Constraints
```

```
set_false_path -to [get_pins -filter {REF_PIN_NAME=~*CLR} -of_objects \
        [get_cells -hierarchical -filter {NAME =~ *_txfsmresetdone_r*}]]
set_false_path -to [get_pins -filter {REF_PIN_NAME=~*D} -of_objects \
        [get_cells -hierarchical -filter {NAME =~ *_txfsmresetdone_r*}]]

############################## mgt wrapper constraints ######################
##----- Set placement for gt0_gtx_wrapper_i/GTXE2_CHANNEL ---
set_property LOC GTXE2_CHANNEL_X0Y9 [get_cells gtwizard_2GHz_i/U0/ \
        gtwizard_2GHz_init_i/gtwizard_2GHz_i/gt0_gtwizard_2GHz_i/gtxe2_i]
```

Used PRN sequences

# bits	# chips	initial state	taps	PRN sequence
3	7	'1**01**'	(0,1)	'1011100' [binary]
4	15	'10**01**'	(0,1)	'100110101111000' [binary]
5	31	'100**01**'	(0,2)	'1000110111010100001001011001111' [binary]
6	63	'1000**01**'	(0,1)	0x4314f4725bb357e0 [hex]
7	127	'10000**01**'	(0,1)	0x41851e459d4fa1c49b5bd8d2ee655fc0 [hex]
8	255	'1000**000**1'	(0,2,3,4)	*-too long to display*
9	511	'10000**000**1'	(0,4)	*-too long to display*
10	1023	'100000**000**1'	(0,3)	*-too long to display*
11	2047	'1000000**000**1'	(0,2)	*-too long to display*

Table A.3: Used LFSR setup parameter and resulting sequences. The first three sequences are given in their used binary form, the next two in hexadecimal to save space, the last four are so long that displaying them even in this form would consume too much space.

Eye-diagram of the EOM driver output

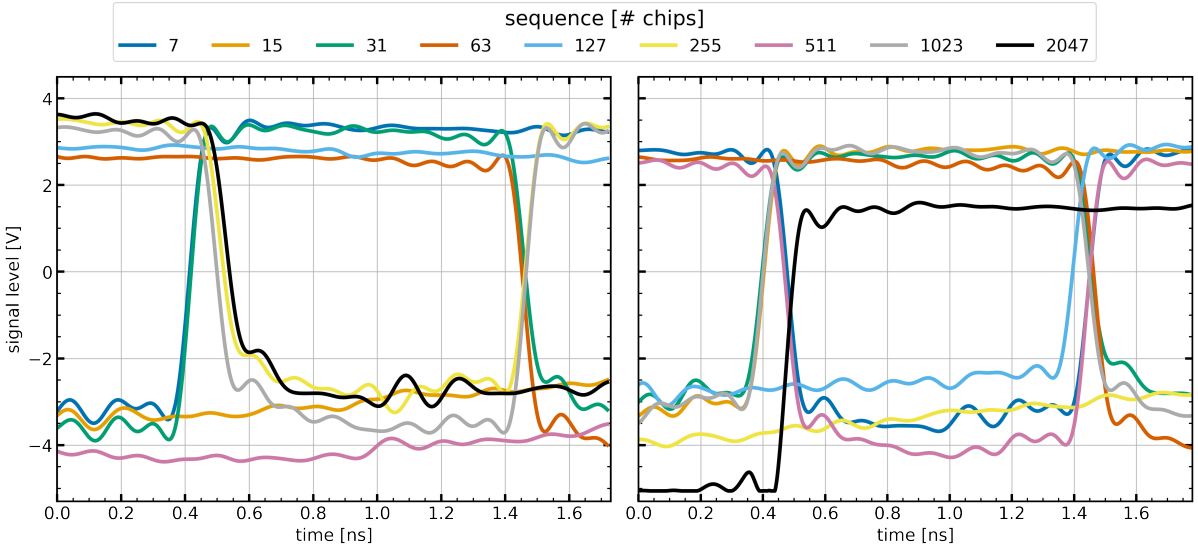

Figure A.3: Eye-diagram constructed from individual traces recorded for all sequences on an GHz-oscilloscope at the output of the GHz-EOM driver for two different gain settings.

A.3 Baffle layout of Advanced LIGO

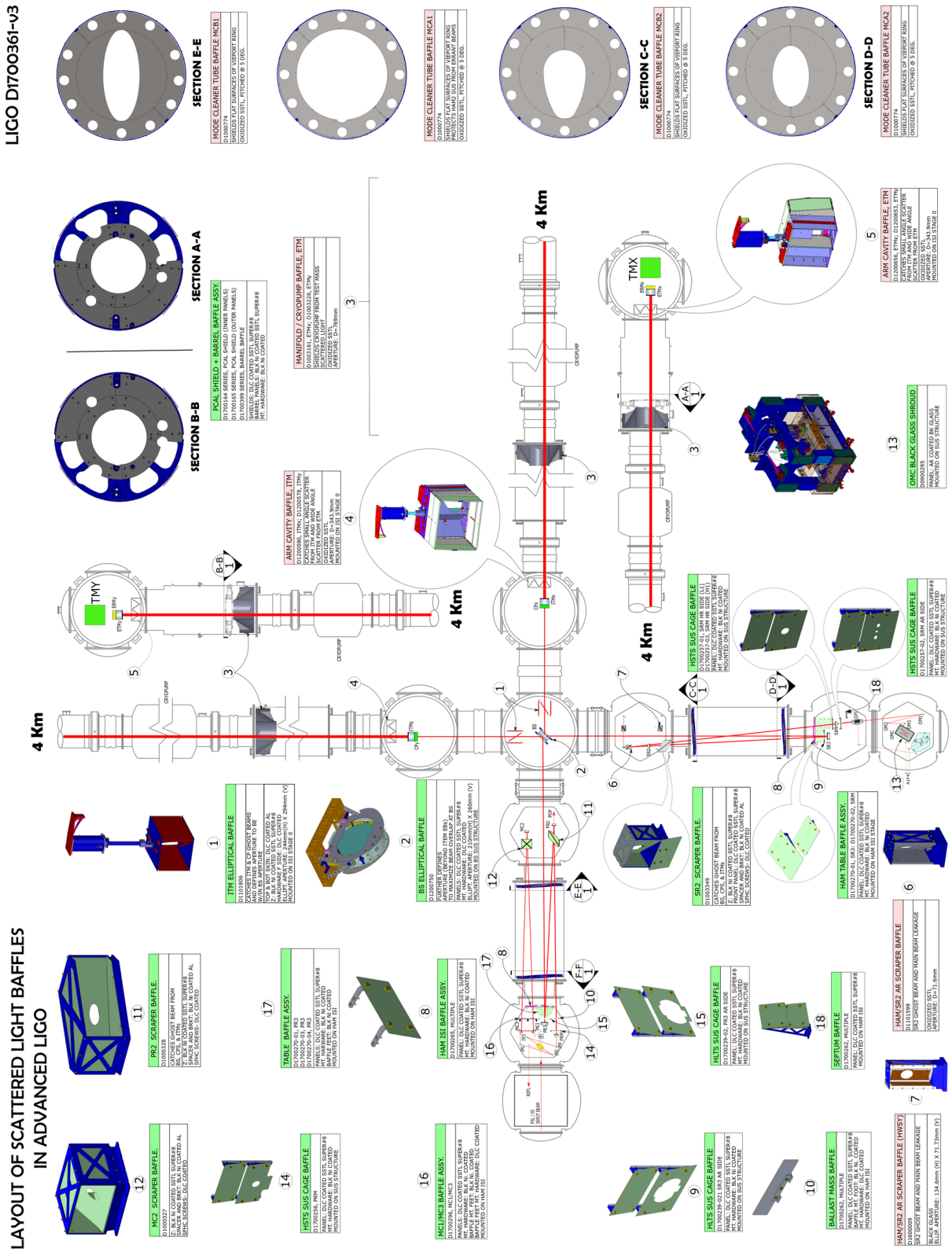

Figure A.4: Baffle layout of the advanced LIGO detectors as of 2017. Source: [202]

A.4 Control electronics

For the project presented in this work, various analog electronic circuits were built. Most of the used designs were originally developed at the Albert-Einstein-Institute at the Leibniz University in Hanover and at the Institute for Laserphysics (now Institute for Quantum Optics) at the University of Hamburg. These circuits are compatible and used with the so-called GEO-infrastructure, developed for GEO600, and include

- 2 channel HV amplifier
- Quadoffset Box (further adapted to a Hexaoffset Box)
- Servo 4 (PID controller with various placement options)
- HomoV3 w/ & w/o mixer (homodyne PD with internal subtraction and optionally mixing with an external LO signal)
- V6TUF (PD including internal mixing with an external LO signal and error-signal shaping)

The HV amplifier were observed to have degraded performance and cross-talk between channels for input signal amplitudes above $20\,\mathrm{mV_{pp}}$ at frequencies above $100\,\mathrm{kHz}$. This limited the available input signal range for most described experiment in regard to signal injection.
From the listed designs, some were adapted to better suit the needs of this project. These include

- HomoV4 w/o mixer (update of the HomoV3 to feature variable gain for the transimpedance amplifier)
- EOM driver controller (based on the Servo 4 to provide the control voltages for the used EOM driver)

Here the latter was explicitly designed to operate the two used EOMs in the experiment. For the MHz-EOM only the supply voltages are generated by the circuit. The part for the GHz-EOM provides the supply voltages and features additional outputs for the two control voltages. These are internally limited to not exceed the absolute maximum rating of the driver and adjustable with a fine-tuning potentiometer. Further, it features PID controller for both voltages that take in an external error signal. If desired, signals from external PID controller can alternatively be used and fed into the circuit. For both EOMs, all needed voltages are provided to the driver by a 4-pin LEMO connector respectively.
All circuits listed are stored and provided internally in a dedicated git-repository.

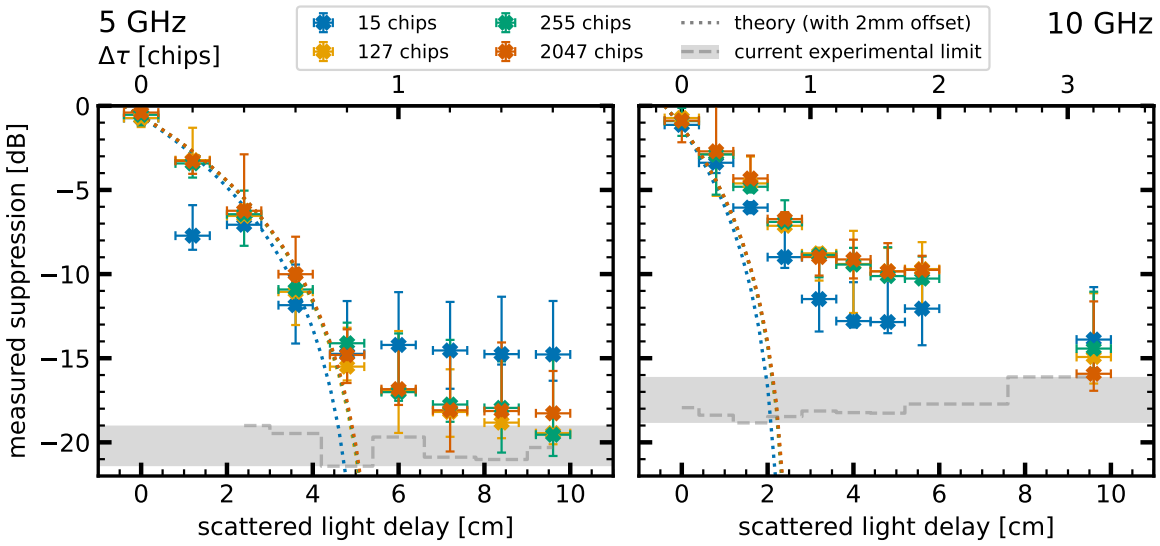

Figure A.5: Measurements showing the dependence of reached suppression on the relative delay of the scattered light for $f_{\mathrm{PRN}} = 5\,\mathrm{GHz}$ (left) and $f_{\mathrm{PRN}} = 10\,\mathrm{GHz}$ (right) and several different sequence length at each frequency. For all measurements, the suppression saturated before the theoretical estimate was reached. The suppression also increased slower with increasing delay than estimated for all except the 15 chips long sequence at 5 GHz. While this 15 chips sequence reached neither its estimate nor the experimental limit, all other sequences at this frequency eventually did reach the experimental limit. For the 10 GHz measurements this limit was only approached for delays longer than three chips.

*Corrected theory estimate with 2 mm offset added post submission.

A.5 Further Michelson interferometer results

Figure A.5 shows additional results gathered in the Michelson interferometer setup prior to optimizations done for the measurements presented in Sec. 8.1.2. The data here shows the measured suppression depending on the relative delay of the scattered light to the interferometer. On the left side plotted for $f_{\mathrm{PRN}} = 5\,\mathrm{GHz}$, here all sequences roughly followed the estimate of the shortest 15 chips long sequence. This shortest sequence then leveled of first towards 15 dB suppression. The three other shown sequences approached the experimental suppression limit at 19 dB for delays around one and a half chips but far off from the expected maximum suppression. While the 15 chips long sequence reached its maximal suppression already after one chip of relative delay, this maximum was only around 60 % of the theoretical estimate. The data for $f_{\mathrm{PRN}} = 10\,\mathrm{GHz}$ showed similar but more deteriorated behavior, here the 15 chips sequence again reached its maximum suppression after slightly more than one chip relative delay. However, this maximum was only around 12.5 dB at this PRN frequency, only a little over half the theoretical estimate. Further, all other shown sequences did not reach the experimental limitations and started slowly leveling off around 10 dB for most of the probed scatter delays. Only for longer delays of more than three chips did they approach the limit caused by the strength of the injected scattered light.

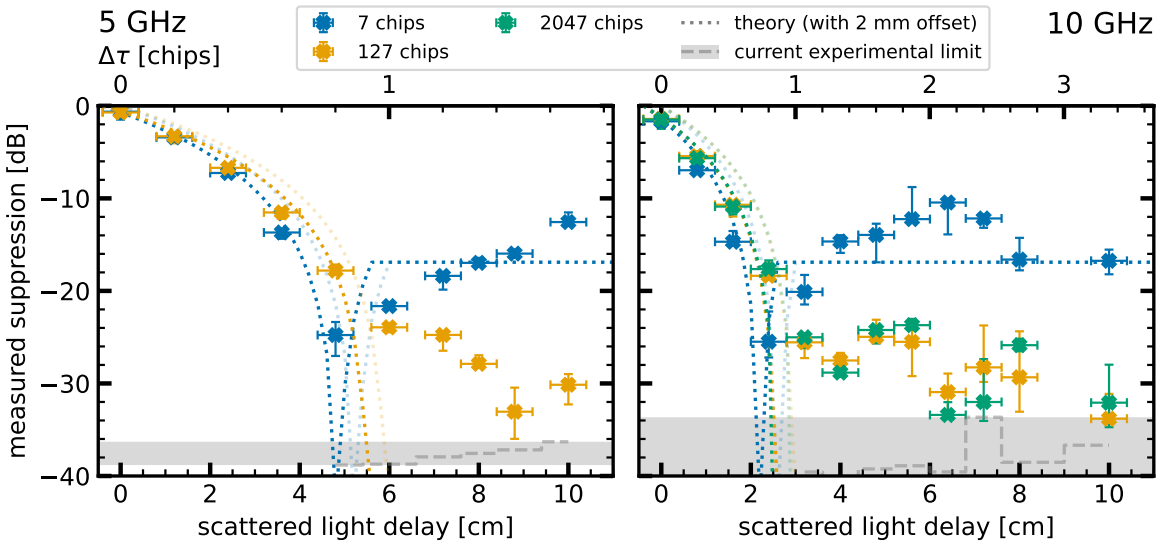

Figure A.6: Version of Fig. 8.8 with corrected theoretical estimate including a static 2 mm offset added post submission. Theory lines without offset are also added grayed out.

A.5.1 Corrected theoretical estimate

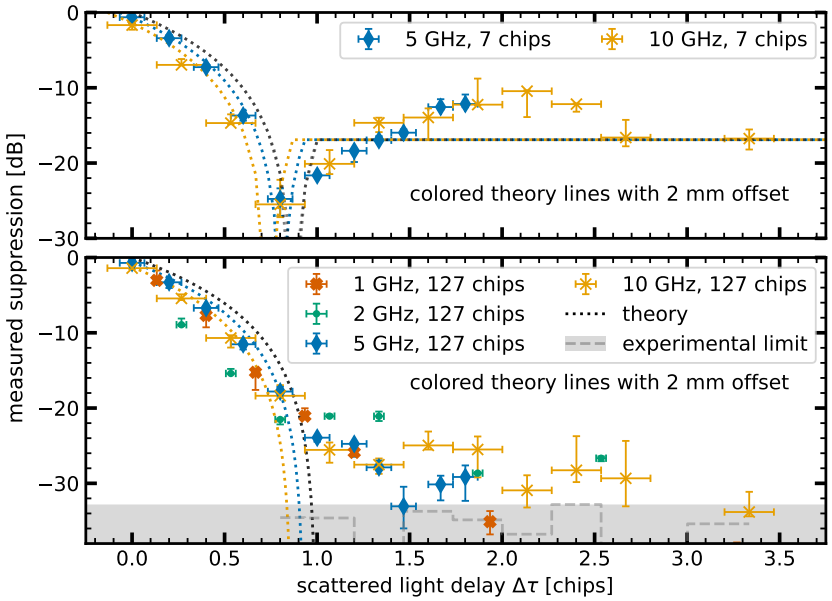

Figure A.7: Version of Fig. 8.10 with corrected theoretical estimate including a static 2 mm offset added post submission. The black theory lines do not include an offset, the colored ones do.

The theoretical estimate used for plots showing measurements of straylight suppression depending on its relative delay in the thesis was oversimplified. It did not take the correct shape of the ACF over the first chip length of delay into account and was thus missing some features. Most prominently the zero-crossing close to a delay of the length of one chip. This was corrected post submission and taken into account in the updated plots shown in Fig. A.6 and Fig. A.7. The former is also adapted for the corresponding publication (10.48550/arXiv.2508.00503). With a static offset of 2 mm added to the physical base length of the straylight path, most data points follow the new theoretical estimate.

A.6 Moku setups

Moku:Lab *Laser Lock Box* setup for interferometer lock

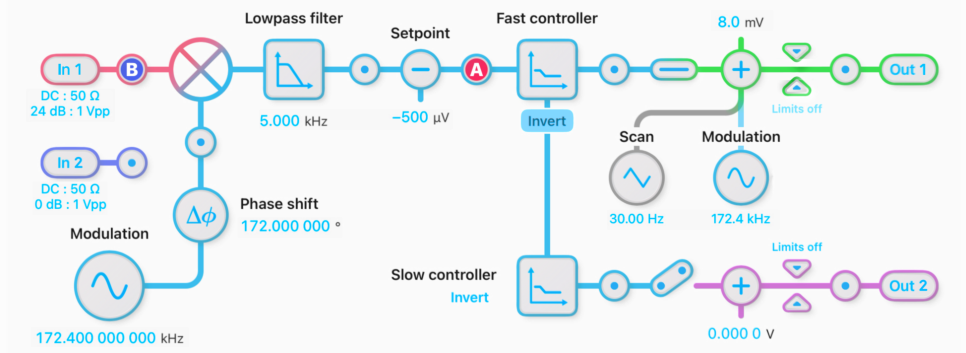

parameter	f_{dither}	$\Delta\phi$	f_{lo}	setpoint	P-value	I-value	IS-value	offset
value	172.4 kHz	172.0°	5 kHz	−500 µV	−5.0 dB	692.8 Hz	49.9 dB	8.0 mV

Figure A.8: Screenshot of the Moku:Lab *Laser Lock Box* used to lock the interferometer to dark-fringe operating point and a list of all parameters set for the lock. (In 1) was the voltage from an in-house built variable gain PD (HomoV4 without mixer). As this circuit was designed for a BHD, it had two PDs of which one was blocked. (Out 1) was connected to an in-house build HV amplifier driving the PZT mirror in one of the interferometer arms.

Moku:Pro Multi Instrument for the PRMI-setup

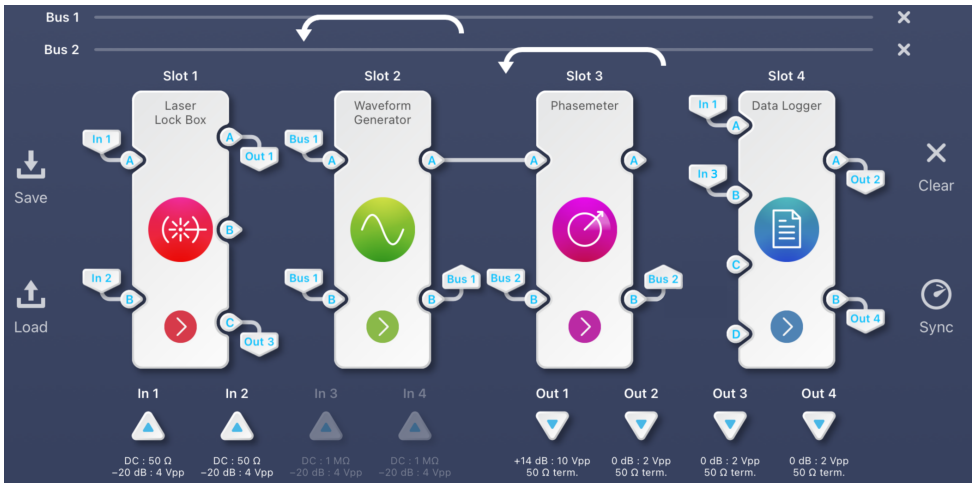

Figure A.9: Screenshot of the Moku:Pro *Multi Instrument* setup for measurements with the PRMI. Input 1 (In 1) was connected to a PD in reflection of the PRC, Input 2 (In 2) to a PD in transmission of the PRC, Input 3 (In 3) to a PD at the asymmetric port of the interferometer. Output 1 (Out 1) was connected to the laser heads frequency modulation input, Output 2 (Out 2) to the PZT mirror in one of the interferometer arms (in addition to the locking signal generated in the *Laser Lock Box* of the Moku:Lab), Output 3 (Out 3) was connected to the MHz-EOM driver used to add side-bands for PDH-locking to the laser and Output 4 (Out 4) was connected to the PZT mirror in the scattered light arm. The looping of the outputs of both the *Waveform Generator* and the *Phasemeter* via Bus 1 and 2 respectively had no effect and was only done as the outputs needed to be connected for the setup to function.

A.7 Additional PRMI results

In addition to the results shown in Chapter 10 obtained in the PRMI-setup, more data was taken which has, however, worse quality. As in these data more parameter could be investigated even though the results are less optimal, they are summarized here.

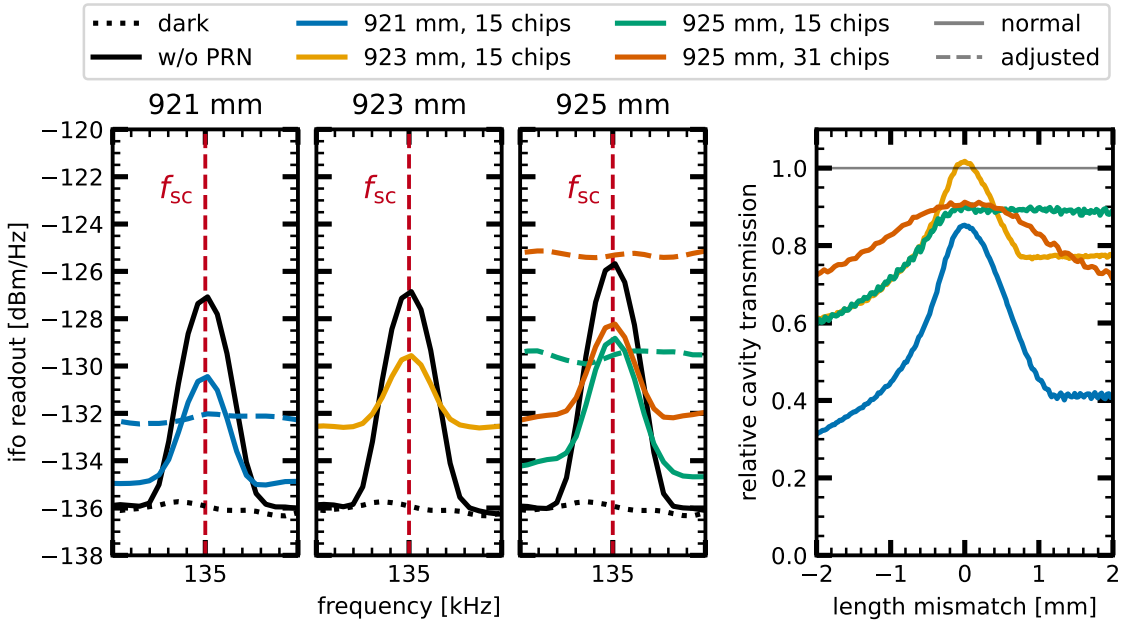

Figure A.10: Suppression measured after attempts to optimize the PRMI-setup. In the left three panels suppression of the scatter peak are shown for different length settings of the adjustable interferometer arm and different adjustments of the modulation depth. On the right are scans over the PRC-resonance introduced by *tunable coherence* shown for the same different length settings. Blue shows the suppression and scan of the 15 chips sequence at a length of 921 mm with the solid line showing the standard modulation depth with best transmitted power achieved on resonance and the dashed line showing results for modulation optimized to reach best suppression in time-series data of a low frequency ramp added onto the scattered light. Yellow shows only the scan and suppression with normal modulation depth setting for a length of 923 mm and green shows the same as blue but for a length of 925 mm. In addition, the orange curve shows the same for the 31 chips long sequence at 925 mm. All data was taken with $f_{\mathrm{PRN}} = 5\,\mathrm{GHz}$.

First in Figure A.10 data is shown recorded in the current setup which was attempted to be optimized. This data was recorded with $f_{\mathrm{PRN}} = 5\,\mathrm{GHz}$ and different length settings of the adjustable interferometer arm. In addition to the PRC-resonance scans with the 15 chips long sequence at different length settings shown on the right, the three left plots show the corresponding suppression of the scattered light for these length settings. For most, two different modulation depth settings were used, *normal* meaning the setting for which the scan was recorded and the transmitted power was maximal and *adjusted* meaning optimized to the observed suppression of the ramp signal used on the scattered light (see Sec. 8.1.1). For the *adjusted* modulation depth, the scattered light peak van-

ished, however, only for an arm length setting of 921 mm this is not caused by the raised noise-floor but actual suppression of the scattered light. Further, even here the noise-floor increases, nevertheless this length setting shows the best performance in suppression and least influence of the unexplained scan abnormality. Even though the scan at 921 mm is least affected by the stagnation to one side, it reaches only around 85 % relative transmission while the scan at 923 mm reaches full transmission. However, at 923 mm length, the noise-floor increase is the highest with the unadjusted modulation depth together with the 31 chip long sequence only shown for a length setting of 925 mm. All in all, the data shown in this figure is inconclusive, showing multiple issues and influence of the sub-optimal alignment.

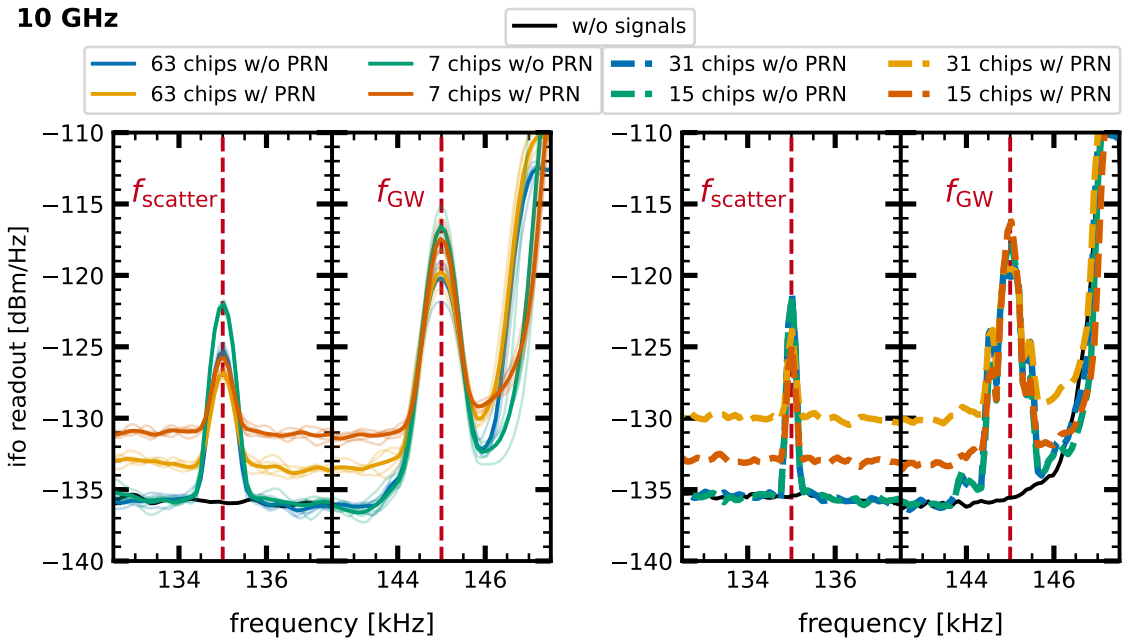

Figure A.11: Suppression measured in the PRMI-setup after optimization attempts at 10 GHz PRN frequency. On the left measured as traces for the longest 63 chips long and the shortest 7 chips long sequence, on the right measured as time-series for the 31 chips long and 15 chips long sequence. All data experience some additional noise at frequencies above the simulated GW-signal injected into the interferometer at 145 kHz which is also present when both the scatter and simulated signal are turned off. While the scatter peak is suppressed in all data, the peak at 145 kHz also fluctuates and the noise-floor increases for all measurements with PRN modulation active.

In Figure A.11 suppression measurements at 10 GHz PRN frequency are shown for all sequences fitting the PRC at this frequency. In addition to all the previously discussed problems, the spectrum also showed some additional noise above the frequency of the simulated GW-signal injected directly into the interferometer. This noise is also present when both the scattered light and simulated signal are turned of and showed up in some other measurements as well. However, in those it was further separated from the used signal frequencies. As other suppression measurements, the data showed increases in noise-

floor and fluctuations in the simulated signal peak, but also suppression of the scattered light with varying success. At a PRN frequency of 10 GHz the setup was most sensitive to any imperfections and mismatches and thus misalignment of any kind, amplifying the problems already seen in data at lower PRN-frequencies. Nevertheless, it is encouraging that some suppression is observable regardless of the limitations present in the current setup.

Eidesstattliche Versicherung

Hiermit versichere ich an Eides statt, die vorliegende Dissertationsschrift selbst verfasst und keine anderen als die angegebenen Hilfsmittel und Quellen benutzt zu haben.

Sofern im Zuge der Erstellung der vorliegenden Dissertationsschrift generative Künstliche Intelligenz (gKI) basierte elektronische Hilfsmittel verwendet wurden, versichere ich, dass meine eigene Leistung im Vordergrund stand und dass eine vollständige Dokumentation aller verwendeten Hilfsmittel gemäß der Guten wissenschaftlichen Praxis vorliegt. Ich trage die Verantwortung für eventuell durch die gKI generierte fehlerhafte oder verzerrte Inhalte, fehlerhafte Referenzen, Verstöße gegen das Datenschutz- und Urheberrecht oder Plagiate.

14. Oktober 2025	
Datum	Unterschrift des Doktoranden